National Library
of Canada

Acquisitions and
Bibliographic Services Branch

395 Wellington Street
Ottawa, Ontario
K1A 0N4

Bibliothèque nationale
du Canada

Direction des acquisitions et
des services bibliographiques

395, rue Wellington
Ottawa (Ontario)
K1A 0N4

Your file Votre référence

Our file Notre référence

NOTICE

The quality of this microform is heavily dependent upon the quality of the original thesis submitted for microfilming. Every effort has been made to ensure the highest quality of reproduction possible.

If pages are missing, contact the university which granted the degree.

Some pages may have indistinct print especially if the original pages were typed with a poor typewriter ribbon or if the university sent us an inferior photocopy.

AVIS

La qualité de cette microforme dépend grandement de la qualité de la thèse soumise au microfilmage. Nous avons tout fait pour assurer une qualité supérieure de reproduction.

S'il manque des pages, veuillez communiquer avec l'université qui a conféré le grade.

La qualité d'impression de certaines pages peut laisser à désirer, surtout si les pages originales ont été dactylographiées à l'aide d'un ruban usé ou si l'université nous a fait parvenir une photocopie de qualité inférieure.

Canada

Numerical Simulation of the Arctic Sea Ice and Ocean Circulation

by

© David M. Holland, M.Sc.

A Thesis Submitted to the School of Graduate Studies
in partial fulfilment of the requirements
for the degree of
Doctor of Philosophy

Department of Atmospheric and Oceanic Sciences and
Centre for Climate and Global Change Research
McGill University, Montréal
April, 1993

ISBN 0-315-87861-4

Abstract

A numerical model study of the seasonal cycle of sea-ice cover and ocean circulation in the Arctic Ocean is presented. The investigation is carried out in four parts using the coupled sea ice - ocean model of Oberhuber (1993a). The Oberhuber model is the first global ocean general circulation model to use Lagrangian isopycnal coordinates. First, a sensitivity study is given of the sea-ice model, which is both dynamic and thermodynamic. The robustness of the sea-ice component in an uncoupled mode is demonstrated. Secondly, the addition of a snow model to the coupled sea ice - ocean model of Oberhuber (1993a) is described. The inclusion of snow is shown to be important for obtaining a good simulation of ice thickness in both the Arctic and the Antarctic. Thirdly, the coupled ice-ocean model is used to investigate the general circulation of the Arctic Ocean and its connection with the North Atlantic. The cyclonic motion of the Atlantic layer within the Arctic is correctly simulated. Fourthly, a sensitivity study of the Arctic mixed-layer circulation is presented.

Résumé

Une étude d'une simulation numérique du cycle saisonnier de la couverture de glace et de la circulation océanique dans l'océan arctique est présenté. L'analyse est réalisée en quatre parties en utilisant le modèle couplé glace-océan de Oberhuber (1993a). Le modèle de Oberhuber est le premier modèle général océanique global à utiliser les coordonnées de Lagrange isopycnales. Premièrement, une étude de sensibilité du modèle de glace, qui est dynamique et thermodynamique, est donnée. La robustesse de la composante de glace dans un mode non-couplé est démontrée. Deuxièmement, l'addition d'un modèle de neige au modèle couplé glace-océan de Oberhuber (1993a) est décrite. Il est montré que l'inclusion d'une composante de neige est particulièrement importante pour obtenir une bonne simulation de l'épaisseur de glace en arctique et en antarctique. Troisièrement, le modèle couplé est utilisé pour analyser la circulation générale de l'océan arctique et sa connection avec l'atlantique nord. Le mouvement cyclonique de la couche atlantique à l'intérieur de l'arctique est simulé correctement. Quatrièmement, une étude de la sensibilité de la circulation de la couche mélangée de l'arctique est présentée.

To Denise

When I heard the learn'd astronomer,
When the proofs, the figures, were ranged in columns before me,
When I was shown the charts and diagrams, to add, divide, and measure them,
When I sitting heard the astronomer where he lectured with much applause in the lecture-room,
How soon unaccountable I became tired and sick,
Till rising and gliding out I wander'd off by myself,
In the mystical moist night-air, and from time to time,
Look'd up in perfect silence at the stars.

Walt Whitman

Table of Contents

Statement of Originality

Sensitivity Study of an Uncoupled Sea-Ice Model

- A systematic and comprehensive investigation of the sensitivity of a dynamic thermodynamic sea-ice model has been carried out for the first time.
- New sensitivity studies of the sea-ice model with respect to numerical aspects, initial conditions, diffusion coefficients, ocean albedo, cloud cover, maximum ice compactness, drag coefficient, and mixed layer parameterizations have been performed.

(A research paper based on this work has been published (Holland *et al.*, 1993)).

A Thermodynamic-Dynamic Sea-Ice Model with Snow

- The addition of a snow model to a global ice-ocean model is shown to be important for simulating realistic ice thickness in both hemispheres.
- It is found that the inclusion of heat content in the ice temperature equation allows the thick Arctic ice to have a memory of the interannual variations in the thermal forcing.

(A book chapter based on this work is now in press (Oberhuber *et al.*, 1993)).

General Circulation of the Arctic Ocean

- The first thorough investigation of the general circulation of Arctic Ocean with a coupled snow - sea ice - mixed layer - isopycnal ocean general circulation model has been performed.
- For the first time, the cyclonic flow of Atlantic layer water has been simulated, which is in opposition to the anticyclonic circulation of the mixed layer.
- It is shown that the modelled Atlantic-layer and deep-ocean flow are strongly constrained by topography.
- The depth-averaged flow in the Canadian basin is found to be weakly cyclonic; the depth-averaged flow in the Eurasian Basin is more strongly cyclonic.

(A research paper will be submitted to a refereed journal based on this work).

Mixed-Layer Circulation of the Arctic Ocean

- The first sensitivity study of the mixed-layer circulation with respect to sea-ice cover, surface boundary conditions, initialization data, the closing of Fram Strait, and to bottom topography is presented.

(A research paper will be submitted to a refereed journal based on this work).

List of Tables

List of Figures

Acknowledgments

It is with deep appreciation that I acknowledge my research supervisor, Prof. Lawrence A. Mysak, for his invaluable assistance. It is with the same deep gratitude that I acknowledge Dr. Josef M. Oberhuber of the Max-Plank Institute (Hamburg, Germany) for guiding me through the intricacies on his coupled sea ice - ocean model. I wish to thank the many staff of the Department of Atmospheric and Oceanic Sciences at McGill University who have assisted me with this project. Ursula Seidenfuss is thanked for drafting some of the figures. Also, I am grateful for the help received from my thesis committee, namely Dr. Grant Ingram, Dr. John Lewis, and Dr. Andrew Weaver. I also gratefully acknowledge others who have taken the time to share with me either their data or their expertise; this group includes Knut Aagaard, Robert Bourke, Eddy Carmack, Max Dunbar, Greg Flato, Gordon Fleming, Peter Jones, Davinder Manak, William Hibler III, Humphry Melling, Bert Semtner, Achim Stössel, James Swift, and John Walsh.

The Ontario Centre for Large Scale Computing (OCLSC) is gratefully acknowledged for computing time provided on their Cray X-MP. Cray Research Inc. is thanked for the awarding of a computing grant for time on the National Center for Atmospheric Research (NCAR) Cray Y-MP. In particular, the assistance of Mr. Chuck Swanson of Cray Research Inc. is much appreciated. Finally, the Arctic Region Supercomputing Centre (ARSC) of the University of Fairbanks is thanked for recently providing computing time on their Cray Y-MP.

I am grateful for financial support from the Newfoundland Government Career Development Awards Programme and the Atmospheric Environment Service (AES) Graduate Studies Awards Programme. This work was also supported by research grants awarded to L.A. Mysak from the Natural Sciences and Engineering Research Council (NSERC), the Atmospheric Environment Service (AES), and the U.S. office of Naval Research.

Finally, I thank my parents James and Theresa and my family for the loving support they have given to me over the years. I am especially grateful to my wife, Denise, for her patience and understanding as she watched me slowly make progress in the complicated business of modelling the Arctic Ocean yet fail to master the simpler task of separating the colours for the laundry.

Preface

Originally it was intended that this thesis would focus on the modelling of the interannual variability of the Arctic sea-ice extent using a coupled sea ice - ocean model with 30 years of specified atmospheric forcing fields. The model chosen for the study was the OGCM of Oberhuber (1993a). OGCMs (with sea ice) contain numerous parameters and parameterizations; therefore, it was decided to first carry out a sensitivity study of the sea-ice part of the model in an uncoupled mode to better understand the physics and the numerics of the Oberhuber model. This is part one of the thesis (Chapter 2) and uses a model domain that consists of all the ocean that is north of the Arctic Circle. During the period of time that this thesis work was being conducted, Oberhuber improved his model by adding a snow component. Part two of the thesis documents the importance of including a snow model. A global model domain is used. This updated model version is also used in parts three and four of the thesis, but in limited model domains. It is noted that Oberhuber was the principal investigator for part two of the thesis (Chapter 3). The third part of the thesis is an investigation of the general circulation of the Arctic Ocean (Chapter 4) using a model domain that includes both the Arctic Ocean and the North Atlantic Ocean. A sensitivity study of the ocean component of the OGCM was not carried out because of the lack of sufficient computing time; however, such a study would be worthwhile and is suggested for future research. The fourth and final part of the thesis is a sensitivity study of the mixed-layer circulation (Chapter 5) using a model domain that includes the Arctic Ocean and the Nordic Seas. This latter study was carried out to isolate the principle mechanism driving the mixed-layer circulation. By carrying out this research, a deeper understanding of the behaviour of the Oberhuber OGCM has certainly been obtained. Current work is now underway

on simulating the interannual variability of the Arctic sea-ice extent, with the goal of testing some of the mechanisms for Arctic climate variability as proposed in Mysak *et al.* (1990) and in Mysak & Power (1992).

§ 1 Introduction

Currently there is considerable interest in improving our understanding of the interactions between the components of the earth's climate system. The polar regions, which form an integral yet distinct part of this system, are believed to be particularly sensitive to anthropogenically induced global warming and therefore are worthy of special study. The polar climate subsystem consists of the atmosphere, the oceans, and the sea ice. The presence of sea-ice on the ocean surface drastically alters the interaction between the atmosphere and the ocean at high latitudes.

Our understanding of the interactions in the polar regions has been hampered by a shortage of physical measurements due to the harsh climate. Numerical modelling thus provides an important tool for investigating the complex mechanisms and interactions that control polar climate. The northern and southern polar regions are very different from one another. The Arctic consists of an ocean surrounded by continental land masses, whereas the Antarctic has a continent surrounded by a high-latitude ocean. This study focuses principally on the Arctic.

§ 1.1 Ocean, Sea-Ice, and Atmosphere Circulation

Our present understanding of the sea-ice and ocean circulation in the Arctic has been summarized in the book Polar Oceanography: Part A Physical Science edited by W.O. Smith (1990). This book treats in detail most aspects of the Arctic atmosphere, sea-ice, and ocean circulation. Other general introductions to the basic physical features of the Arctic may be found in the works by Parkinson *et al.* (1987), Rey (1982), Coachman & Aagaard (1974), and Zubov (1943). Only a brief description of the Arctic basin, the ocean and sea-ice, and the atmospheric circulation is presented here.

The Arctic Ocean is essentially contained within a closed basin (see Fig. 1.1). It has the largest continental shelves in the world oceans. These shallow and broad margins cover about one-third of the surface area of the Arctic Ocean. The basin is divided into two subbasins, namely the Canadian Basin and the Eurasian Basin. These basins are separated by the Lomonosov Ridge which extends from Siberia across the Arctic Ocean to Greenland. The waters of the basin communicate with the Pacific Ocean through the narrow and shallow Bering Strait and with the Atlantic Ocean via the relatively wider and deeper Fram Strait as well as the wide opening between Spitsbergen and Norway. There is also a flow from the western Arctic through the Canadian Arctic Archipelago into Baffin Bay. Freshwater is received along the periphery of the basin from numerous rivers.

The Arctic Ocean is well stratified because of the annual cycle of sea-ice growth and melt, and also because of river input. There is a strong pycnocline at about 300 m which separates the cold, fresh surface waters from the relatively warm, salty deep waters. The general circulation of the waters within this basin are not well known. It is assumed that the surface mixed layer is dragged along by the moving ice surface and thus follows an anticyclonic path in the Canadian basin and then exits the basin through Fram Strait. The deeper waters are thought to flow in the opposite sense (*i.e.* cyclonically). The deeper waters may be strongly constrained by topography and thus flow along the contours of bottom topography.

Sea ice covers the central Arctic for most of the year. The annual cycle of ice extent causes the ice to double its areal extent in winter as compared to that of summer. To give an idea of the climatological minimal ice extent, Fig. 1.2 shows the mean ice edge position at the end of summer. Although not shown in Fig 1.2, the thickest ice builds up along the northern coast of Greenland and along the Canadian Arctic Archipelago. The Arctic sea ice is relatively

thick (typically about 3 m), and it can be several years old since it can survive the summer melt season.

The most dominant feature of the atmospheric circulation is the presence of a weak high pressure system located over the western Arctic. This high is flanked by the much more intense Aleutian and Icelandic Lows (Fig. 1.3). The surface winds associated with the high pressure system over the western Arctic causes the entire ice pack to rotate in an anticyclonic direction. The atmospheric circulation also forces ice to flow out through Fram Strait and southward along the East Greenland coast. There is little precipitation in the Arctic as the cold temperatures prohibit the air mass from containing significant amounts of water vapour. The position of the Arctic at the top of the world means that it is in darkness for six months of the year and thus its diurnal cycle of forcing is very much different from that in lower latitudes.

§ 1.2 Numerical Model

The present work was motivated in part by two previous modelling studies of the Arctic Ocean, namely those of Hibler & Bryan (1987) and Semtner (1987). Both of these studies used a coupled sea ice - ocean model with specified atmospheric forcing to simulate the general circulation of the Arctic sea ice and ocean. Hibler & Bryan vastly improved the simulation of the ice edge in the Greenland Sea (as compared to that found in an uncoupled ice model) because their model included the large heat fluxes that occur in regions of convective overturning. Furthermore, they obtained an upper-ocean circulation which is in general agreement with the observed pattern. They were not able to investigate the deeper circulation as they had imposed an artificial damping of the salinity and temperature fields back to climatology (*i.e.* a relaxation constraint) at all depths below the top level of their ocean model. Semtner (1987), who used a

simplified ice rheology, removed the relaxation constraint of Hibler & Bryan and simulated an anticyclonic circulation at all depths in the Canadian Basin while obtaining a cyclonic flow below 200 m depth in the Eurasian Basin.

A shortcoming of the above works is the absence of a sensitivity study of the simulated ice and ocean circulation to model parameters and parameterizations. Also, these studies did not correctly simulate the circulation of the Atlantic layer and the deeper waters in the Arctic.

Using the numerical model of Oberhuber (1993a), we try to address these shortcomings. The Oberhuber model is a general circulation model based on the following ideas: isopycnals are used as Lagrangian vertical coordinates, a realistic equation of state is included, the primitive equations together with the hydrostatic approximation are applied, and a surface mixed layer and a snow and sea-ice model are coupled to the interior ocean. The sea-ice model incorporates both thermodynamics and dynamics. A fundamental difference from other sea-ice models is that Oberhuber uses a different numerical scheme, and also solves the sea-ice equations in spherical coordinates. The sea-ice rheology is viscous-plastic, as in Hibler (1979). The Oberhuber model is applicable to a global domain although in Chapters 2, 4, and 5 it is used in various limited domains confined to the Northern Hemisphere.

To date, the Oberhuber model has been used to simulate the circulation in the North Atlantic (Oberhuber, 1993b), and in the Greenland, Iceland, and Norwegian Seas (Aukrust & Oberhuber, 1993), and in the tropical Pacific Ocean (Miller *et al.*, 1992). The work presented in this thesis is the first application of the Oberhuber model to the Arctic Ocean.

§ 1.3 Thesis Outline

This thesis presents an investigation of the seasonal cycle of sea-ice extent and ocean circulation of the Arctic Ocean using a numerical model. The thesis consists of four investigations carried out with the goal of improving our understanding of the Arctic Ocean circulation and the Oberhuber ice-ocean model. Throughout the thesis, detailed comparisons of model simulations with observations are not made other than to qualitatively check that the model simulations are reasonable. The emphasis is placed on understanding how and why the model produces the simulations that it does. This is a necessary step towards the ultimate goal of producing a realistic Arctic sea-ice and ocean circulation model suitable for incorporation into a climate model that includes a state-of-the-art atmospheric general circulation model.

The outline of this thesis is as follows. Chapter 2 presents a sensitivity study of an uncoupled sea-ice model. Chapter 3 describes the addition of a snow model to a coupled sea ice - ocean model. Chapter 4 contains a simulation and discussion of the general circulation of the Arctic Ocean obtained from the coupled sea ice - ocean model. Chapter 5 presents a sensitivity study of the Arctic Ocean mixed-layer circulation using the coupled model. Chapter 6 highlights the main conclusions drawn from Chapters 2 through 5.

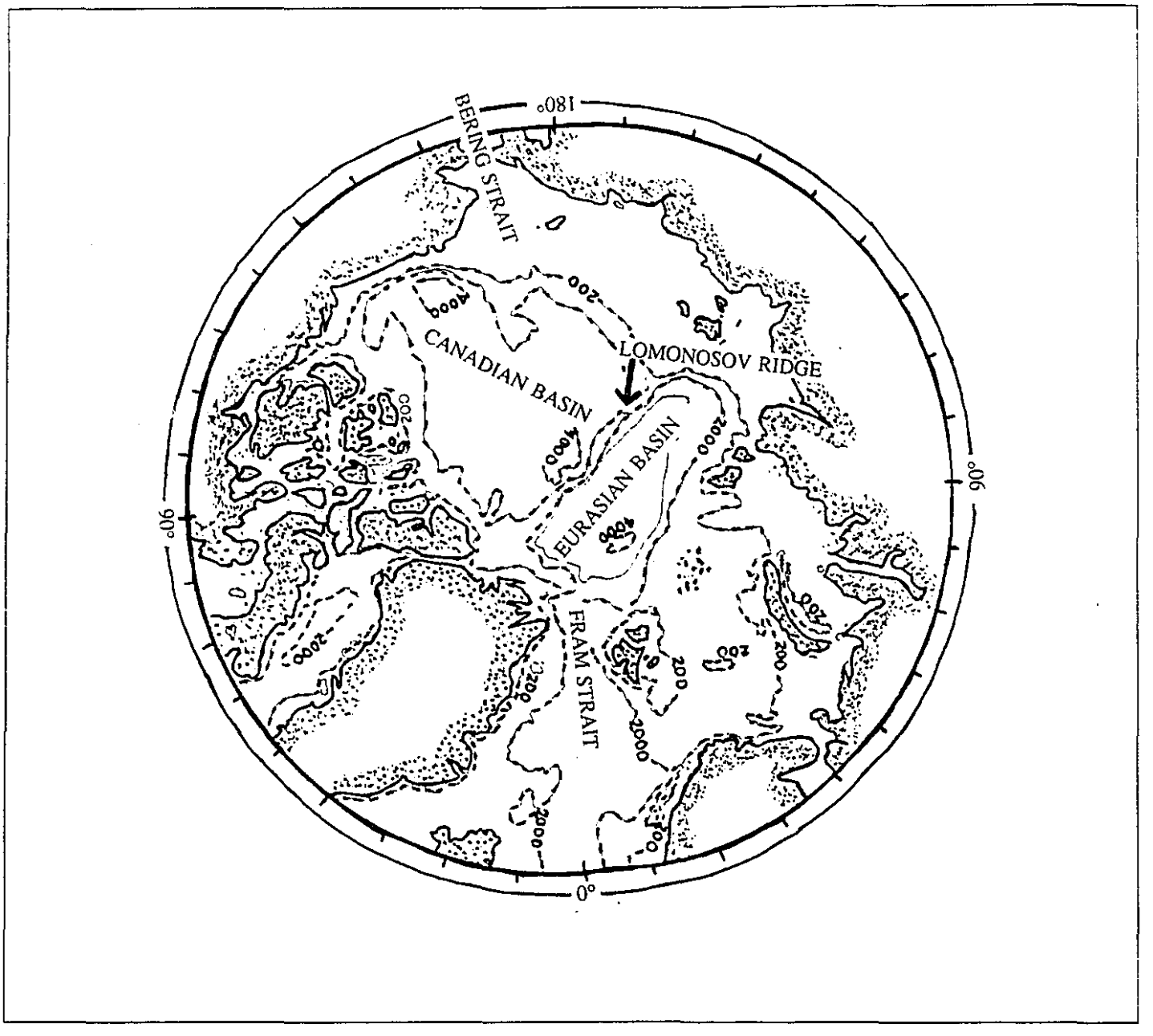

Figure 1.1 The bathymetry of the Arctic Basin showing the Canadian and the Eurasian Basins separated by the Lomonosov Ridge. The 200 *m* depth contour outlines the continental shelf (from Lewis (1982)).

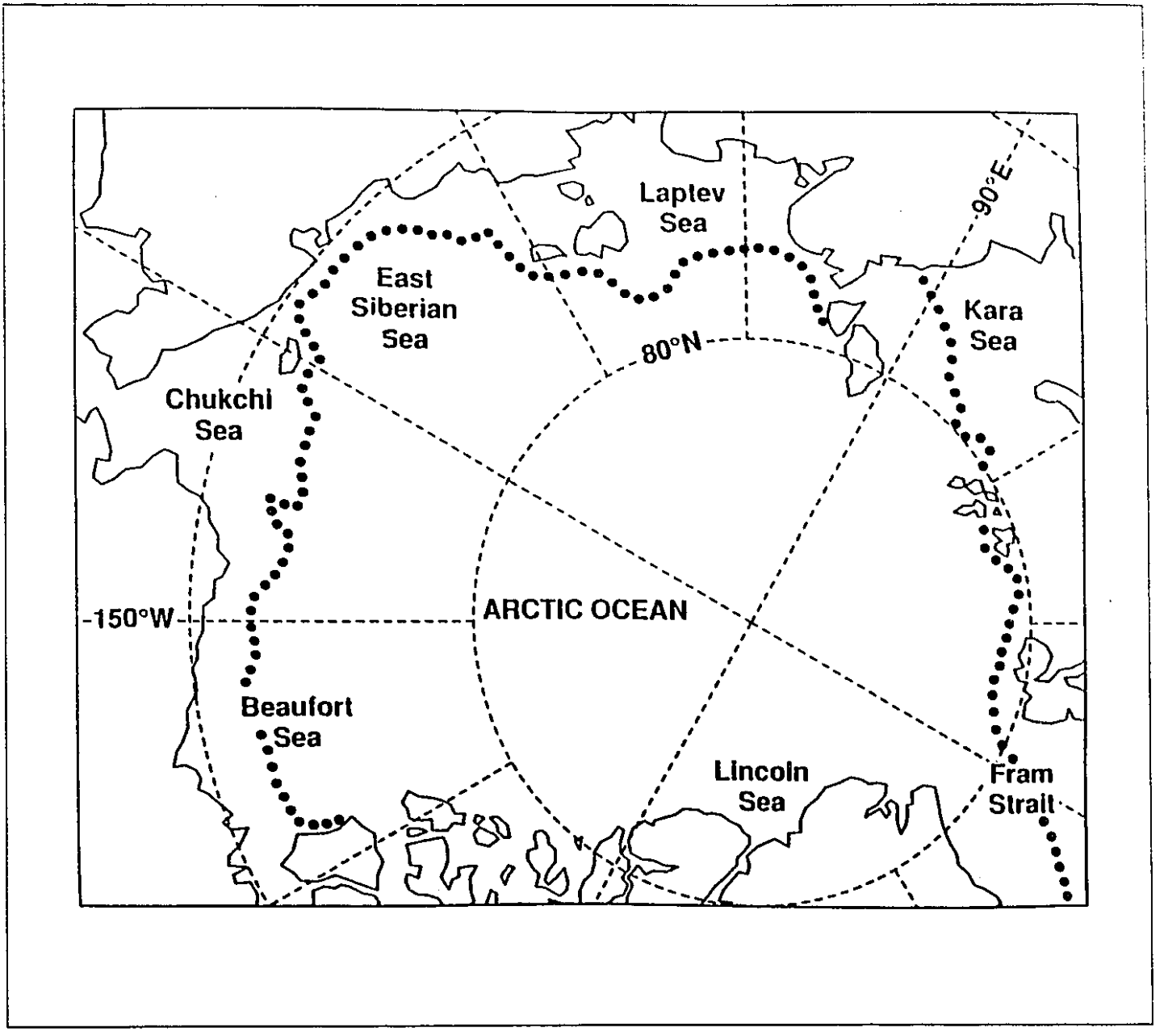

Figure 1.2 The mean ice edge position at the end of summer (September 15th). Also indicated are the locations of the Kara, Laptev, East Siberian, Chukchi, Beaufort, and Lincoln Seas (from Colony (1991).

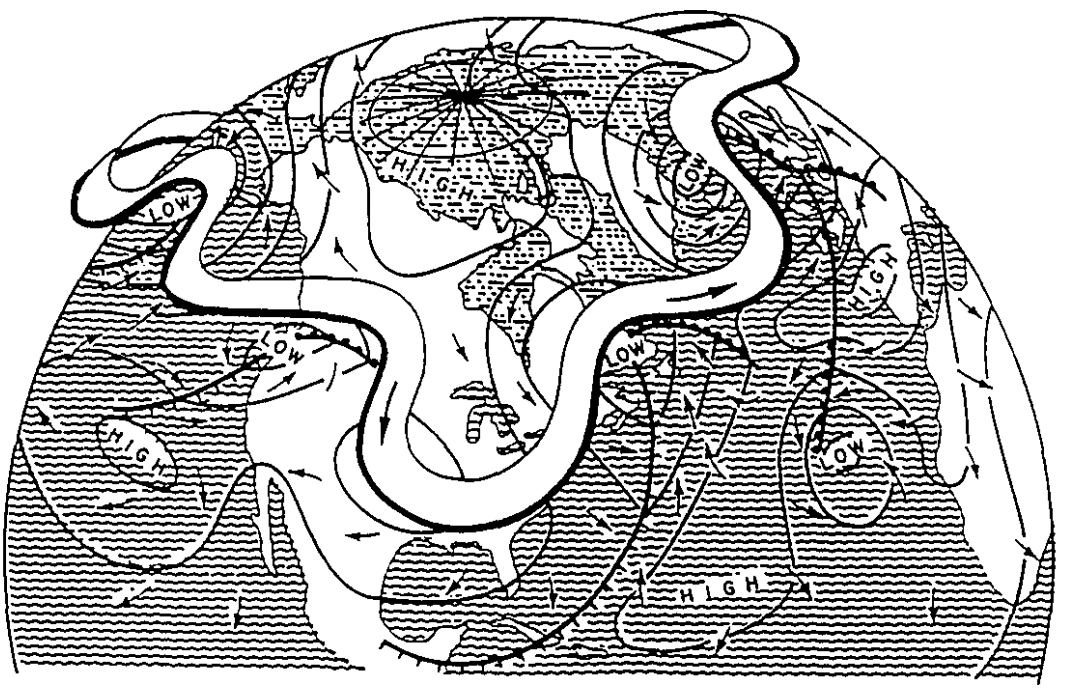

Figure 1.3 Typical winter atmospheric circulation pattern. There is evidence of a weak high pressure cell located over the western Arctic. This high is flanked by the strong Icelandic and Aleutian Lows (from Fletcher *et al.* (1966)).

§ 2 Sensitivity Study of Uncoupled Sea-Ice Model

§ 2.1 Introduction

Sea ice plays an important role in the behaviour and modelling of the earth's climate system. For example, it serves as a highly insulating and reflective boundary layer between the atmosphere and the ocean. Thus, it is capable of profoundly modulating atmosphere-ocean interaction at high latitudes. Sea ice is also important for the storage and transport of freshwater in the climate system. It is for these reasons that sea-ice models are presently coupled to global atmospheric and ocean general circulation models in climate studies. The purpose of this chapter is to study thoroughly the sea-ice component of the climate system, in a form recently introduced by Oberhuber (1993a).

In this study an uncoupled dynamic thermodynamic sea-ice model of the Arctic sea-ice cover is integrated for a variety of parameters to an equilibrium seasonal cycle using prescribed atmospheric and oceanic forcing. The model is fully described in a report by Holland *et al.* (1991a). In brief, Oberhuber (1993a) solves similar sea-ice equations as in Hibler (1979); however, Oberhuber introduces a new numerical scheme for the equations and solves them on a spherical grid. Here a broad spectrum of sensitivities studies are carried out on the parameters which characterize the sea-ice physics. As well, experiments are performed on the various atmospheric and oceanic forcing fields used to drive the uncoupled model. The aim of this study is to identify the relative importance of each process in the model. The results should help modellers identify those aspects of sea-ice physics that need to be improved in the present generation of global climate models.

Previous sensitivity studies start with the pioneering work of Maykut & Untersteiner (1971) who provided a rather complete and detailed description of a multi-layer one-dimensional

thermodynamic sea-ice model. This paper was followed by Semtner (1976a) who simplified the Maykut & Untersteiner thermodynamics by using a three-layer system which did not, however, compromise model performance. As well, Semtner provided an analysis of the sensitivity of his model to various changes. However, these models ignore both the three-dimensional extent of sea ice and ice dynamics. The model sensitivity results found in these studies do not necessarily carry over to the three-dimensional case, as will be seen later in this chapter. Studies by Washington *et al.* (1976), Parkinson & Washington (1979) and by Hibler (1979) introduced both the three-dimensionality and the dynamics of sea ice. Some sensitivity analyses of the models were conducted. The coupling of a dynamic thermodynamic sea-ice model to an ocean general circulation model has been carried out by Hibler & Bryan (1987), and Semtner (1987). Fleming (1990) has investigated the sensitivity of a coupled sea ice - ocean model to various parameters and mechanisms. To the best of the authors' knowledge, no sensitivity studies have been carried out on sea-ice models incorporated into fully coupled atmosphere-ocean-sea ice models.

It is difficult to evaluate the relative importance of the sensitivity results described above because they each use different sea-ice models. In this study we repeat many previous sensitivity studies with an uncoupled sea-ice model and also carry out many new experiments, all in a controlled environment. This allows comparison of each sensitivity experiment result to a basic control run simulation. Each sensitivity experiment is performed by changing only one condition, parameter, or process from the control run environment. This places each individual sensitivity experiment in a context where it can be confidently compared and related to the other sensitivity experiments conducted here.

The major limitation of this study is that it does not allow for a sensitivity analysis of the important feedback processes that occur in a completely coupled atmosphere-ocean-sea ice model. One barrier to such an investigation is the immense computing effort required; another is the

many-fold increase in the number of sensitivity analyses envisaged. The number of degrees of freedom in such a system include not only those of the individual components but also those representing the interactions and feedbacks between components. Nevertheless, such work is of fundamental importance and would serve as an important aid in interpreting the simulations created by such models.

In this study, the sensitivity of the sea-ice model to a particular change is gauged by the response of the prognostic output fields of the model. For selected experiments, time series of the equilibrium seasonal cycle of model domain-averaged ice thickness, areal coverage, compactness, and kinetic energy are presented. The control run time series is overlayed in each instance for comparison. A given sensitivity run may impact on some, none, or all of the ice prognostic fields mentioned above.

The remainder of this chapter is organized as follows. Section 2.2 describes the sea-ice model equations and numerical methods. Section 2.3 presents the control run simulation. Section 2.4 provides a summary in tabular form of all the experiments performed as well as a discussion of the results of the experiments judged to be the most interesting. Section 2.5 summarizes the conclusions of the chapter.

§ 2.2 Sea-Ice Model

As described by Hibler (1979), the components of the model are as follows: a) a momentum balance which includes numerical diffusion, Coriolis force, sea-surface tilt, air and water stresses, and internal ice stress; b) a constitutive law which relates the internal ice stress to the strain rate (*i.e.* ice velocity gradients) and the ice strength; c) an ice strength which is a function of the ice thickness and fraction of open water; d) balance equations for the change of

ice compactness (*i.e.* concentration) and ice thickness due to growth or ablation, advection and deformation; and e) an ocean mixed layer which serves as a heat reservoir.

The thermodynamic and dynamic aspects of the model are interrelated because ice motion causes local changes in ice thickness as ice is advected into or out of a region, while changes in ice thickness due to ablation or growth alter the ice strength characteristics which in turn affect the ice motion. On the large scale, ice is exported from the Arctic Ocean through Fram Strait into the Greenland, Iceland, and Norwegian Seas, hereafter referred to as the GIN Sea.

§ 2.2.1 Sea-Ice Equations

For the momentum balance the ice is considered to move in a two-dimensional spherical plane with forcing fields operating on the ice via simple planetary boundary layers. The nonlinear terms are neglected (see Hibler, 1979). The equation, in flux form, is given by

$$\frac{\partial \vec{u} h}{\partial t} = \vec{\nabla} \cdot A^m \vec{\nabla} \vec{u} h - \vec{f} \times \vec{u} h - g h \vec{\nabla} \Gamma + \frac{\vec{\tau}_{air}}{\rho_{ice}} + \frac{\vec{\tau}_{ocn}}{\rho_{ice}} + \frac{\vec{I}}{\rho_{ice}} \quad , \qquad (2.1)$$

where $\vec{u} = (u,v)$ is the horizontal ice velocity vector, h the ice floe thickness evenly distributed over a grid cell, A^m the horizontal diffusion coefficient for momentum, $\vec{f}$ the Coriolis vector, g the acceleration due to gravity, Γ the sea surface dynamic height, $\vec{\tau}_{air}$ the ice stress due to surface winds, $\vec{\tau}_{ocn}$ the ice stress due to surface ocean currents and bottom drag, ρ_{ice} the ice density, and $\vec{I}$ the internal ice stress. The formulation of the ice stress is based on a viscous-plastic rheology (Hibler, 1979) and is fully discussed in section 3.2.1.

Oberhuber (1993a) has rewritten Hibler's (1979) equations in a momentum and mass conserving flux form since the latter provides an easier numerical treatment of the ice edge behaviour. This is because the flux $h\vec{u}$ is a much more well-behaved quantity at the ice edge than is $\vec{u}$ alone. Thin ice of low compactness near the ice edge may have large velocities in

response to dynamic forcing; however, when such velocities are multiplied by a small thickness the resulting ice flux $h\vec{u}$ becomes a smoother and more well-behaved quantity than the velocity at the ice margin.

Furthermore, this formulation avoids having the advection term $\vec{u}\cdot\vec{\nabla}h$ appear in Eqn. 2.2. Such a term can result in undershooting (*i.e.* negative ice thickness). Also, both $\vec{u}$ and $\vec{\nabla}h$ are large near the ice edge and their product is not well-behaved. The formulation in Eqn. 2.2 avoids this problem by dealing instead with the term $\vec{\nabla}\cdot\vec{u}h$ which is small near the ice edge.

The ice-cover has a thickness h which is averaged over an entire grid cell. A compactness q (also known as the ice concentration) is now introduced which is defined as the fraction of a grid cell area covered by ice; the rest of the cell is covered by open water. The spatial and temporal variations in thickness and compactness are modeled by the continuity equations

$$\frac{\partial h}{\partial t} = -\vec{\nabla}\cdot\vec{u}h + \vec{\nabla}\cdot A^s\vec{\nabla}h + F_h \quad , \tag{2.2}$$

$$\frac{\partial q}{\partial t} = -\vec{\nabla}\cdot\vec{u}q + \vec{\nabla}\cdot A^s\vec{\nabla}q + F_q \quad , \tag{2.3}$$

where F_h and F_q are thermodynamic forcing or source terms, and the second last terms are numerical diffusion terms with coefficient A^s. To ensure that stable solutions are found for h and q, it is necessary to include the diffusion terms; furthermore, diffusion is justified in that it can be argued to represent the effect of ocean eddies on the ice behaviour.

Physical constraints are imposed on these two equations. The thickness equation (2.2) is constrained such that $h \geq 0$ at all times to avoid negative ice thickness. The compactness equation (2.3) is constrained such that $0 \leq q \leq q_{max}$ at all times. The maximum ice compactness

q_{max} cannot physically exceed unity. Setting q_{max} to some value slightly less than unity ensures that a fraction (1 - q_{max}) of every grid cell will always be open water.

The thermodynamic forcing term F_h in Eqn. 2.2 resulting in ice growth or melt is given as a contribution over the fraction (1-q) of thin ice and the fraction q of thick ice as

$$F_h = - \frac{(1-q)\,Q_{air} + q\,Q_{ice} + Q_{ocn}}{\rho_{ice}\,L_f} \quad , \tag{2.4}$$

where Q_{air} is the total atmospheric heat flux at the surface of open water or leads due to solar, longwave, sensible and latent heating, Q_{ice} is the conductive heat flux through the ice into the ocean, Q_{ocn} is the oceanic heat flux supplied to the oceanic mixed layer from the deep ocean due to advective and convective processes, and L_f the latent heat of fusion of water. The sign convention for F_h is such that a positive value indicates a source term for ice growth in Eqn 2.2. In such an instance the ice is losing heat and increasing in thickness.

The forcing function for the ice compactness F_q in Eqn. 2.3 is of the same sign as the thickness term F_h. This means that when the ice is growing, corresponding to F_h positive, the ice compactness is simultaneously increasing and vice versa. The relation between F_h and F_q is given by

$$F_q = \begin{cases} C_{frez}\,\dfrac{F_h}{h_o}\,(1-q) & F_h > 0 \quad \textit{freezing} \\ C_{melt}\,\dfrac{F_h}{2h}\,q & F_h < 0 \quad \textit{melting} \end{cases} \tag{2.5}$$

The quantity h_o is introduced as in Hibler (1979). The two empirical coefficients C_{frez} and C_{melt} determine the relative rates at which the ice compactness increases and decreases respectively. The model is more sensitive to C_{frez} than C_{melt} as the growth of thin ice under freezing conditions is a more rapid process than the melting of thick ice under thawing conditions.

Beneath the ice an ocean mixed layer causes changes in the ice both thermodynamically, through a specified ocean heat flux, and dynamically, through an ocean current stress and a surface tilt. The mixed layer currents do not advect heat laterally as the oceanic forcing is diagnostic. The ocean mixed layer is of uniform depth and of constant heat capacity. The temperature and salinity are uniform throughout the vertical extent of the mixed layer; however, these quantities vary horizontally and in time. The ocean density is uniform everywhere and equal to a constant in a Boussinesq sense. Horizontal variations in density are not important as the ocean currents are specified.

§ 2.2.2 Numerical Methods

The equations for sea-ice momentum, thickness, and compactness are solved on a spherical grid in finite difference form using a semi-implicit time-step scheme combined with a predictor-corrector scheme. The predictor step for the ice thickness (see Eqn. 2.2) treats the divergence of the ice thickness flux explicitly. The corrector step for the ice thickness treats the diffusion term implicitly. The same procedure applies to the compactness (see Eqn. 2.3). The predictor step for the momentum equation (2.1) treats the stresses and Coriolis force implicitly. The corrector step for Eqn. 2.3 treats the rheology and momentum diffusion implicitly. It is important to recognize that the implicit treatment of the momentum diffusion in this manner produces smooth momentum fluxes. This allows for the explicit treatment of the divergence of ice thickness and compactness at the next time step.

The equations for ice momentum, thickness, and compactness are discretized in space using a centred finite difference approach. In time, the equations are integrated using an Euler-implicit scheme in which terms are averaged between the old and the new time level. No-slip boundary conditions are applied for momentum.

The numerical grid is in spherical coordinates with grid points every three degrees of longitude and every one degree of latitude; thus the east-west resolution increases towards the North Pole. An important aspect of the numerical technique employed by Oberhuber (1993a) is that he only iterates the solution in a north-south direction. As the grid spacing is uniform in this direction, the problem of a converging grid spacing is avoided. There is, however, grid convergence in the east-west direction as one increases in latitude. Solving the equations using a direct (*i.e.* non-iterative) solver at each latitude circle allows one to avoid the problem of converging grid spacing. In effect, the equations are solved directly in the east-west direction at each latitude circle while they are iterated in the north-south direction. The model domain extends in latitude from 65° N to the North Pole. Although Baffin Bay and the Canadian Arctic Archipelago are within the model domain, they are not modelled here. Baffin Bay is not considered to have a direct impact on the sea ice in the Arctic Ocean or the GIN Sea. An ocean/land mask is placed over the spherical grid such that any grid point corresponding to a geographical position in either the Arctic Ocean or the GIN Sea is masked as an ocean point and as such is permitted to have sea ice. All other points on the grid are masked as land points and do not enter into the computations.

The numerical scheme is not fully implicit and thus there exists a finite limit on the time step δt due to stability requirements. Although derived for explicit schemes, the Courant-Friedrichs-Lewy (CFL) condition (Press *et al.*, 1988) gives an indication of the maximum value of δt (*i.e.* the time step) for this semi-implicit scheme. This condition states that one must be able to resolve the fastest propagating physical quantity on a numerical grid. In this instance, the fasting moving quantity is the advection of the ice which has a characteristic velocity on the order of 10 *cm/s*. The numerical grid speed is the ratio of $\delta\lambda$ to δt, where $\delta\lambda$ is a characteristic

longitudinal grid spacing, which is variable on a spherical grid. It turns out that it is the minimum grid spacing that controls the numerical grid's ability to resolve the fastest propagating physical quantity. Near the North Pole, the spherical grid has a minimum spacing of 5 *km*. Upon, applying the CFL condition, the maximum time step is found to be

$$\delta t \; < \; \frac{\delta \lambda}{u} \approx 13 \; \textit{hours} \quad . \tag{2.6}$$

Thus the choice of time step is taken to be 1/2 *day*.

The model is run on a Cray X-MP computer. One year of computer simulation requires approximately six minutes of computing time on the Cray. The greatest fraction of the computing effort (80 %) is spent on ice dynamics; thermodynamics uses only 20 % of the time. The code has been optimized by Oberhuber (1993a) and runs at rate of just over 100 megaflops. Overall, the computing requirements are extremely modest in comparison to the requirements of an atmospheric or an ocean general circulation model for one year of simulation. Given the importance of the ice cover to atmosphere - ocean interaction, the use of a dynamic thermodynamic sea-ice model written in spherical coordinates with a viscous-plastic rheology is justified in coupled climate models.

A no-slip boundary condition for ice velocities is used along coastlines. The no-slip condition is also used at open boundaries where the Arctic Ocean or the GIN Sea would normally exchange sea ice with other ocean basins. Thus, there is no ice transport through the Bering Strait, the Canadian Arctic Archipelago, the Denmark Strait, or the passage between Iceland and Norway.

The mapping of the spherical grid onto a rectangular computer array introduced an artificial boundary along the meridian 180 degrees East. A cyclic boundary condition was used for velocity, thickness and compactness along this meridian.

At the pole a no-slip condition was used for velocity. This is equivalent to placing a stick at the North Pole. A more complex boundary formulation is possible at the pole whereby the ice would be allowed to freely pass over the North Pole. Such a formulation was not included in the control run simulation. Nevertheless, the use of a no-slip condition at the pole is felt to be justified as this is an advection problem and not a wave-type problem whereby wave reflections at the Pole would be important. The boundary conditions for thickness and compactness over the pole are reasonable as they simply ensure that thickness and compactness are continuous there.

As seen earlier, both the vector momentum equation and the scalar thickness and compactness equations include numerical diffusion. For the momentum equation the coefficient is A^m (see Eqn. 2.1), while for the scalar equations it is A^s (see Eqns. 2.2 & 2.3). Numerical diffusion is included to eliminate the nonphysical two grid point computational mode which may be present when centred spatial finite differences are used. Furthermore, the justification for including these coefficients are the presence of eddies in the ocean which redistribute the ice due to the ice-ocean drag. Thus the coefficients are a paramterization of the effect of such eddies. The requirement for computational stability in an explicit scheme (Roach, 1985) is that the grid-cell Reynolds number R_e satisfies the inequality

$$R_e \equiv \frac{u\,\delta\lambda}{A} < 2 \quad , \tag{2.7}$$

where u is a characteristic ice velocity, $\delta\lambda$ the grid spacing, and A the diffusion coefficient. On a spherical grid with variable grid spacing it is the largest grid spacing which constrains the choice of diffusion coefficient. This is in contrast with the constraint for the time step whereby the smallest grid spacing is the constraint. The largest grid spacing in this instance is 140 *km* which occurs along the southern boundary of the domain. Again, a characteristic ice velocity is

of order 10 *cm/s*. Thus, to satisfy the grid-cell Reynolds number criterion we require a diffusion coefficient of order of 7000 m^2/s. However, because we are using an implicit scheme we are able to get stable solutions for smaller diffusion coefficients of order 2000 m^2/s (for both A^m and A^s). Implicit schemes allow the use of smaller diffusion coefficients as compared to explicit schemes because of better phase advection properties in the nonlinear terms.

As in Hibler (1979), mass is conserved for the diffusion terms by setting the diffusion coefficient to zero along the boundaries. As velocity is also zero on the boundaries, mass is conserved for the incompressible portion of the velocity field (Hibler, 1979).

The various atmospheric and oceanographic fields used to force the sea ice-model are discussed by Holland *et. al.* (1991a). All fields are monthly varying with the exception of salinity, which is seasonal. All fields are interpolated onto the model's spherical grid. The fields are interpolated to daily values using simple weighted linear interpolation from values for neighbouring months. High-frequency fluctuations due to synoptic-scale atmospheric activity are not present.

A summary of all the values used for the various physical constants and model parameters is presented in Table 2.1.

§ 2.3 Control Run Simulation

The sea-ice model was integrated for a ten year period from an initial state of zero ice thickness and no ice motion. The mixed layer temperature was set close to the freezing temperature (-1.8°*C*) everywhere. Climatological (seasonal) atmospheric and oceanic forcing fields were repeatedly applied for each year of the simulation. Below is a discussion of the various ice characteristics of the control simulation.

Time series of the seasonal variation of the domain-averaged ice thickness, areal coverage, compactness and kinetic energy (*i.e.* proportional to mass) over the 10 year period are illustrated in Fig. 2.1. In Fig. 2.1(a) the effective thickness h/q is presented as it is more representative of the actual floe thickness than h (which, we recall, is the ice thickness evenly distributed over a grid cell). The time series shows the evolution of the effective ice thickness as the model spins up towards an equilibrium state. The ice areal coverage (Fig. 2.1(b)) is defined by adding up the geographical surface area of each grid cell in which ice is present, and weighting each such cell by its compactness. The compactness time series in Fig. 2.1(c) is defined as the average compactness for all grid cells containing ice. The model quickly approaches its equilibrium state within five years of integration for each of these signals. The domain averaged kinetic energy time series (Fig. 2.1(d)) is defined as the sum total of the kinetic energy of each ice floe in all grid cells. It has reached a quasi-equilibrium after five years; however, due to the non-linear ice rheology it continues to show small perturbations throughout the ten year simulation.

The time series of the equilibrium annual cycle of the ice characteristics are presented in Fig. 2.2. This figure illustrates the same ice quantities as in the previous figure except that it focuses on the final year of the simulation. The annual cycle of ice thickness indicates a peak in May of about 2.4 *m* and a minimum in October of about 1.5 *m*, with an average thickness of about 2 *m*. This average thickness is computed by including leads and open water contributions. This is significantly lower than the generally accepted value of 3 *m* for the overall ice thickness. However, as with all of the ice characteristics, parameter values can be tuned within acceptable ranges to produce the desired result. The amplitude of the seasonal cycle is roughly 50 *cm*, which is in good agreement with observations (Maykut & Untersteiner, 1971). The seasonal cycle of areal coverage ranges from an April peak of 9 million km^2 to a September minimum of

3 million km^2. Observations indicate that sea ice varies from a March maximum of about 15 million km^2 to a September low of 8 million km^2 (Parkinson *et al.*, 1987). However, these numbers are based on the 20 million km^2 of observed area of sea ice cover in the Northern Hemisphere. The domain modelled here is a 12 million km^2 subset area of that greater domain. Observations indicate that the areal coverage roughly halves during the summer melt season. In the simulation, the summer coverage was a third of the winter value; thus the amplitude of the seasonal cycle is excessive in the simulation. The seasonal cycle of ice compactness indicates an April maximum greater than 90 % and a September minimum of about 55 %. The ice kinetic energy is large during the winter months, from November through to April, and relatively low during the summer months (May through to October). The kinetic energy shows prominent peaks both in November and in April. These peaks would appear to be related to the ice rheology. For example, the November peak indicates the relatively fast response of low compactness ice-pack to increased winter atmospheric forcing. The subsequent decrease in kinetic energy after November may be explained by the increasing ice compactness during the early winter season, a process which hinders ice motion. Finally, there is an increase in kinetic energy in April as the ice begins to break up.

The seasonal cycle of the spatial variation of the simulated ice thickness is presented in Fig 2.3. The cutoff thickness of 50 *cm* (shown as a heavy line) is used to distinguish the ice pack from the open sea. The results indicate that the greatest ice thickness occurs north of the Canadian Arctic Archipelago throughout the seasonal cycle, in good qualitative agreement with observations (Bourke & Garrett, 1987). However, the magnitude of the thickness is underestimated in the model. The maximum model thickness is about 3 *m*, whereas observations suggest a maximal thickness of about 6 *m*.

The seasonal cycle of the spatial variation of the simulated ice compactness is presented in Fig. 2.4. The ice edge (heavy line) is defined as the $1/10^{th}$ compactness contour. The simulated compactness agrees reasonably well with that as observed by satellite (Parkinson *et al.*, 1987, their Figs. 4-3 to 4-8). The compactness remains high along the coastline of the Canadian Arctic Archipelago throughout the seasonal cycle. The observed compactness indicates that the $1/10^{th}$ contour persists along the Greenland east coast throughout the year, but the simulation has an excessive melt of ice along this coast during summer. There is also excessive melt of the ice pack in the central Arctic during summer and early fall as well.

The spatial variation of the simulated ice velocity as presented in Fig. 2.5 reproduces the basic features of Arctic ice drift. There is a strong Beaufort Gyre during winter with velocities of order 5 *cm/s* and a slightly weakened gyre in summer. The Beaufort Gyre does not change its sense of rotation throughout the seasonal cycle despite the fact that the atmospheric winds in that region briefly do so in early fall. This is because the ocean currents are also inputting momentum into the ice pack in the form of an anticyclonic gyre in this region. The Transpolar Drift Stream is clearly evident in March and June, as is a strong ice drift which extends along the East Greenland coast during winter. Ice velocities along the East Greenland Coast reach realistic speeds of up to 15 *cm/s*. The impact of the no-slip boundary condition at the North Pole can be seen from the ice velocities. Near the pole, the velocities tend to be smaller than elsewhere; however, the boundary condition does not adversely affect the simulation away from the pole. Observed ice drifts (Colony, 1991) based on buoy drift tracks agree well with the drifts simulated here.

The model also produces a prognostic simulation of the ice and ocean surface temperature. Where there is ice, the surface temperature is taken to be a weighted average of the ice surface temperature and the mixed layer temperature of the leads. Where there is no ice, the surface

temperature is that of the mixed layer. Fig. 2.6 shows the seasonal cycle of the surface temperature. The heavy line indicates the surface zero degree isotherm. In the central Arctic during winter surface ice temperatures are less than -20 °C, which is realistic (Parkinson *et al.*, 1987). In June the surface temperatures in the central Arctic are spatially uniform (near 0 °C) as a result of the summer melt season. A problem with the thermodynamic calculations is illustrated by the surface temperatures along the coast of Norway. Throughout the seasonal cycle these temperatures are too high, being on the order of 15 °C. However, away from the Norwegian Coast, these fields compare favourably with those given in Parkinson *et al.* (1987, their Fig. 2.5).

§ 2.4 Sensitivity Experiments

The sensitivity experiments were carried out according to three main themes, namely (A) numerical conditions, (B) parameter values, and (C) physical processes. The last theme refers to experiments in which physical processes are newly added or completely removed from the model. Tables 2.2, 2.3, and 2.4, which correspond to the above themes, succinctly indicate the change made in the control run environment in each instance. In each experiment, only a single change was made from the control run computer code. Each sensitivity experiment was integrated for a 10 year period. For each experiment, figures analogous to those of the control run (i.e. Figs. 2.1 through to 2.6) were produced. The tremendous number of resulting figures prevents their reproduction here; however, they are available in full in a report by Holland *et al.* (1991b). That report also contains a complete discussion of each experiment. In the discussion that follows only selected sensitivity experiments are discussed.

§ 2.4.1 Numerical Conditions (Theme A)

Experiments A1 and A2 : Timestep, δt

A semi-implicit technique is used to integrate the model equations. To avoid numerical instability a timestep of 1/2 *day* was chosen based on the CFL condition (see Eqn. 2.4).

A1: A reduced timestep of 2 *hours* results in a more energetic (> 50 %) winter and springtime ice pack. Spatially, the fields of thickness, compactness, velocity, and surface temperature are smoother for the shorter timestep than in the control run, particularly in December.

A2: Using an increased timestep of 1 *day* produces a much less energetic ice pack (50 % decrease in winter). The ice fields show signs of instabilities, particularly in December. An attempt was made to run the model with a timestep of 2 *days*; however, the model became unstable and failed to converge to a solution.

Experiment A10 : Boundary Condition at North Pole

Since the model is written in spherical coordinates, there is a convergence of the model grid points at the geographic North Pole. Oberhuber (1993a) has provided a technique whereby the spherical coordinate grid of the sea ice model may be rotated through Eulerian angles, and thus placed outside the modelled domain, to avoid this undesirable convergence of grid cells at the North Pole. However, in fully coupled global atmosphere-ocean-sea ice models, such a rotation is not performed.

The control run used a no-slip boundary condition at the pole. Effectively this is like placing a stick at the North Pole since the boundary condition involves setting the ice velocity to zero at that grid point. Introducing a more elegant boundary condition whereby the ice is allowed to flow freely over the pole (a so called open pole boundary condition) results in little change from the control run (see Figs. 2.7-2.9). In the modified boundary condition, the velocity

of the ice at the pole is taken to be the vector average of all neighbouring velocity points. In overlaying the ice velocity fields from this experiment onto those of the control run, one finds only marginal differences of about 2 %.

Oberhuber (1993a) now uses an open pole boundary condition in his fully-coupled global simulations. He finds that the open pole helps to stabilize the model as quantities are now diffused across the pole. The net effect is that there is now less noise in that region (Oberhuber, *pers. comm.*, 1992)

Recently, Flato and Hibler (1992) have investigated the difficulty of having a singularity at the North Pole. They have written an ice model in spherical coordinates using a cavitating fluid rheology. This formulation of rheology ignores shear stresses. They achieved a good simulation in the vicinity of the pole because the absence of shear stresses in the cavitating fluid formulation allows free slip past an obstruction, such as a stick at the pole. Otherwise there would be a pronounced thickness buildup there. However, the results here indicate that the original Hibler (1979) model formulation using a viscous-plastic rheology, which does include shear stresses, does not lead to pronounced thickness buildup at the pole.

§ 2.4.2 Parameter Values (Theme B)

Experiments B7 and B8 : Coefficient of Freezing, C_{frez}

The forcing term F_q for the ice compactness (see Eqn. 2.3) describes the manner in which the ice compactness increases in a given grid cell under ice growth conditions. It controls the rate at which leads close or freeze over. The introduction of C_{frez} is justified as Eqn. 2.5 is not based on rigorous physical principles, but rather on intuitive reasoning for the behaviour of ice during growth. Essentially, C_{frez} controls the rate at which open water is converted to ice-covered ocean. The control value is 1.[11] It is shown below that C_{frez} is a key parameter that readily

controls the ice thickness. Note that according to Eqn. 2.5, there is a corresponding (but inverse) sensitivity to h_o, which is also a very arbitrary parameter in this formulation. It is worth noting that Eqn. 2.5 uses the ice growth rate F_h averaged over a grid cell, which includes contributions from thick and thin ice. A more appropriate formulation would use the ice growth rate over open water only, as in Hibler (1979).

B7: Decreasing C_{freez} to 1/2 results in a decrease in the growth rate of compactness in a cell. This means that open water is slower to freeze over and consequently more heat is lost to the atmosphere and greater ice production is experienced. The average ice thickness increases by about 1 m while the seasonal cycles of areal coverage and compactness become less pronounced. This is a very realistic ice thickness simulation. The kinetic energy increases due to both the increase in ice thickness mentioned above, and the more vigourous ice circulation.

B8: Increasing C_{freez} to 2 results in exactly the opposite behaviour to the above. Leads in the ice are now quicker to freeze over and ice production is inhibited. Since there is much more thin ice produced, the seasonal cycle of areal coverage and compactness are accentuated because this ice has little thermal inertia.

Experiments B9 and B10 : Coefficient of Melting, C_{melt}

The forcing term F_q also describes the manner in which the ice compactness decreases in a given cell due to melting introduced by the thermodynamic forcing F_h. A coefficient of melting C_{melt} is introduced into this relation between F_q and F_h as in Eqn. 2.5. Essentially, C_{melt} modifies the rate at which thick ice-covered ocean is converted to open water. It can be thought of as a parameter to control the rate at which leads open. The control value is 1.

B9: Decreasing C_{melt} to 1/2 results in a slower conversion of ice to open water during the melting season; thus there is greater areal coverage and compactness during the melting season. The kinetic energy is largely unaffected. There is no change during the freezing season.

B10: Increasing C_{melt} to 2 increases the rate of conversion of ice-covered ocean to open water. The result is less areal coverage and less compactness during the melting season. Again, there is little change in the kinetic energy of the ice. Interestingly enough, the seasonal cycle of the domain-averaged thickness indicates the ice to be thickest in August. Recall that the thickness is defined as the effective thickness in the time series; thus with this parameter setting, we see that most of the thin ice is melted during the course of the summer, leaving only very thick ice at the end of the summer. By contrast, in winter there is much more thin ice, in addition to the thick ice, and this gives rise to an effective winter thickness which is less than the summer thickness.

Experiments B17, B18, B19 : Ice albedo, α_{ice}

In contrast to the ice conductivity, the ice albedo is an adjustable parameter. It is difficult to assign an appropriate value for α_{ice} because the surface reflective properties are highly variable. For instance, the surface may be covered by new snow, old snow, wet snow, ice, or melt ponds, thus giving rise to a large range of surface albedos. It is estimated that between 20 to 40 % of the surface area is covered by low albedo melt ponds during the critical months of July and August. As with the preceding experiments, the idea here is to vary α_{ice} through extreme variations in order to observe the model's response. This also serves the purpose of assessing the model's robustness with respect to albedo. The control value is .40.

B17: Decreasing the ice albedo to .10 results in a decrease in all of the ice fields. The most noticeable impact is on the September ice thickness and compactness fields. The ice, however, does not completely disappear.

B18: Making the ice surface highly reflective, by increasing the ice albedo to .90, results in an increase in the ice thickness field to an average of about 4 *m*. There is a large decrease in the amplitude of the seasonal cycles of areal coverage and ice compactness. The greatest changes are evident during the melt season.

B19: A further experiment in which the surface albedo varied continuously with the air temperature was carried out. This is a modification of the surface albedo representation given by Ross & Walsh (1987):

$$\alpha_{ice} = \begin{cases} .60 & T_{air} < -5\,^{o}C \\ .40 - .04\,T_{air} & -5\,^{o}C < T_{air} < +5\,^{o}C \\ .20 & T_{air} > +5\,^{o}C \end{cases} \qquad (2.8)$$

Such a representation captures the decrease in albedo which occurs when relatively warm air appears over the ice surface; similarly, an increase in albedo occurs in the presence of a relatively cold air mass. Nevertheless, the results indicate that the model is not very sensitive to these details. This relative insensitivity is in agreement with similar results obtained by Fleming (1992) using a coupled ice-ocean model. As a possible explanation for this relative insensitivity, Fleming suggested that the ocean heat flux, ocean currents, and wind stress may be more dominant in controlling the ice edge than the atmospheric heat flux changes to the ice resulting from albedo modifications.

Experiments B20 and B21 : Ocean Surface Albedo, α_{ocn}

The ocean surface albedo has an impact both in the ice-free part of the model domain as well as in the leads between the ice floes. As with the ice albedo experiments, the model is expected to show the greatest sensitivity during the summer season. The control run value is .17

B20: Decreasing the ocean surface albedo to .05 gives an ocean surface which is more absorptive to incoming shortwave radiation. However, the impact on the ice simulation is minimal with only a slight decrease in the ice characteristics. As expected, the greatest sensitivity is observed in September, i.e. at the end of the melt season.

B21: Increasing the ocean albedo to .50 simulates an unrealistically high-reflective ocean surface. Nevertheless, the changes to the control run simulation are moderate. There is an increase in the ice characteristics. Again, this change is most prominent at the end of the melting season.

Experiments B22, B23, and B24 : Air Drag Coefficient, C_{air}

The input of momentum to the ice from the atmosphere is based on a bulk aerodynamic formulation. In the control run the drag coefficient is taken as 1.2×10^{-3}. In this set of experiments, the drag parameter is changed to extreme values to observe the model's response. In reality, such extreme variations are likely to happen for a variety of reasons. First, the variations in atmospheric stability allow for enormous variations in the downward flux of momentum. Secondly, irregularities in the ice surface due to either ridging or leads can produce large fluctuations in the momentum flux via form drag.

B22: The reduction of C_{air} by an order of magnitude to $.12\times10^{-3}$ reduces the ice kinetic energy to about 30 % of its control value. Interestingly enough, the modification of C_{air} does not significantly affect the thermodynamic properties (*i.e.* the ice thickness, areal coverage, or compactness).

The kinetic energy of the ice pack integrated over the entire basin depends upon the momentum input from both the atmospheric winds and the oceanic currents. In comparing the seasonal fields of winds and currents, one can see that although these two fields have large scale features in common (for instance, the Beaufort Gyre), over most grid points the vectors of wind and current have different directions. Consequently, the winds and currents may act in concert, or they may act in opposition when forcing ice motion. A scale analysis of the atmospheric and ocean bulk drag formulations reveal that they are of the same order of magnitude. This fact coupled with the non-linear nature of the drag laws plus the non-linear nature of the ice rheology terms prohibit one from making simple predictions on the effect of altering the bulk drag coefficients.

B23: The increase of the drag coefficient by an order of magnitude to $12.\times10^{-3}$ makes the ice pack extremely energetic and noisy, with November peak average kinetic energy 5 times the control value. At the same time, a larger C_{air} also increases somewhat the ice thickness because of the increased percentage of open water during winter. Furthermore, the large ice velocities suggest the onset of numerical instability in the thickness and compactness fields.

B24: The variation of the air drag coefficient with ice compactness q has been investigated by Anderson (1987). In Fig. 2.10 one can see that the coefficient varies by a factor of 5 depending on ice conditions. Note that it has a maximum value at a compactness of approximately 80 percent. The dependence of drag coefficient on ice compactness is modelled from Fig. 2.10 as

$$C_{air} = \begin{cases} 5\times10^{-3} \cdot \left(\frac{q}{.8} \right) & q \le .8 \\ 5\times10^{-3} \cdot \left(\frac{1. - q}{.2} \right) & q > .8 \end{cases} \qquad (2.9)$$

Utilizing this dependency of drag coefficient on compactness, the major impact is to create a significant increase in the ice kinetic energy at the onset of winter, i.e. November (see Fig. 2.11). Presumably, later in winter the ice compactness is too high to allow efficient transfer of momentum from the atmosphere. In direct contrast to the preceding experiment (B23), the average ice thickness actually decreases slightly. Hence, one cannot make the statement that increased ice motion gives rise to increased production of open water (leads) and hence to increased ice growth.

Experiments B29, B30, B31, B32, B33, and B34 : Cloud Fraction C_f

The following set of experiments investigates the impact of the cloud fraction on the shortwave radiation, and then on the shortwave and longwave radiations combined. The monthly varying incoming solar radiation Q_{short} was calculated as in Parkinson & Washington (1979) by applying the cloudiness factor of Laevastu (1960) to an empirical equation given by Zillman (1972) for global radiation under cloudless skies. The cloudiness correction factor applied to Q_{short} is

$$1. - .6 \cdot C_f^3 \qquad (2.10)$$

where C_f is the cloud fraction; in the control run, C_f is set to 85 %. This is in agreement with the summer time cloud cover values provided by Huschke (1969).

B29: Decreasing the shortwave cloud fraction to 55 % causes the ice to almost completely disappear in September, due to the increased flux of solar radiation present at the

surface of the ice. There is a reduction in all of the ice characteristics. The largest changes occur during the melt season.

B30: Increasing the shortwave cloud fraction C_f to 100 % results in an increase in all the ice characteristics. Note that 100 % cloud cover does not imply zero solar radiation flux at the ice surface (Laevastu, 1960). Again, the greatest changes take place during the melt season. The ice compactness fields of the control run indicate too large a meltback in the ice edge in June and September in comparison with observations from satellite (Parkinson *et al.*, 1987). This experiment demonstrated the exact opposite, i.e. insufficient meltback during the summer months. Nevertheless, there is an improvement with respect to the control run simulation. Furthermore, this simulation produced a realistic increase of the average ice thickness to just over 3 m compared to 2 m for the control run. Also, the surface temperature fields in the GIN Sea become much more realistic than in the control run. Consequently, tuning the shortwave cloud parameter to lie between 85 % and 100 % may produce an improved simulation.

B31: A monthly varying cloud fraction is simulated using data from Huschke (1969), and is reproduced in Table 2.5. These values are incorporated into the shortwave radiation calculations. Clearly, the cloud fraction during the six months in which sunlight is absent are irrelevant. As for the six sunlit months, the cloud fraction specified is always less than that of the control run. The result of this experiment was a decrease in the ice characteristics with respect to the control simulation.

B32: A more interesting experiment is to incorporate the monthly cloud fractions into the longwave calculations as well as the shortwave. This allows the clouds to contribute to both heating (increased downwelling longwave) and cooling (decreased downwelling shortwave) in the net energy budget. The cloud fraction has an impact on the longwave radiation throughout the seasonal cycle, whereas the shortwave radiation is active only during the sunlit months. The

net longwave radiation Q_{long} at the surface is the sum total of the downward longwave radiation from the atmosphere Q_{down}, and the upwelling longwave radiation at the surface. The monthly varying downward component Q_{down} was specified as in Parkinson & Washington (1979) by using the Idso & Jackson (1969) formula for clear skies. The upwelling radiation is expressed linearly in terms of the surface temperature using a polynomial expansion (Parkinson & Washington, 1979). The effect of clouds on downward longwave radiation is parameterized using Marshunova (1966):

$$(1 + .16 \cdot C_f) \times Q_{down} \quad . \tag{2.11}$$

Evidently, the impact of this modification, through increased heating, is to produce a decrease in the ice characteristics beyond that of the control run. In fact, the Arctic becomes ice free in September (see Fig. 2.12).

Shine & Crane (1984) studied the sensitivity of a one-dimensional thermodynamic sea-ice model to changes in cloudiness. They utilized the same monthly cloud fraction as in Table 2.5. Based on the variability of cloud data collected over the period 1955-1960 they stated that departures from the mean cloud amount can exceed 20 % and are generally highest during winter in all parts of the Arctic. As seen in the following two experiments, this 20 % uncertainty in cloud amount can lead to large changes in the ice simulation.

B33: Uniformly decreasing all the cloud fractions in Table 2.5 by 20 % produces an even more drastic ice meltback. The Arctic now remains ice free for almost the entire two months of August and September. Thus, less cloud cover means less ice cover in this model. Shine & Crane (1984) speculated that a grid point model, such as used here, would simulate an expanded ice pack under decreased mean cloud conditions. The opposite result of this speculation was found here.

B34: Uniformly increasing all the cloud fractions in Table 2.5 by 20 % produces a simulation closer to the control simulation. The impact of increased cloud cover is to increase the ice characteristics. Shine & Crane (1984) also speculated that a grid point model would simulate an increased amplitude in the seasonal cycle of the areal extent under increased cloud conditions. However, because of the dominance of the ocean heat flux in the GIN Sea, the wintertime ice edge extent is relatively insensitive to cloud cover there. Thus, wintertime ice-edge extent is relatively insensitive to small variations in cloud cover. The summertime ice extent, however, is more sensitive to cloud cover.

Based on the results of the three-dimensional dynamic thermodynamic model used here, the exact opposite conclusion to that of Shine & Crane (1984) is drawn. They found that with respect to changes in cloud cover, changes in the longwave flux dominate the radiation flux; however, here it is found that the shortwave flux causes the greatest change in the net radiation flux under changing cloud conditions. The parameterization of the effect of clouds on the shortwave (Eqn. 2.10) and the longwave radiation (Eqn. 2.11) used in this study differ slightly from the corresponding parameterizations used by Shine & Crane (1984). Consequently, the difference noted here between our results and those of Shine & Crane may be as much dependent upon the longwave and shortwave cloud parameterizations as in the difference between a one-dimensional and three-dimensional model.

To answer the question as to whether the net effect of clouds is to heat or to cool the Arctic surface, one requires further study into the sensitivity of this net cloud effect with respect to surface albedo, longwave flux parameterization, and shortwave parameterization. It should be noted that first-year and multi-year ice have different thermal properties with respect to melting and freezing, and albedo. These differences are expected to be an important factor in the

response of sea ice to cloud forcing. Thus, the distinction between these two classes of ice would have to be incorporated into the model before further progress can be made.

Experiments B36 and B37 : Maximum ice compactness, q_{max}

The solution for the ice compactness (Eqn. 2.3) in a grid cell may not exceed some maximum value. In the control run this maximum value is taken as 100 %. In the central Arctic a certain percentage of open water is always observed in the ice pack, even during winter. Such leads can be important for the heat budget as the presence of a lead allows for a heat loss which is two orders of magnitude larger than occur for an ice covered surface.

B36: In the central Arctic, estimates of the fraction of open water have been placed at 1 to 2 %. This sea ice model is insensitive to the specification of such a fraction of open water. Setting q_{max} at 99 % resulted in an almost identical simulation to that of the control run.

B37: Decreasing q_{max} to 95 % and thus forcing each grid cell to have at least 5 % open water at all times does generate a 20 cm thicker average ice cover. This is because of the increased heat loss through the leads which in turn results in greater ice production. At the same time, the amplitudes of the seasonal cycles of areal coverage and ice compactness are marginally decreased.

Experiments B43, B44, and B45 : Ocean Heat Flux Q_{ocn}

The diagnostic ocean heat flux used in the control run was obtained from output of a prognostic ocean general circulation model (Semtner, 1987). The most prominent feature is that of a large upward heat flux during the winter months, just south of Spitsbergen. The fluxes are of the order of 500 W/m^2 which are far in excess of the solar radiation flux during summer. Such a large heat flux is dominant in melting the ice and, as it turns out, determines the position of

the ice edge in the GIN Sea (Hibler & Bryan, 1987). The ocean heat flux Q_{ocn} enters the model calculations through the thermodynamic forcing term F_h in Eqn. (2.4).

B43: Completely eliminating Q_{ocn}, by setting it to zero, leads to a 25 cm increase in the average annual ice thickness. There is a large increase in areal coverage, as well as an increase in summertime compactness. The ice compactness fields indicate that the ice extents in March and December are far too great both in the Barents Sea and the GIN Sea. The spatial fields of thickness and compactness resemble those of Parkinson & Washington (1979) in that there is a grossly exaggerated ice margin in the GIN Sea. However, the surface temperature fields along the Norwegian Coast are cooler and ,in fact, are more realistic.

Semtner (1987) performed a sensitivity experiment with a coupled ice-ocean model in which he effectively replaced the prognostic ocean component by a simple mixed layer, which did not model either ocean currents or the upward ocean heat flux. He stated that removing the prognostic ocean led to thicker and more compact ice. In the experiment performed here, in which only the upward ocean heat flux was eliminated, the ice also became thicker and more compact throughout the year. In particular, the 10 % increase in compactness Semtner quoted for September is very similar to the increase in September seen in this experiment.

B44: Previous studies have set Q_{ocn} to 2 W/m^2 everywhere (Maykut & Untersteiner, 1971; Parkinson & Washington, 1979). Using such a value leads to an average ice thickness very similar to the control run. However, once again, the southward ice extent in the GIN Sea in December and March is grossly exaggerated (see Fig. 2.13).

B45: Increasing Q_{ocn} to a constant value of 10 W/m^2 everywhere produced an unrealistic seasonal cycle of both ice areal extent and compactness. The ice extent is far too small in

September and far too great in March. Thus a spatially and temporarily varying field of Q_{sw} is crucial to a realistic simulation.

§ 2.4.3 Physical Processes (Theme C)

Experiments C8 and C9 : Ice Rheology, $\vec{I}$

The internal ice stress term $\vec{I}$ in the momentum equation (2.1) is the viscous-plastic formulation of Hibler (1979) as applied to a spherical grid. This rheology is believed to be most appropriate to daily synoptic forcing, as opposed to the monthly forcing employed here. The reasoning is that daily forcing contains synoptic-scale weather events which may produce large shearing forces in the ice pack. The viscous-plastic rheology models the shearing stresses experienced by ice under such conditions.

C8: Another form of the ice internal stress $\vec{I}$ is the cavitating fluid formulation in which the ice is resistive to compressive stresses but not to shear stresses (Flato & Hibler, 1992). This is accomplished in practice by setting e (the eccentricity) to a very large number. Such a rheology formulation is believed to be more appropriate to monthly wind forcing which does not contain synoptic scale events. Eliminating the shear stresses results in a more energetic ice pack (30 % higher) between the months of December and May. Clearly, the shear stresses present in the viscous-plastic formulation only play a significant role during that part of the year when the average compactness is very high (*i.e.* above 90 %). Interestingly enough, there is no accompanying change in the average ice thickness or areal coverage.

C9: Eliminating completely the internal ice stress $\vec{I}$ gives a free drift simulation. The average ice thickness in the Beaufort Sea is just over 3 m, although there is still some buildup of thick ice along the Canadian Arctic Archipelago and Northern Greenland. The increased ice thickness gives the ice pack greater thermal inertia; thus there is a decrease in the amplitudes of

the seasonal cycle of average ice areal extent and compactness. With this elimination of internal stresses between ice floes, the average kinetic energy increases between the months of November and May. In particular, the ice velocity field in December highlights this increased kinetic energy by giving a much stronger Transpolar Drift Stream, as well as a strong anticyclonic flow in the centre of the Canadian Basin.

Experiments C14 and C15 : Ice Heat Storage

Sea ice has two mechanisms for the storage of heat. First, the ice has a specific heat capacity. This is a thermal inertia that requires the input of energy to raise the temperature of the ice; likewise energy is released when the ice is cooled. Secondly, the ice has internal brine pockets which store energy from incoming solar radiation in the form of latent heat. These brine pockets release this stored heat in the fall during refreezing. Neither of these heat storage mechanisms is modelled in the control run.

C14: Consider an ice floe of effective thickness h/q, surface temperature T_{surf}, bottom temperature T_{ocn}, density ρ_{ice}, and heat capacity $c_{p,ice}$. The amount of heat that must be extracted to lower the surface temperature of the ice to T'_{surf} is

$$\frac{1}{2}\,\rho_{ice}\,\frac{h}{q}\,c_{p,ice}\,(T'_{surf} - T_{surf}) \qquad (2.12)$$

This amount of heat is represented by the shaded area in Fig. 2.14. This additional heat term was added to the thermodynamic heat budget for the model.

Assigning the ice a heat capacity equal to 2090 J/kgK serves to shift the phase of the seasonal cycle of ice compactness. The ice reaches minimum compactness about two weeks later than in the control run. This is a result of the delay introduced to the heating and cooling process by the heat capacity. There are no other noticeable changes.

C15: The modelling of heat storage by internal brine pockets is carried out as in Semtner (1976a). With the appearance of the sun in spring, heat is accumulated in the brine pockets throughout the summer by absorbing 17 % of the incident solar radiation (Maykut & Untersteiner, 1971). The heat accumulation is arbitrarily limited to 30 % of the heat required to melt the ice. In fall, the heat reservoir is fully exhausted prior to the recommencement of ice growth.

Introducing brine pockets into the ice reduces the average ice thickness by about 20 *cm* or 10 % (Fig. 2.15). There are comparable decreases in the ice areal coverage, compactness, and kinetic energy. Particularly interesting is the change in the seasonal cycle of compactness. The inclusion of brine pockets delays the fall freeze-up by approximately six weeks (see Fig. 2.15c). Including the effects of the brine pockets has a bigger change than changing the ice specific heat (experiment C14).

Experiments C16 and C17 : Snow Cover

The presence of a snow cover on the ice surface can alter the thermodynamic response of the ice. The snow does not affect the dynamics of the ice as snow contributes little to the mass of an ice floe and has negligible strength. However, the presence of snow may lead to either a decreased or an increased ice melt rate. The higher albedo of the snow causes it to reflect more solar radiation than snow-free ice; this leads to a decreased ice melt rate. In contrast, snow has a smaller thermal conductivity than ice, thus leading to greater insulation of the atmosphere from the ocean than for snow-free ice. This means a decrease in both the ice melt and growth rates. The monthly snow rates for the Arctic are taken from Maykut & Untersteiner (1971) and are given in Table 2.6. The total annual snowfall is about 50 *cm/year*, with the greatest snowfall occurring during the fall. The snow accumulates at the prescribed rate provided the surface temperature is not above the freezing point. The values of the snow

physical parameters are (i) conductivity = .3 W/mK (ii) albedo = .70 (iii) density = 330. kg/m^3 and (iv) emissivity = .99. In essence, the layer of snow and the layer of ice are treated as a single layer with an effective thermal conductivity. This effective conductivity is obtained by taking a weighted average of the ice and snow thicknesses (Hibler, 1980), *viz.*,

$$k_{eff} = \frac{h_{ice}\, k_{ice}}{h_{ice} + \frac{k_{ice}}{k_{snow}}\, h_{snow}} \tag{2.13}$$

where h_{ice} and h_{snow} are respectively the ice and snow thickness, while κ_{ice} and κ_{snow} are respectively the ice and snow thermal conductivities. This treatment means that it is unnecessary to solve for the interface temperature between the snow and the ice. It is reasonable to assume that there is no net divergence of heat flux at this ice-snow interface.

C16: The desire to include snow cover in the sea-ice model was motivated by the interesting multi-year cycle of ice thickness reported by Semtner (1976a) in his thermodynamic model (Fig. 2.16). Semtner found a "natural oscillation" in the sea ice thickness with a period of six years, even though the same forcing was applied each year. He attributed this behaviour to the differing conductivities of the snow and ice. He suggested that this may be an important feature leading to multi-year anomalies in the observed ice cover. Washington *et al.* (1976) extended the Semtner model to three dimensions and reported finding a similar multi-year cycle in the ice thickness. Parkinson & Kellogg (1979), using a three-dimensional dynamic thermodynamic model, did not find a multi-year cycle. In a one-dimensional thermodynamic sea ice model, Shine & Crane (1984) reported finding a multi-year cycle of ice thickness. However, they argued that these oscillations are unlikely to be real features of the ice behaviour. Instead they suggested that the oscillations may be due to the rigid specification of snowfall rates on particular dates, whereas in nature it is possible the periods of maximum snowfall are related to

dates of freeze-up. These rates are poorly known and probably undergo large spatial and interannual variations.

The introduction of snow cover into this sea-ice model gives a slightly thicker ice cover from June through to December. There is also a noticeable increase in both areal coverage and compactness between June and October. The presence of the snow cover leads to colder ice surface temperature fields in March and December, with temperatures in the central Arctic being approximately 5 $^{\circ}C$ colder than in the control run. In contrast to the findings of Semtner, of Washington *et al.*, and of Shine & Crane, no such multi-year cycle was observed in this dynamic thermodynamic model. In a further experiment, dynamics were eliminated from the model and still a multi-year cycle in ice thickness was not detected.

C17: This experiment was motivated by an experiment of Maykut & Untersteiner (1971) in which the snowfall rate was increased above the 50 *cm/year* rate specified in Table 2.6. They found that for an annual snowfall rate in excess of about 120 *cm/year* the mean annual ice thickness increased without bound (Fig. 2.17). Semtner (1976a) was led to the same result using his simplified one-dimensional thermodynamic sea-ice model.

In this model, increasing the annual snow rate by a factor of 5 (giving an annual total snowfall of 250 *cm/year*) produces significant changes in the model response (see Fig. 2.18). However, unlike in the Maykut & Untersteiner model, the sea-ice thickness did not increase in an unbounded manner. The average ice thickness increases by about .5 *m*, while the areal coverage and compactness are much greater in September compared with the control run cases. Again, a large areal extent of the central Arctic is about 5 $^{\circ}C$ colder in the presence of this increased snow cover. The results indicate that the ice pack is not unstable with respect to a

significant increase in precipitation. Such an increase in precipitation could occur under a climate change scenario.

These results indicate that a dynamic thermodynamic model is less sensitive to parameter changes than a simple thermodynamic model. This conclusion has also been noted by Owens & Lemke (1990). In a modelling study of the Weddell Sea, they performed a sensitivity study in which they concluded that snow cover affects a thermodynamic sea-ice model more than a dynamic thermodynamic model. They provided an interesting explanation for this phenomena in terms of a negative feedback between the dynamics and the thermodynamics of the sea-ice model. In regions where the thermodynamics reduces the ice thickness, the ice gets weaker and the dynamics (under favourable conditions, *i.e.* convergence) can readily increase the ice thickness (by importing ice into the region). In regions where the dynamics reduce the ice thickness (divergence), the thermodynamics (under favourable conditions, *i.e.* cooling) can easily increase the sea ice thickness. These interactions provide a negative, i.e. stabilizing feedback (Owens & Lemke, 1990).

Experiments C18 and C19 : Changes in Air Temperature

It is interesting to study the response of the sea-ice model to changes in atmospheric temperature that have been predicted, for example, from nuclear winter or from global warming experiments using coupled atmosphere-ocean models with a simple sea-ice component (*e.g.* Manabe *et al.*, 1991). It is also important to keep in mind, however, that the simplistic experiments C18 and C19 can only identify the first order response of sea ice to a hypothetical cooler or warmer Arctic. As such, they ignore other changes that would accompany cooler or warmer temperatures, such as changes in the atmospheric winds and precipitation.

The control run was forced with monthly fields of atmospheric temperatures. In the following experiments uniform spatial changes through each month of the year were made to

these fields. These changes in atmospheric temperature directly affect the calculation of downward longwave radiation, and the sensible and latent heat fluxes. These quantities in turn feed into the calculation of the total atmospheric heat flux Q_{atr} which appears in Eqn. (2.4).

C18: Uniformly decreasing the atmospheric temperature by 5 °C produces an approximate 40 *cm* increase in sea ice thickness. There is also greater areal extent and compactness in the fall associated with the colder temperatures. The ice surface temperature fields show a decrease of about 5 °C in the central Arctic during winter.

C19: Uniformly increasing the atmospheric temperatures by 5 °C produces the opposite effect. The reduction in ice thickness is approximately 40 *cm*, yet the ice does not completely disappear at any time during the seasonal cycle (see Fig 2.19). Thus, the ice pack is stable to perturbations in air temperature of ± 5 °C. Using a heat budget calculation for a given point in the central Arctic, Budyko (1966) determined that a positive anomaly of summer temperatures of only 4 °C would cause ice of 4 *m* thickness to melt completely after four years. Using a dynamic thermodynamic model with a more simplistic ice rheology than the one presented here, Parkinson & Kellogg (1979) found that the ice pack disappeared completely in August and September but reformed in the central Arctic in mid fall. Semtner (1987) found that a 2 °C increase was sufficient to cause a dramatic disappearance of the sea ice in late summer (Fig. 2.20). He used a coupled ice-ocean model for his experiment. However, there are differences in the two sea-ice models with respect to the rheology formulation, the number of layers for temperature, the coordinate system, and in the computation of net heat flux. As his integration was carried out for only a two-year period, it can not be expected that the imposed temperature increase would affect the ocean circulation; thus, the only effect is on the thermodynamic aspects of the ice. Thus, there is a noticeable difference in air temperature sensitivity between Semtner's

sea-ice model and the one presented here. It is difficult to speculate on the reasons for this difference; however, the subtle differences between each model's formulation of ice thermodynamics, dynamics, numerical methods, and atmospheric fields may be enough to account for the difference in results obtained.

§ 2.5 Conclusions

This study has demonstrated that the Oberhuber spherical coordinate sea-ice model produces a reasonable simulation of the seasonal cycle of sea ice in the Arctic. All the known major features of the seasonal cycle of ice thickness, compactness, and velocity have been reproduced. Furthermore, a stable time integration is guaranteed by the appropriate choice of time step increment determined by the CFL condition and by the choice of a numerical diffusion coefficient estimated by the grid-cell Reynolds number condition. As well, an appropriate value for the maximum bulk viscosity is given. The use of a predictor-corrector technique coupled with a semi-implicit scheme gives reliable and efficient convergence for the difficult non-linear rheology terms in the ice equations.

The main aim of this study has been to carry out a thorough sensitivity analysis of a dynamic thermodynamic sea-ice model. Although several of the sensitivity experiments have been carried out elsewhere, it is difficult to estimate the relative importance of various effects because different models have been used. By contrast, all the experiments done here use the same model and the results are compared against one control run. Also, this study has examined the effect of certain processes and parameter variations that have not previously been carried out.

This sensitivity study has shown that the sea-ice model produces a robust simulation of the seasonal cover of Arctic sea ice. Sensitivity studies have been presented under three different

investigative themes, namely, (A) numerical conditions, (B) parameter variations, and (C) physical processes. The results of these studies are summarized below.

The numerical condition experiments (theme A) show the model to be essentially insensitive to initial conditions. Upon spinning up from a motionless and ice-free Arctic, the model produces a reasonable simulation in the fifth year of integration. However, it was noted that when spinning up with the unrealistic ice thickness of 10 *m* everywhere, the model did not reach equilibrium even after ten years of integration. A second finding was that the choice of boundary condition at the model pole, where grid cells converge, is not crucial to the simulation. Thus, the use of a spherical coordinate system with convergence at the pole does not adversely affect the simulation away from the poles. This suggests the presence of the model coordinate pole at the North Pole in a global simulation using the fully coupled Oberhuber ice-ocean model would not degrade the model's performance.

The parameters investigated (theme B) relate to or include ice rheology, thermodynamic coefficients, diffusion coefficients, conductivity, albedo, drag coefficients, turbulent heat transfer coefficients, cloud fraction, emissivity, minimum fraction of leads, mixed layer salinity, depth, and turbulent heat flux. From this set of parameters, the model was found to be particularly insensitive to the mixed layer properties such as ocean albedo, salinity, and depth. The parameter that probably contains the greatest uncertainty is the cloud fraction, and changing it has drastic effects. An experiment with increased cloud cover, relative to the control run, leads to a more realistic seasonal ice simulation.

The final set of experiments dealt with the removal or addition of specific dynamic and thermodynamic processes (theme C). These experiments highlight the relative importance of the different components of the model. With regard to the heat budget, the latent heating was found to be a minor contributor to the overall budget; thus elaborate parameterizations of this process

are unwarranted. Although the atmospheric winds make a greater contribution (70 %) to the ice kinetic energy than the ocean currents (30%) (Thorndike & Colony, 1982), it is necessary to include both in the surface stress calculations. Using a bulk-viscous rheology, in which shear stresses have been eliminated, leads to more energetic ice circulation. The inclusion of the ocean surface tilt term in the momentum balance was not found to be important. Removal of the Coriolis force from the simulation displaces the ice velocity vectors about 10 degrees to the left of those in the control run. Completely eliminating the ice dynamics leads to an unrealistic simulation. Concerning heat storage within the ice, it was found that assigning the ice a realistic specific heat capacity (instead of zero) does not affect the simulation, but that the inclusion of brine pockets has a significant impact by delaying the onset of freezing during the fall. Including snowfall in the model was not felt to be crucial to the simulation.

Discrepancies have been noted between sensitivity studies carried out here and those carried out elsewhere. Maykut & Untersteiner (1971) found that in a thermodynamic-only model, sea-ice thickness would increase uncontrollably if the snow fall exceeded 120 *cm/year*; in this study the sea-ice model was stable to annual snowfall rates as high as 250 *cm/year*. Semtner (1976a) reported that adding snow to a sea ice model introduces natural interannual oscillations in the sea-ice cover with a six year period; no such interannual variation was found in this study. Regarding the ice rheology parameters, Hibler (1979) found that increasing the compressive strength substantially reduces the relative geographical ice thickness variations. Such a sensitivity was not noted here. Hibler also removed the ice compactness equation and found that the simulation does not change significantly. In this model, however, complete removal of this equation led to a drastic change in the simulation. Concerning cloud cover, Shine & Crane (1984) concluded that on an annual basis, clouds act to warm the surface and reduce the ice thickness. The opposite result was found in this study; clouds were found to cool the surface and

to increase ice thickness. It is concluded that the competing effects of clouds on the radiation budget through longwave and shortwave radiation require further investigation in a three-dimensional dynamic thermodynamic sea-ice model. Semtner (1987) obtained an ice-free Arctic during the month of September in an experiment in which he increased the atmospheric temperatures by two degrees everywhere. In the present study, a five degree increase in temperature produced a significant decrease in all ice characteristics, but did not lead to an ice-free Arctic at any time during the seasonal cycle. Thus we wish to caution the reader against assuming these issues are settled. Further investigations with coupled atmosphere-ocean models are required to answer these open questions.

A technical weakness of the sensitivity tests is the absence of feedbacks to the prescribed forcing variables. For example, the specification of 5% open water (Exp. B37) would almost certainly increase the surface air temperatures to values above those now prescribed during the non-summer months, thus leading to a greater impact on the ice than was obtained here. Similarly, snowfall (Exps. C16, C17) will alter the surface energy balance and the real world's surface air temperatures. A final example is Exp. B21, in which a drastic change in the ocean albedo is buffered in the model by the inability of the air temperature to change accordingly. Thus the real world -- or even a coupled model -- may respond quite differently than the artificially constrained model used here.

A major impediment to progress in sea-ice modelling at present is the lack of sufficient observations to either validate or to assimilate into the models. The future increase in satellite observations will be helpful; however, it will not provide all the measurements needed. Sea-ice thickness data, for instance, are scarce over the Arctic and the data that do exist are sporadic in both space and time. As another example, measurements of upward heat flux from the deep

ocean, which is of paramount importance to a realistic simulation, are virtually non-existent. The accuracy of simulations cannot progress until this situation is rectified.

This study has implications for atmospheric models that are coupled to a dynamic thermodynamic sea-ice model in which the ocean is represented as a simple mixed layer. Mixed layer currents contribute significantly to the ice drift and cannot be ignored. Specification of seasonally and spatially varying mixed layer salinity or mixed layer depth is not important; specification of upward deep ocean heat flux is important. In particular, it is well known that it is the spatial and temporal variations in this heat flux that is crucial. It is unsatisfactory to specify this flux as a time and space invariant quantity.

Table 2.1 Numerical values of parameters and constants

Parameter	Value
Velocity Diffusion Coef., A^m	2000 m^2s^{-1}
Earth's Angular Velocity, Ω	7.292 x 10^{-5} s^{-1}
Gravity, g	9.806 ms^{-2}
Ice Density, ρ_{ice}	910 kgm^{-3}
Earth Radius, r	6400 km
Air Density, ρ_{air}	1.2 kgm^{-3}
Air Drag Coef., C_{air}	.0012
Water Density, ρ_{ocn}	1025 kgm^{-3}
Water Drag Coef., C_{ocn}	.0055
Yield Curve Eccentricity, e	2
Ice Strength, P^*	10.000 Nm^{-2}
Minimum Strain Rate, $\varepsilon_{..}$	$1.0x10^{-9}$ s^{-1}
Ice Strength Decay Constant, C^*	10
Grid Spacing, $\delta\lambda$	5 - 140 km
Grid Spacing, $\delta\phi$	111 km
Scalar Diffusion Coef., A^s	2000 m^2s^{-1}
Latent heat Fusion, L_f	$3.34x10^5$ Jkg^{-1}
Specific Heat Capacity of Ice, $c_{p,ice}$	2090 $Jkg^{-1}K^{-1}$
Ice Conductivity, κ_{ice}	2 $Wm^{-1}K^{-1}$
Ice Albedo, α_{ice}	.40
Ocean Albedo, α_{ocn}	.17
Emissivity Ice Surface, ε_{ice}	.97
Emissivity Ocean Surface, ε_{ocn}	.97
Stefan-Boltzmann Constant, σ	$5.67x10^{-8}$ $Wm^{-2}K^{-4}$
Sensible Heat Coef., C_{sens}	.0015
Latent Heat Coef., C_{lat}	.0015
Cloud fraction, C_f	.85
Specific Heat Air, $c_{p,air}$	1005 $Jkg^{-1}K^{-1}$
Surface Air Pressure, p_{surf}	10^5 Pa
Latent Heat of Evaporation, L_e	$2.5x10^6$ Jkg^{-1}

Parameter	Value
Cutoff Ice Thickness, h_o	.5 *m*
Coef. of Freezing, C_{freeze}	1.
Coef. of Melting, C_{melt}	1.
Maximum Ice Compactness q_{max}	100 %
Mixed Layer Depth, h_{ocn}	30 *m*
Specific Heat of Ocean Water, $c_{p,ocn}$	3930 $Jkg^{-1}K^{-1}$
Time Step Increment, δt	1/2 *day*
Total Integration Time	10 *years*

Table 2.2 Numerical Conditions (Theme A)

Experiment Label	Experiment Description	Experiment Value	Control Value
A1	Timestep δt	2 *hours*	12 *hours*
A2	Timestep δt	1 *day*	12 *hours*
A3	Total Integration Time	100 *years*	10 *years*
A4	Initial Ice Compactness	100 %	0 %
A5	Initial Ice Thickness	10 *m*	0 *m*
A6	Initial Ice Velocity	.50 ms^{-1}	0 ms^{-1}
A7	Initial Mixed Layer Temperature	+5.0 °C	-1.8 °C
A8	Maximum Number of Iterations	50	100
A9	Machine Accuracy Constant	10^{-20}	10^{-100}
A10	Boundary Condition (North Pole)	Free Flow over Pole	Stick at Pole

Table 2.3 Parameter Values (Theme B)

Experiment Label	Experiment Description	Experiment Value	Control Value
B1	Ice Strength P^*	$1\times10^3\ Nm^{-2}$	$10\times10^3\ Nm^{-2}$
B2	Ice Strength P^*	$30\times10^3\ Nm^{-2}$	
B3	Ice Strength Decay Constant C^*	5	10
B4	Ice Strength Decay Constant C^*	20	
B5	Yield Curve Eccentricity e	1	2
B6	Yield Curve Eccentricity e	4	
B7	Coefficient of Freezing C_{frez}	1/2	1
B8	Coefficient of Freezing C_{frez}	2	
B9	Coefficient of Melting C_{melt}	1/2	
B10	Coefficient of Melting C_{melt}	2	
B11	Coefficient of Diffusion for Ice Thickness and Compactness A^s	$1\times10^3\ m^2s^{-1}$	$2\times10^3\ m^2s^{-1}$
B12	Coefficient of Diffusion for Ice Thickness and Compactness A^s	$20\times10^3\ m^2s^{-1}$	
B13	Coefficient of Diffusion for Ice Momentum A^m	$.2\times10^3\ m^2s^{-1}$	
B14	Coefficient of Diffusion for Ice Momentum A^m	$20\times10^3\ m^2s^{-1}$	
B15	Thermal Conductivity of Ice κ_{ice}	$.1\ Wm^{-1}K^{-1}$	$2\ Wm^{-1}K^{-1}$
B16	Thermal Conductivity of Ice κ_{ice}	$10\ Wm^{-1}K^{-1}$	
B17	Ice Surface Albedo α_{ice}	.10	.40
B18	Ice Surface Albedo α_{ice}	.90	
B19	Ice Surface Albedo α_{ice} Dependent on Atmospheric Surface Temperature	Eqn. 8	
B20	Ocean Surface Albedo α_{ice}	.05	.17
B21	Ocean Surface Albedo α_{ocn}	.50	
B22	Atmospheric Drag Coefficient C_{air}	$.12\times10^{-3}$	1.2×10^{-3}
B23	Atmospheric Drag Coefficient C_{air}	$12.\times10^{-3}$	
B24	Atmospheric Drag Coefficient C_{air} Dependent on Ice Compactness q	Eqn. 9	
B25	Oceanic Drag Coefficient C_{ocn}	$.55\times10^{-3}$	5.5×10^{-3}
B26	Oceanic Drag Coefficient C_{ocn}	55×10^{-3}	

Experiment Label	Experiment Description	Experiment Value	Control Value
B27	Coefficient for Sensible and Latent Heat Transfer C_{sens} and C_{lat}	$.15\times10^{-3}$	1.5×10^{-3}
B28	Coefficient for Sensible and Latent Heat Transfer C_{sens} and C_{lat}	$15.\times10^{-3}$	
B29	Shortwave Cloud Fraction C_f	.55	.85
B30	Shortwave Cloud Fraction C_f	1.00	
B31	Monthly Varying Shortwave Cloud Fraction C_f	Table 6	
B32	Monthly Varying Longwave and Shortwave Cloud Fraction C_f	Table 6	
B33	Monthly Varying Longwave and Shortwave Cloud Fraction C_f Decreased Uniformly by .20	Table 6	
B34	Monthly Varying Longwave and Shortwave Cloud Fraction C_f Increased Uniformly by .20	Table 6	
B35	Longwave Emissivity of Ice ε_{ice} and Ocean ε_{ocn}	.90	.97
B36	Maximum Ice Compactness q_{max}	.99	1.00
B37	Maximum Ice Compactness q_{max}	.95	
B38	Mixed Layer Salinity S_{ocn}	30 *psu*	Fig. 2.12*
B39	Mixed Layer Salinity S_{ocn}	0 *psu*	
B40	Mixed Layer Depth h_{ocn}	3 *m*	30 *m*
B41	Mixed Layer Depth h_{ocn}	300 *m*	
B42	Mixed layer Depth h_{ocn}	Spatially Varying	
B43	Deep Ocean Heat Flux Q_{ocn}	0 Wm^{-2}	Spatially Varying
B44	Deep Ocean Heat Flux Q_{ocn}	2 Wm^{-2}	
B45	Deep Ocean Heat Flux Q_{ocn}	10 Wm^{-2}	

Table 2.4 Physical Processes (Theme C)

Experiment Label	Experiment Description
C1	Downward Shortwave Radiation Eliminated
C2	Upward and Downward Longwave Radiation Eliminated.
C3	Sensible Heat Transfer Eliminated
C4	Latent Heat Transfer Eliminated
C5	Ice Compactness Equation Eliminated
C6	Atmospheric Winds Eliminated
C7	Oceanic Currents Eliminated
C8	Cavitating Fluid Rheology Introduced
C9	Ice Rheology Eliminated
C10	Ocean Surface Tilt Eliminated
C11	*f*-plane Approximation
C12	Coriolis Force Eliminated
C13	Ice Dynamics Eliminated
C14	Specific Heat Capacity Introduced
C15	Internal Brine Pockets Introduced
C16	Monthly Snowfall Introduced
C17	Monthly Snowfall (Rate increased by factor of 5)
C18	Atmospheric Air Temperatures Decreased Uniformly by 5 $^{\circ}C$
C19	Atmospheric Air Temperatures Increased Uniformly by 5 $^{\circ}C$

Table 2.5 Monthly Cloud Fractions

Jan	Feb	Mar	Apr	May	Jun	Jul	Aug	Sep	Oct	Nov	Dec
.50	.50	.50	.55	.70	.75	.75	.80	.80	.70	.60	.50

Table 2.6 Monthly Snowfall Rates (*cm/month*)

Jan	Feb	Mar	Apr	May	Jun	Jul	Aug	Sep	Oct	Nov	Dec
.83	.83	.83	.83	5.0	.0	.0	12.8	12.8	12.8	.83	.83

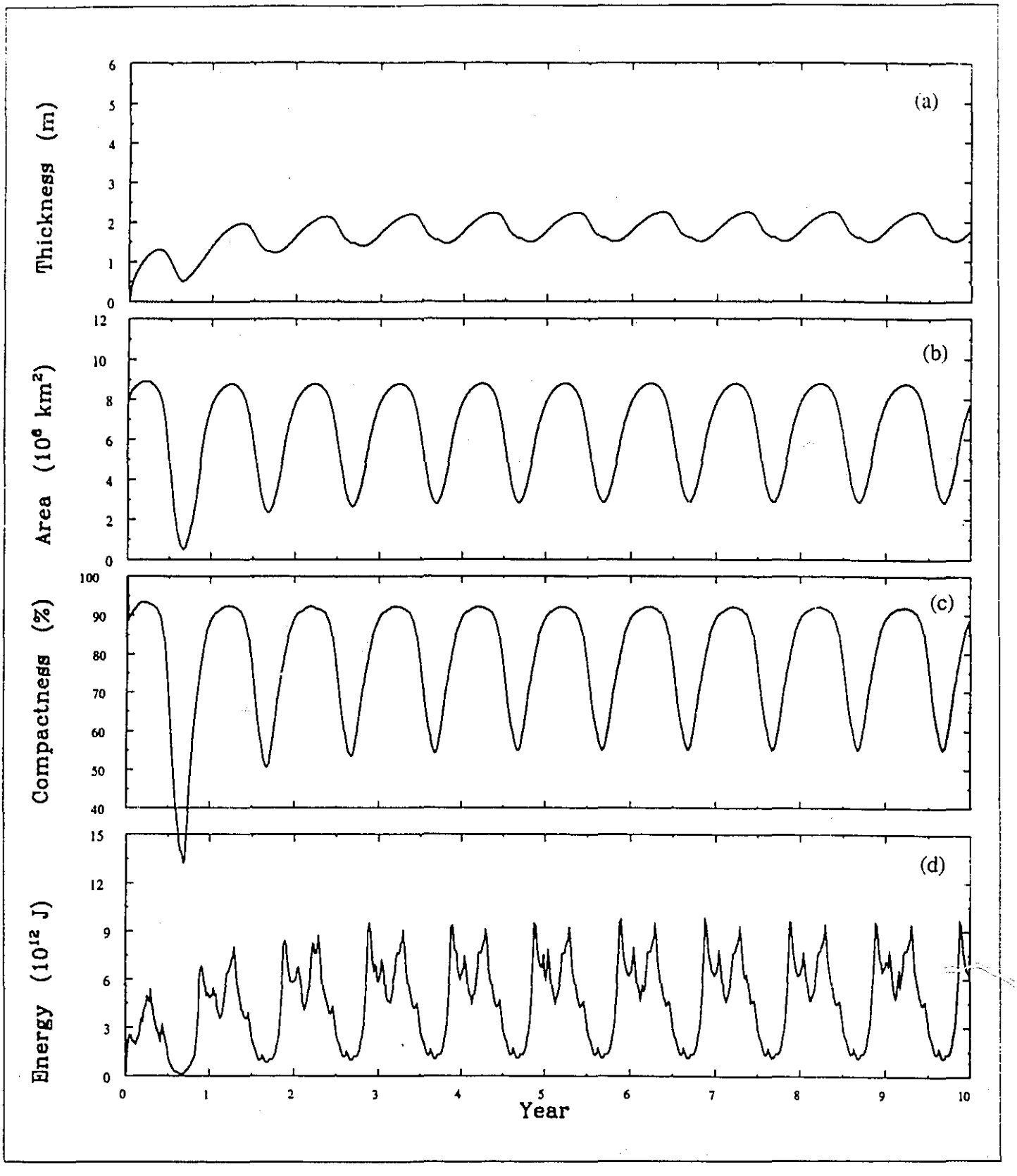

Figure 2.1 Time series of effective ice thickness, areal coverage, compactness, and kinetic energy over a 10 year spin-up period. All signals are area averaged over all grid points in the domain that contain ice.

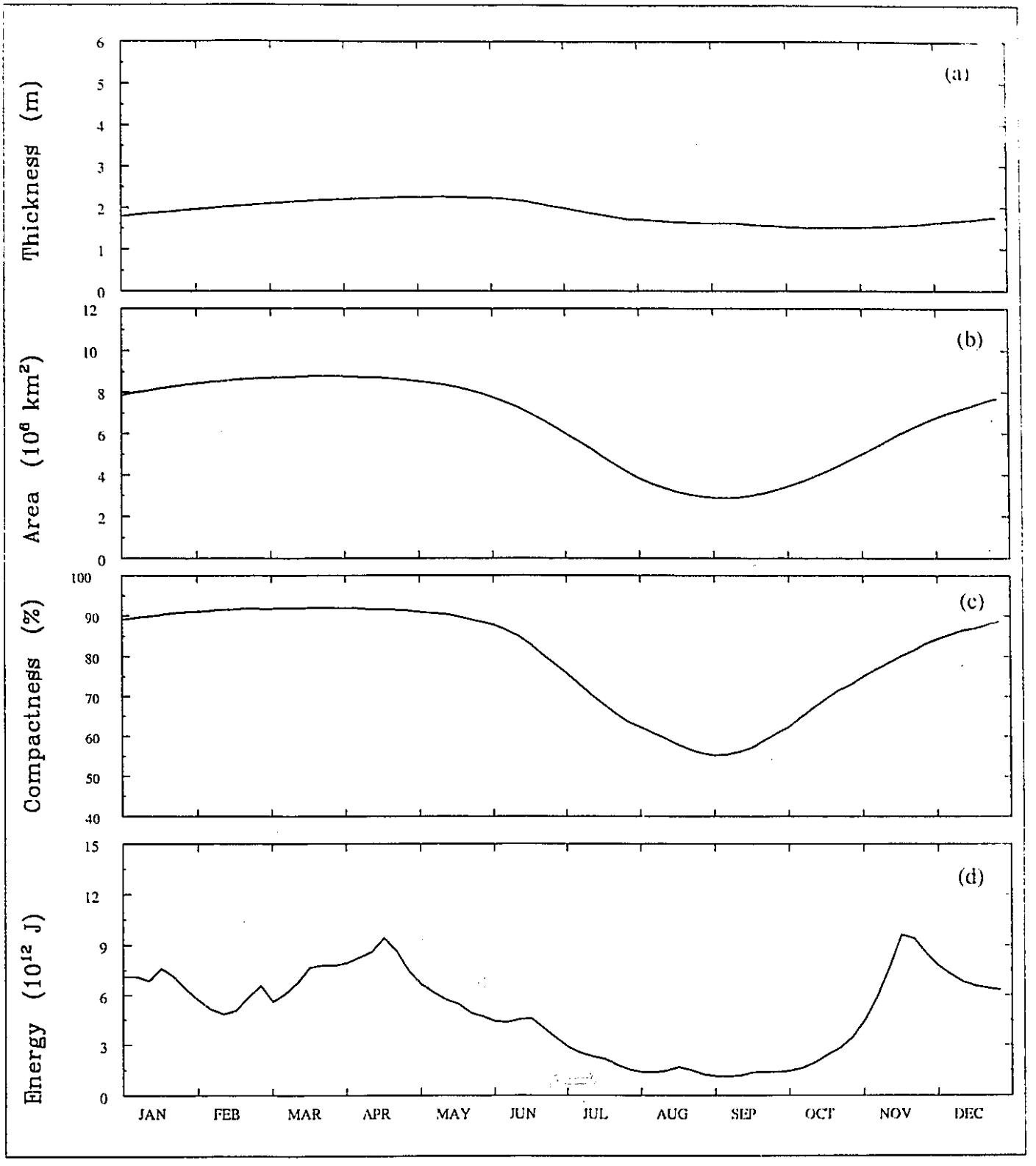

Figure 2.2 Time series of effective ice thickness, areal coverage, compactness, and kinetic energy over the equilibrium annual cycle (*i.e.* over the final year of the spin-up simulation) for the control parameters. All signals are area averaged over all grid points in the domain that contain ice.

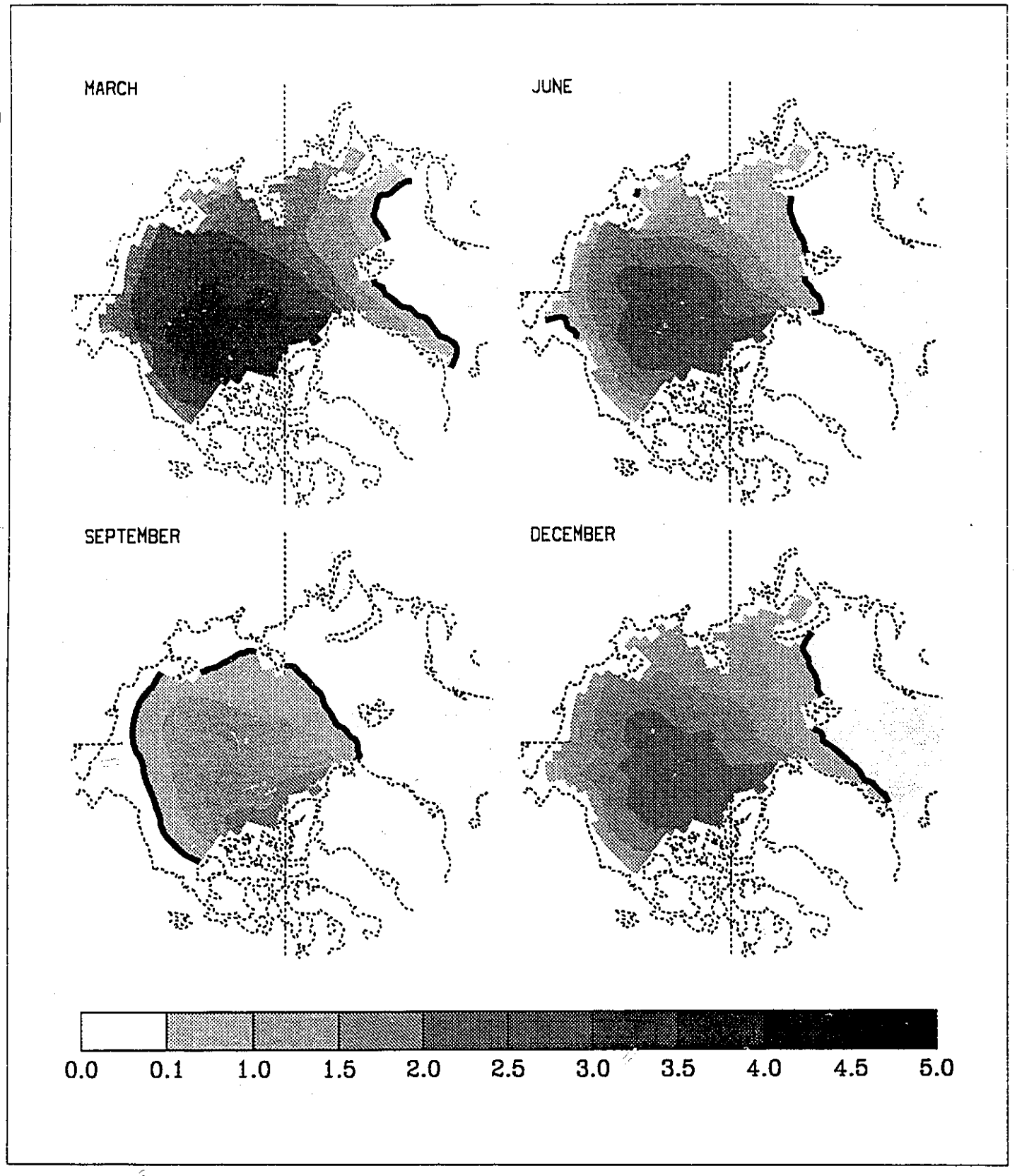

Figure 2.3 Seasonally varying ice thickness fields (in units of *m*) from the control simulation. The heavy black line indicates the 0.5 *m* thickness contour.

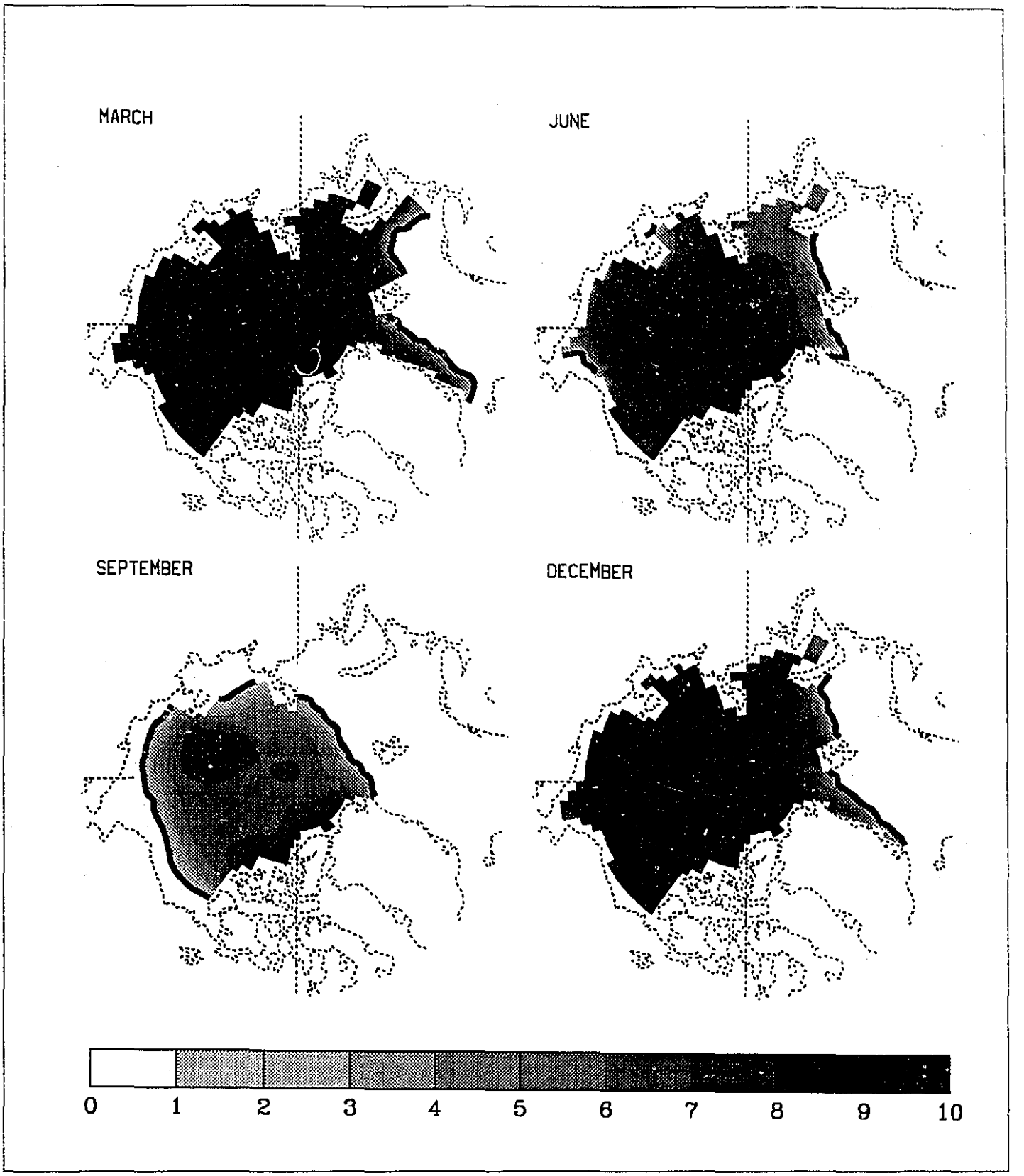

Figure 2.4 Seasonally varying ice compactness fields (in units of 10^{ths}) from the control simulation. The heavy black line indicates the $1/10^{th}$ compactness contour.

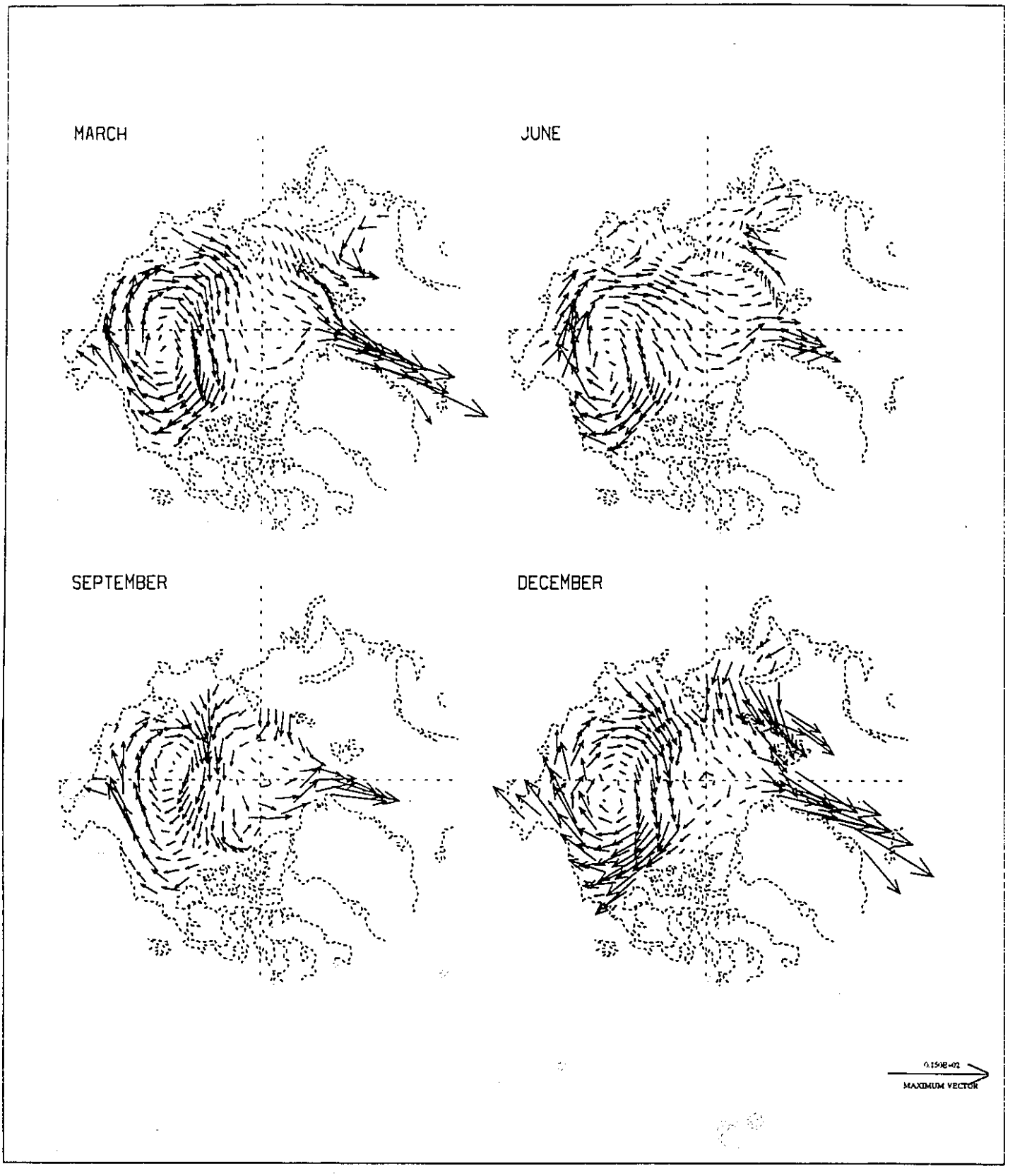

Figure 2.5 Seasonally varying ice velocity fields from the control simulation. The largest vector represents an ice velocity of 15 *cm/s*. The main features are the Beaufort Gyre, the Transpolar Drift Stream, and the East Greenland Current Drift.

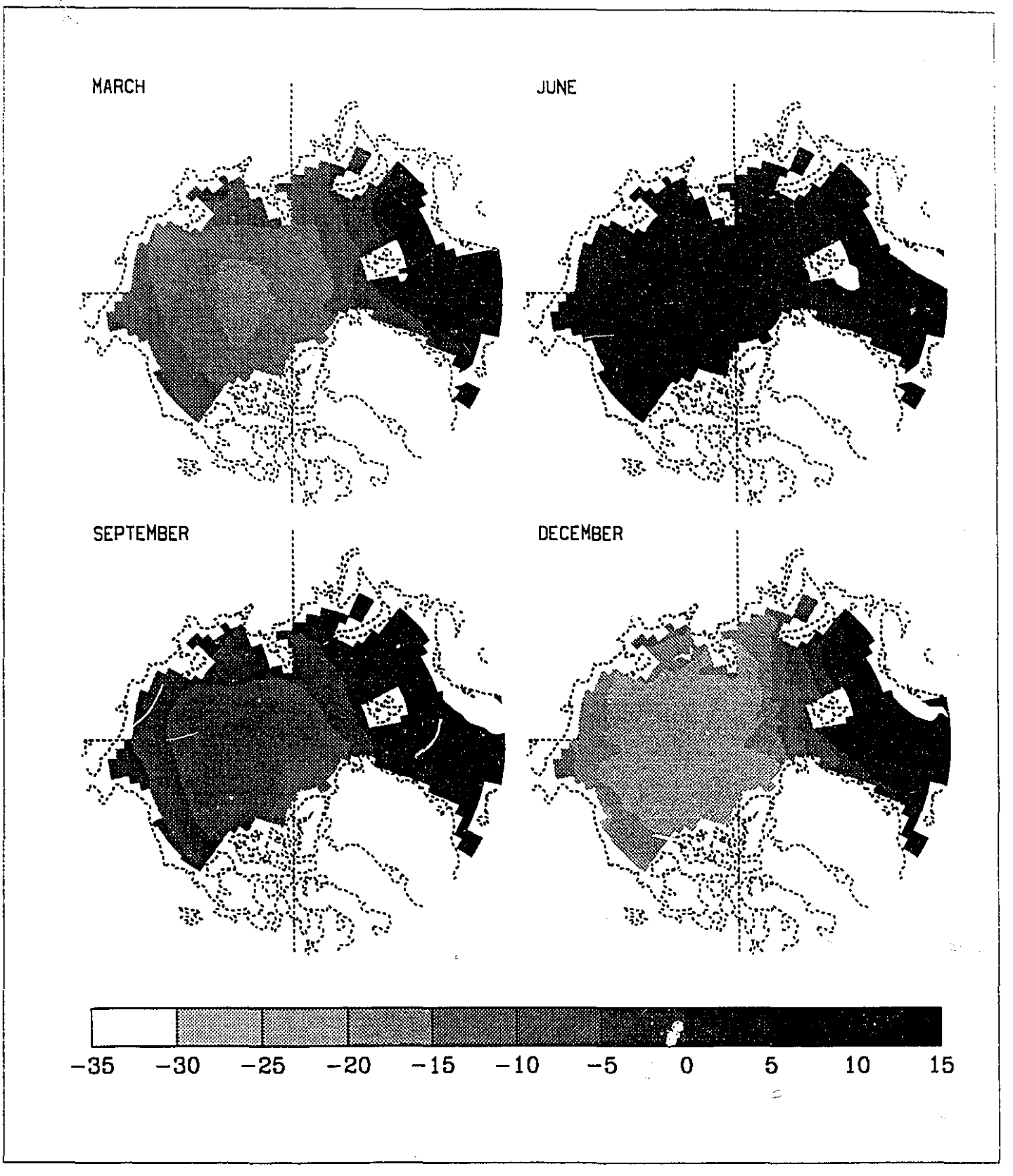

Figure 2.6 Seasonally varying ice or ocean surface temperatures (in degrees *C*) from the control simulation. Where ice exists the temperature given is the weighted average of the ice surface and of the leads; where there is no ice the temperature shown is that of the ocean surface. The heavy black line indicates the zero degree contour.

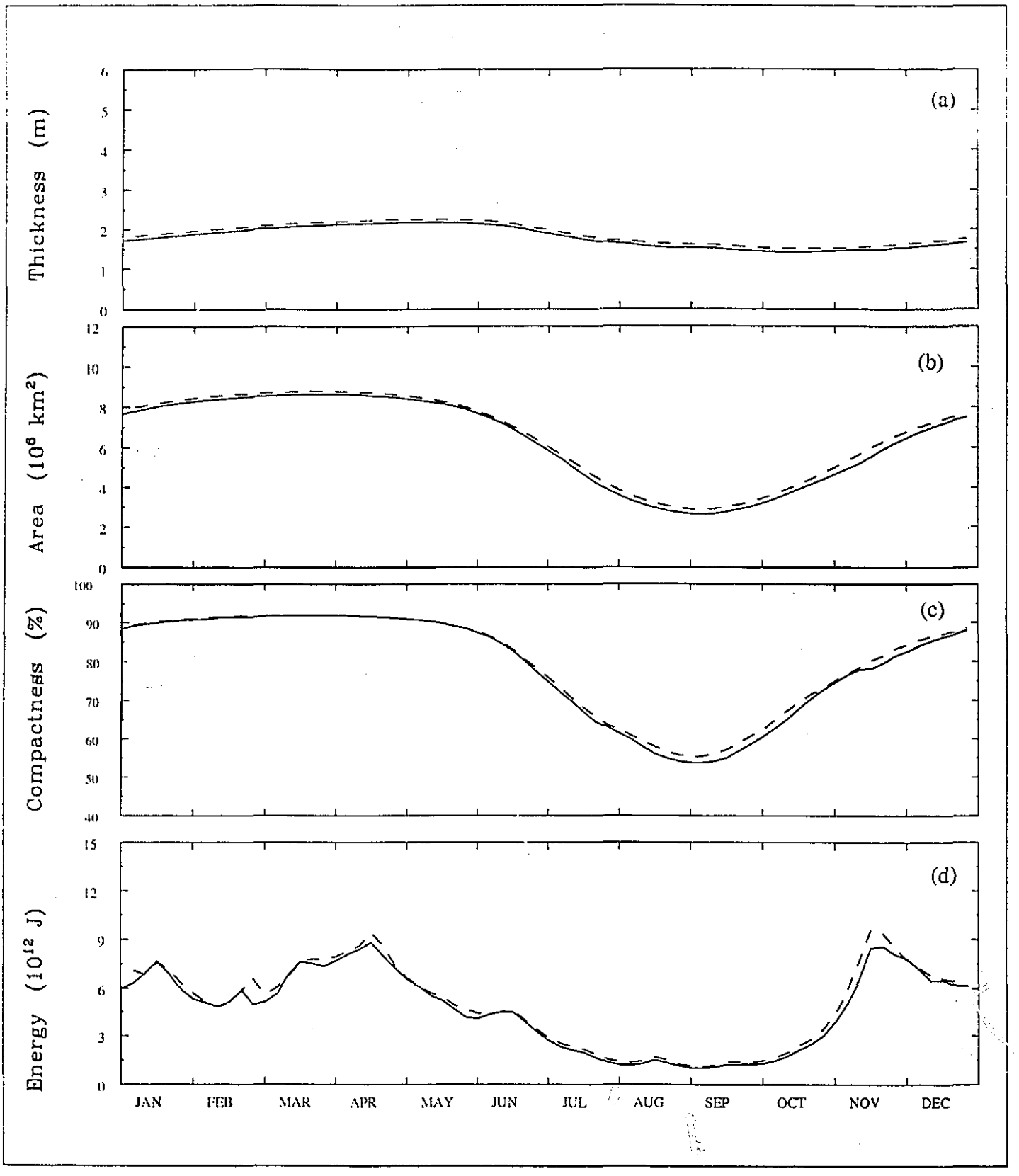

Figure 2.7 Experiment A10 (boundary condition at pole). Time series of ice thickness, areal coverage, and kinetic energy over the equilibrium annual cycle. The dashed lines are the results from the control run.

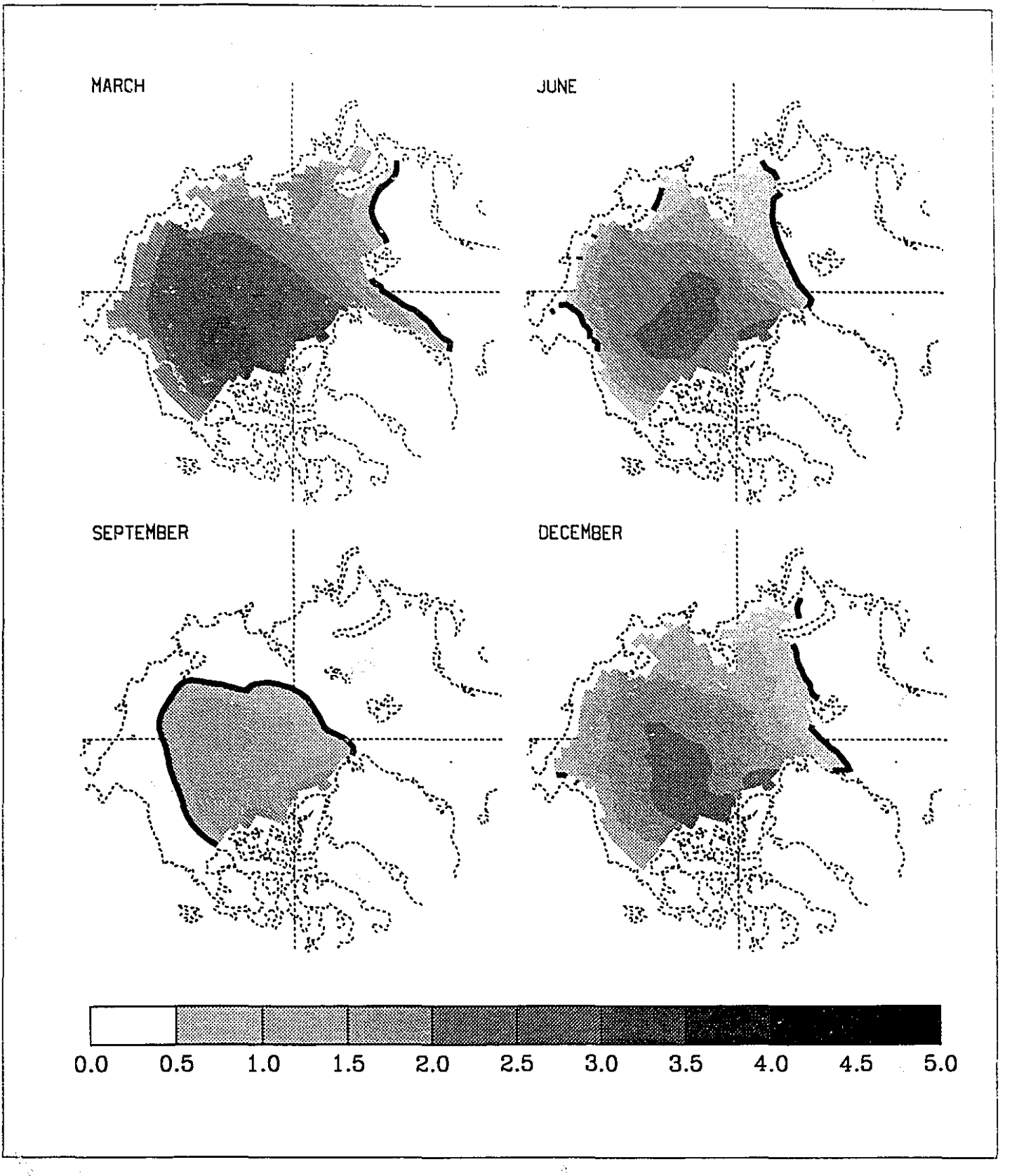

Figure 2.8 Experiment A10 (boundary condition at pole). Seasonally varying ice thickness fields (in units of *m*) from the simulation. The heavy black line indicates the .5 *m* thickness contour.

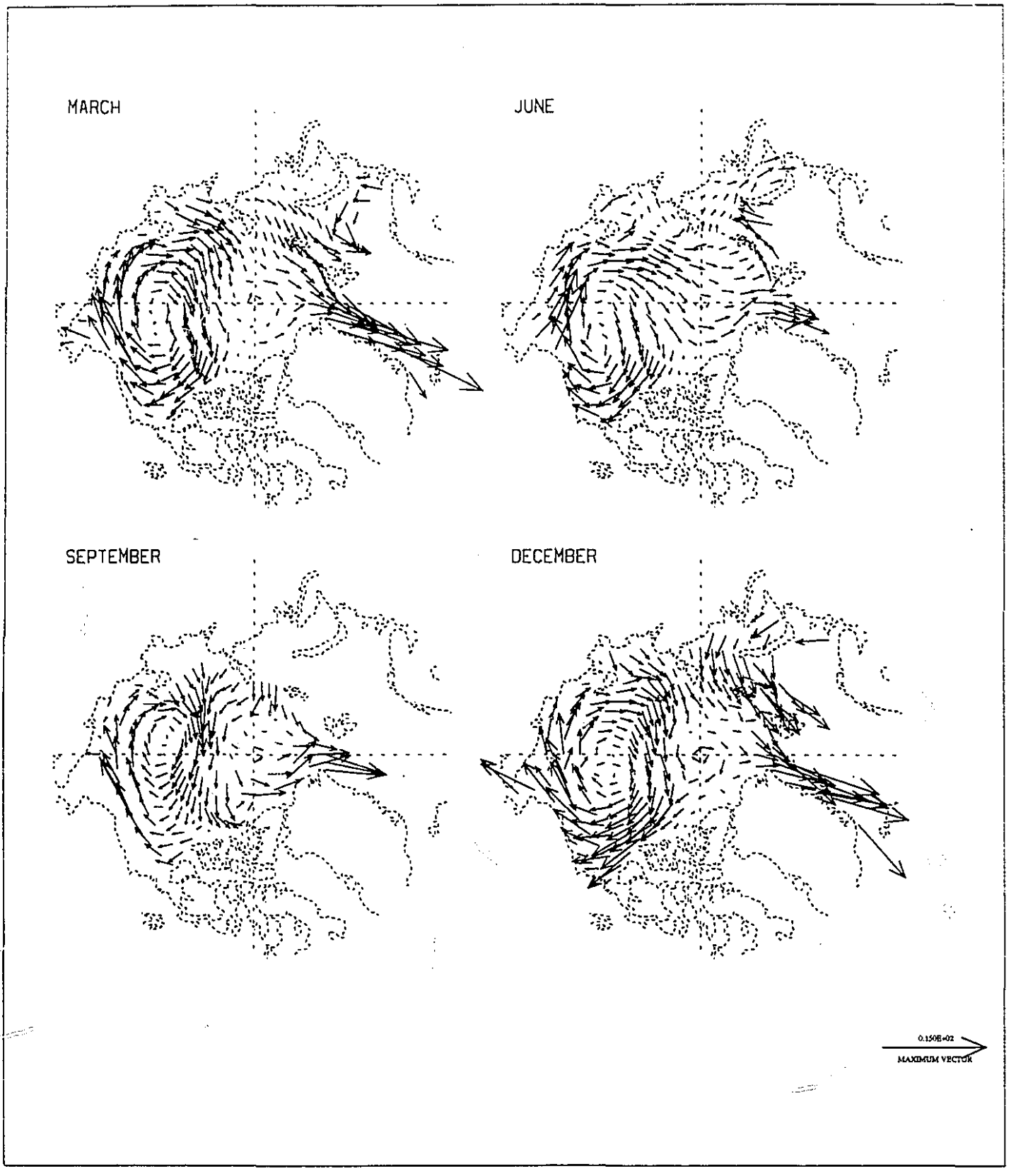

Figure 2.9 Experiment A10 (boundary condition at pole). Seasonally varying ice velocity fields from the simulation. The largest vector represents an ice velocity of 15 *cm/s*.

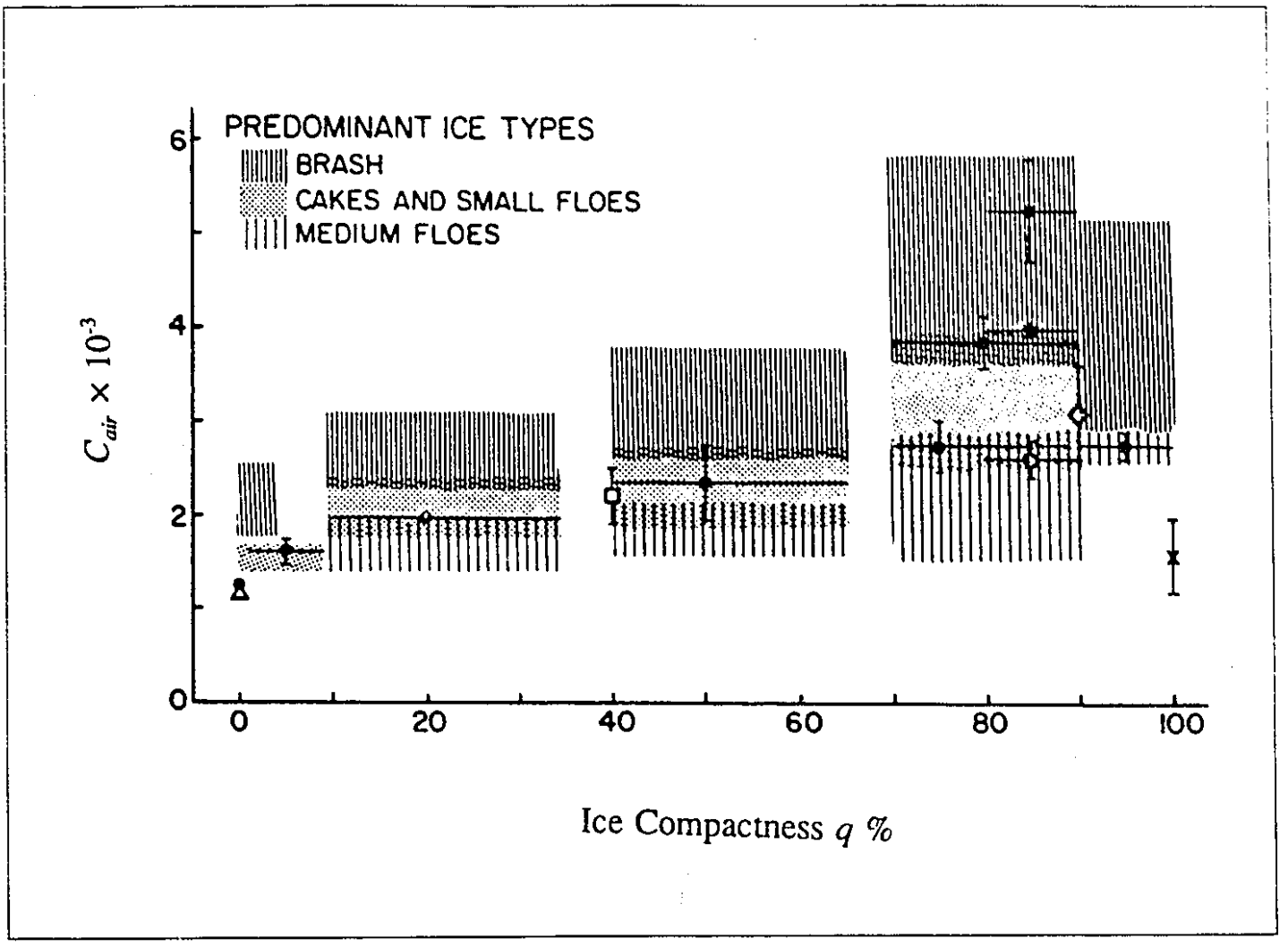

Figure 2.10 Atmospheric drag coefficient C_{air} as a function of ice compactness q. The data is taken from several sources. It applies to several predominant ice types as indicated in the figure. (from Anderson, 1987).

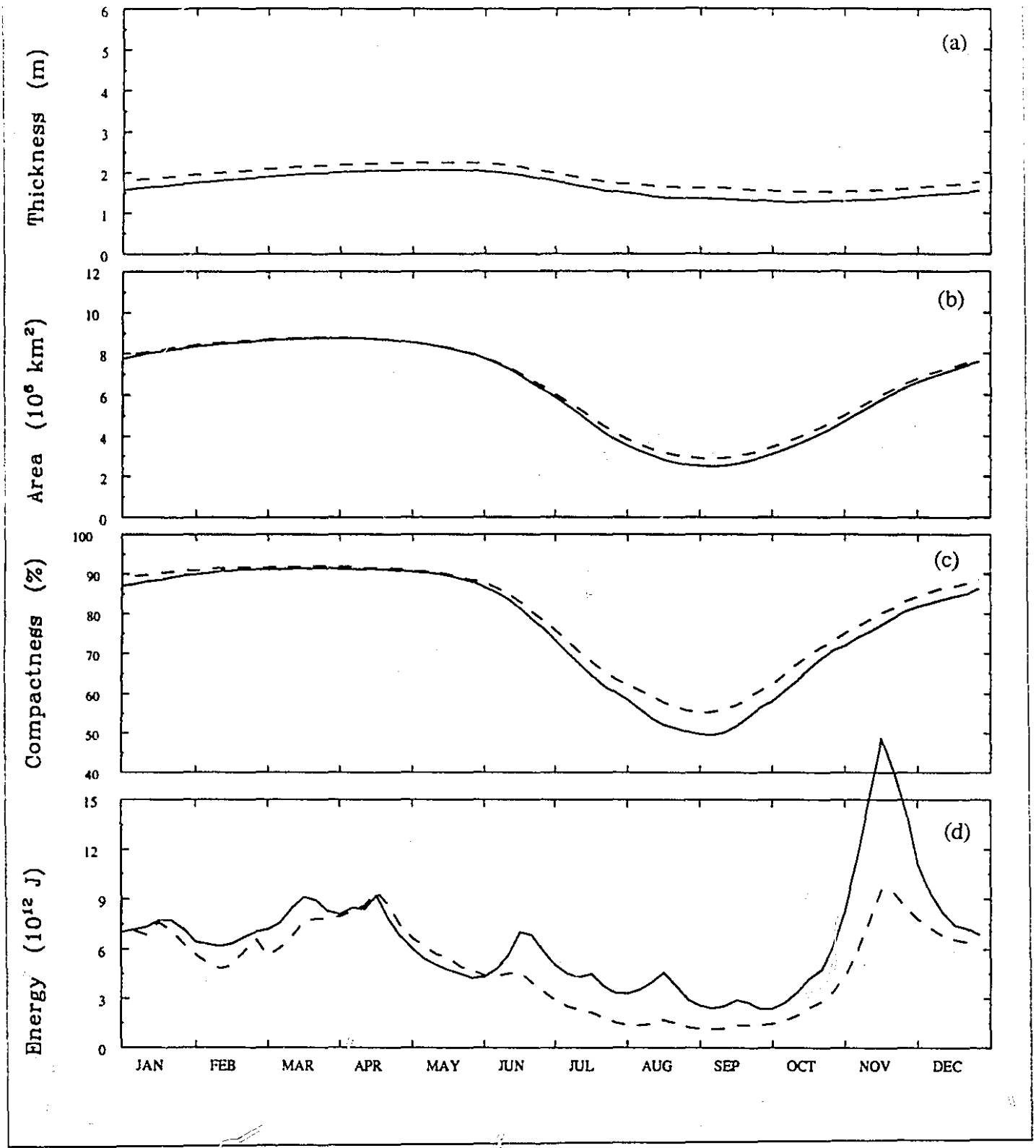

Figure 2.11 Experiment B24 (air drag coefficient). Time series of ice thickness, areal coverage, compactness, and kinetic energy over the equilibrium annual cycle. The dashed lines are the results from the control run.

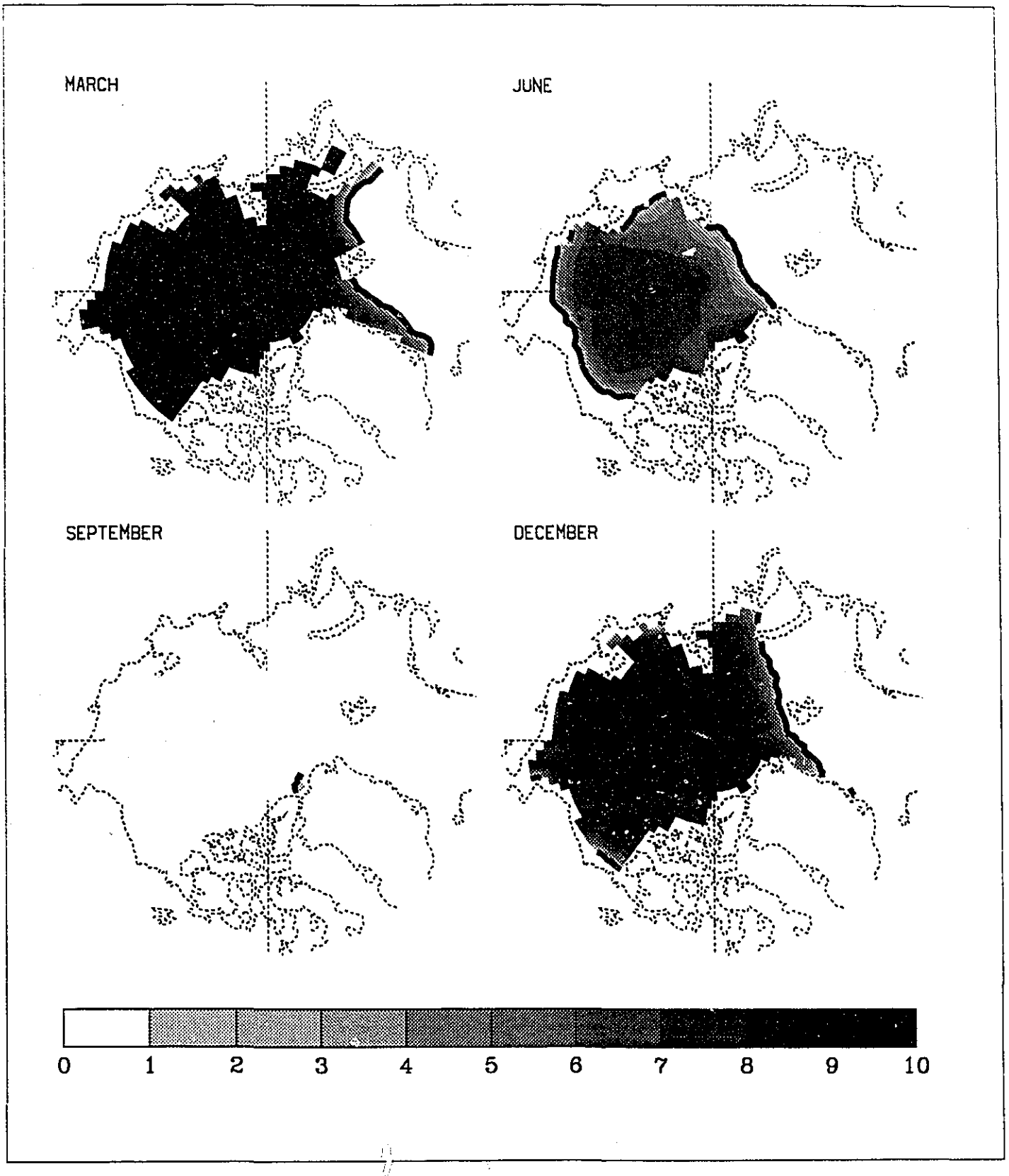

Figure 2.12 Experiment B32 (shortwave and longwave cloud fraction). Seasonally varying ice compactness fields (in units of 10^{ths}) from the simulation. The heavy black line indicates the $1/10^{th}$ compactness contour. This is considered as the ice edge.

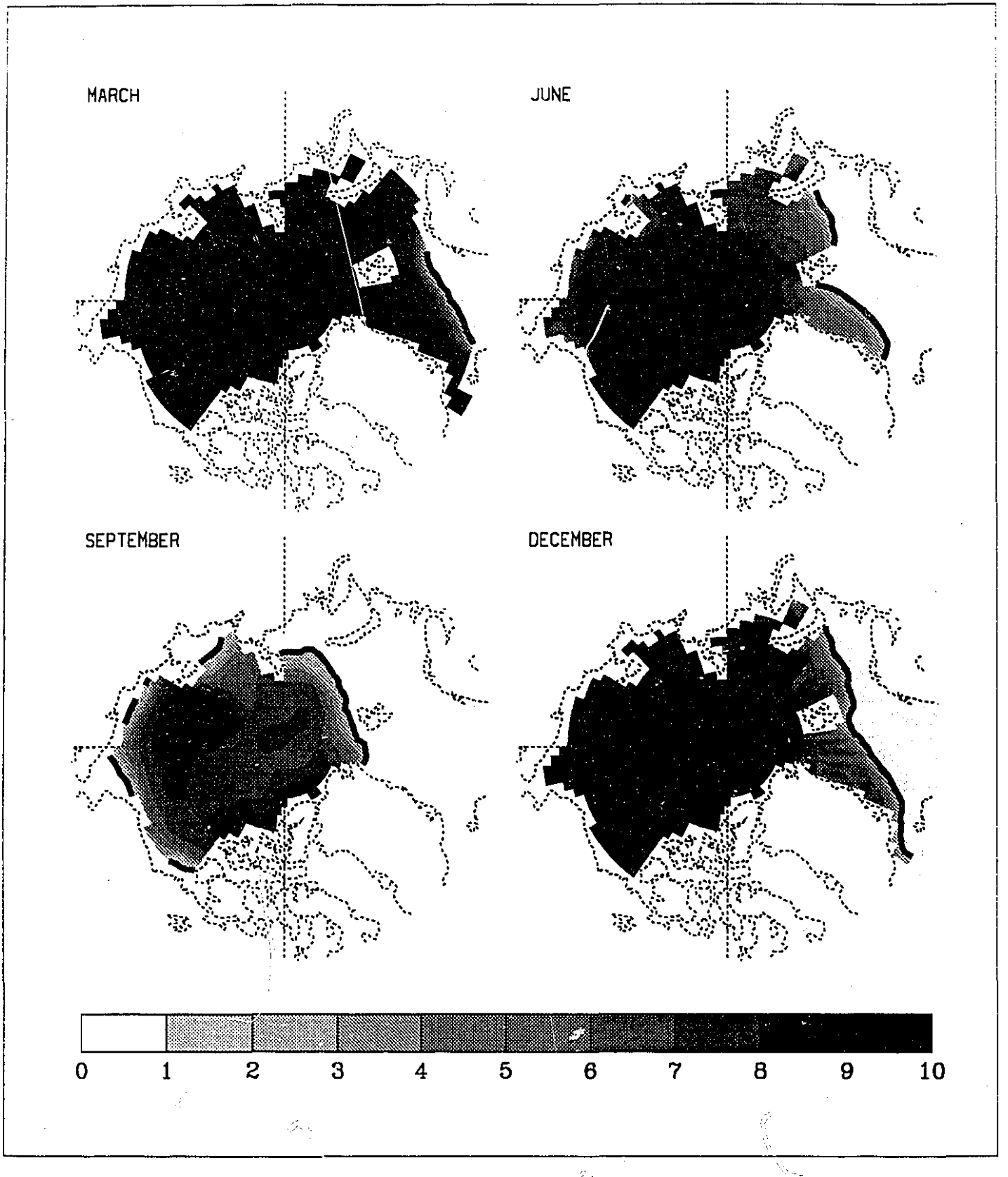

Figure 2.13 Experiment B44 (ocean heat flux). Seasonally varying ice compactness fields (in units of 10^{ths}) from the simulation. The heavy black line indicates the $1/10^{th}$ compactness contour. This is considered as the ice edge.

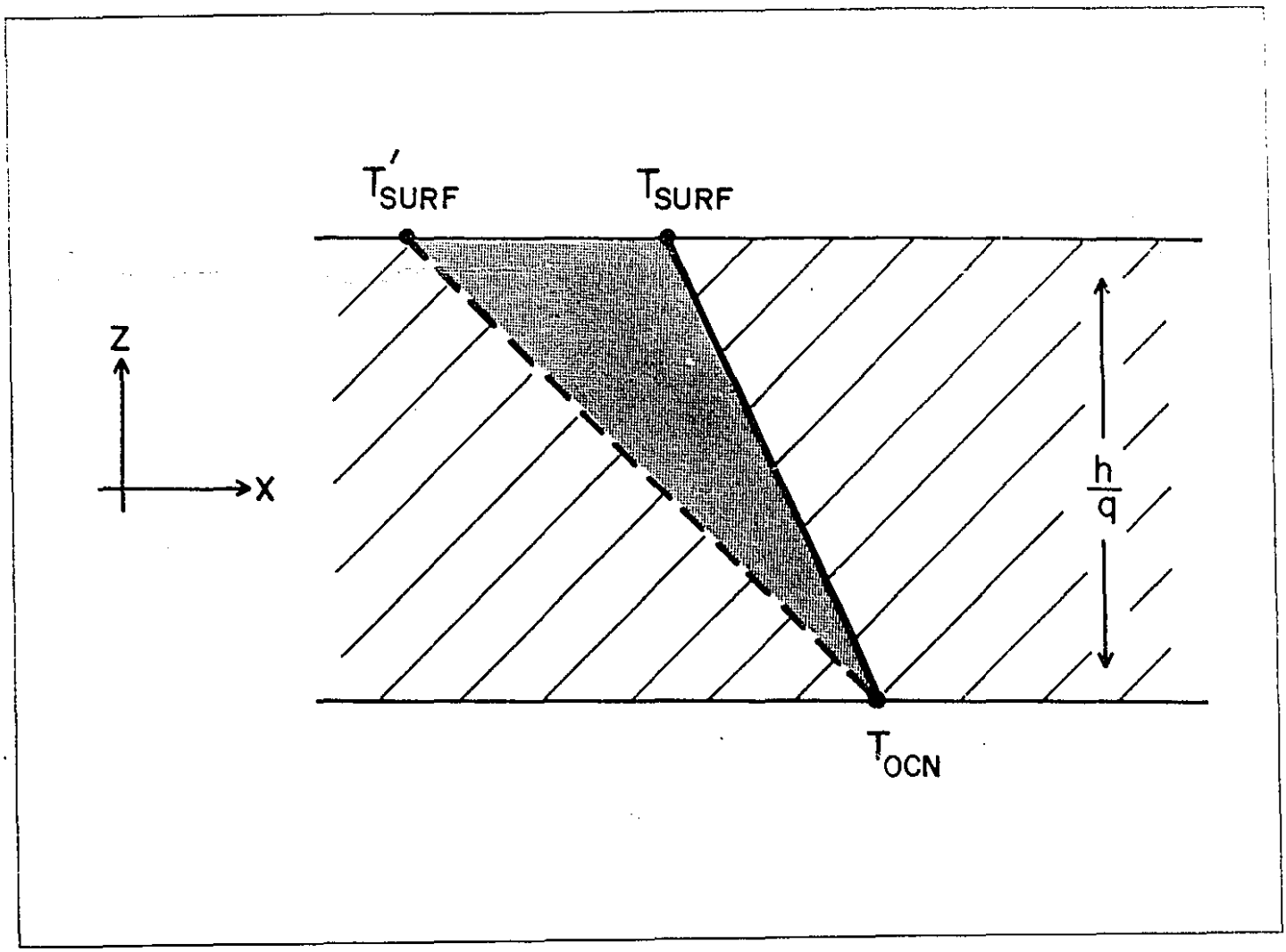

Figure 2.14 Specific heat change in sea ice associated with a change of surface temperature from T_{surf} to T'_{surf}. The ice is shown in vertical profile and is of effective thickness h/q, with bottom temperature T_{ocn}. The specific heat is proportional to the stippled area.

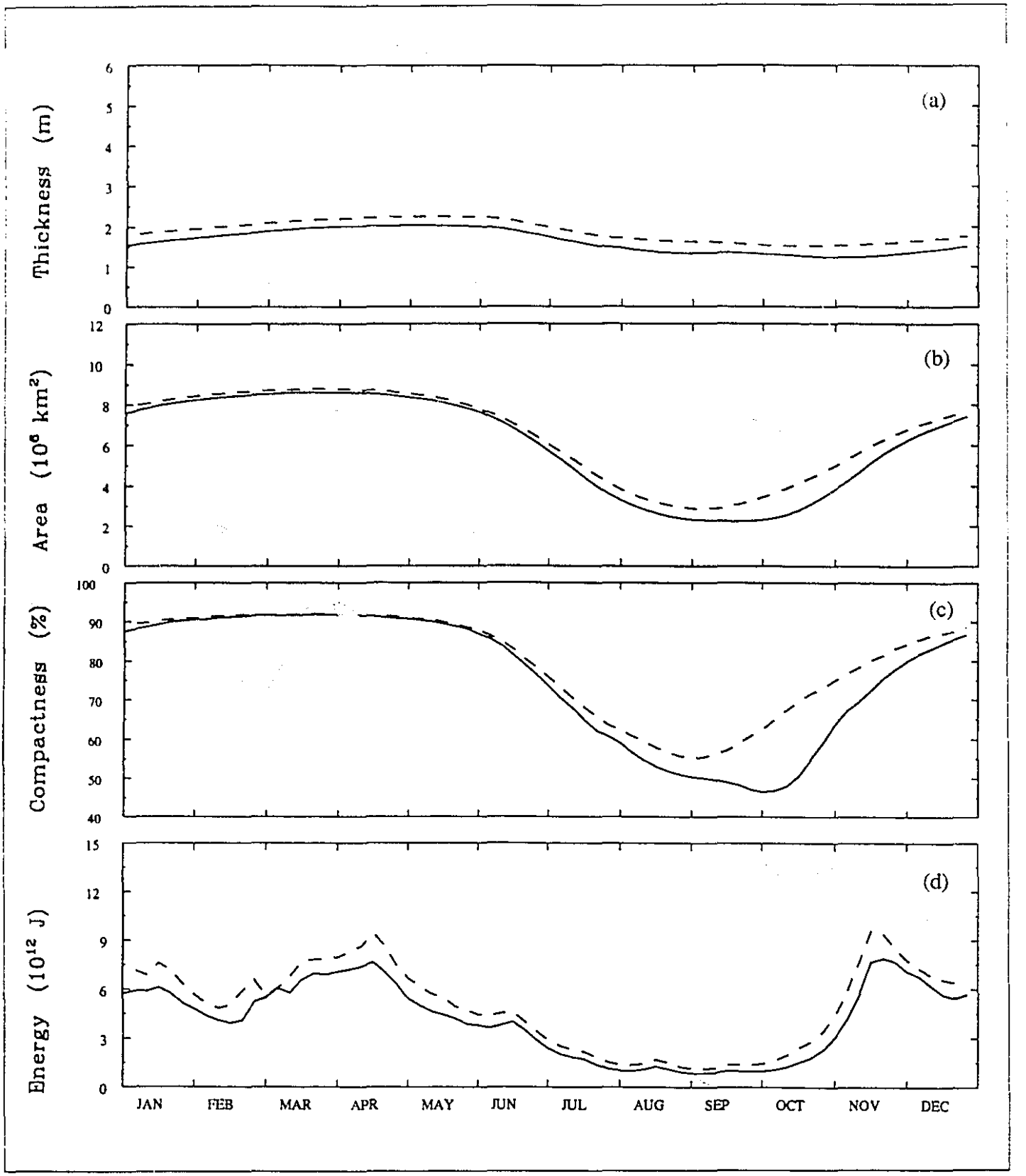

Figure 2.15 Experiment C15 (brine pockets). Time series of ice thickness, areal coverage, compactness, and kinetic energy over the equilibrium annual cycle. The dashed lines are the results from the control run.

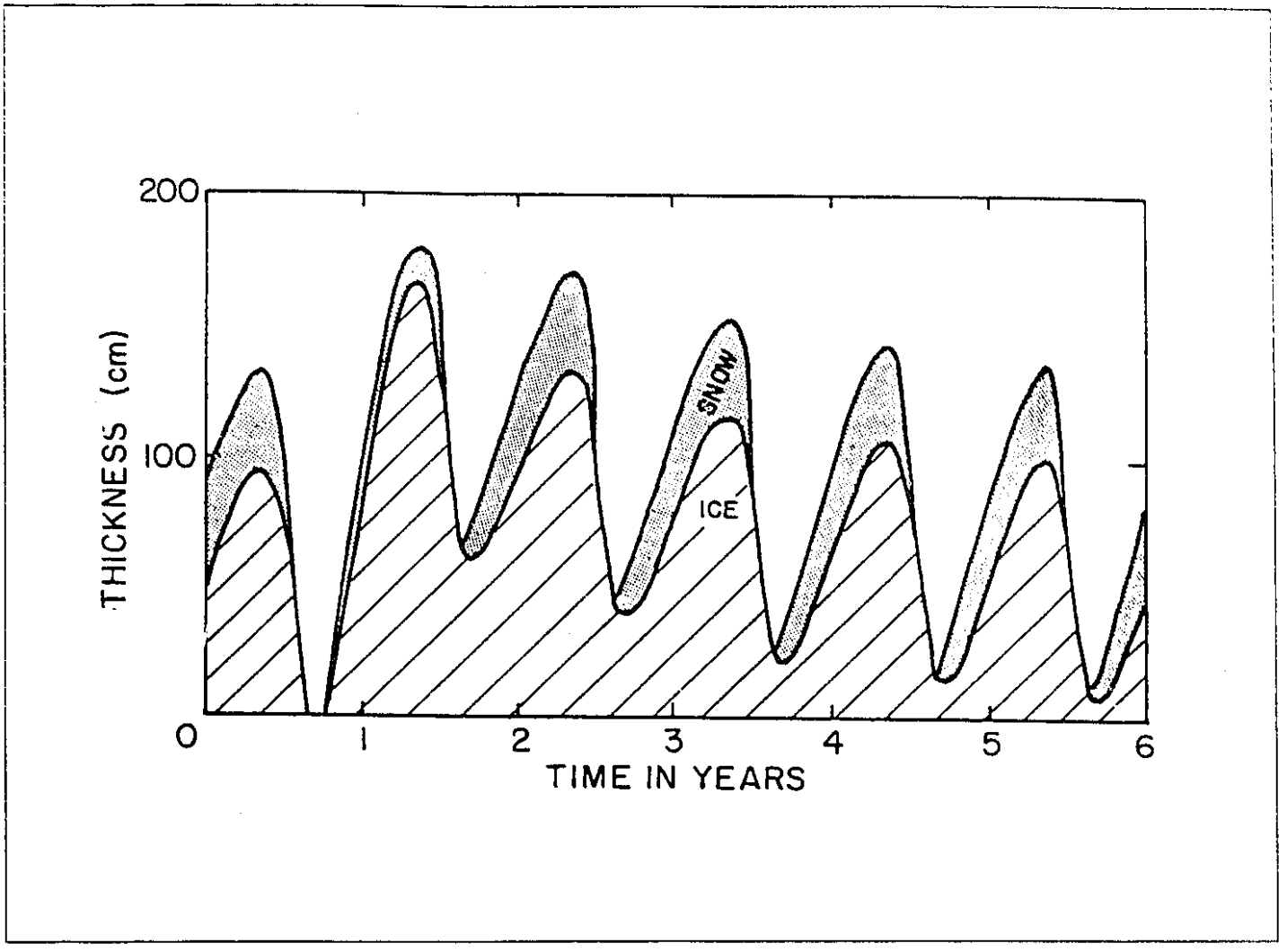

Figure 2.16 Multi-year equilibrium cycle of ice thickness, as predicted by the thermodynamic model of Semtner (1976). Washington *et al.* (1976) extended this model to three dimensions and again found such an interannual cycle. No such interannual cycles are found in the model investigated here. Note that in the figure the cycle period is 6 years.

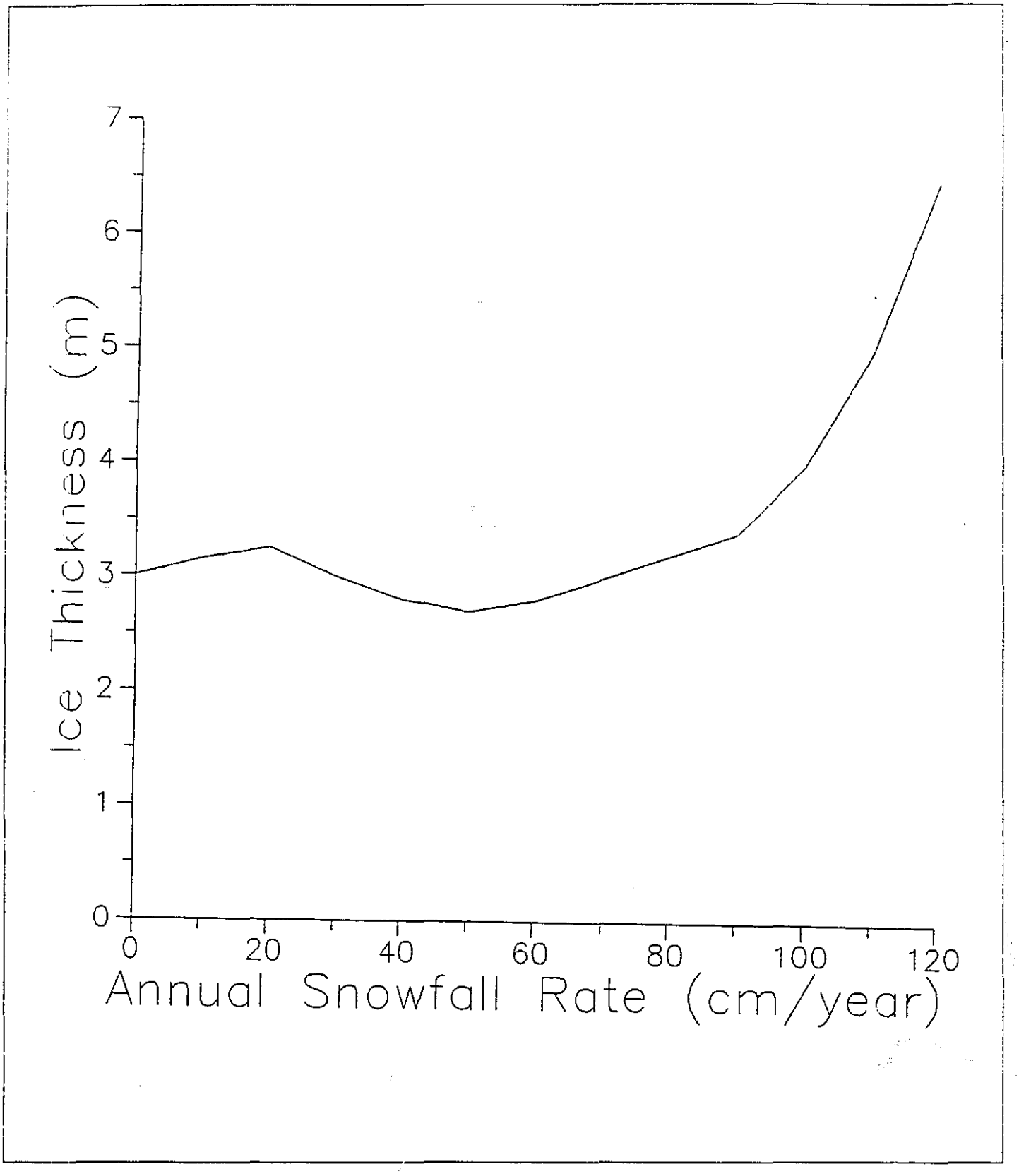

Figure 2.17 Average equilibrium thickness of Arctic sea ice as a function of maximal annual snow depth from the thermodynamic model of Maykut and Untersteiner (1971). Annual snow accumulations in excess of 120 *cm* result in incomplete melting of the snow cover and the equilibrium sea ice thickness increases dramatically. No such increase is detected in the model investigated here.

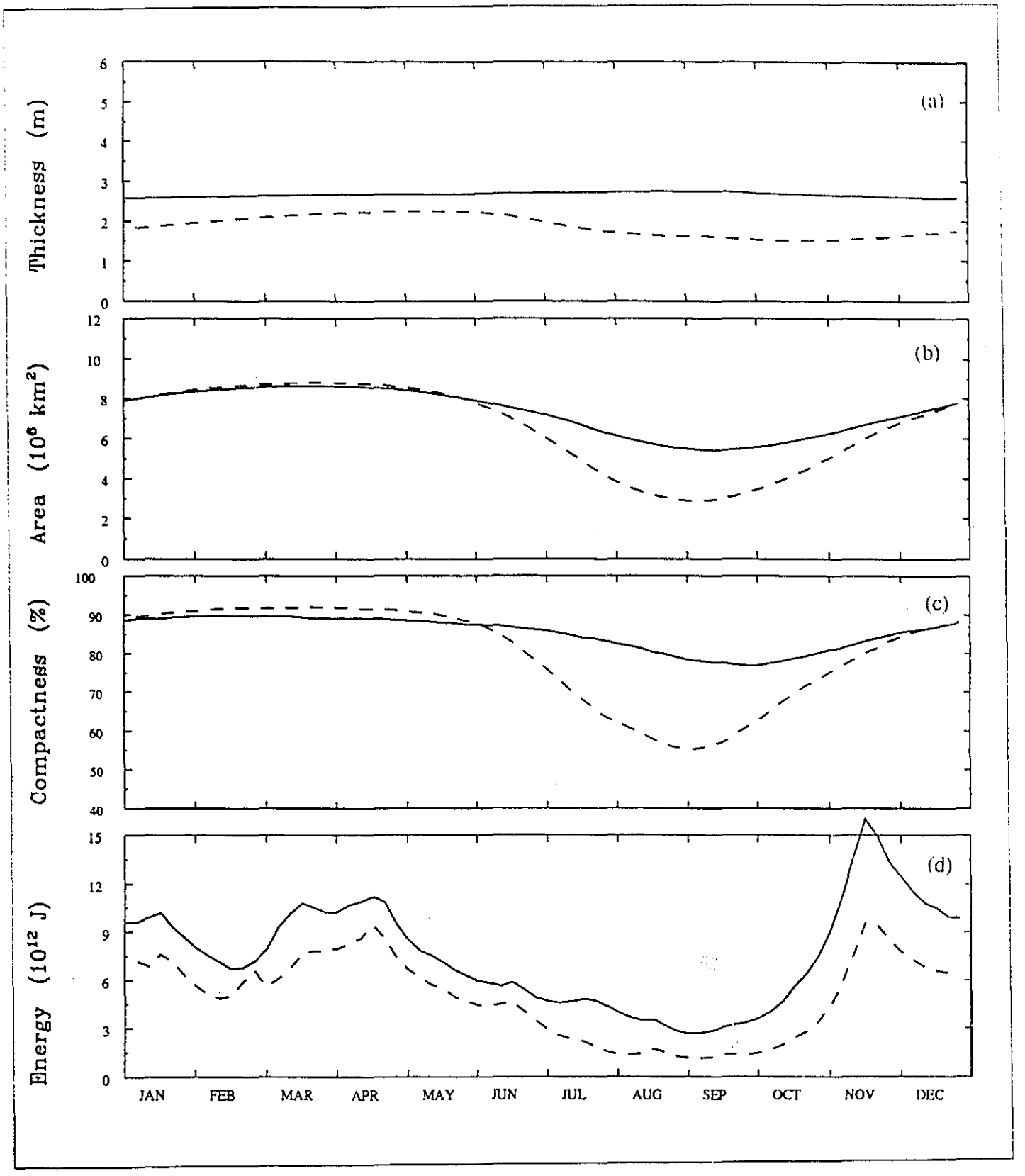

Figure 2.18 Experiment C17 (snow cover). Time series of ice thickness, areal coverage, compactness, and kinetic energy over the equilibrium annual cycle. The dashed lines are the results from the control run.

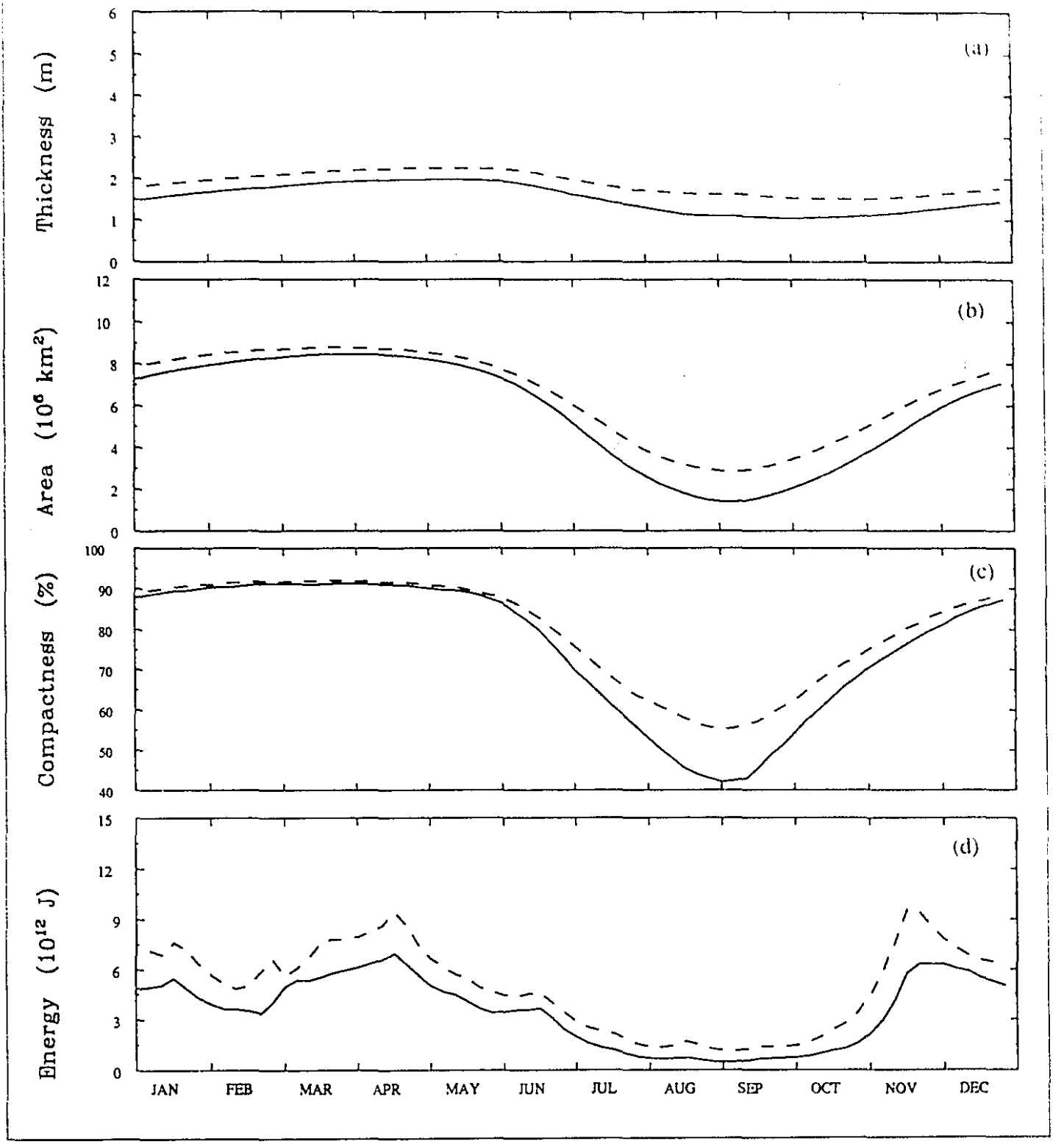

Figure 2.19 Experiment C19 (air temperature). Time series of ice thickness, areal coverage, compactness, and kinetic energy over the equilibrium annual cycle. The dashed lines are the results from the control run.

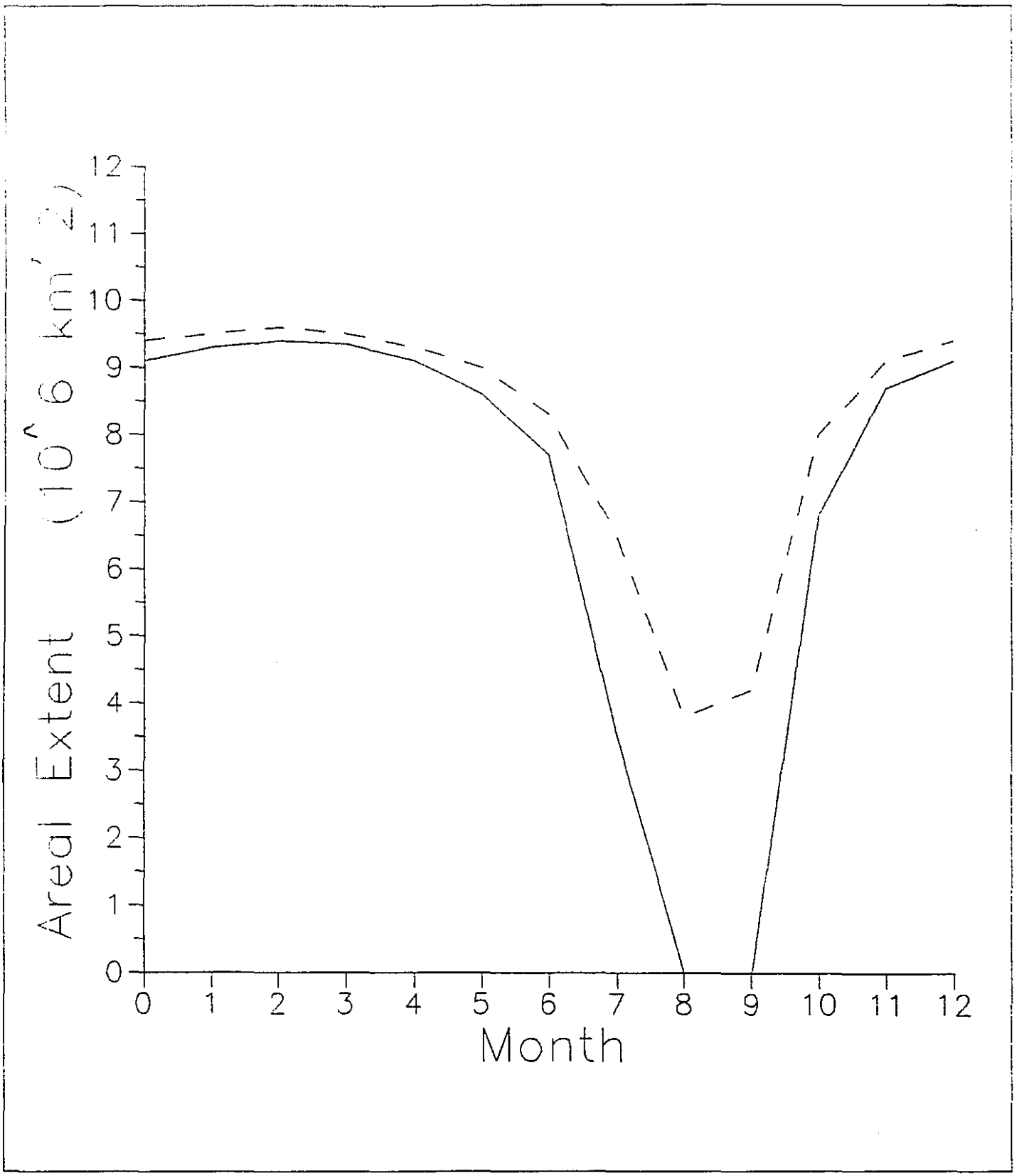

Figure 2.20 Seasonal cycle of areal ice extent of Semtner (1987). The solid curve indicates the case in which the atmospheric temperatures have been uniformly increased by two degrees everywhere. The dashed line represents the control run which includes the fully prognostic ocean model. (redrawn from Semtner, 1987).

§ 3 A Thermodynamic-Dynamic Sea-Ice Model with Snow

§ 3.1 Introduction

Recently there have been several modelling studies which use coupled atmosphere - ocean general circulation models (GCMs) to estimate the global temperature increase due to a slowly increasing concentration of greenhouse gases in the earth's atmosphere (*e.g.* Manabe *et al.*, 1991, Cubasch *et al.*, 1992). The largest predicted temperature increase is found in the Arctic; however, it is in this region (as well as in the Antarctic) where the atmospheric and oceanic components of these models least represent reality when run over a climatological seasonal cycle. Also, in the oceanic case there are insufficient data to help make improvements in the ocean GCMs. Further, in some coupled models (e.g. Washington & Meehl, 1989) the sea-ice component omits a key feature such as ice dynamics (see Mysak, 1991, for a discussion) or snow.

As noted earlier in this thesis, ice is an important intermediary between the atmosphere and ocean at high latitudes. The seasonal cycle of ice thickness and ice extent influences the transfer of heat and momentum at the air-sea interface. The seasonal cycle of ice melt and growth also affects the stratification of the mixed layer. During cold periods, ice formation ejects salt into the mixed layer and contributes to the production of denser water, which can lead to convection. During warm periods, ice melt decreases the salinity in the mixed layer and therefore leads to a stabilization of the upper-ocean water column. Snow cover on the ice modifies the heat fluxes through the ice and snow layers. Thus, snow has an impact on the thermodynamics of the ice; by contrast, it has a negligible dynamic impact since its mass and strength are much less than that of sea ice.

In this chapter, we present a discussion of the snow model which is added to the Oberhuber (1993a) global ice-ocean GCM. The combined snow - sea ice model presented is quite simple, yet physically complete, so that it may be used with confidence in a coupled global atmosphere-ocean general circulation model.

The outline of this chapter is as follows. Section 3.2 describes the snow - sea ice model, with an emphasis on the thermodynamic component since the dynamic part of the ice model is thoroughly described in Oberhuber (1993a) and in Holland *et al.* (1993). Section 3.3 presents simulation results for both hemispheres from an integration of the global model. Section 3.4 gives the conclusions of the chapter.

§ 3.2 The Snow - Sea Ice Model

Hibler (1979) proposed a rheology for a dynamical sea-ice model which can be used for a wide range of space and time scales. In order to implement spherical coordinates and a flux form of the momentum and mass conservation equations, which permit an easier treatment of the ice edge, the Hibler model was rewritten from scratch by Oberhuber (1993a). In this chapter, a snow model is added to this ice model. The heat content of snow and ice are also included via two prognostic temperature for the skin temperature at the upper snow and ice surfaces.

§ 3.2.1 The Dynamic Equations

The basic equations for the cell averages of the ice momentum $(\overline{u}\,\overline{h})$, the scaled snow thickness s, the ice thickness h, and the ice concentration q are given by

$$\frac{\partial(\vec{u}h)}{\partial t} = \nabla\cdot A\nabla(\vec{u}h) - \vec{f}\times(\vec{u}h) - gh\nabla\Gamma - \frac{\vec{\tau}_a}{\rho_h} - \frac{\vec{\tau}_o}{\rho_h} - \frac{\vec{I}}{\rho_h} \quad (3.1)$$

$$\frac{\partial s}{\partial t} = \nabla\cdot A\nabla s - \nabla\cdot(\vec{u}s) + F_s - F_a \quad (3.2)$$

$$\frac{\partial h}{\partial t} = \nabla\cdot A\nabla h - \nabla\cdot(\vec{u}h) + F_h + F_a \quad (3.3)$$

$$\frac{\partial q}{\partial t} = \nabla\cdot A\nabla q - \nabla\cdot(\vec{u}q) + F_q \quad , \quad (3.4)$$

where $\vec{\tau}_a$ and $\vec{\tau}_o$ are the surface wind stress and the stress at the bottom of the ice, Γ is the sea surface elevation, A is a constant diffusion coefficient, $\vec{f}$ is the Coriolis vector, g is the acceleration due to gravity, ρ_h is the density of ice, $\vec{I}$ represents the internal ice stress for a viscous-plastic sea-ice rheology, F_s is the change of snow mass due to snowfall or snowmelt, F_a is the conversion rate from snow to ice, F_h is the ice thickness change due to freezing or melting, and F_q is the change of ice concentration due to external heat fluxes. In the momentum equations, the nonlinear inertial terms have been neglected. The above equations (3.1 - 3.4) are similar to those presented in Chapter 2 except that the equation for snow thickness (3.2) has been added as well as the snow forcing terms F_s and F_a.

The quantities h and s are grid cell averaged quantities, and further s is a compressed snow thickness such that $s\rho_h/\rho_s$ would be the uncompressed (grid cell averaged) snow thickness. The physically measurable snow and ice thickness would be $s\rho_h/q\rho_s$ and h/q respectively. The values of the densities are ρ_s=300 kg/m^3 and ρ_h= 910 kg/m^3.

The ice rheology is defined as viscous-plastic. For strain rates ϵ greater than a small value ϵ_n, the rheology describes a plastic fluid in which the compressive and shear stresses are

independent of strain rates. The viscous rheology applies for strain rates ϵ less than ϵ_o. The viscous part of the rheology is used only for numerical convenience and appears to play no physically meaningful role. Following Hibler (1979), the components of the ice stress are

$$I_x = \frac{\partial}{\partial x}\left[(\zeta+\eta)\frac{\partial u}{\partial x} + (\zeta-\eta)\frac{\partial v}{\partial y} - \frac{P}{2}\right] + \frac{\partial}{\partial y}\left[\eta\left(\frac{\partial u}{\partial y} + \frac{\partial v}{\partial x}\right)\right] \qquad (3.5)$$

$$I_y = \frac{\partial}{\partial y}\left[(\zeta+\eta)\frac{\partial v}{\partial y} + (\zeta-\eta)\frac{\partial u}{\partial x} - \frac{P}{2}\right] + \frac{\partial}{\partial x}\left[\eta\left(\frac{\partial u}{\partial y} + \frac{\partial v}{\partial x}\right)\right] \quad , \qquad (3.6)$$

where the bulk viscosity ζ and shear viscosity η are defined as

$$\zeta = \frac{P}{2}\frac{1}{\max(\epsilon, \epsilon_o)} \quad , \qquad \eta = \frac{\zeta}{e^2} \quad , \qquad (3.7)$$

and where the ice pressure P and the ice strain rate ϵ are defined as

$$P = P^* h e^{-c(1-a)}$$
$$\epsilon^2 = \left[\left(\frac{\partial u}{\partial x}\right)^2 + \left(\frac{\partial v}{\partial y}\right)^2\right]\frac{e^2-1}{e^2} + \left[\frac{\partial u}{\partial y} + \frac{\partial v}{\partial x}\right]^2\frac{1}{e^2} + 2\left[\frac{\partial u}{\partial x}\frac{\partial v}{\partial y}\right]\frac{e^2-1}{e^2} \quad . \qquad (3.8)$$

The values for the constants used here are $P^*=10^4\ N/m^2$, $e=2$, $c=20$, $\epsilon_o=10^{-8}\ s^{-1}$, which are the same values as used in Table 2.1, except the minimum strain rate, ϵ_o, which was previously set to a much larger value (i.e. $10^{-6}\ s^{-1}$). This large value for ϵ_o effectively means that the sea ice was being described as a viscous rheology (as for an ordinary fluid such as air or water) and not as a viscous-plastic fluid (Flato, *pers. comm.*, 1992). The sea-ice model as used in Chapter 2 did not allow ϵ_o to be decreased below 10^{-6} because the rheology terms (i.e., Eqns. 3.5 & 3.6) were not solved for in a completely implicit manner. Oberhuber rewrote the numerical scheme for the sea-ice equations presented in this chapter such that the rheology terms are solved for in a

completely implicit manner. The result is that ϵ_{11} can indeed be reduced to the more realistic value of $10^{-8}\ s^{-1}$.

§ 3.2.2 The Thermodynamic Equations

§ 3.2.2.1 The Skin Temperatures T_s and T_h

The thermodynamic fluxes of the model are shown in Fig. 3.1. In the atmosphere, the snow, the ice, and the ocean the respective vertical heat fluxes are Q_a, Q_s, Q_h, and Q_o. These heat fluxes control the changes in both the thickness and the heat content of the snow and the ice. Over the fraction of a grid cell that is ice free, only the fluxes Q_a and Q_o are present. The four heat fluxes are parameterized to be functions of the atmospheric temperature T_a, the surface temperature of the snow T_s, the surface temperature of the ice T_h, and the surface temperature of the ocean T_o (which is at the freezing point of sea water when ice is present). From the point of view of the snow - sea ice model, the atmospheric and oceanic temperatures T_a and T_o are taken as specified; the snow and ice skin temperatures T_s and T_h are computed prognostically. The purpose of this section is to describe the computation of these two temperatures. Once these temperatures are known, we can determine the forcing functions F_s, F_h, and F_a in Eqns. 3.2 -3.4. It will be seen that (see Eqn. 3.18 below) that F_a is independent of T_s and T_h.

The heat flux terms are defined using the convention that an upward flux is a positive quantity. We now define the four heat flux terms in Fig. 3.1. Starting at the top, the atmospheric heat flux Q_a consists of contributions from shortwave, longwave, sensible, and latent heat terms.

The shortwave term depends upon the albedo of the surface. For snow, the albedo is taken as α_s=60%, while for bare ice it is α_h=50%. When heat is being input into the snow layer

and the snow layer is at the melting point, T_m, then the effective albedo is decreased by an amount α_j=20 %. This decrease in albedo is intended to model the effects of melt ponds. The surface albedo also depends upon the thickness of the snow layer. The empirical formulation of the effective albedo α_e is

$$\alpha_e = \alpha_h - \alpha_j e^{-\frac{(T_m - T_s)}{2}} - (\alpha_s - \alpha_h)(1 - e^{-10s}) \quad , \tag{3.9}$$

where T_m is the melting temperature of snow.

The longwave, sensible, and latent heat terms depend upon the atmospheric temperature T_a and the snow skin temperature T_s. A detailed description of the Q_a term is provided by Oberhuber (1993a).

Moving down to the snow and ice layers, the conductive heat fluxes through the snow and ice are defined, respectively, as

$$Q_s = -\frac{k_s q \rho_s}{s \rho_h}(T_s - T_h) \quad , \qquad Q_h = -\frac{k_h q}{h}(T_h - T_o) \quad , \tag{3.10}$$

where k_s is the thermal conductivity of snow (assigned the value of .33 W/mK) and k_h is the thermal conductivity of ice (assigned the value of 2. W/mK). Note that Q_s and Q_h have units of W/m^2. Effects of salinity and temperature upon the thermal conductivity of the ice have been ignored. Finally, at the bottom of the ice the oceanic heat flux is specified as Q_o, and it is provided by the oceanic model.

The snow and ice are assigned to have a non-zero heat content, which is proportional to the average temperature in the layer. The heat content of the snow and ice layers are thus respectively

$$H_s = \rho_h \, c_p \, s \, \frac{(T_s + T_h)}{2} \quad , \qquad H_h = \rho_h \, c_p \, h \, \frac{(T_h + T_o)}{2} \quad , \tag{3.11}$$

where c_p is the specific heat of ice (assigned a value of 2090 J/kgK). Note that the units of H_s and H_h are J/m^2. The dependence of the specific heat and conductivities of the ice and snow on salinity and temperature have been ignored as these effects are small (see Maykut & Untersteiner, 1971). Brine pockets are not modelled. The temperature profile within a layer is assumed to be linear (Fig. 3.2). Between the winter and summer curves shown in Fig. 3.2 a shaded area is indicated. Starting at the winter profile (at left), the shaded area (to the right) is proportional to the amount of heat that must be added to the snow-ice layer in order to reach the summer profile. Continuing the seasonal cycle, this is also the amount of heat that must be removed from the snow and ice in order to return to the winter profile. Thus, because of the heat content of the snow-ice layer, the latter acts as a heat reservoir, thereby storing and releasing heat that would otherwise be used in phase changes for the snow and ice. The existence of this reservoir implies a time lag for the onset of phase changes during both the melt and growth seasons.

We are now in a position to formulate equations for the two unknowns T_s and T_h. At the air-snow interface the divergence of heat flux is zero in the case when no heat is used to melt snow. The case of melting snow is dealt with later. The resulting equation is

$$Q_a(T_a, T_s) \; - \; Q_s(T_s, T_h) \; = 0 \quad . \tag{3.12}$$

At the snow-ice interface the divergence of heat flux equals the time rate of change of the heat content of the snow and ice

$$Q_h(T_h, T_o) - Q_s(T_s, T_h) = \frac{\partial}{\partial t}(H_s + H_h) \quad . \tag{3.13}$$

In order to treat the special case of no snow or of no ice and snow, the equations are rewritten to give $T_h=T_s$ or $T_s=T_h=T_o$ respectively.

A complicating factor is that Q_a is a highly nonlinear function of T_s. We circumvent this by approximating Q_a as a linear function of T_s via a Taylor series expansion. This avoids a two-stream radiation calculation in an atmospheric model when it is coupled to this snow and sea-ice model, and thus reduces computation time. The Taylor expansion is implemented by using the atmospheric heat flux from the previous time step to estimate the heat flux at the present time step:

$$Q_a(T_s) = Q_a(\bar{T}') + \frac{\partial Q_a}{\partial T_s}(T_s - \bar{T}') \tag{3.14}$$

where $\bar{T}'$ is the average snow/water skin temperature of the previous time step. It is made up of contributions from the temperature of the snow-covered ice T'_s and of the open water T'_o at the previous time step:

$$\bar{T}' = q\,T'_s + (1 - q)\,T'_o \quad . \tag{3.15}$$

The partial derivative of Q_a with respect to T_s is known from the functional dependence of the longwave, sensible, and latent components of Q_a upon surface temperature T_s. The final result is that we have Q_a as a linear function of T_s making Eqns. 3.12 - 3.13 easier to solve for T_s and T_h.

Another complicating factor arises in that the turbulent transfer coefficients of sensible and latent heat are functions of the atmospheric stability. The atmospheric stability is of course

a function of the temperature difference T_a - T_s (Large & Pond, 1982). This is dealt with by iterating the solution for T_s and T_h until all the constraints are satisfied.

The snow or ice surface temperature cannot exceed the fresh-water melting temperature T_m=273.16 K. Whenever a nonphysical $T_s > T_m$ is calculated, the condition $T_s = T_m$ is imposed for the snow surface. The ice surface temperature T_h is then recalculated with T_s set equal to the melting temperature T_m in Eqn. 3.12. The reason that we get $T_s > T_m$ is because Eqn. 3.12 ignores the melting of snow. The rate of snow melt M_s (which is always a negative quantity in units of m/s) can be diagnosed by imposing T_s=T_m in Eqn. 3.12 and by noting that the resulting heat flux imbalance at the snow-ice interface gives the rate of snow melt as

$$M_s = \frac{Q_a(T_a,T_m) - Q_s(T_m,T_h)}{L_f \rho_h} \quad , \tag{3.16}$$

where L_f is the latent heat of fusion of snow (assigned the value 3.34 x 10^5 J/kg).

§ 3.2.2.2 The Forcing Functions F_s, F_a, F_h, and F_q

We recall that our goal is to solve the Eqns. 3.1 - 3.4 for the four unknowns $(\vec{u}\,h)$, s, h, and q. In order to do so we need to specify the thermodynamic forcing functions F_s, F_a, F_h, and F_q, which we are now in a position to do.

The forcing term for the rate of change of snow thickness, F_s, consists of terms representing the melting of snow (M_s), atmospheric precipitation minus evaporation (R_{P-E}), and loss of snow mass due to the reduction of ice concentration; thus

$$F_s = q\,M_s + q\,R_{P-E} + \begin{cases} 0 & F_q \geq 0 \quad \textit{freezing} \\ \dfrac{s}{q}\,F_q & F_q < 0 \quad \textit{melting} \end{cases} . \tag{3.17}$$

The last term is active only when the ice areal coverage is decreasing, *i.e.* $F_q < 0$. When this occurs, the cell averaged snow thickness s must decrease to account for the fact that if a fraction

of the ice beneath the snow disappears then so must a fraction of the snow disappear. In the opposite case in which the ice areal coverage is increasing, *i.e.* $F_i > 0$, there is no justification for increasing the cell averaged snow thickness s.

The rate of conversion F_a of snow to ice involves two processes. The first is snow aging, which describes the transformation of snow into ice; it is a process that is dependent upon the snow depth s and a time scale γ. A value of γ of $2 \times 10^{-7}\ s^{-1}$ represents an e-folding time of 55 days for the conversion process. The second process arises when the snow has sufficient weight to displace the ice surface below the sea surface. In such an instance, the ice surface is flooded with sea water and the submerged snow is instantly converted to sea ice. The equation for F_a is thus

$$F_a = [\gamma\, s] + \left[s - h \frac{(\rho_o - \rho_h)}{\rho_o} \right] \frac{\rho_s}{\rho_h} \quad , \tag{3.18}$$

where ρ_o is the density of the ocean layer. The second term on the right hand side describes the growth of ice due to suppression of the ice surface. It is included only when the condition

$$s > h \frac{(\rho_o - \rho_h)}{\rho_o} \tag{3.19}$$

is satisfied.

The forcing term for the rate of change of ice thickness, F_h, consists of the divergence of heat flux over open water at the air-water interface and the divergence of heat flux over ice at the ice-water interface. The resulting forcing is

$$F_h = \frac{(1 - q)\, Q_a(T_a, T_o) + q\, Q_h(T_h, T_o) - Q_o}{\rho_h\, L_f} \quad . \tag{3.20}$$

The forcing term for the ice concentration F_q is of the same sign as the thickness term F_h. When ice is growing, corresponding to F_h positive, the ice concentration is simultaneously increasing, and vice versa for when ice is melting. The relation between F_h and F_q is given by

$$F_q = \begin{cases} \dfrac{F_h}{h_o}\,(1 - q)\,, & F_h > 0 \quad \textit{freezing} \\ \dfrac{F_h}{2\,h}\,q\,, & F_h < 0 \quad \textit{melting} \end{cases} \tag{3.21}$$

where h_o is a free parameter with assigned value of .25 m. The interpretation of the F_q term according to Hibler (1979) is that the areal fraction of open water decreases rapidly under freezing conditions, and increases slowly under melt conditions. The freezing term is the most important because it affects the fraction of open water in winter. The melting term is less important because it accounts for only a few percent of the open water found in summer.

§ 3.2.3 Thermal Inertia

Since the ice layer is modelled to have a realistic heat content, we may derive an estimate for the time scale for temperature changes through the ice layer. Recall that in section 3.2.2.1 expressions for the conductive flux Q_h through the ice and for the heat content H_h of the ice were presented. We now assume that for thick ice of high concentration ($q \approx 1$), the conductive flux Q_h equals the time rate of change of the heat content H_h of the ice layer; this gives

$$\frac{\partial (T_h - T_o)}{\partial t} = \frac{2 k_h}{h^2 c_p \rho_h} (T_h - T_o) \quad . \tag{3.22}$$

The inverse of the coefficient of $(T_h - T_o)$ on the right hand side defines a time constant for the time rate of change of the quantity $(T_h + T_o)$. We denote the time scale by τ, where

$$\tau = \frac{h^2 c_p \rho_h}{2 k_h} \quad . \tag{3.23}$$

We now estimate the value of this expression for typical Arctic conditions. For the case of very thick Arctic ice, of order 6 *m*, a time scale τ of six months is obtained. For the thin Antarctic ice, of order 1 *m*, we obtain a time constant of only five days. The derivation of the above expression for τ is not strictly valid for such thin ice because phase changes would play a dominant role in the heat balance. Nevertheless, we argue that the thermal inertia due to the heat content is negligible for the Antarctic but it is not for the Arctic. This means that the Arctic sea ice contains a thermal memory that may have some influence on interannual variability. This is to say, the thick Arctic sea ice would remember conditions from the previous winter.

The present model, however, is still missing some components that may ultimately be of significance. Sea ice contains brine pockets which serve to store heat in the ice due to solar insolation. Another process that is presently ignored is the horizontal advection of heat by the ice. Since ice moves a significant distance over a time period of one year, it may be important to advect the ice heat content with the ice flow to obtain a realistic simulation of ice interannual variability. The same comments apply to the salt content of the ice.

§ 3.3 Simulation Results

The snow - sea ice model described in section 3.2 is coupled to the global ocean general circulation model of Oberhuber (1993a). The coupled model is forced by prescribed monthly atmospheric fields at the surface. In particular, the snowfall is specified by using the Legates & Willmott (1990) data set. The horizontal resolution is approximately 1 degree by 1 degree (T106) and the vertical is resolved using nine isopycnal layers. The simulation is carried out for 3 years, which is judged to be a sufficient time for the snow and sea ice to reach an equilibrium annual cycle. The ocean currents and heat flux are provided to the sea ice by the ocean component of the model. For the Arctic the modelled ocean circulation will be discussed in Chapters 4 and 5; the ocean circulation for the Antarctic is not presented.

It is important to note that a single set of parameter values has been employed to simultaneously simulate the Arctic and Antarctic ice regimes. In modelling only one hemisphere at a time, it is possible to optimize the simulation by adjusting the snow - sea ice parameters until a desirable sea-ice simulation is obtained (*i.e.* one close to that observed). However, such an optimization of parameters for one hemisphere may lead to a poor simulation in the other hemisphere.

Ice growth occurs because of low temperatures on the ice surface. Snow insulates the ice surface and hence helps to prevent heat loss from the ice, which in turn reduces ice growth. Fig. 3.3 displays the model-predicted surface temperature pattern of the snow over the Antarctic sea ice during the austral winter. There is a strong latitudinal gradient with very cold temperatures of less than -20 $^{\circ}C$ over much of the Weddell and Ross Seas. Fig 3.4. shows the model-predicted temperatures at the snow-ice interface. The latitudinal gradient is smaller and the temperatures are much warmer (by about 10 $^{\circ}C$) than at the snow surface. The resulting ice thickness distribution is given in Fig. 3.5. The computed average thickness over the entire domain is about .6 *m*; however, in the Weddell sea it is about 2 *m*. An ice model without a snow

cover would have a larger ice growth because the ice surface would be in direct contact with the cold atmosphere. The ice surface in such a case would then feel colder air temperatures, similar to those shown in Fig. 3.3 and not the relatively warmer ones shown in Fig. 3.4. The resulting ice thickness would thus be much greater and therefore unrealistic. This problem can be overcome by adjusting, for example, the ice conductivity or the ice surface albedo. These adjusted parameter values may then, however, cause difficulties with the simulation in the other hemisphere.

There is a strong asymmetry between the Arctic and the Antarctic regions. This asymmetry is characterized not only by the profound difference in geography, but also by the difference in thickness of the sea ice. The Arctic sea ice has an average thickness 3 *m* whereas the Antarctic has an average thickness of only 1 *m*. A further asymmetry exists in the snow cover. The Antarctic receives much more snowfall than the Arctic. The Arctic has a snow fall rate of about 5 *cm/month* (except, for example, near the ice edge in the Greenland Sea where atmospheric eddies carry more snow onto the ice), whereas the Antarctic snowfall rate is several times that in the Arctic. In the summer, the snow almost completely disappears in the Arctic (Fig. 3.6), whereas in the Antarctic, the snow survives during summer (Fig. 3.7) and in fact only disappears when the ice beneath it melts. Also contributing to the asymmetry is the fact that the Arctic does not have areas of strong ice divergence or convergence that could lead to large spatial inhomogeneities in the snow cover. In the Antarctic, however, strong ice divergence in the Weddell and Ross Sea leads to a thin snow cover there: on the other hand the existence of ice convergence along the ice edge leads to snow accumulation. The Antarctic snow cover in spring is shown in Fig. 3.8. The snow-cover pattern indicates that in the Weddell Sea there is greater snow cover far from the coast than near the coast. That results in a pronounced insulation effect far away from the Antarctic coast.

For the Arctic, northward travelling atmospheric eddies may deposit large amounts of snow where they pass over the ice edge. The Arctic spring snow-cover pattern (Fig. 3.9) shows significant snow cover in Bering Strait, the Labrador Sea, Denmark Strait, and also to the northeast of Spitsbergen. The resulting ice thickness distribution is shown in Fig. 3.10.

The springtime ice thickness distribution in the central Arctic may seem unreasonable since it does not reproduce the climatological situation in which there is thick ice of order 6 *m* along the coast of the Canadian Arctic Archipelago which uniformly decreases to a thickness of 2 *m* along the coast of Siberia (see Bourke & Garret (1987), their Fig. 3.2.). However, as will be seen in Chapter 4, a more realistic ice thickness simulation is obtained by changing the ice strength parameter, P^*, from its value here of 10,000 N/m^2 to a more realistic value of 30,000 N/m^2 (Flato, *pers.comm.*, 1992).

An interesting feature simulated by this model occurs in the vicinity of the Weddell Sea. During spring of 1973-1976 a large area of open water was detected by satellite just east of the Weddell Sea at approximately 65 °*S* and 0 °*E*. It is referred to as the Weddell Sea polynya. The simulation of ice concentration for the Antarctic summer (Fig. 3.11) indicates the presence of a polynya in the geographical area of the observed polynya. However, the simulation of ice concentration in Fig. 3.11 is somewhat unrealistic because we know from ice climatologies (Zwally *et al.*, 1983, their Fig. 4-2) that most of the Antarctic sea ice has melted by January. The simulated ice does in fact eventually disappear, but not until fall (Fig. 3.12). The model thus appears to have a phase lag in that the melting comes too late. A possible explanation is that the cloudiness may be over estimated in that region; hence, the insolation is underestimated. Nevertheless, the appearance of a low compactness area in the vicinity of the Weddell polynya

suggests that there is a forcing mechanism present in the model that tends to create open water in that particular geographic location. This phenomenon will be investigated in future research.

§ 3.4 Conclusions

This chapter has described the incorporation of a snow model into the coupled sea ice - mixed layer - isopycnal ocean general circulation model of Oberhuber (1993a). The inclusion of a snow model is important because the snow modifies the surface energy budget in two ways: (i) the shortwave surface albedo is increased when ice is present and (ii) snow, having a smaller thermal conductivity than ice, reduces the heat flux into the atmosphere.

The results presented highlight the asymmetry of the Arctic and the Antarctic regions. The Antarctic has relatively thin ice and is consequently sensitive to snow cover. The sensitivity of the Antarctic to snow cover is also enhanced by the greater snowfall amount than in the Arctic. In fact, the snow cover does not disappear during summer in the Antarctic while it does disappear during the Arctic summer.

The modelling of the snow-ice layer with a realistic heat content allows for a further asymmetry between the two hemispheres. The thick Arctic ice has a thermal inertia that provides it with a memory of about six months; the thin Antarctic ice has a memory of only 5 days. This means that the Arctic sea ice may carry forward information on atmospheric variations from previous years, whereas the Antarctic ice will be sensitive to the atmospheric forcing of only the previous weeks. This asymmetry in memory is also obvious from the fact that most of the Antarctic sea ice melts during summer while the Arctic ice does not.

The inclusion of a snow model in modelling studies of climate change would seem imperative based on the following argument. In the real climate system we may expect that

global warming may result in more water vapour and more precipitation. Provided it is cold enough, this would result in a thicker snow cover in polar regions. In fact, recent observations of snow accumulation over Greenland (Zwally *et al.*, 1989) suggest that warming does result in more water vapour and hence more precipitation. In a model of the climate system, the accumulation of snow insulates the ice, and even if the ice becomes thinner under a warming scenario, the temperatures will not rise as fast as simulated using a model without snow cover. This is because the snow-cover introduces a negative feedback mechanism into the model. This negative feedback may compete with the ice-albedo positive feedback that is generally invoked to support temperature increases in polar regions under warming scenarios. Given that both mechanisms are present, it is then unclear how the polar regions will behave under a warming scenario.

Since the modelled Arctic snow cover is only a fraction of that modelled for the Antarctic, it could be that the negative feedback is too weak to negate a temperature increase in the Arctic. The only exception could be in areas along the ice edge in the Greenland Sea. Such areas receive a lot of snow from atmospheric eddies travelling northward from the North Atlantic so that the thin ice there may become more insulated. Thus, the ice-edge position may not change as much as has been predicted in earlier global warming scenarios.

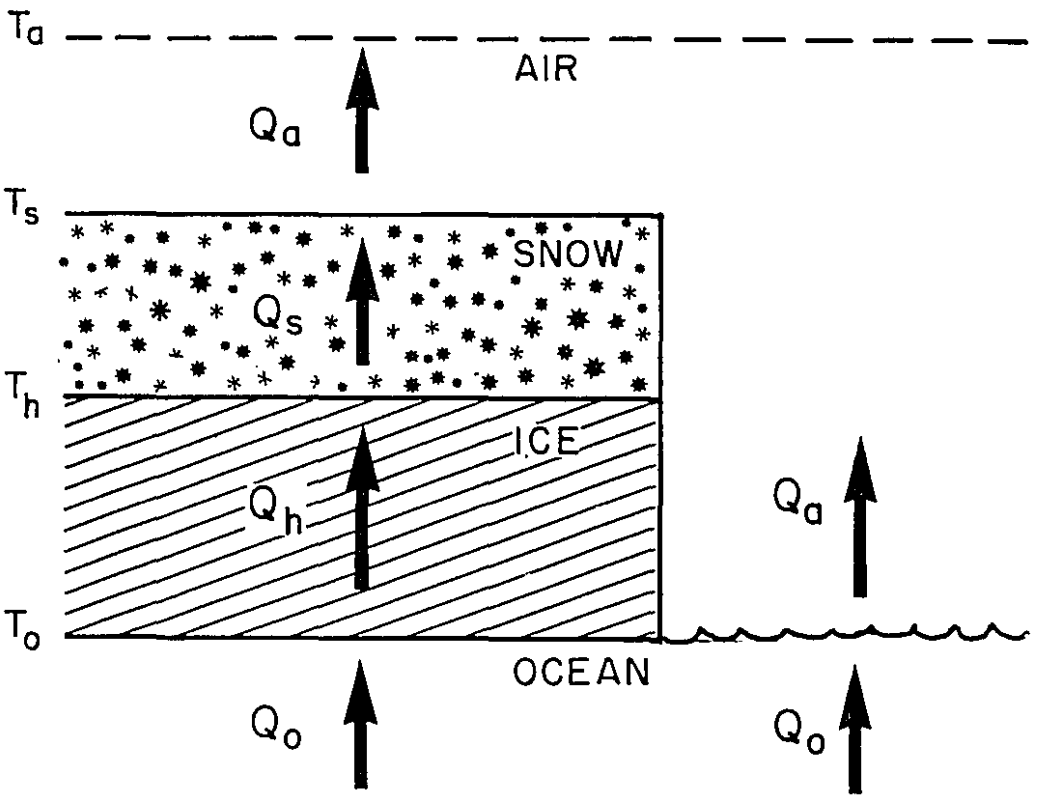

Figure 3.1 Schematic of thermodynamic fluxes through the ocean, ice, snow, and atmosphere. Positive fluxes are directed upwards by convention. The net heat flux over a model grid cell is a weighted average of that over the ice-covered and ice-free ocean.

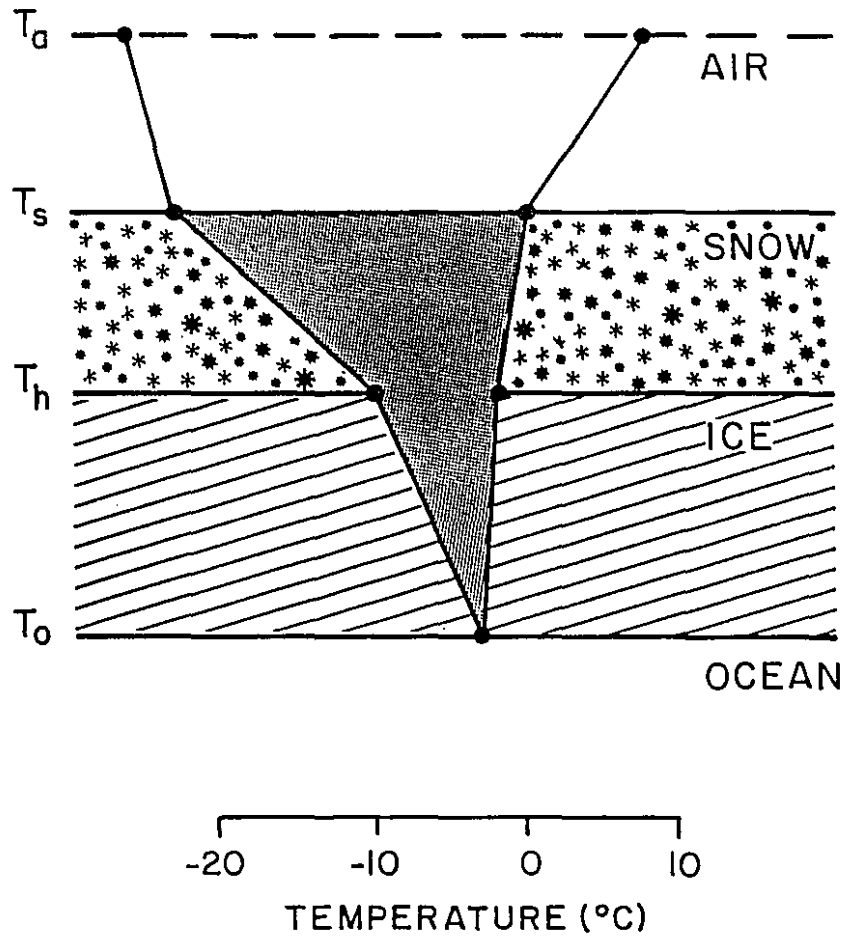

Figure 3.2 Typical temperature profiles through the snow-ice layer during winter and summer. The shaded area represents the amount of heat stored internally in the snow-ice layer between the winter and summer seasons.

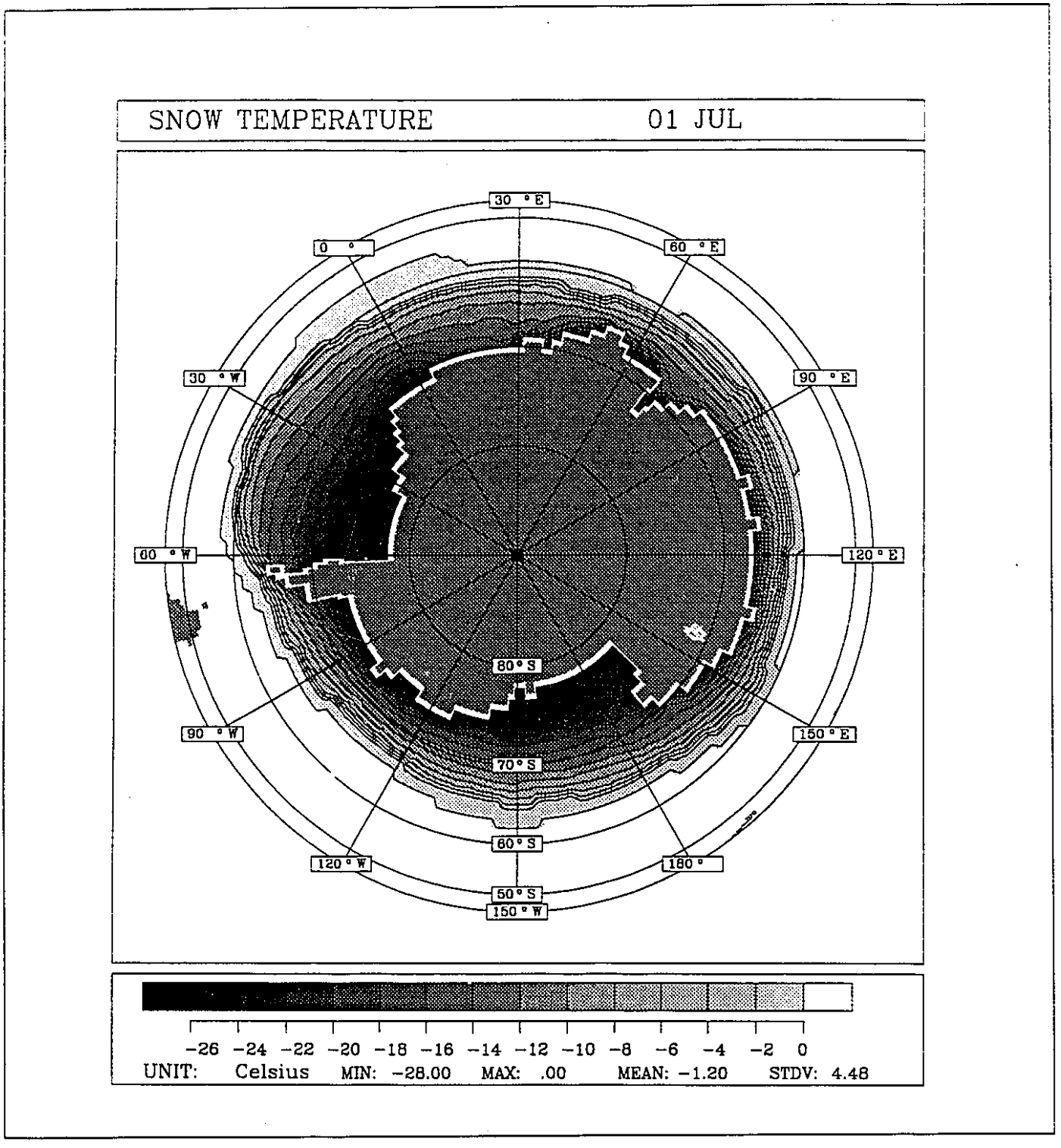

Figure 3.3 Antarctic winter snow-surface temperature predicted by the model. There is a strong latitudinal gradient with the coldest temperatures being found in the Weddell and Ross Seas.

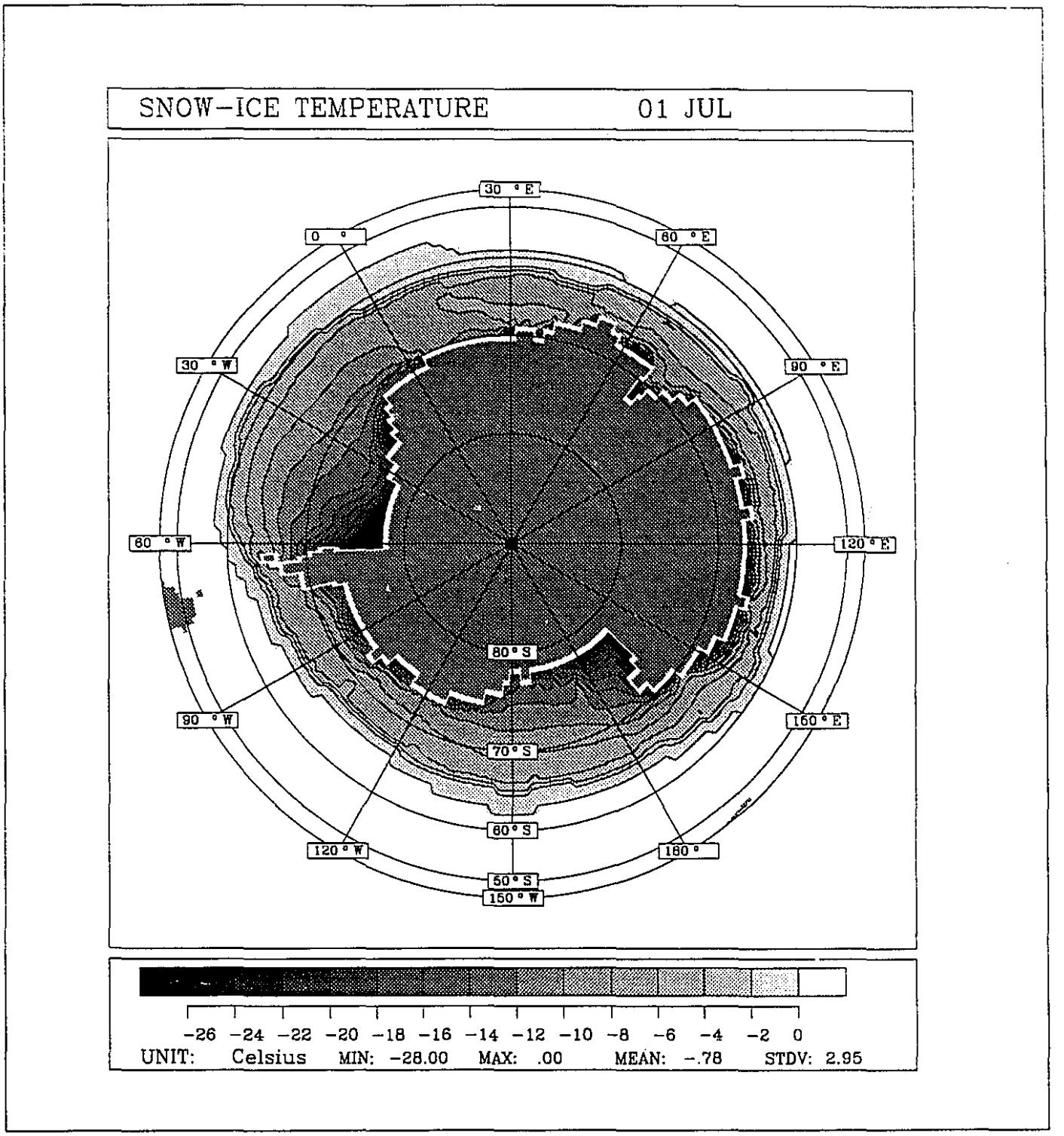

Figure 3.4 Antarctic winter snow-ice interface temperature predicted by the model. The temperatures are warmer than those of Fig. 3.3 and the latitudinal gradient is not as large as in Fig. 3.3.

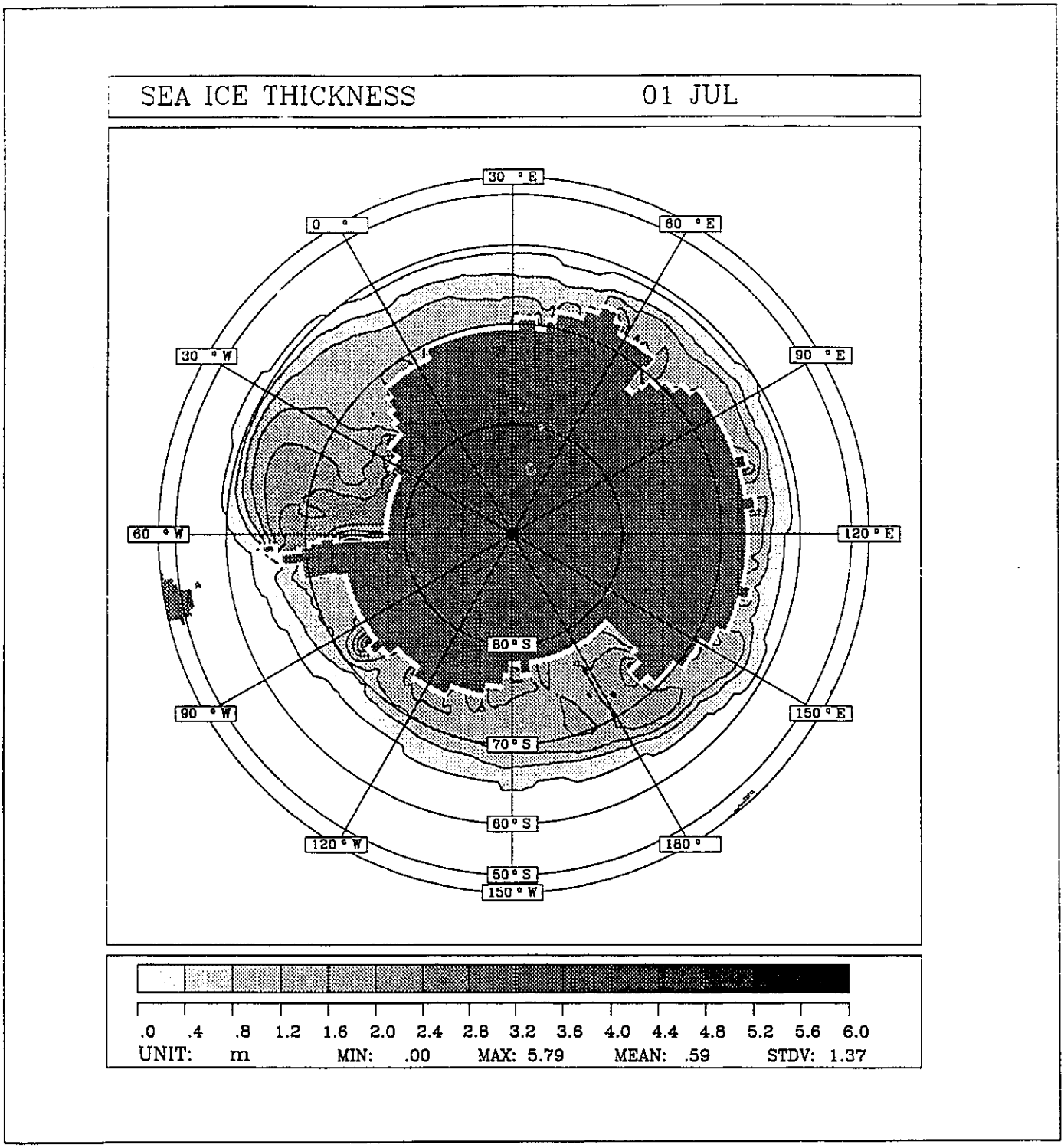

Figure 3.5 Antarctic winter ice thickness predicted by the model. The thickest ice occurs along the western boundaries of the Weddell and Ross Seas. The average ice thickness is much less than that which is simulated in a model without snow cover.

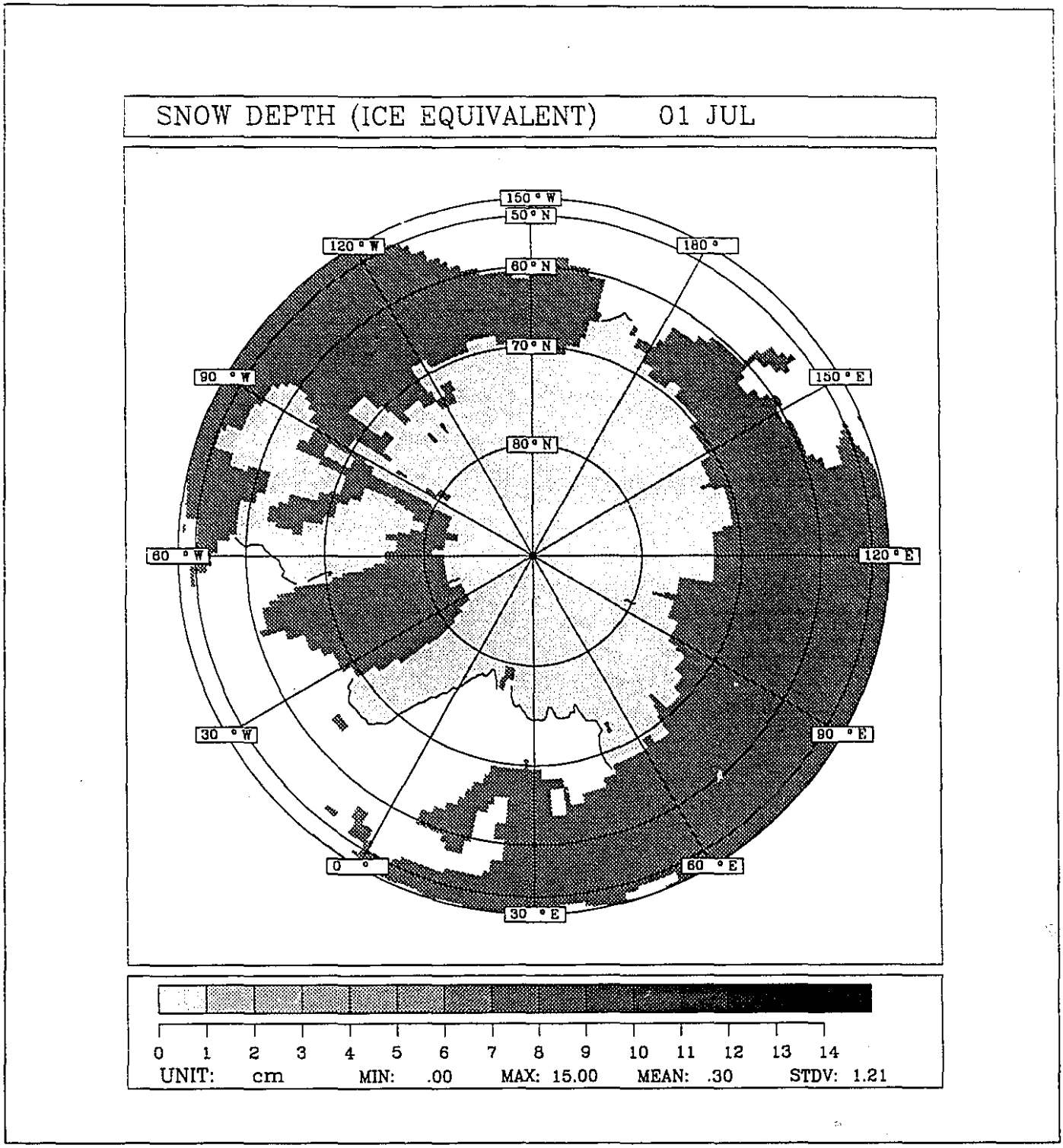

Figure 3.6 Arctic summer snow depth predicted by the model. Most of the snow in the Arctic melts during the summer.

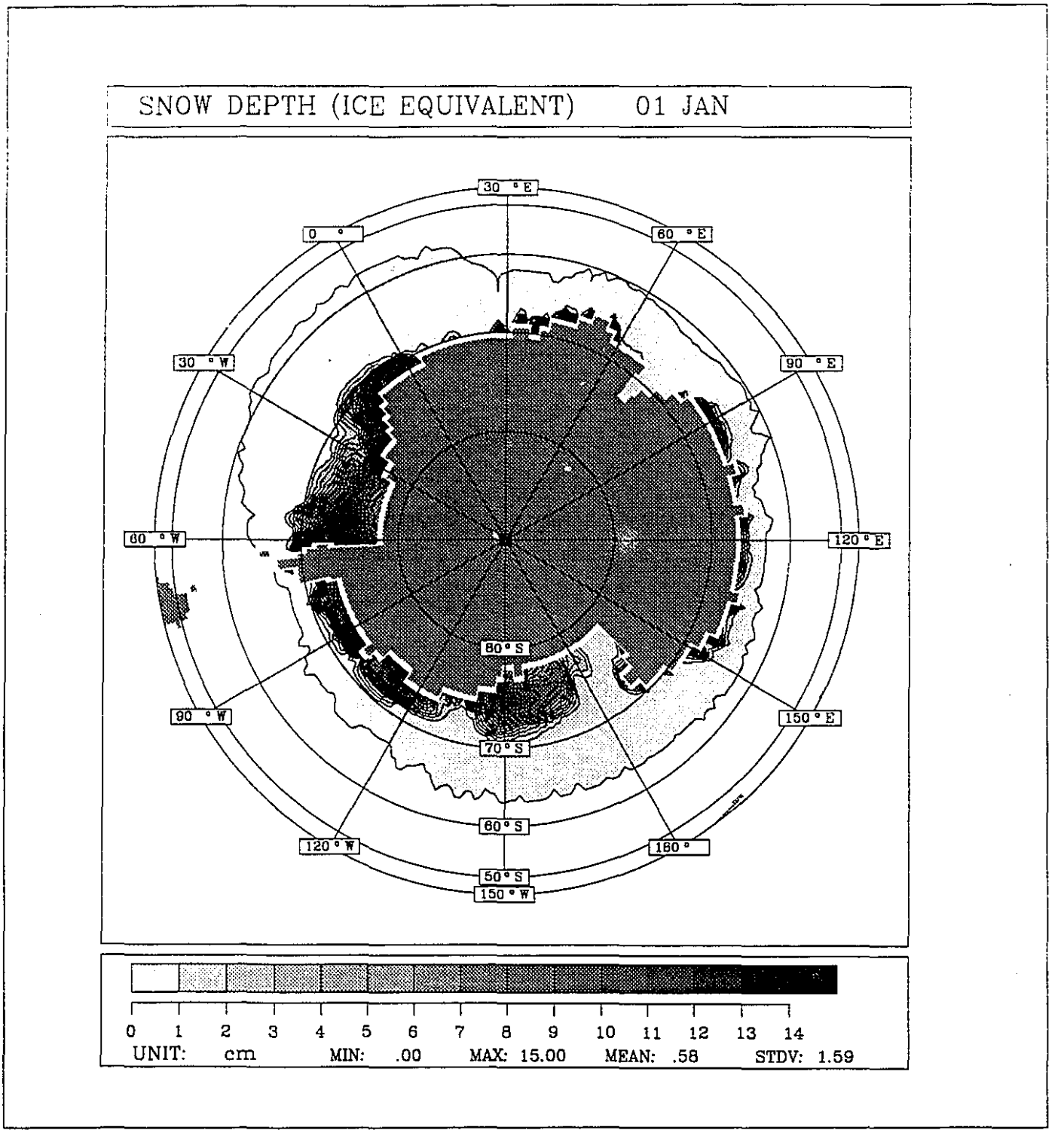

Figure 3.7 Antarctic summer snow depth predicted by the model. The Antarctic receives a greater amount of snow than the Arctic. Furthermore, the Antarctic snow does not all melt during the summer season as in the Arctic.

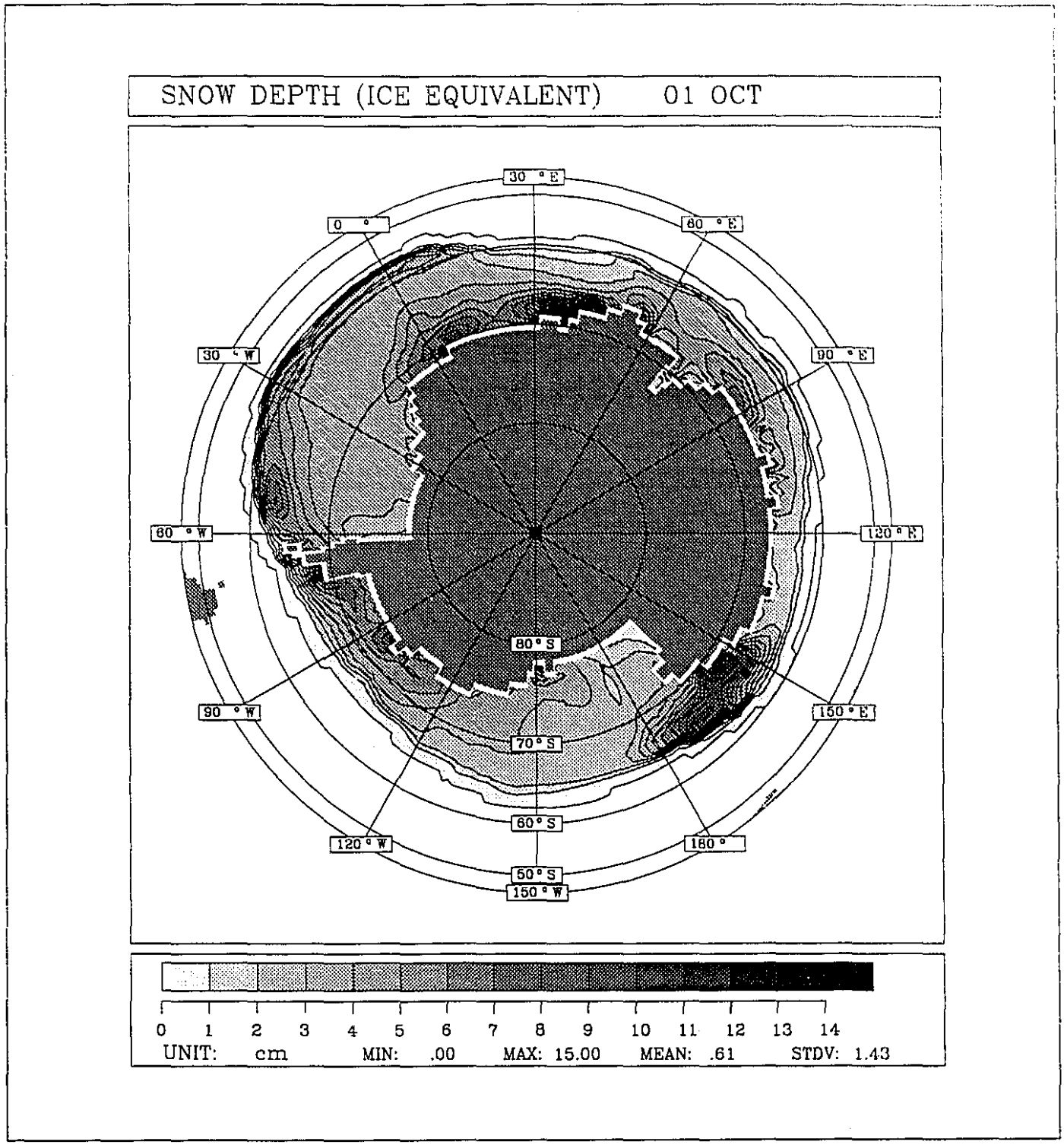

Figure 3.8 Antarctic spring snow depth predicted by the model. There is a considerable buildup of snow along the marginal ice zone. Divergence of the ice motion results in shallow snow depths in the central Weddell and Ross Seas.

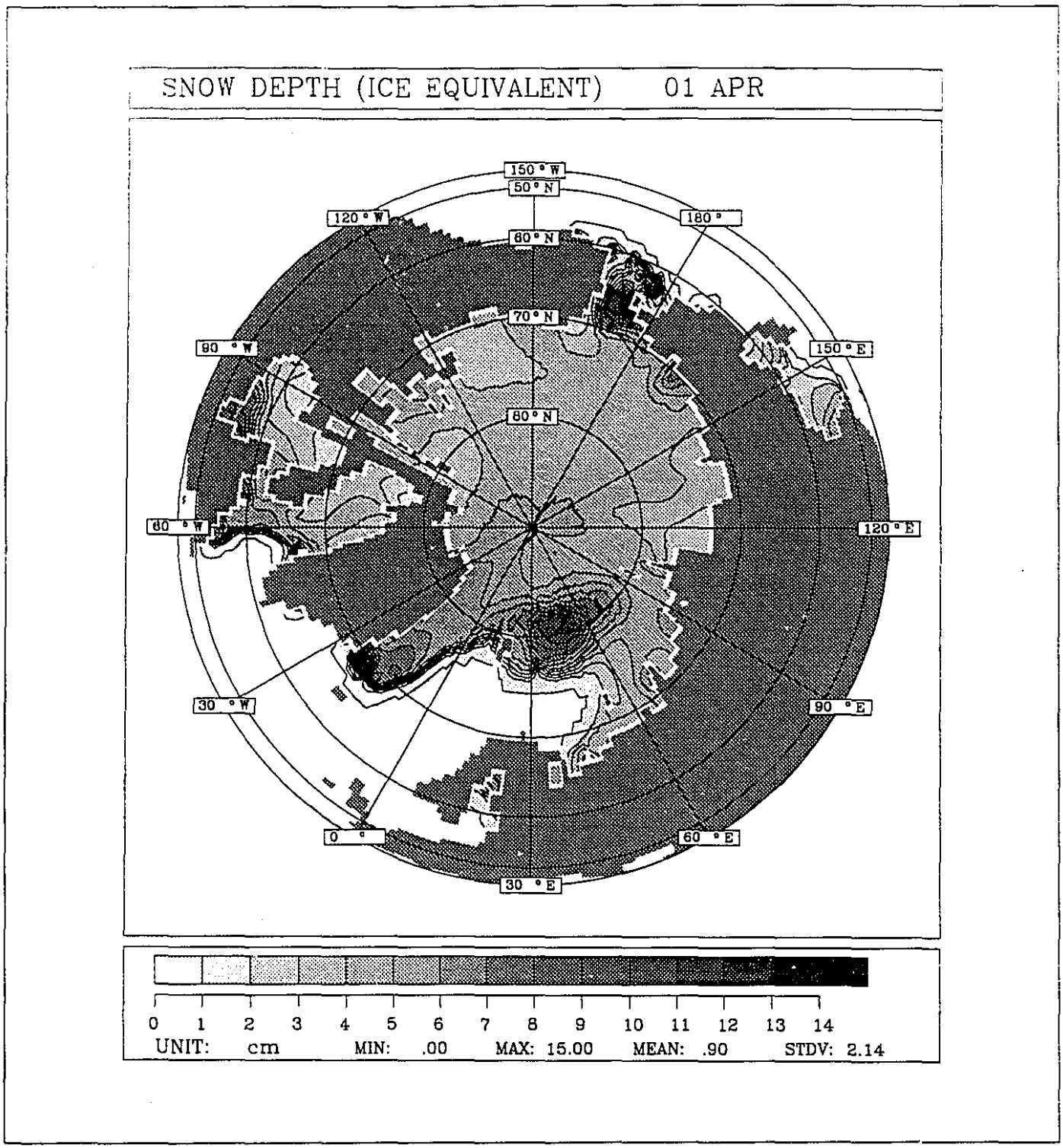

Figure 3.9 Arctic spring snow depth predicted by the model. Excessive snow buildup occurs along the marginal ice zone. Presumably, northward travelling atmospheric eddies produce this snowfall when they impinge upon the ice cover.

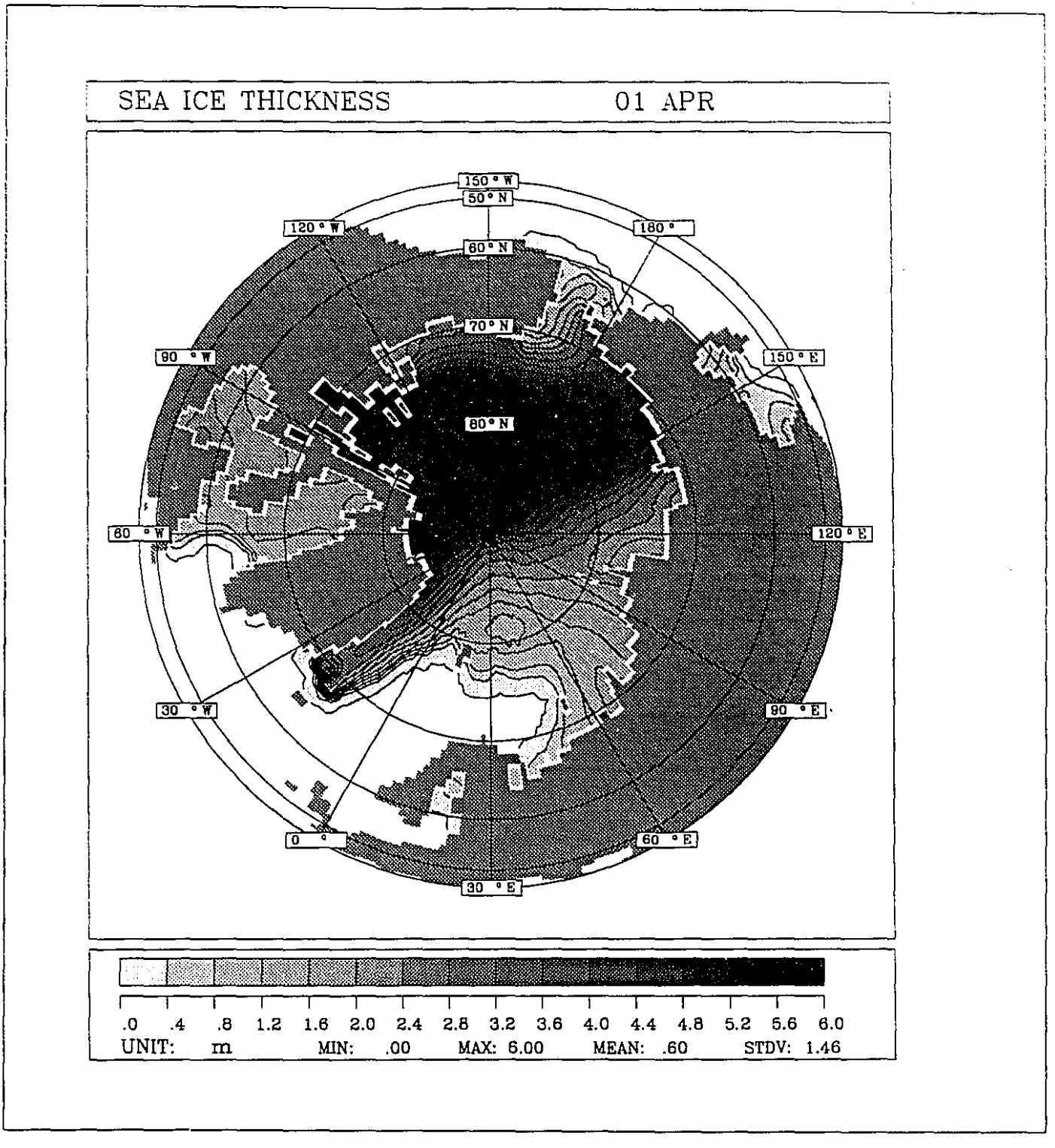

Figure 3.10 Arctic spring ice thickness predicted by the model. The Arctic ice is considerably thicker than the Antarctic ice. The distribution of ice thickness is somewhat unrealistic as the thickest ice should occur north of Greenland.

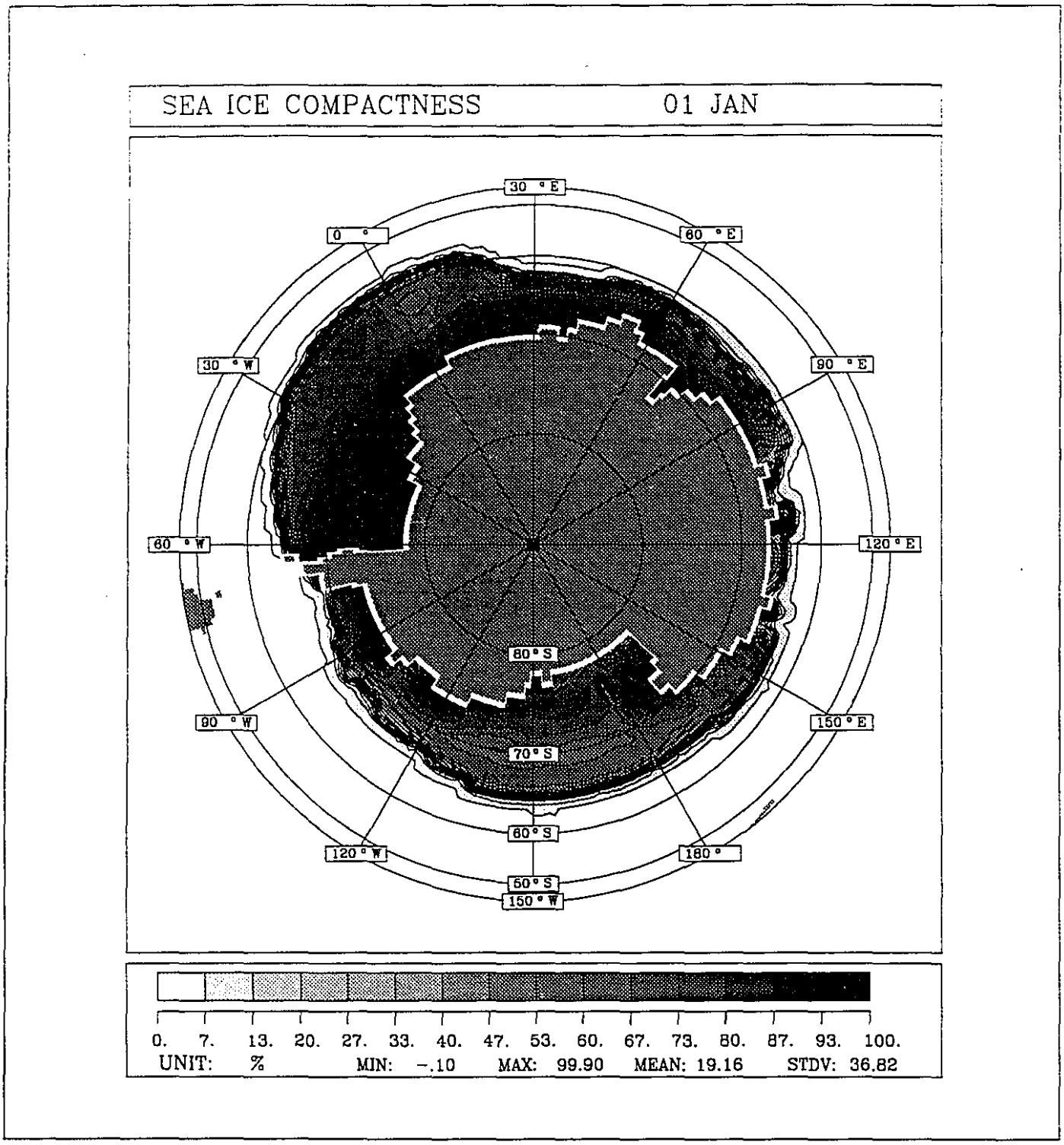

Figure 3.11 Antarctic summer sea-ice concentration predicted by the model. Although the sea-ice extent is exaggerated, the interesting point is that indications of a polynya occur in the same geographical location as the observed Weddell polynya.

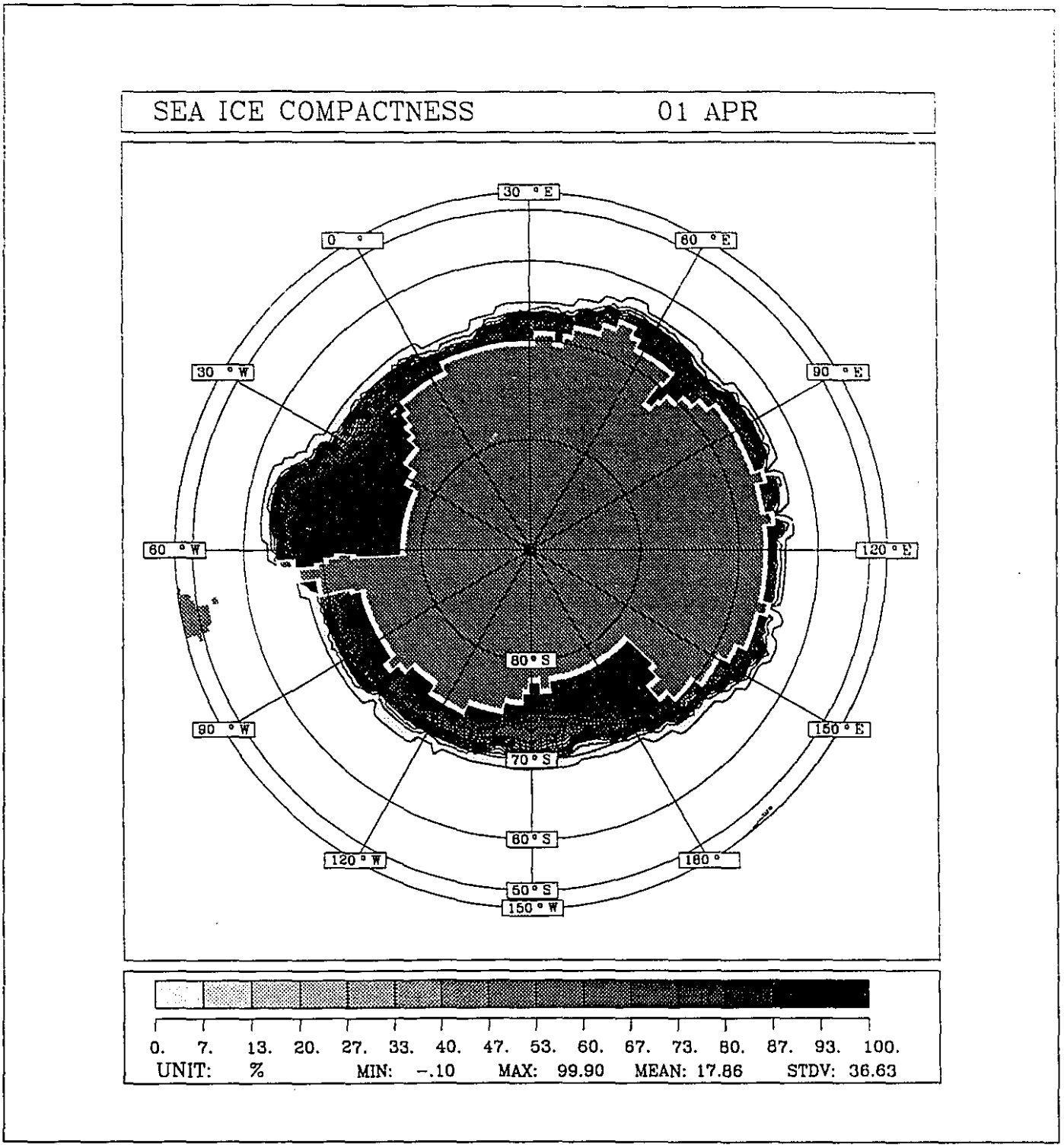

Figure 3.12 Antarctic fall sea-ice concentration predicted by the model. The sea-ice extent for this season is more realistic than that of the summer season shown in Fig. 3.11. Low ice concentration is simulated in both the Weddell and Ross Seas, consistent with ice divergence in those locations.

§ 4 General Circulation of the Arctic Ocean

§ 4.1 Introduction

This chapter investigates the general circulation of the Arctic Ocean using the coupled sea ice - mixed layer - isopycnal ocean general circulation model developed by Oberhuber (1993a). Much of the research in physical oceanography in the Arctic has concentrated on understanding the nature and variability of the sea-ice cover in the ocean and not on the general circulation of the ocean itself. Although simulation results of the sea-ice and mixed layer are presented here, this chapter focuses on the circulation and water-mass properties below the mixed layer. The observational and modelling studies that have been carried out on these latter two topics are now briefly reviewed below.

§ 4.1.1 Observed Features

A review of the large-scale physical oceanography of the Arctic Ocean has been recently done by Carmack (1990). He discusses in detail the bathymetry, hydrology, ice cover, water masses, and current systems. The most salient features are highlighted below.

The Arctic Basin (hereafter simply referred to as the basin) is deep, with an average depth of about 4000 *m* (see Fig. 1.1 in Chapter 1). It consists of two basins, the Canadian and the Eurasian Basins, which are separated by the Lomonosov Ridge. The ridge is at a depth of 1500 *m* below the surface and extends across the basin from Siberia to Greenland. The Arctic communicates with the Atlantic Ocean via the relatively wide (460 *km*) and deep (2500 *m*) Fram Strait; by contrast, communication with the Pacific Ocean occurs through the much narrower (65 *km*) and shallower (45 *m*) Bering Strait. Exchanges also occur with the Canadian Arctic Archipelago and the Barents Sea.

The waters entering via Bering Strait are much fresher (30 *psu*) than those entering through Fram Strait (35 *psu*). Since the typical surface waters of the Arctic Ocean have a salinity of 32 *psu*, the Bering Strait flow contributes substantially to the freshwater influx to the basin (2000 km^3/yr). An even greater influx of freshwater is produced by the numerous rivers located along the periphery of the basin (3500 km^3/yr) (see Aagaard & Carmack (1989)).

The net transport of sea water into the basin via Bering Strait is estimated to be 0.8 *Sv* (Aagaard & Carmack, (1989)). This is considerably smaller than the Fram Strait flows which are composed of an influx of about 7 *Sv* of warm, saline water (the West Spitsbergen Current (WSC)) and an outflow of about 7 *Sv* of relatively cool, fresh water (the East Greenland Current (EGC)).

The water column (see Fig. 4.1) is considered to be composed of three main layers: a cold-fresh surface layer (0 to 200 *m* depth) which is influenced by the sea-ice formation and river runoff, a warm, saline intermediate layer (200 *m* to 900 *m*) due to an influx from the Atlantic via the WSC, and a deep (900 *m* to the bottom) cold, saline layer formed by convection. The water column in the Canadian Basin is much more stably stratified than in the Eurasian Basin. The salinity distribution in the surface layer (Fig. 4.2) clearly reflects the influx of saline Atlantic water through Fram Strait. Similarly, the temperature distribution in the core of the Atlantic Layer (Fig. 4.3) shows a tongue of warm water which indicates the penetration of warm Atlantic water through Fram Strait.

Inside the basin, the surface flow is considered to consist of the anticyclonic Beaufort Gyre (BG) in the Canadian Basin and the Transpolar Drift Stream (TDS), directed toward Fram Strait, in the Eurasian Basin. The flow of sea ice follows this pattern as well. The Atlantic

Layer flow (Fig. 4.4) consists of a cyclonic circulation in each of the Canadian and Eurasian Basins. The deeper flow is speculated to be the same as that of the Atlantic Layer (Fig 4.5).

§ 4.1.2 Previous Modelling Results

Galt (1973) carried out the first large-scale modelling study of the Arctic Ocean which involved solving a barotropic vorticity equation forced by the curl of the wind stress. The resulting flow consisted of an anticyclonic BG and a TDS directed toward Fram Strait (his Fig. 14). This was a wind-driven flow which ignored the thermohaline circulation and the exchange of water masses with various straits.

Semtner (1976b) used a baroclinic model which simulated the anticyclonic surface flow of the BG (his Fig. 7). He obtained a stable stratification maintained by a halocline. The Eurasian Basin received both an intermediate layer of warm Atlantic water and bottom water from the WSC, and it exported surface water of low salinity into an intense EGC. However, the sense of circulation in the Atlantic Layer (his Fig. 10) in the central Arctic was opposite to that inferred from water-mass properties.

The first coupled sea ice - ocean model was presented by Hibler & Bryan (1987). Although they emphasized the sea-ice simulation, some results were presented for the ocean surface circulation. The modelled flow showed an anticyclonic BG and a TDS (their Fig. 11). Results for the deeper circulation were not presented since the model was diagnostically constrained below the surface layer.

Semtner (1987) presented a coupled sea - ice ocean model in which the diagnostic constraint of Hibler & Bryan was removed and a simpler ice rheology was employed. The ocean circulation in the Canadian Basin was anticyclonic at all depths, but changed to cyclonic in the Eurasian basin below 200 m. He was able to simulate the inflow of warm Atlantic water into

the Arctic Basin (his Fig. 12); however, the spatial distribution of temperature across the basin did not mimic the observed pattern (see Fig. 4.3).

Further modelling efforts to study the Arctic Ocean climatology have been carried out using coupled sea ice - ocean models, *e.g.* Ranelli & Hibler (1991), Ries & Hibler (1991), Warn-Varnas *et al.* (1991); however, the focus has been on the sea-ice simulation and not on the ocean circulation and water-mass properties. To date, almost all modelling studies have been based on a variant of the Bryan-Cox ocean model (Cox, 1984). Part of the motivation for the present work is the availability of a new type of ocean general circulation model that has been developed by Oberhuber (1993a). This new model differs from the Bryan-Cox model in that it uses isopycnal surfaces as the vertical coordinate. The vertical coordinate is thus Lagrangian rather than Eulerian. The flow in the horizontal plane is then naturally directed along isopycnal surfaces. This new model is applied to the Arctic Basin with the goal of obtaining an improved simulation of the water mass and circulation properties, most of which have not been correctly simulated in previous studies.

The remainder of this chapter is organized as follows. Section 4.2 briefly describes the coupled sea ice - mixed layer - isopycnal ocean model. The simulation results for the sea-ice, mixed-layer, and deep-ocean isopycnal-layer models are presented in section 4.3. Section 4.4 concludes the chapter.

§ 4.2 The Model

The model chosen for this study is that of Oberhuber (1993a). The present work is distinct from that of Oberhuber (1993b) in that he discussed principally the circulation of the North Atlantic and not that of the Arctic. The Oberhuber model consists of three coupled

submodels. The sea-ice is represented by a dynamic-thermodynamic model with viscous-plastic rheology (see Chapter 2), the mixed layer by a turbulent kinetic energy model (based on models due to Niiler & Kraus (1977) and Garwood *et al.* (1985)), and the deep ocean by an isopycnal-layer model. A schematic of the models is presented in Fig. 4.6. The models interact via the exchange of momentum, mass, heat, and salt. Forcing occurs via the specification of monthly climatological atmospheric fields and realistic topography is employed. The equations describing each model are fully described by Oberhuber (1993a). They are briefly presented here to highlight the physical processes that are represented. This section ends by describing the physical layout of the model.

§ 4.2.1 Sea Ice

For the momentum balance the ice is considered to move in a two-dimensional spherical plane with forcing fields operating on the ice via simple planetary boundary layers. The nonlinear inertial terms are neglected. The equation is

$$\frac{\partial \vec{u} h}{\partial t} = \vec{\nabla} \cdot A^m \vec{\nabla} \vec{u} h - \vec{f} \times \vec{u} h - g h \vec{\nabla} \Gamma + \vec{\tau}_a + \vec{\tau}_o + \vec{I} \quad , \qquad (4.1)$$

where $\vec{u} = (u,v)$ is the horizontal velocity vector, h the ice thickness, A^m the horizontal diffusion coefficient for momentum, $\vec{f}$ the Coriolis vector, g the acceleration due to gravity, Γ the sea surface dynamic height, $\vec{\tau}_a$ the ice surface wind stress, $\vec{\tau}_o$ the ice bottom current stress, and $\vec{I}$ the internal ice stress which is based on a viscous-plastic ice rheology.

The snow-cover thickness s and the ice-cover thickness h are modelled as continuous nonnegative variables. The presence of leads in the ice is modelled using a variable called the ice compactness q and is defined as the fraction of a grid cell area covered by ice; the rest of the cell is covered by open water.

The spatial and temporal variations in thickness and compactness are modeled by the continuity equations

$$\frac{\partial s}{\partial t} = -\vec{\nabla}\cdot(\vec{u}\,s) + \vec{\nabla}\cdot A^s\vec{\nabla}s + F_s - F_a \tag{4.2}$$

$$\frac{\partial h}{\partial t} = -\vec{\nabla}\cdot(\vec{u}\,h) + \vec{\nabla}\cdot A^s\vec{\nabla}h + F_h + F_a \tag{4.3}$$

$$\frac{\partial q}{\partial t} = -\vec{\nabla}\cdot(\vec{u}\,q) + \vec{\nabla}\cdot A^s\vec{\nabla}q + F_q \quad , \tag{4.4}$$

where F_s, F_a, F_h, and F_q are thermodynamic forcing or source terms (see § 3.2.2.2). The numerical diffusion terms for these scalar equations have coefficient A^s.

§ 4.2.2 Mixed Layer

The sea-ice and deep-ocean models are coupled through an ocean mixed-layer model. The mixed layer has vertically uniform velocity, density, temperature, and salinity. The uniformity is produced by both wind-stirring and surface buoyancy fluxes. The mixed-layer depth is controlled by both local mixing and the horizontal convergence of mass and heat. The mixed layer is in fact the uppermost layer of the deep-ocean model and it always has a nonzero thickness and a temporally and spatially varying potential density. This is in contrast to all deeper layers which may have a zero thickness and always have a prescribed potential density.

The mixed layer differs from the deeper layers in that it is directly forced by a surface

buoyancy flux due to heat and freshwater fluxes. As a result, the mixed layer depth, h_1, changes through the processes of entrainment and detrainment. The equation for the entrainment rate w is

$$w g' h_1 - w Ri_c (\Delta u^2 + \Delta v^2) = a u_*^3 + b B \quad , \qquad (4.5)$$

where g' is the reduced gravity, Ri_c the critical Richardson number, Δu^2 and Δv^2 the difference in velocity component between the mixed layer and the layer below it, a and b weighting coefficients, u_* the friction velocity, and B the surface buoyancy flux. The first term on the left hand side of Eqn. 4.5 describes the production of mean potential energy due to the vertical displacement of isopycnals; the second term describes the production of mean kinetic energy due to vertical velocity shear. On the right hand side, the first term stands for the production of turbulent kinetic energy due to wind stirring; the second term is the buoyancy flux which is induced by heat and fresh water fluxes.

§ 4.2.3 Deep Ocean

The representation of the oceanic flow along isopycnal layers is motivated by the assumed diabatic nature of the subsurface ocean. The use of isopycnal coordinates allows flow to occur naturally along isopycnal surfaces. There are many difficulties in the physical realization of such a model, such as the intersection of isopycnal surfaces either with the sea surface or with the bathymetry, the parameterization of cross-isopycnal mixing, and the representation of convection. The reader is referred to Oberhuber (1993a) for a discussion of these issues.

The model discretizes the water column (below the mixed layer) into layers of prescribed potential density. Both the depth of a layer beneath the surface and its thickness vary temporally and spatially due to mass flux divergence, entrainment, and cross-isopycnal mixing. A layer is permitted to migrate vertically up or down, increase or decrease its thickness, and intersect with

the mixed layer or bathymetry. This freedom of movement allows the model to optimally represent a highly stratified water column by having many thin isopycnal layers near the pycnocline. At the same time the model can represent a well mixed water column by a few relatively thick layers. The benefit of isopycnal coordinates is that as the water column changes its stratification either spatially or temporally, the coordinate system adjusts to adequately represent it.

Within each layer (of depth h say) the mass flux, the mass content, the heat content, and the salt content are prognostically computed. The basic equations are formulated in flux form and represent conservation equations for the vertically averaged mass flux $(\vec{u}\rho h)$, mass content (ρh), heat content $(\theta\rho h)$, and salt content $(S\rho h)$:

$$\frac{\partial(\vec{u}\,\rho\,h)}{\partial t} = -\vec{\nabla}(\vec{u}(\vec{u}\,\rho\,h)) - h\,\vec{\nabla}p - \vec{f}\times(\vec{u}\,\rho\,h) + \vec{\nabla}\cdot A^m\,\vec{\nabla}(\vec{u}\,\rho\,h) + \Omega[\rho\,\vec{u}] + \vec{\tau} \tag{4.6}$$

$$\frac{\partial(\rho\,h)}{\partial t} = -\vec{\nabla}\cdot(\vec{u}\,\rho\,h) + \Omega[\rho] + R^{P-E} \tag{4.7}$$

$$\frac{\partial(\theta\,\rho\,h)}{\partial t} = -\vec{\nabla}\cdot(\vec{u}(\theta\,\rho\,h)) + \vec{\nabla}\cdot A^s\,\vec{\nabla}(\theta\,\rho\,h) + \Omega[\theta\,\rho] + \frac{Q}{c_p} \tag{4.8}$$

$$\frac{\partial(S\,\rho\,h)}{\partial t} = -\vec{\nabla}\cdot(\vec{u}(S\,\rho\,h)) + \vec{\nabla}\cdot A^s\,\vec{\nabla}(S\,\rho\,h) + \Omega[S\rho] + R^{\prime}\ , \tag{4.9}$$

where $\vec{u} = (u,v)$ is the horizontal layer velocity, h the thickness, θ the potential temperature, S the salinity, ρ the potential density, p the *in situ* pressure, $\vec{f}$ the Coriolis vector, A^m the diffusion coefficient for momentum, A^s the diffusion coefficient for heat and salt, $\Omega[\gamma]$ the cross-isopycnal transfer of a quantity γ, $\vec{\tau}$ the stress between neighbouring layers, Q the heat flux into a layer,

c_p the specific heat capacity, R^{P-E} the fresh water flux due to precipitation minus evaporation, and R' the fresh water flux due to the sea ice - ocean coupling.

§ 4.2.4 Model Layout

The domain chosen for this study includes the Arctic Ocean, the GIN Sea, and the North Atlantic. The motivation for including the North Atlantic is the need to simulate the influx of warm, saline water into the GIN Sea from the North Atlantic as well as the outflow of cold, fresh water from the Arctic. The model places a solid wall across the southernmost boundary of the domain, which is located near the equator. A realistic simulation of the interhemispheric thermohaline circulation is thus not possible as cross-equatorial flow is *a priori* blocked. Possibly of greater consequence to the Arctic circulation is the artificial boundary placed across the Bering Strait; thus the model does not allow for the inflow of warm, fresh Pacific water via Bering Strait. The magnitude of the missing flux is of order 1 *Sv*. The Canadian Arctic Archipelago is open and is represented by a single channel of uniform depth of 100 *m*; the model does permit the outflow of cold, fresh Arctic Surface water into Baffin Bay via the Canadian Arctic Archipelago.

The model's bathymetry is obtained by interpolating a high resolution (5 *min*) bottom topographic data set onto the model's grid, which is of lower resolution. The main bathymetric features of the Arctic and GIN Basins are preserved (Fig. 4.7).

A problem with numerical models written in spherical coordinates for the Arctic Ocean is the convergence of the east-west grid spacing near the North Pole. The small grid spacing near the Pole requires unrealistically small time step constraints for numerical stability. This is overcome by rotating the model coordinates by Eulerian angles such that the model coordinates converge to a point in the North Pacific, which is outside the defined model domain. All figures

presented in this chapter indicate the rotated latitude and rotated longitude coordinates along their axes. The geographical coordinates are superimposed as thin lines on the figures (e.g. Fig 4.7).

The model resolves the water column using seven vertical layers of prescribed potential density. The initially prescribed density and thickness of each layer is obtained via interpolation of the temperature and salinity data of Levitus (1982). An example of the vertical discretization of layers is indicated in Fig. 4.8. As the model integrates in time, these layer thicknesses vary in time and space; however, the densities do not. The first layer, which is the mixed layer, is allowed to change its potential density in response to entrainment and surface buoyancy fluxes. At any instant all layers may be present, or one or more may be absent as the result of a mass flux divergence or of detrainment from that layer into neighbouring layers. At a later time, a layer may reappear as the result of mass flux convergence or entrainment into that layer. In this manner the layers both migrate in the vertical coordinate direction as well as change their thickness. This coordinate scheme is particularly relevant for the GIN Sea where convective overturning occurs. Where the water column is highly stratified, more layers are required to resolve the vertical structure than when the water column is well mixed. The vertical coordinate scheme adopted automatically satisfies this demand.

The model uses spherical coordinates in the horizontal with a resolution of 2 degrees in latitude and longitude. Since the model coordinates are rotated by Eulerian angles with respect to geographical coordinates, the spatial resolution is about 100 *km* in the Arctic. To adequately resolve the flow through Fram and Denmark Straits, the model uses a nested grid in the GIN Sea. The nested grid has a minimum horizontal resolution of about 20 *km*. To avoid numerical problems, the spatial transition from the coarse resolution grid spacing to the fine resolution spacing occurs smoothly. The horizontal resolution, including the nested grid, can be inferred

from Fig. 4.9, which shows the wind stress forcing field. Note that only that part of the model domain that includes the Arctic Basin and the GIN Sea is shown.

The model is forced using monthly climatological fields of wind stress, radiation, air temperature, humidity, rainfall, and cloud cover. These fields are described by Oberhuber (1988) and Wright (1988). The model derives the forcing at a particular time step by linearly interpolating between climatological fields of neighbouring months.

The spinup of the model is optimized by first integrating the model for 100 years using a coarse resolution grid in which the nested grid is not present. The nested grid is then introduced and the model is integrated for another 100 years. This is an adequate time for the sea-ice and mixed-layer models to reach an equilibrium; however, the deep-ocean circulation almost certainly is not in equilibrium after such a short period. One simulated year requires one hour of CPU time on a Cray-YMP; consequently, integrations for thousands of years are not feasible.

The surface boundary condition on salinity is a relaxation to the observed monthly salinity field. The time constant with which the actual salinity relaxes to the observed salinity is approximately 6 months. Temperature is not directly relaxed to the observed ocean values; instead, sea surface temperature is essentially relaxed to an apparent surface temperature that is from a complete surface energy balance that includes longwave, shortwave, sensible, and latent heat terms (see Oberhuber (1993a) for details).

Prior to analyzing the model's simulation of the general circulation it must be established that the model has reached a cyclo-stationary equilibrium. Time series for the first 100 years of the horizontally averaged model-domain temperature and salinity were constructed. Fig 10.a presents both the surface and deep-ocean average temperature. The sea-surface temperature shows a reasonable annual excursion of about 4 degrees. The deep-ocean temperature has a

gentle positive slope which indicates that the deep ocean is in fact heating up throughout the entire integration period. This heating amounts to about 1 degree over a 100 year period. Fig 10.b presents both the surface and deep-ocean average salinity. Again the sea-surface salinity indicates a reasonable seasonal cycle while the deep-ocean indicates salinity is gradually increasing throughout the integration period. The gradual increases in deep-ocean temperature and salinity are not an impediment to this study as the total integration period is only 200 years. Oberhuber (*pers. comm.*, 1993) has modified his code so that this drift will no longer occur. The drift occurs because the version of the model used here does not properly treat the situation in which the mixed layer becomes heavier than the deeper layers.

§ 4.3 Simulation Results

The purpose of this section is to give an overall impression for the model's simulation of the sea-ice and ocean circulation of the Arctic Ocean. Results are only shown for one particular day, *i.e.* January 1st. Certainly, the sea-ice and the mixed-layer do undergo considerable variation over an annual cycle. This seasonal variation will be discussed in the results of Chapter 5.

§ 4.3.1 Sea Ice

The sea-ice velocity field (Fig. 4.11a) and thickness field (Fig. 4.11b) represent quite realistic simulations. Oberhuber (*pers. comm.*, 1992) has recently revamped his numerical sea-ice code. In particular, improvements have been made in the treatment of the important sea-ice rheology terms. Essentially, these terms are now treated implicitly; previously this was not the case. The result is that Oberhuber can now use more realistic values for certain ice rheology parameters than was possible earlier; the strength parameter used was $P^* = 30{,}000\ N/m^2$, while

the minimum strain rate used was $\epsilon_{\min} = 10^{-8}\ s^{-1}$. This modified code has been used in the simulations presented in this chapter. The thickness field of Fig. 4.11b indicates that the thickest ice occurs along the North Coast of Greenland and along the Canadian Arctic Archipelago, as is observed (Bourke & Garrett, 1987).

§ 4.3.2 Mixed Layer

The mixed-layer simulation for the Arctic is presented in detail in Chapter 5; however, that chapter shows the results for a model domain that does not include the North Atlantic. The results presented in Fig. 4.12 offer the opportunity to compare the simulation of the Arctic Ocean surface features with those of the North Atlantic.

The sea-surface velocity (Fig. 4.12a) indicates reasonable circulation patterns for the subtropical and subpolar gyres. The high density of grid points in the GIN Sea makes it difficult to see clearly the circulation pattern of the subpolar gyre. Thus Fig. 4.12b shows a blowup of the circulation in the GIN Sea, as well as a strong East Greenland current, and a small Greenland Sea gyre. The Canadian Basin surface circulation shows a generally anticyclonic gyre, *i.e.* motion following the ice drift. There is also a flow from the Canadian Basin through the Canadian Arctic Archipelago into Baffin Bay.

Consistent with the sea-surface velocity field is the sea-surface elevation field (Fig. 4.12c). There is an elevation of about 60 *cm* over the Gulf Stream, and a sea-surface depression of about 50 *cm* in the GIN Sea. Over the Canadian basin of the Arctic there is a sea surface elevation of about 50 *cm* relative to the elevation at Fram Strait. This is in good agreement with the dynamic heights for that region as presented by Coachman & Aagaard (1974) (see Fig. 5.1).

The mixed-layer depth (Fig. 4.12d) shows that the greatest values should occur along the border between the Barents Sea and the Norwegian Sea. It was expected that the greatest values

should occur in the Greenland Sea since it is there that the greatest convective overturning takes place in reality.

The importance of the GIN Sea to the global thermohaline circulation is evident in Fig. 4.12e which shows the surface potential density over the model domain. The high potential density values of the waters over the GIN Sea means that these waters are easily overturned to contribute to the production of deep water in the North Atlantic. By contrast, the surface waters of the Arctic are extremely fresh and stable.

§ 4.3.3 Eurasian Basin

Based on data collected over the Eurasian Basin, Coachman & Barnes (1962) indicated that there exists a relatively cold pool of subsurface water to the north of the Barents and Kara Seas (see Fig. 4.13a). They indicated that on the isohaline (*i.e.* isopycnal) surface of salinity equal to 33.8 *psu*, the average water temperature is less than -1.7 degrees, which is very close to the freezing point of water of that salinity. The model simulation of potential temperature at a depth of 200 *m* indicates a similar pool of cold water (see Fig. 4.13b).

Coachman & Barnes indicated that tongues of this cold surface extended into the Barents Sea via the topographic troughs that extend from the Eurasian Basin inward towards the Barents shelf. They suggested that water travels along these troughs from the Barents shelf into the Eurasian Basin. This would provide a mechanism for creating the cold pool in the Eurasian Basin. Surface water over the Barents shelf would cool, convectively overturn, and then slide down the trough from the shelf into the subsurface water of the Eurasian Basin. There may be some evidence of this in the model simulation of surface convection. The depth of convection from the sea surface (see Fig. 4.13c) for the last 100 years of the model run indicates the presence of convection along the continental shelf edge of the Barents Shelf. Furthermore, there

is an extension of the convection onto the Barents shelf, exactly where the model topography indicates a trough like feature. The model domain topography for the Arctic Ocean only is indicated in Fig. 4.13d.

§ 4.3.4 Atlantic Layer

Warm and salty water penetrates into the Arctic Ocean via Fram Strait. This water is heavier than the surface Arctic waters and slowly subducts as it travels north of Fram Strait, occupying the water column between 300 and 1000 *m* below the surface. The model simulation of the velocities, temperatures, and salinities at the 1000 *m* level are shown in Fig. 4.14. The velocity pattern at 1000 *m* depth indicates that the waters there are basically constrained to follow the topography (see Fig. 4.13d). The modelled circulation in Fig. 4.14a consists of three cyclonic gyres which simply mimic the pattern of ocean subbasins (again, see Fig. 4.13d). This circulation can be compared with the circulation inferred from temperature and salinity measurements in Fig. 4.4 which shows only one basin-wide gyre. There is some support for a multi-gyre circulation pattern based on observations taken during the Oden 91 North Pole Expedition (E.P. Jones, Bedford Institute of Oceanography, *pers. comm.* 1992). During that expedition the concentration of various chemical tracers was measured at various locations over the Eurasian Basin. Anderson *et al.* are presently preparing this work for publication.

The modelled fields of temperature (Fig. 4.14b) and salinity (4.14c) show patterns that are consistent with the circulation pattern of (Fig. 4.14a). The temperature field shows the warm, saline Atlantic water entering via Fram Strait. The temperature decreases as the water circulates cyclonically in the Eurasian Basin. This cooling of the Atlantic layer water is due to mixing and diffusion of the Atlantic layer water with the waters above and below it. Similarly, the temperature field suggests a cyclonic circulation in the Canadian Basin. The Atlantic layer water

enters the Canadian Basin by flowing over the Lomonosov Ridge near where the ridge intersects the continental slope. Furthermore, the modelled field of temperature is consistent with the observed field (Fig. 4.3).

§ 4.3.5 Deep Layer

Below the surface layer, the Arctic Ocean has very little stratification (see Fig. 4.1). Consequently, the ocean response is expected to be basically barotropic in the deep ocean. The model simulations of velocity, temperature and salinity (Fig. 4.15) indicate similar patterns to that at 1000 *m* (see Fig. 4.14). There does exist some measurements of the deep circulation in the Canadian Basin due to Hunkins *et al.* (1969). They used a photographic nephelometer to infer currents from light scattering. Their observations suggested a cyclonic deep circulation in the Canadian Basin of speeds 4 to 6 *cm/s* with the currents primarily confined to the sloping margins of the basin. Furthermore, this pattern of deep circulation is in agreement with ideas and experiments on deep circulation with a concentrated source and distributed surface sink (Stommel *et al.*, 1958).

§ 4.3.6 Two-Dimensional Transects

An alternate view of the simulated fields of temperature and salinity is offered by taking two-dimensional transects of the model output. All the geographical headings referenced below refer to that of the model domain coordinates (which are rotated with respect to geographical coordinates). The rotated model domain coordinates are labelled along the axes of all plots. First, from a vertical slice in a north-south direction positioned at 8 degrees East longitude (see Fig. 4.13d for orientation), one can see how the warm and salty Atlantic layer water penetrates into the Arctic Ocean from the Greenland Sea (see Fig. 4.16a). Secondly, from a vertical slice in an east-west direction positioned at 59 degrees North latitude (again, see Fig. 4.13d for

orientation), one can see that the warmest and saltiest of the Atlantic layer water is constrained to stay in the Eurasian Basin (see Fig. 4.16b). There is evidence of a strong vertical gradient of temperature and of salinity over the Lomonosov Ridge. The ridge is the major topographic feature that subdivides the Arctic Basin. The Lomonosov Ridge is located at O degrees East in Fig. 4.16b.

§ 4.3.7 Barotropic Stream Function

The barotropic stream function represents the vertically averaged flow (see Fig. 4.17). The stream function indicates anticyclonic flow for the subtropical gyre and cyclonic flow for the subpolar gyre. For the Arctic Basin, the depth averaged transport is cyclonic for both the Canadian and Eurasian Basins. In this model simulation, the generally anticyclonic transport of the surface waters in the Canadian Basin is dominated by the cyclonic deeper transports producing an overall net cyclonic transport in that basin.

§ 4.4 Conclusions

The application of Oberhuber's (1993a) coupled sea ice - mixed layer - isopycnal ocean general circulation model to the Arctic Ocean has proved useful in simulating many of the known circulation and water-mass properties.

The model simulated realistic cyclonic flows at deep and intermediate layers in both the Canadian and Eurasian Basins. The simulated surface flow in the Canadian Basin is questionable as it does not indicate a large-scale anticyclonic flow over the entire Canadian Basin as observed. The simulation showed a flow through the Canadian Arctic Archipelago. It was noted that the sea-ice simulation was satisfactory in that it showed a well developed Beaufort Gyre and

Transpolar Drift Stream. This indicates the dominance of the winds in controlling the ice drift pattern over most of the Arctic.

The influx of warm, saline Atlantic water via Fram Strait and the subduction of this water forms a distinctive intermediate layer in the entire Arctic Basin. However, it is principally confined to the Eurasian Basin due to the presence of the Lomonosov Ridge.

One must exercise caution in the interpretation of the simulation results presented here because of the artificial boundaries along the Bering Strait and of the crude treatment of the Canadian Arctic Archipelago. These representations of the coastal geometry are not felt to be crucial to the simulation of the intermediate and deeper layer flow, but may influence the surface flow. A further limitation was the use of only seven discrete isopycnal layers in the vertical. This choice was dictated by the limited computing resources available. Future studies will involve an increased number of vertical layers, an improved throughflow via the Canadian Arctic Archipelago, and an increased model domain to include part of the northern Pacific so as to include the exchange through Bering Strait. This model will be used to study the interannual variability of the Arctic.

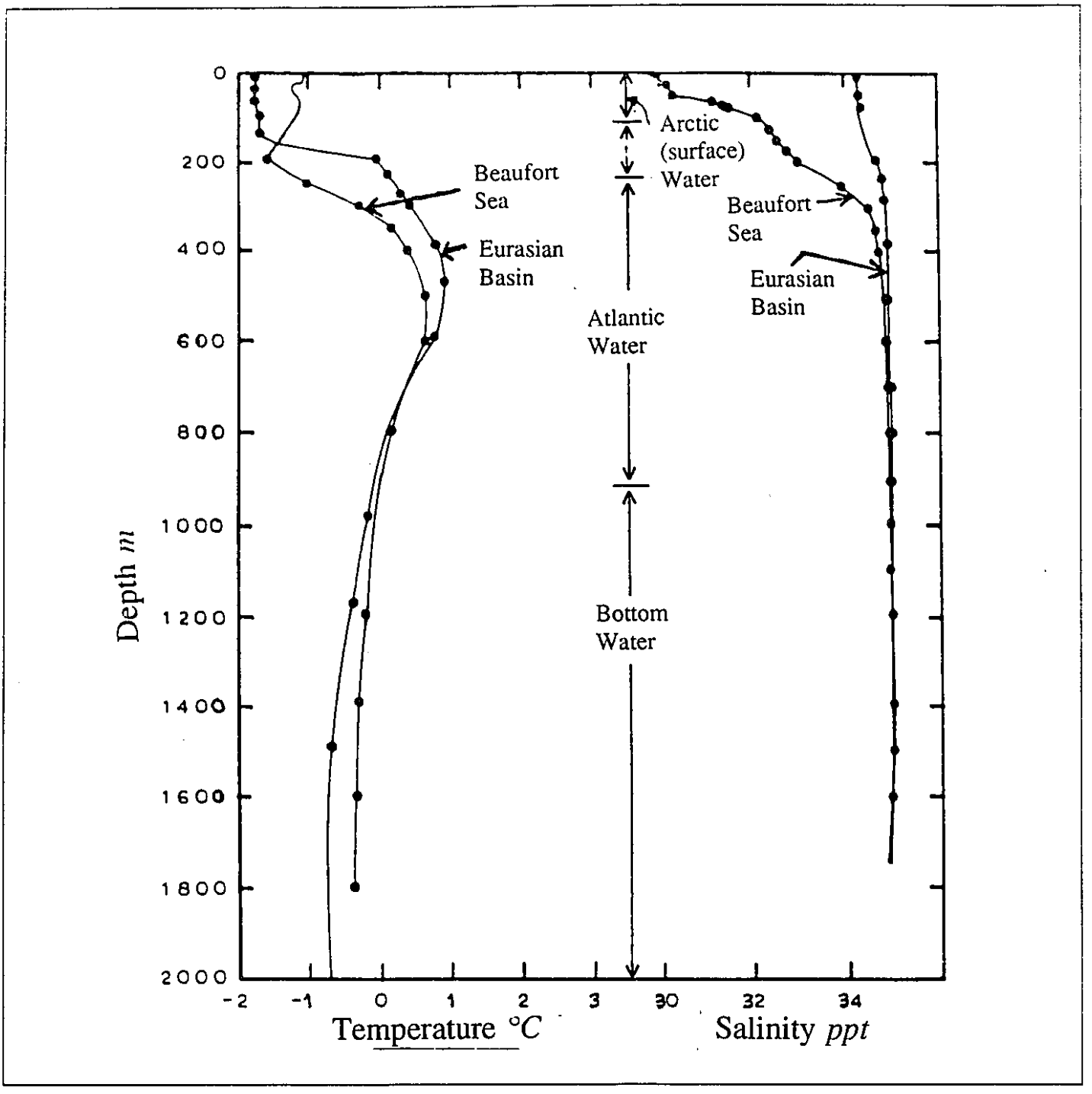

Figure 4.1 Temperature and salinity profiles from the Eurasian Basin and the Beaufort Sea (the southern part of the Canadian Basin) showing the division into (1) the Arctic surface water (polar mixed layer plus halocline), (2) Atlantic intermediate water, and (3) Arctic bottom water (after Coachman & Aagaard (1974)). The Arctic waters are in fact composed of more than just three layers; however, a simple three-layer model is appropriate to the study presented here.

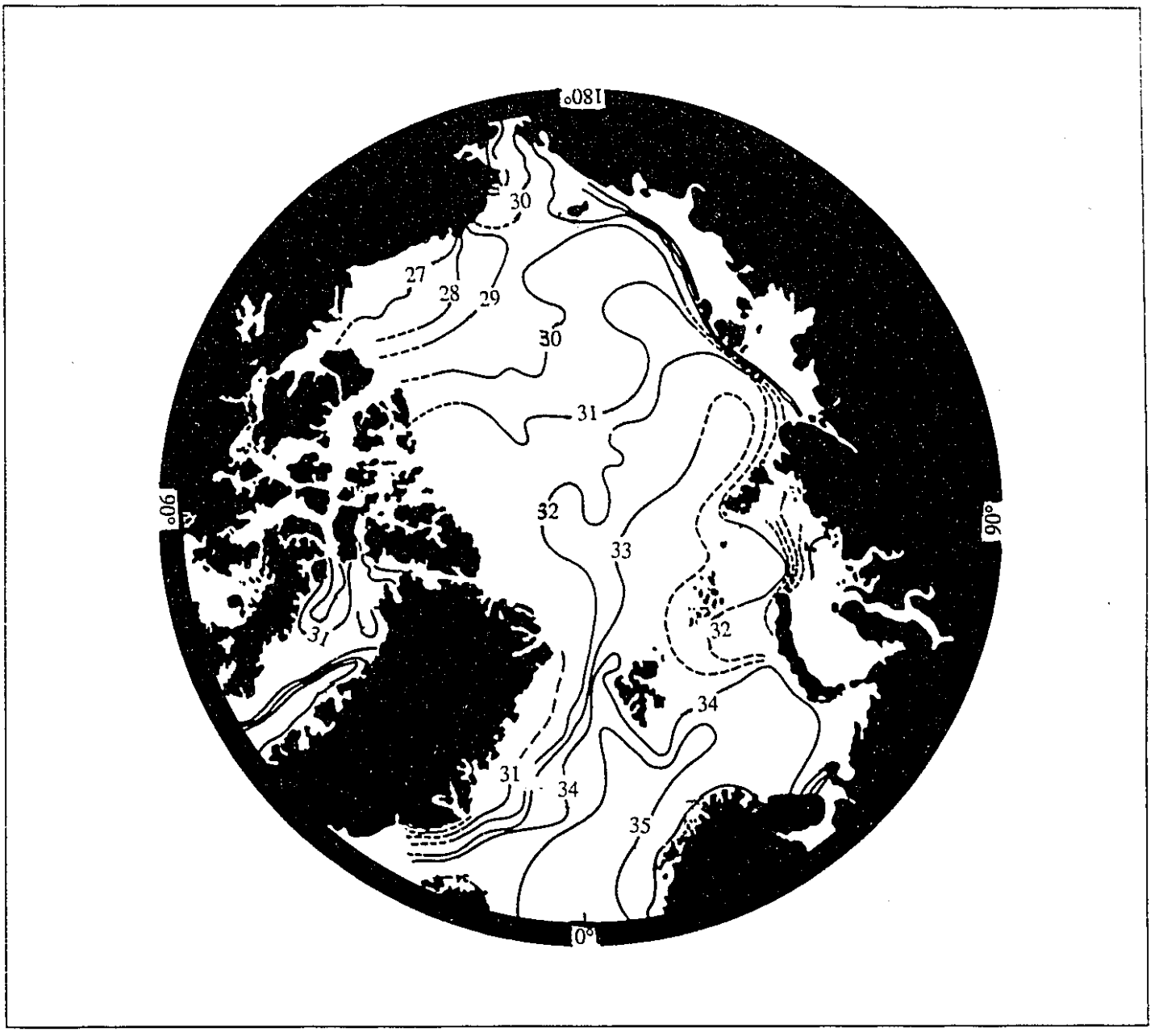

Figure 4.2 Salinity distribution (in *psu*) at 5 *m* depth in the Arctic Ocean (after Coachman & Aagaard (1974)).

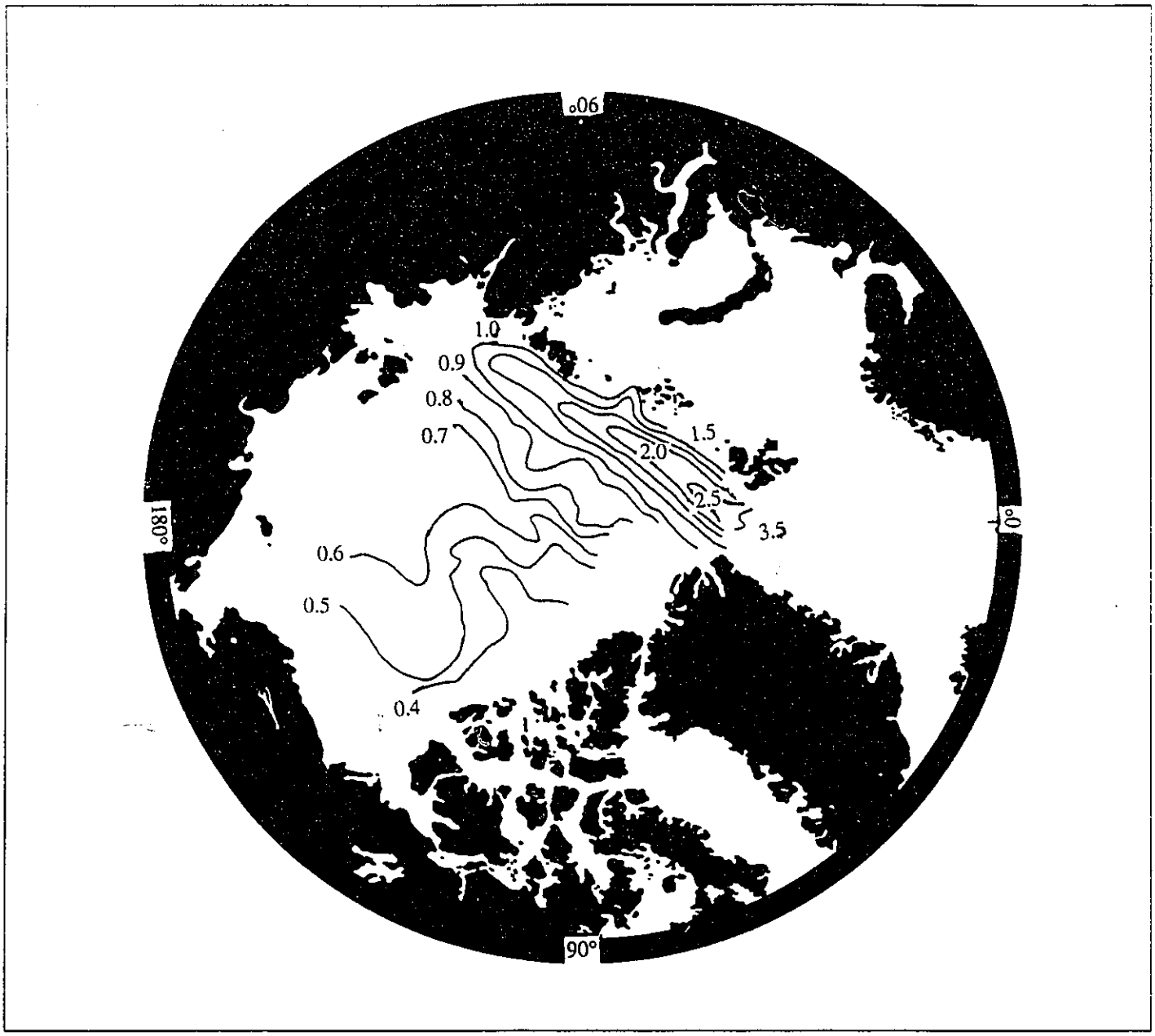

Figure 4.3 Temperature distribution (in degrees *C*) within the core of the Atlantic layer of the Arctic Basin (after Treshnikov (1977)).

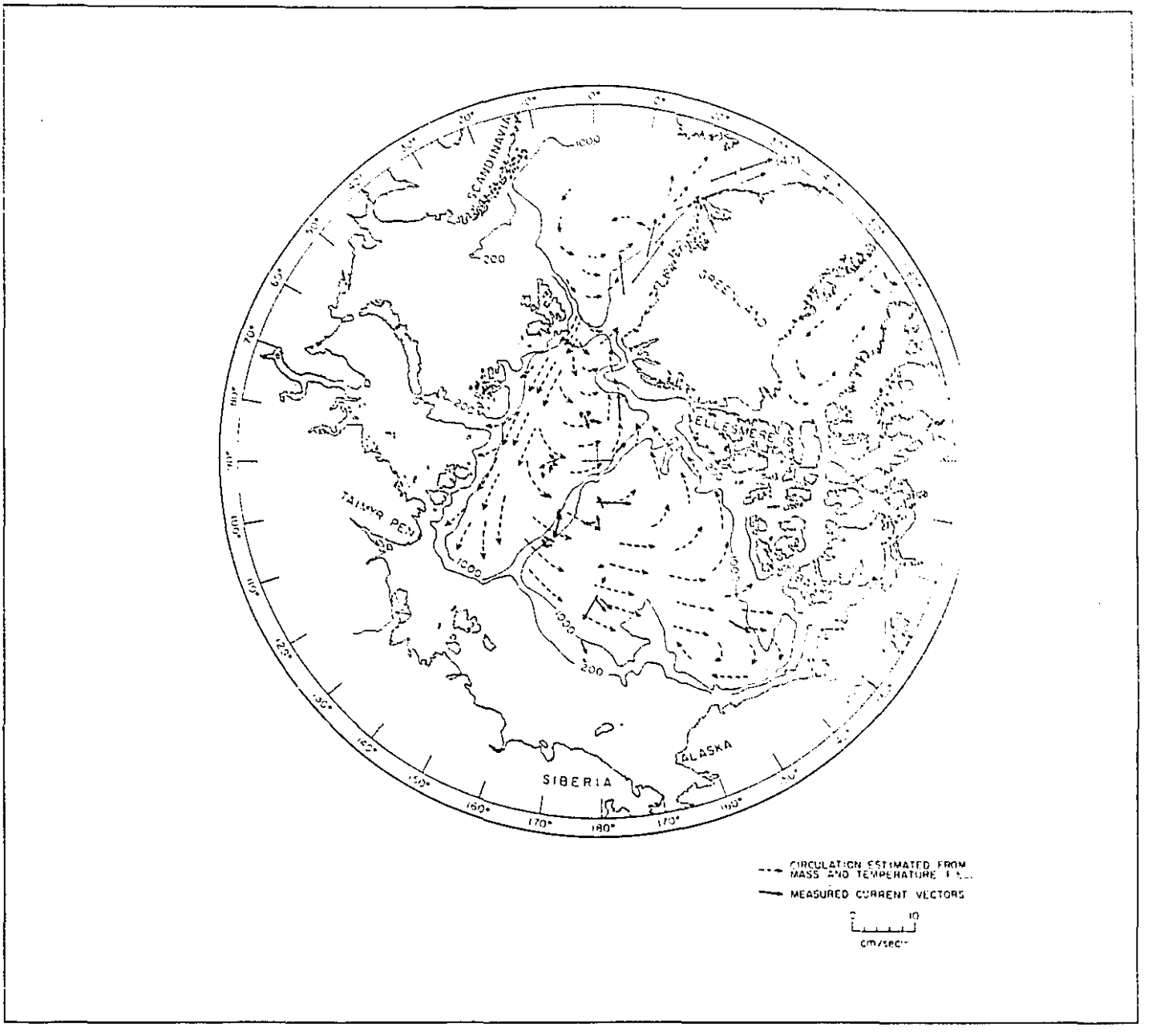

Figure 4.4 Circulation of Atlantic water in the Arctic Ocean, as inferred from temperature and salinity profiles supplemented by directly measured currents, indicated by solid arrows (after Coachman (1963)).

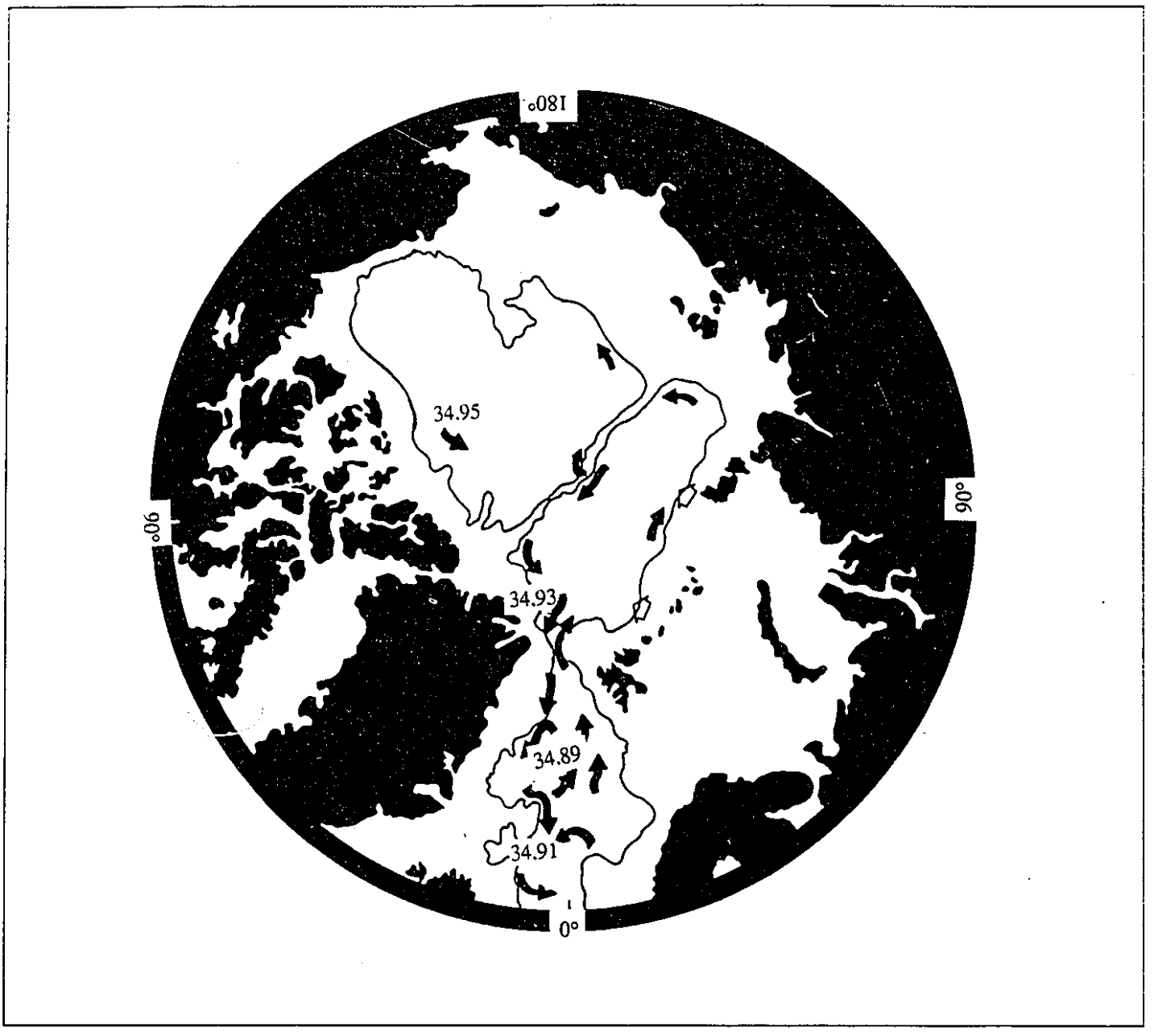

Figure 4.5 Abyssal salinities and supposed interbasin exchange in the Arctic Ocean (after Carmack (1990)).

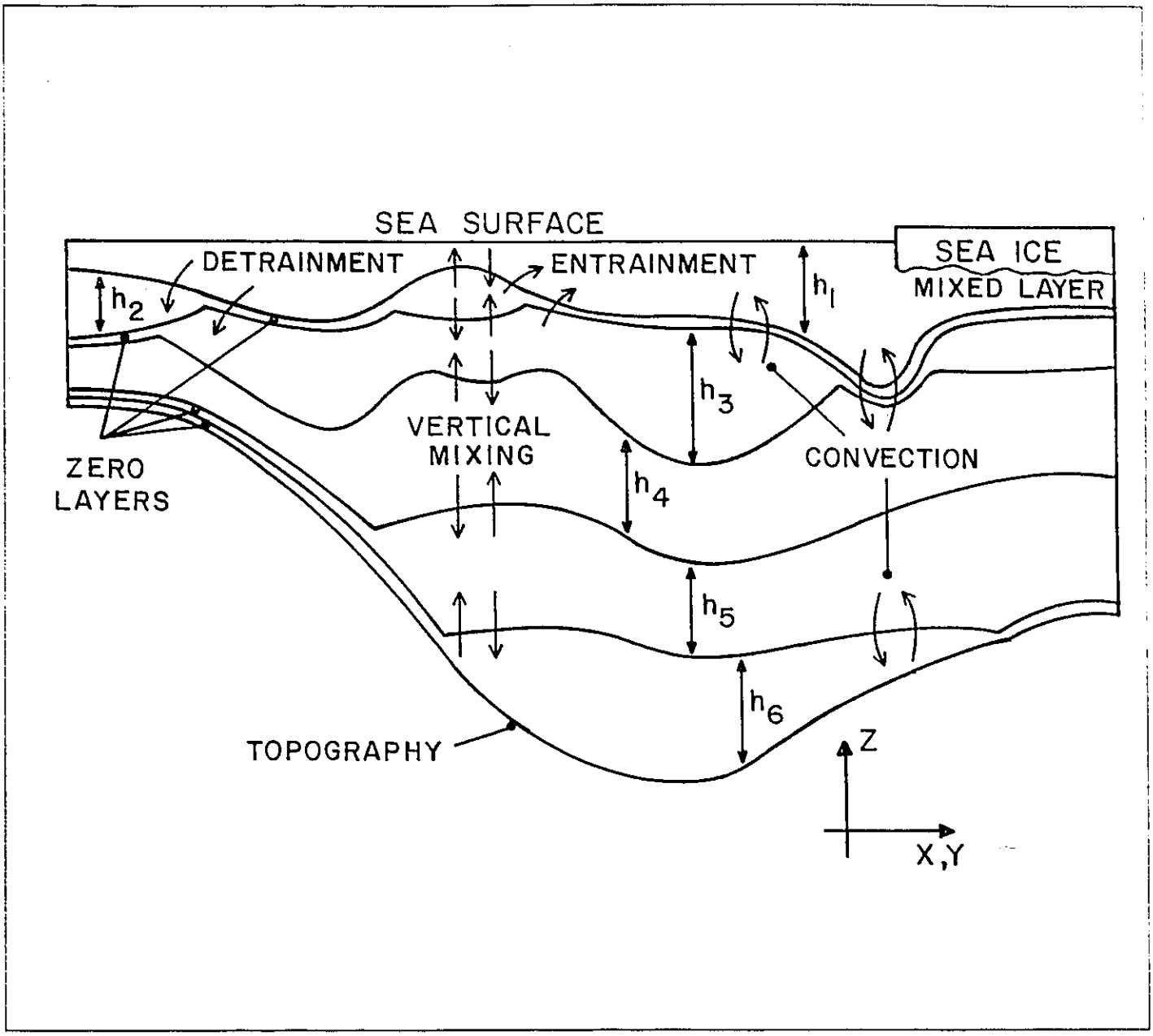

Figure 4.6 Vertical cross section of the layer thickness distribution. The mixed layer is the uppermost layer, lower layers are the isopycnal layers. Arrows indicate mass transfer rates representing various mixing parameterizations (from Oberhuber (1993a)).

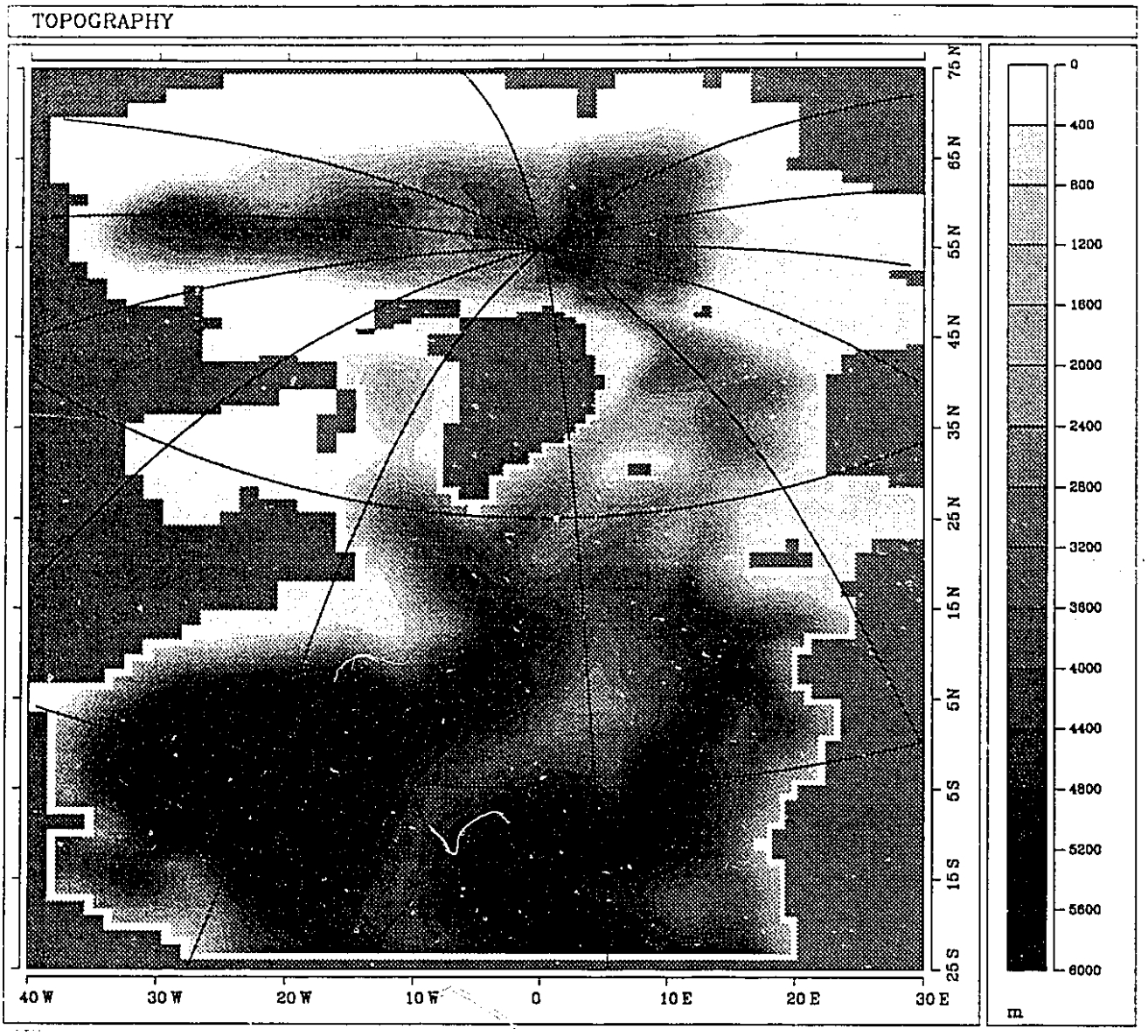

Figure 4.7 Bathymetry of model domain. The bathymetry resolves the Canadian Basin and the Eurasian Basin by the Lomonosov Ridge which runs from Siberia to Greenland as it passes beneath the North Pole. The Fram Strait sill has a depth of about 2500 *m*. The coordinate axes indicate latitude and longitude in the rotated coordinate system of the model domain. For reference, the true geographic coordinates are overlayed on the figure as thin lines.

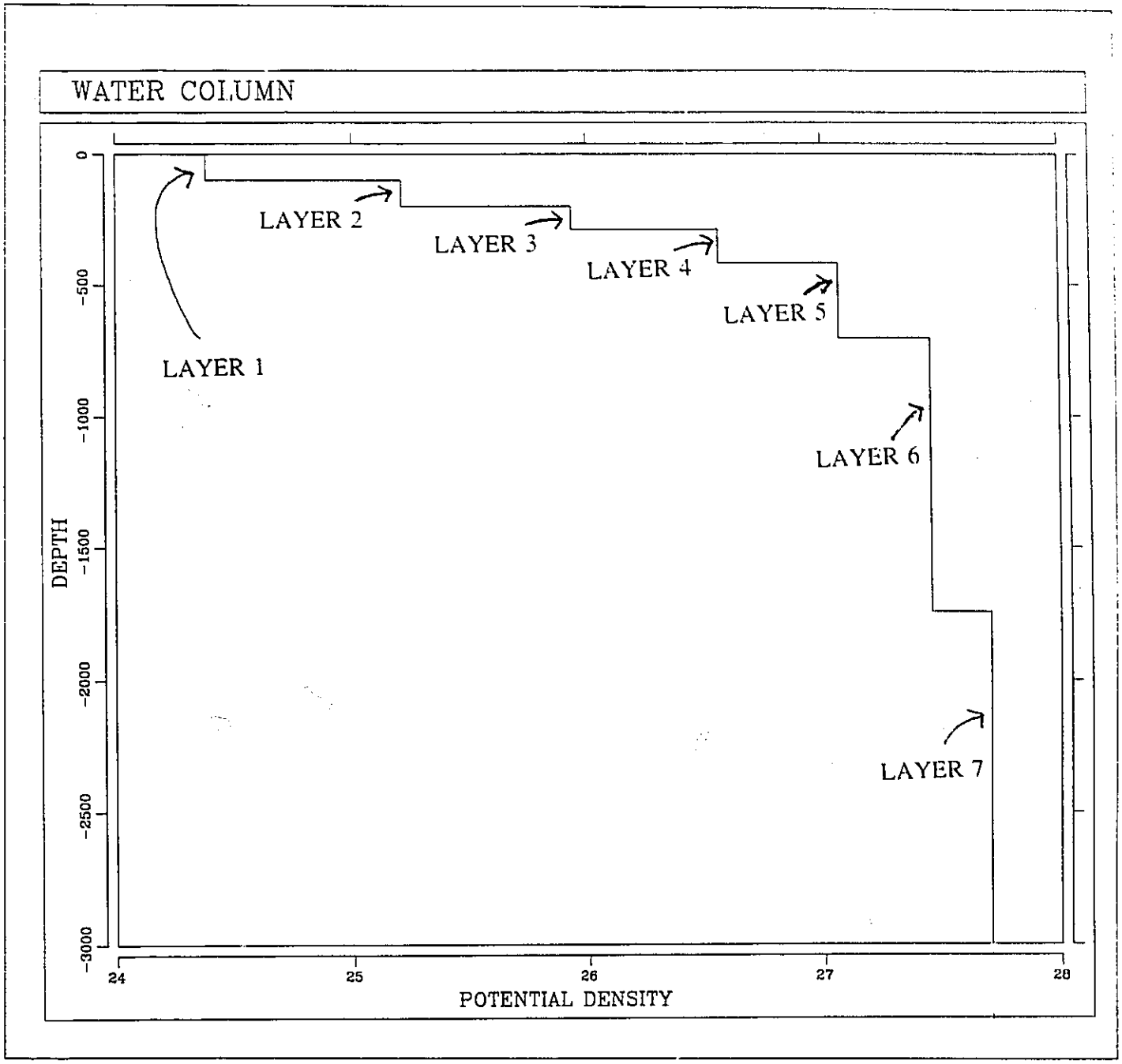

Figure 4.8 Discretization of the water column into seven isopycnal layers of varying thickness. The model is initialized with this prescribed distribution of layer thicknesses and densities everywhere. As the model integrates in time, the layer thickness distribution evolve freely while the potential densities remain fixed. Note that the vertical scale only shows the top 3000 *m* of the ocean.

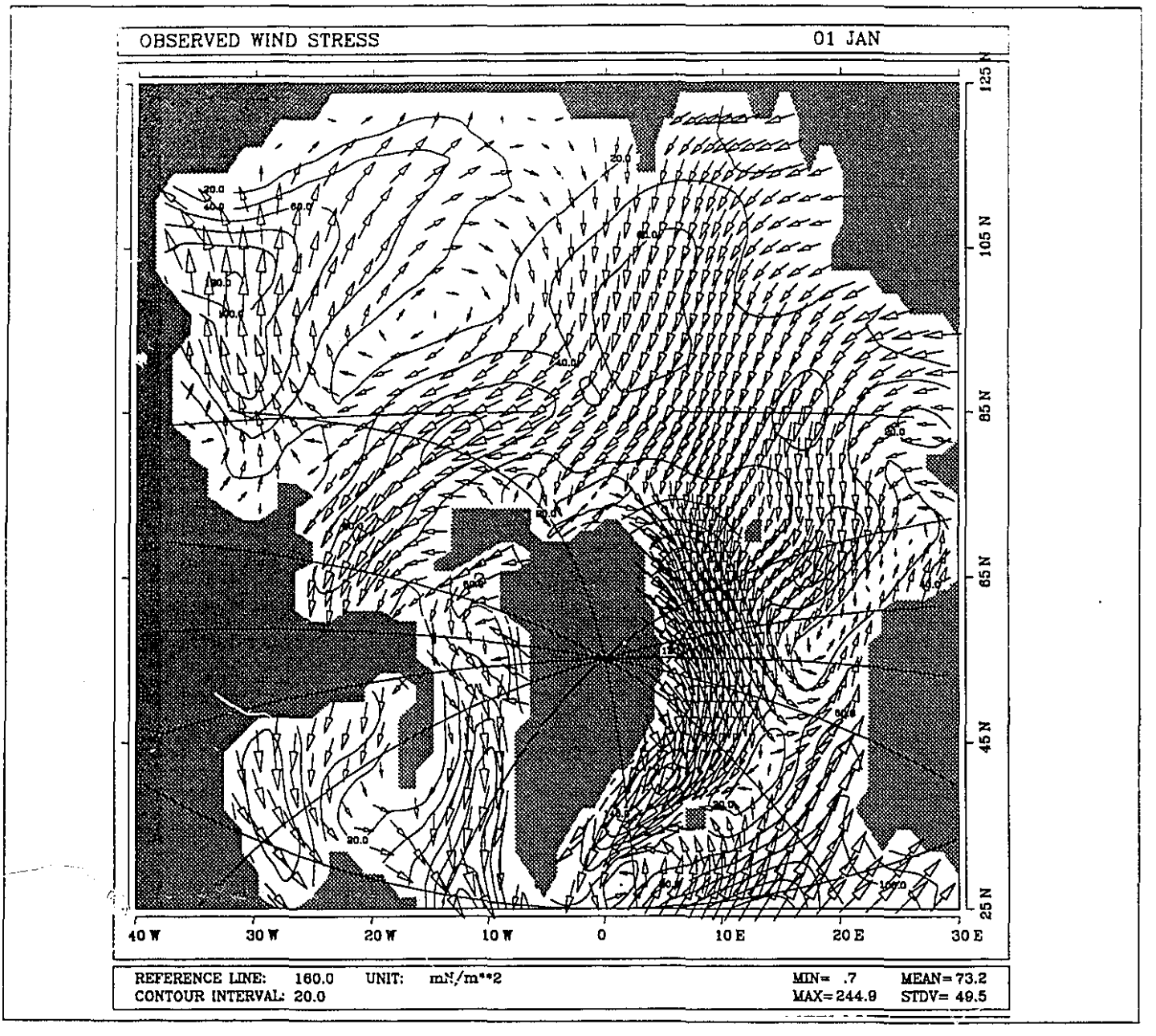

Figure 4.9 The wind stress (N/m^2) on January 1st. Only that part of the model domain covering the Arctic Ocean and the GIN Sea is shown. A large-scale anticyclonic gyre is evident over the Arctic Basin. As well, there is a strong flow directed across the Eurasian Basin towards Fram Strait. The density of the nested grid is evident in the GIN Sea.

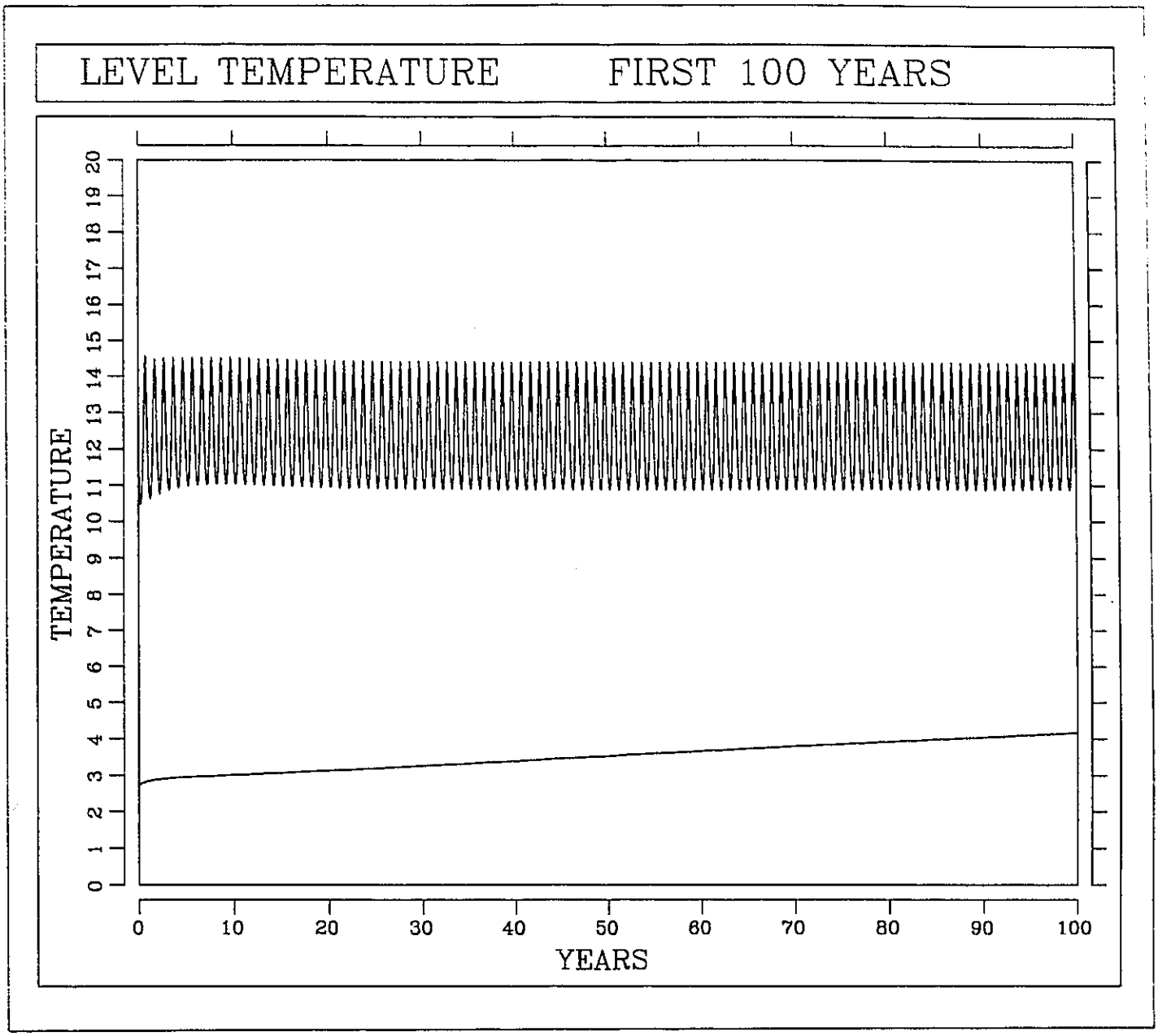

Figure 4.10a Time series of two horizontally averaged temperatures for the entire model domain for the first 100 years of the model spinup. The wigly curve indicates the sea surface temperature while the gently sloping line indicates the deep ocean temperature.

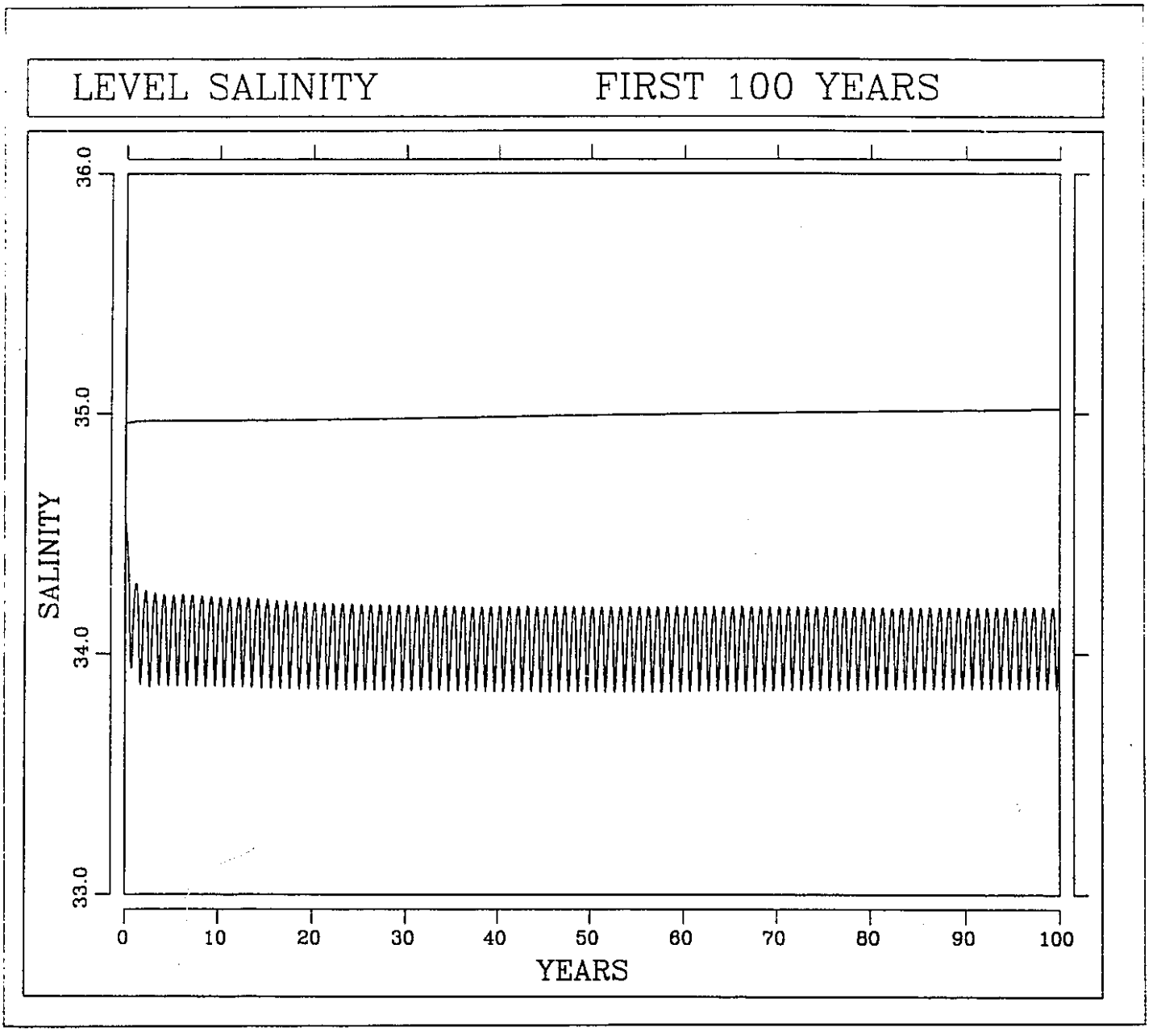

Figure 4.10b Time series of two horizontally averaged salinities for the entire model domain for the first 100 years of the model spinup. The wigly curve indicates the sea surface salinity while the gently sloping line indicates the deep ocean salinity.

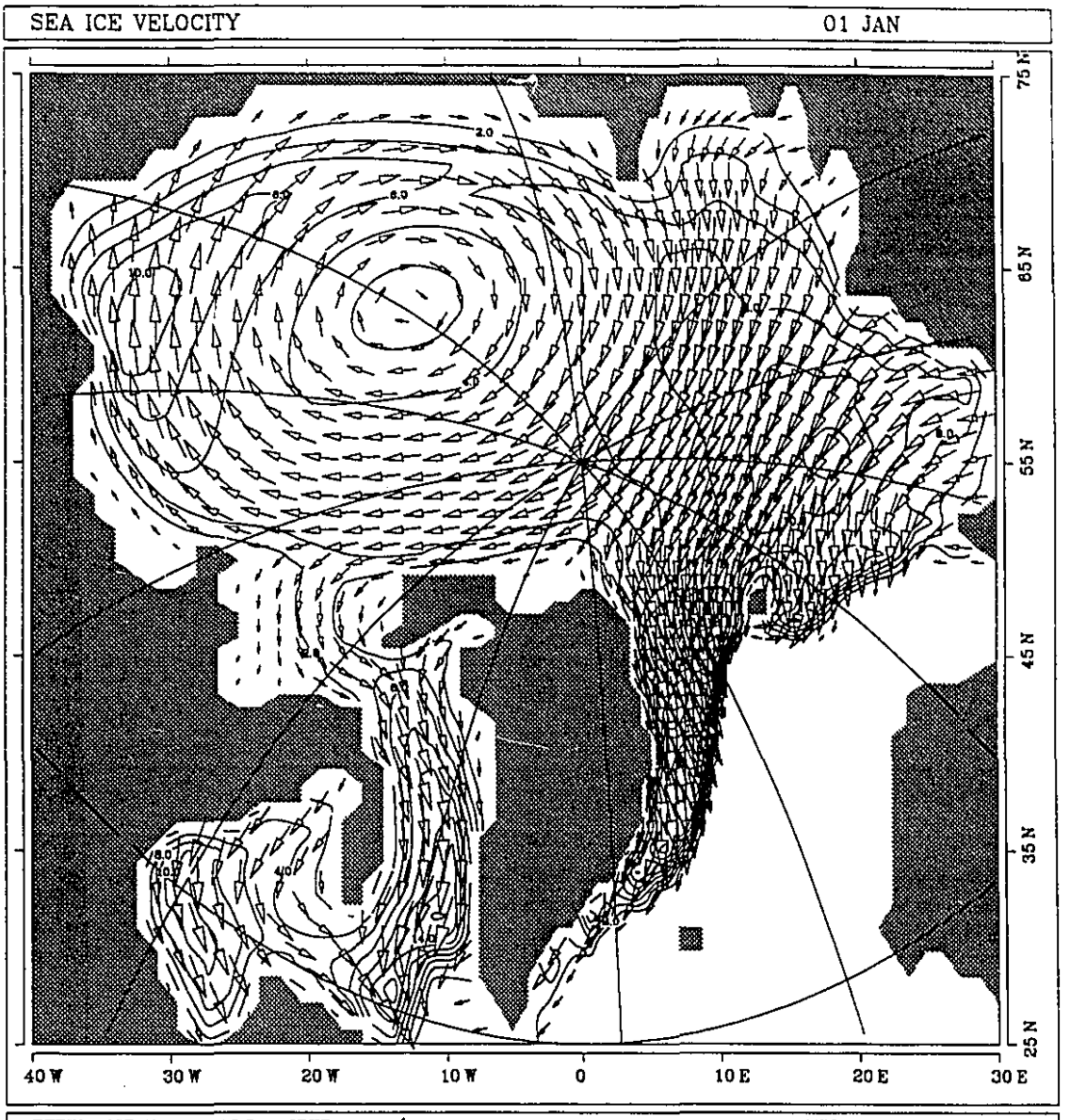

Figure 4.11a Sea-ice velocity field for January 1st. The greatest velocities are noted in the East Greenland current and just North of Bering Strait, which is also as observed from buoy data from Colony (1991).

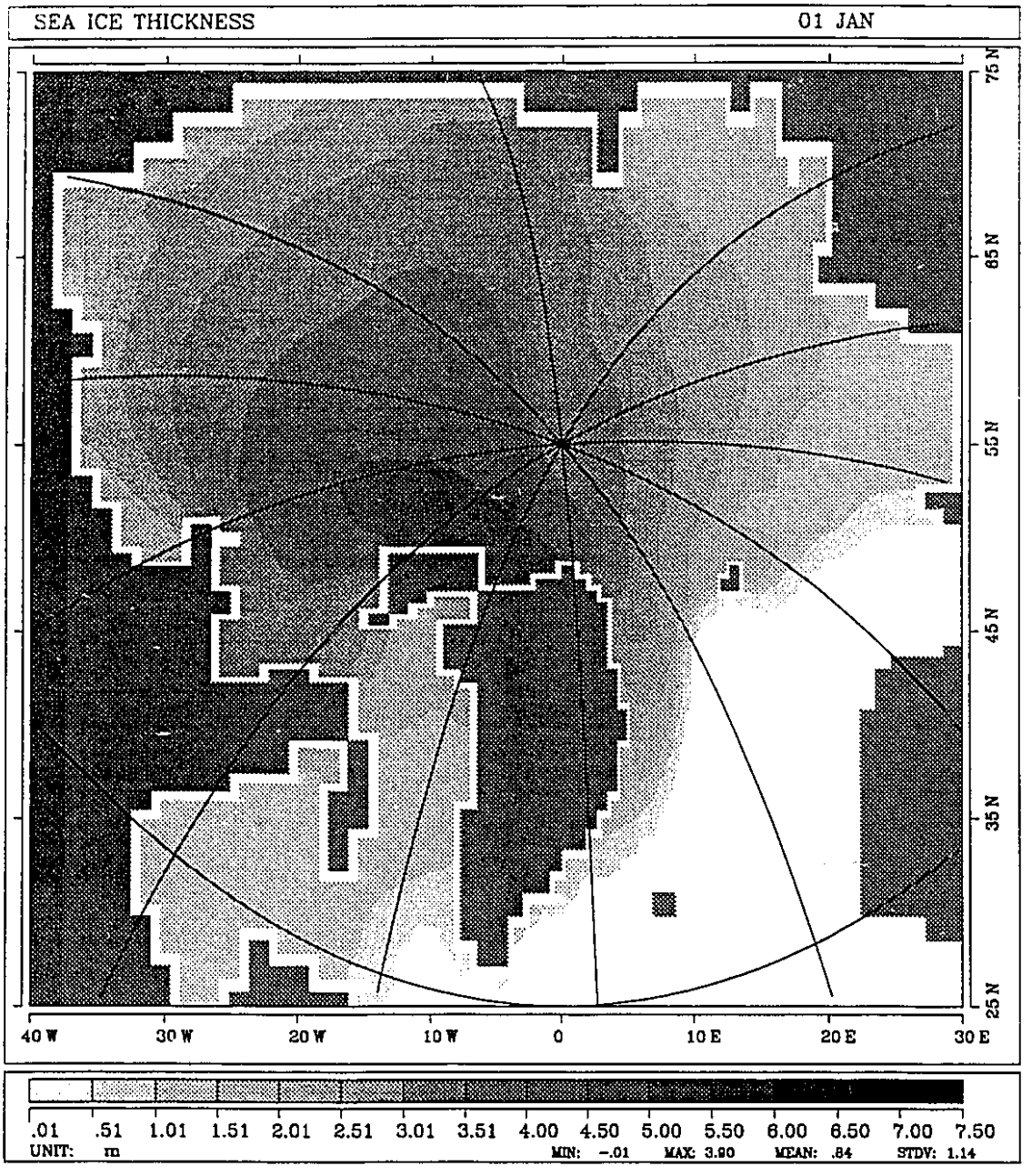

Figure 4.11b Sea-ice thickness field for January 1st. The ice-edge position in the Greenland Sea is reasonable as is the occurrence of the thickest ice along the North Coast of Greenland and along the Canadian Arctic Archipelago.

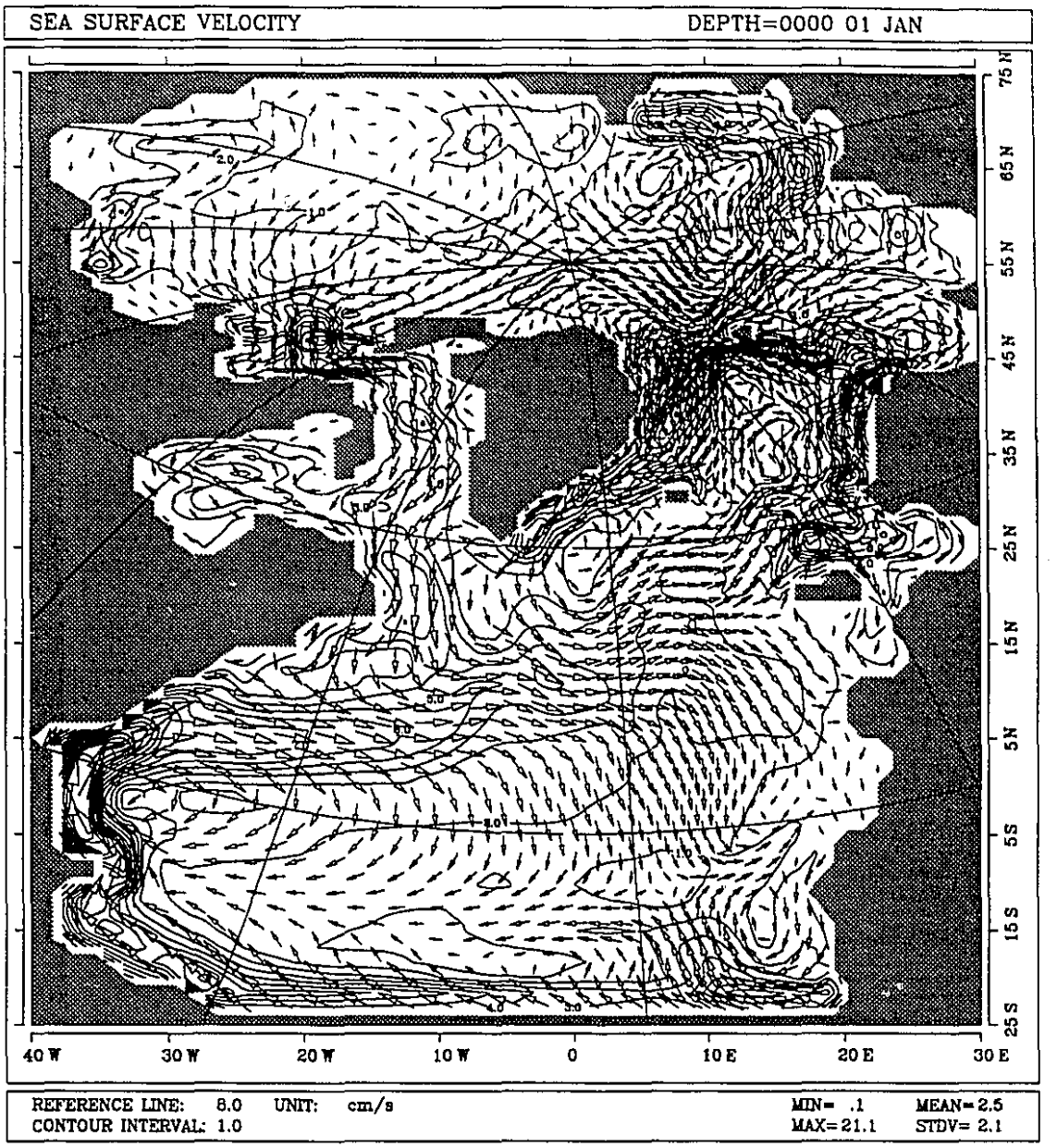

Figure 4.12a Sea-surface velocity field for January 1st. There is an excessive flow through the Canadian Arctic Archipelago possibly due to a too large artificial channel constructed there.

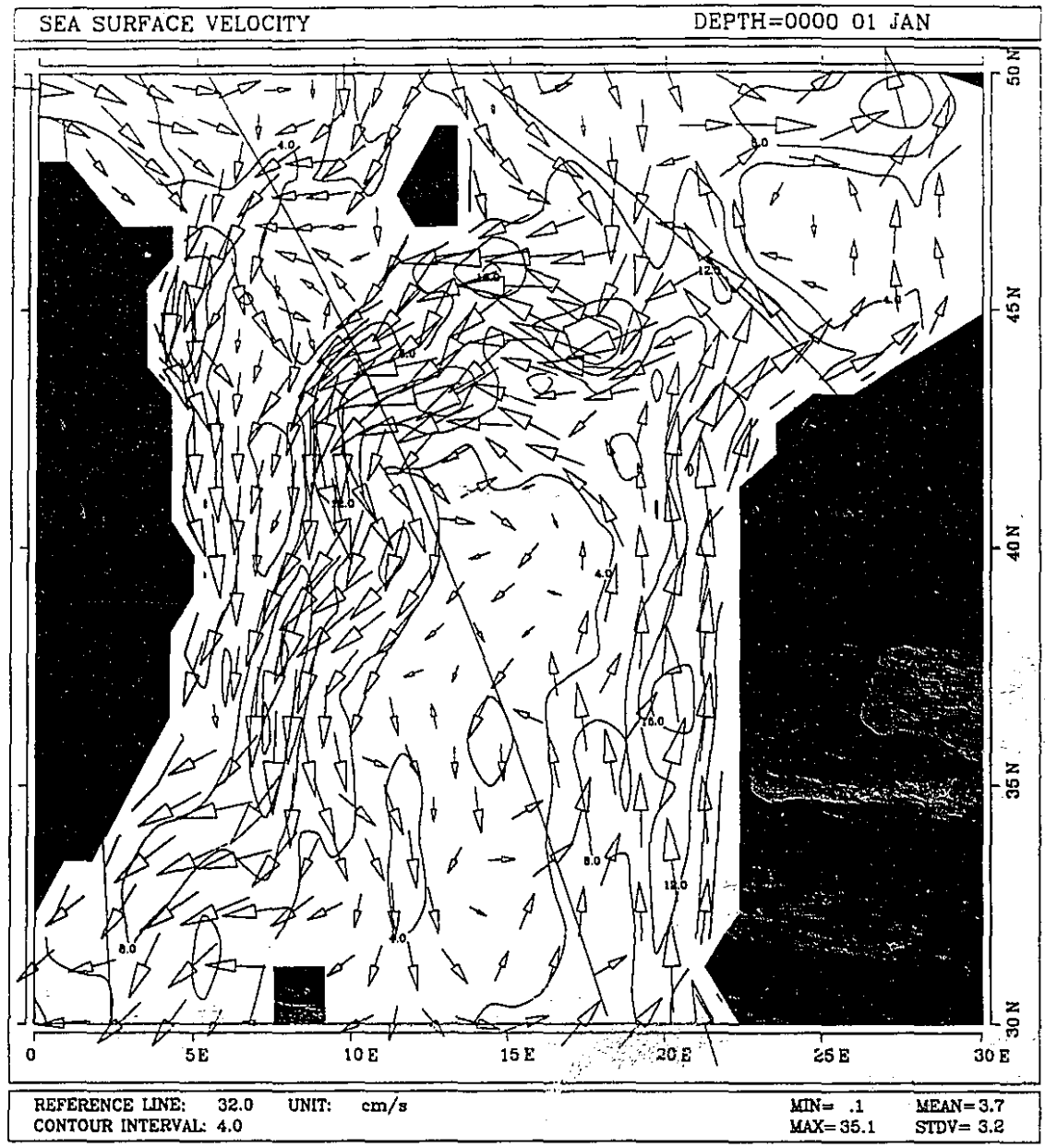

Figure 4.12b Sea-surface velocity field for January 1st as in the previous figure; however, this figure shows in detail the surface circulation in the GIN Sea.

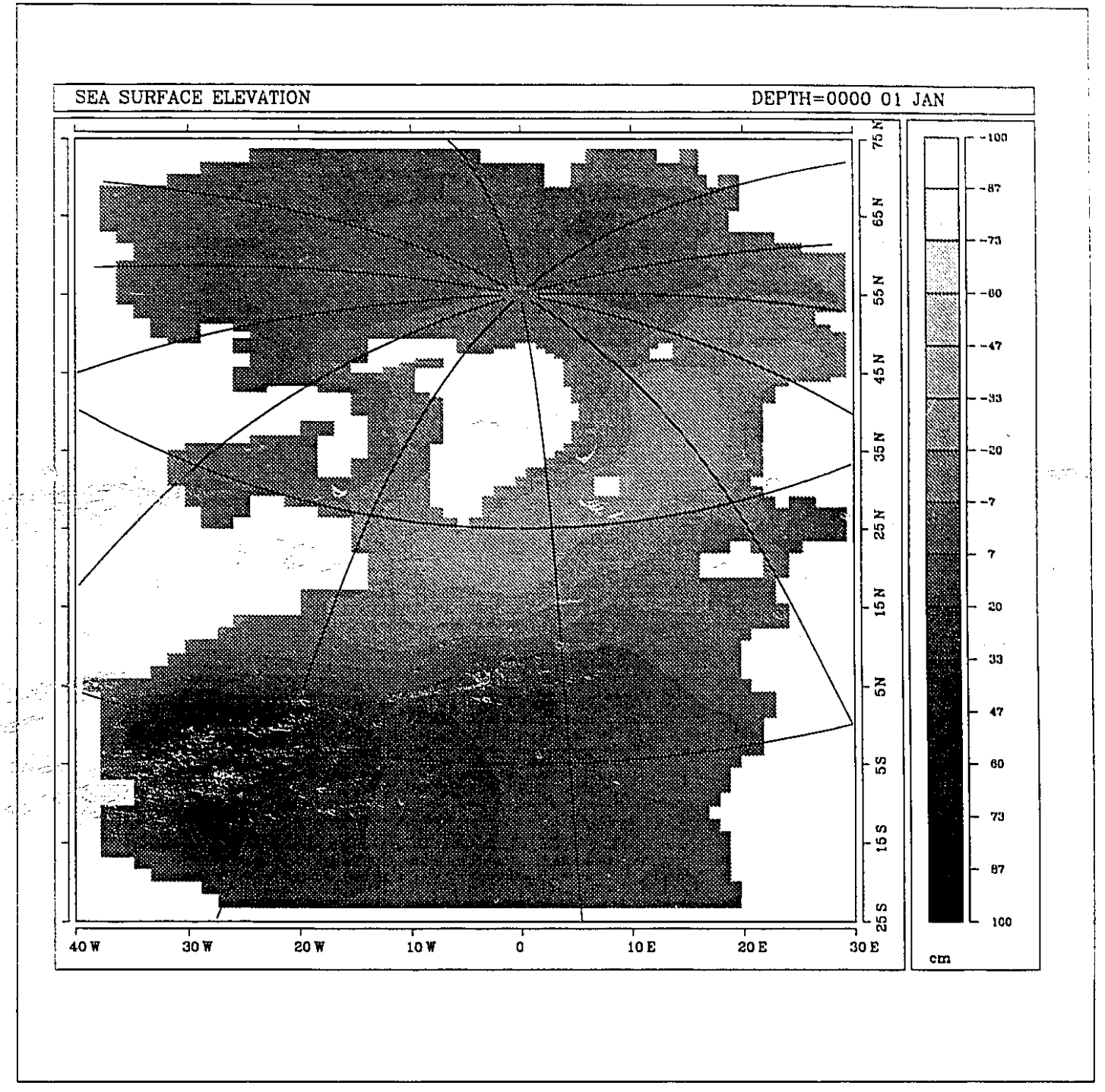

Figure 4.12c Sea-Surface elevation field for January 1st. The white areas represent land. The highest elevation occurs over the Gulf Stream and the lowest occurs in the GIN Sea. Over the Canadian Basin of the Arctic there is a slight elevation in the sea surface.

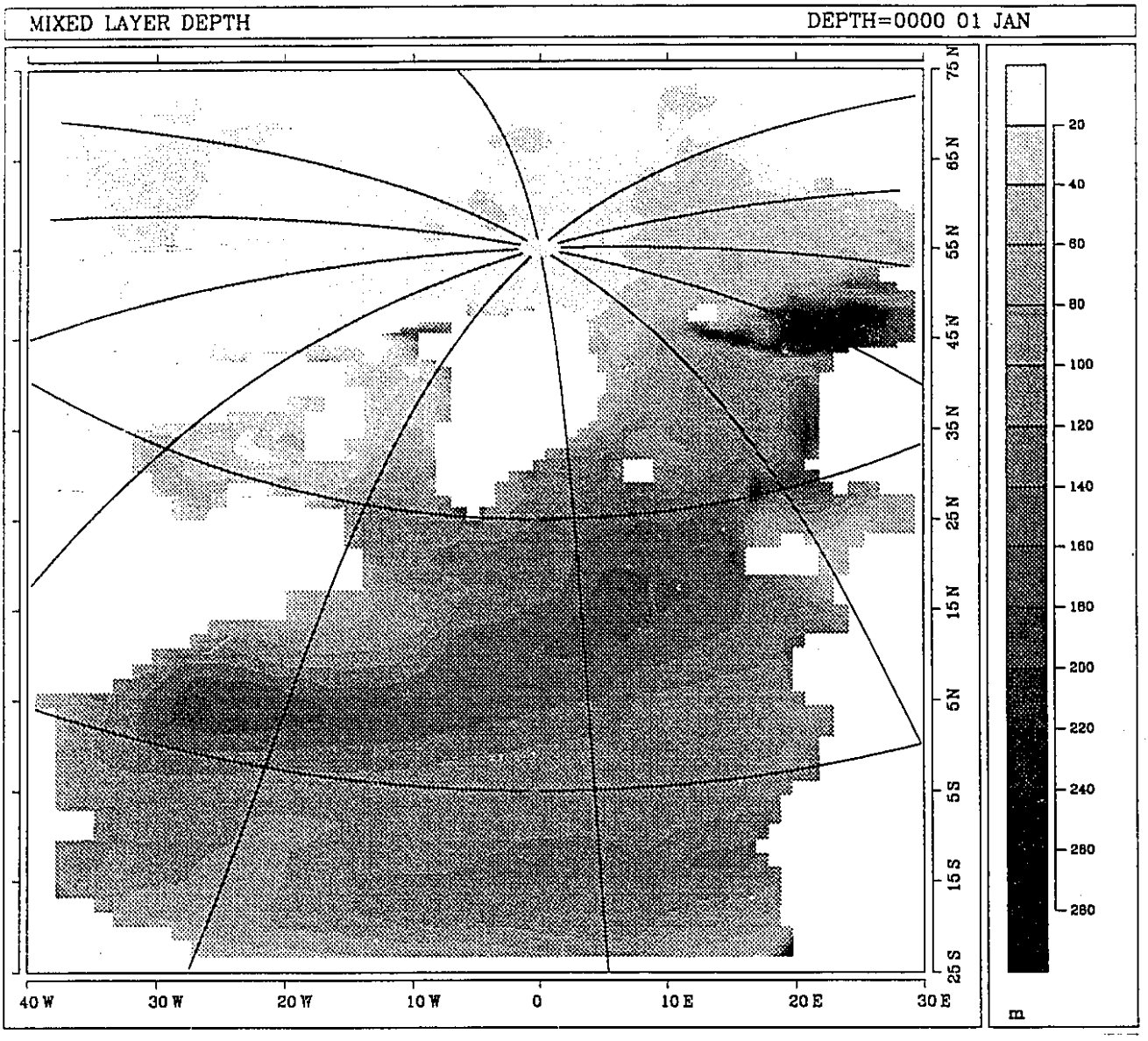

Figure 4.12d Mixed-layer depth distribution for January 1st. The white areas represent land. The mixed-layer is deepest along the border between the Barents Sea and the Norwegian Sea.

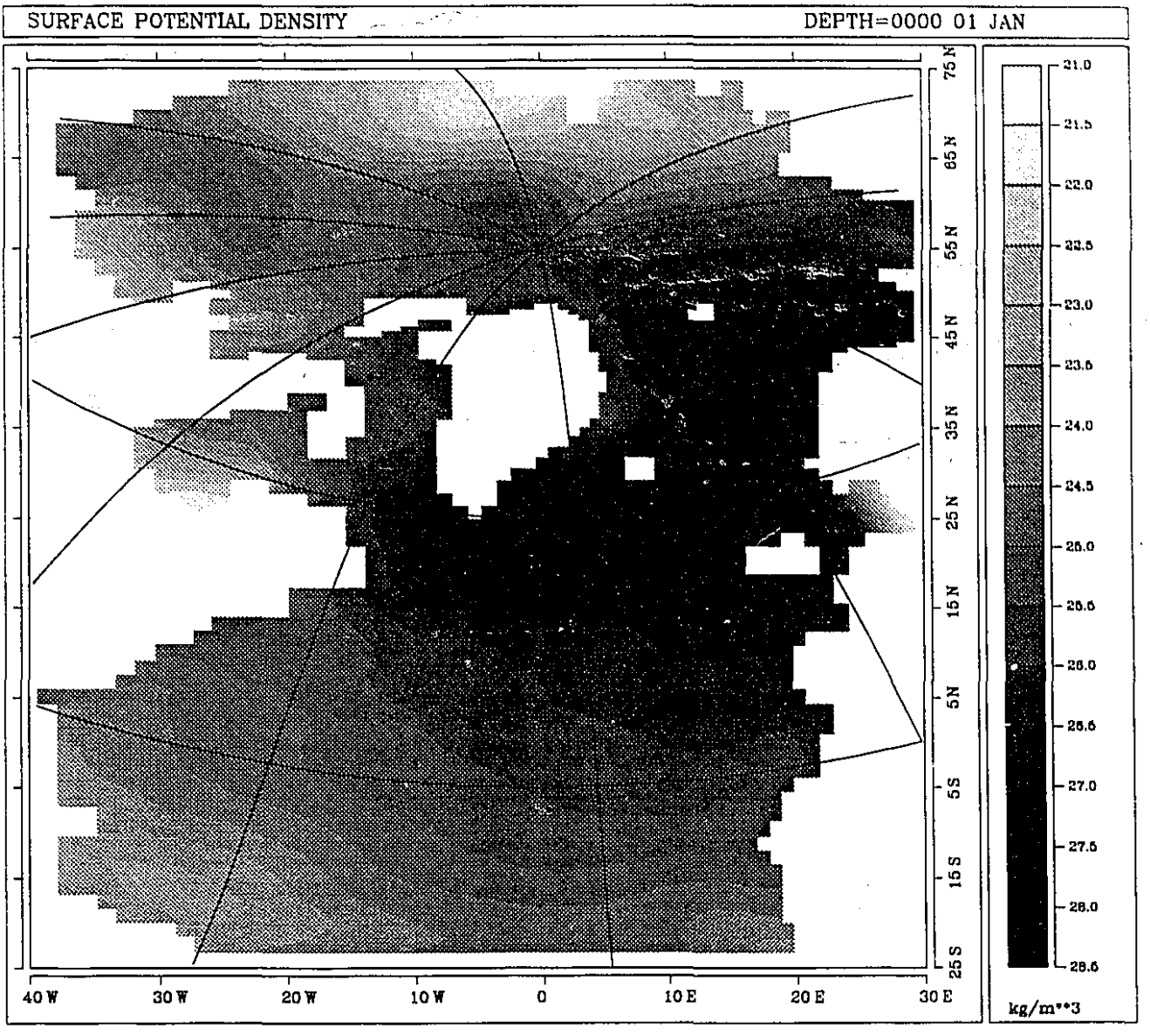

Figure 4.12e Sea-Surface potential density field for January 1st. The white areas represent land. The surface potential density is relatively large in the GIN Sea as compared to all other parts of the domain.

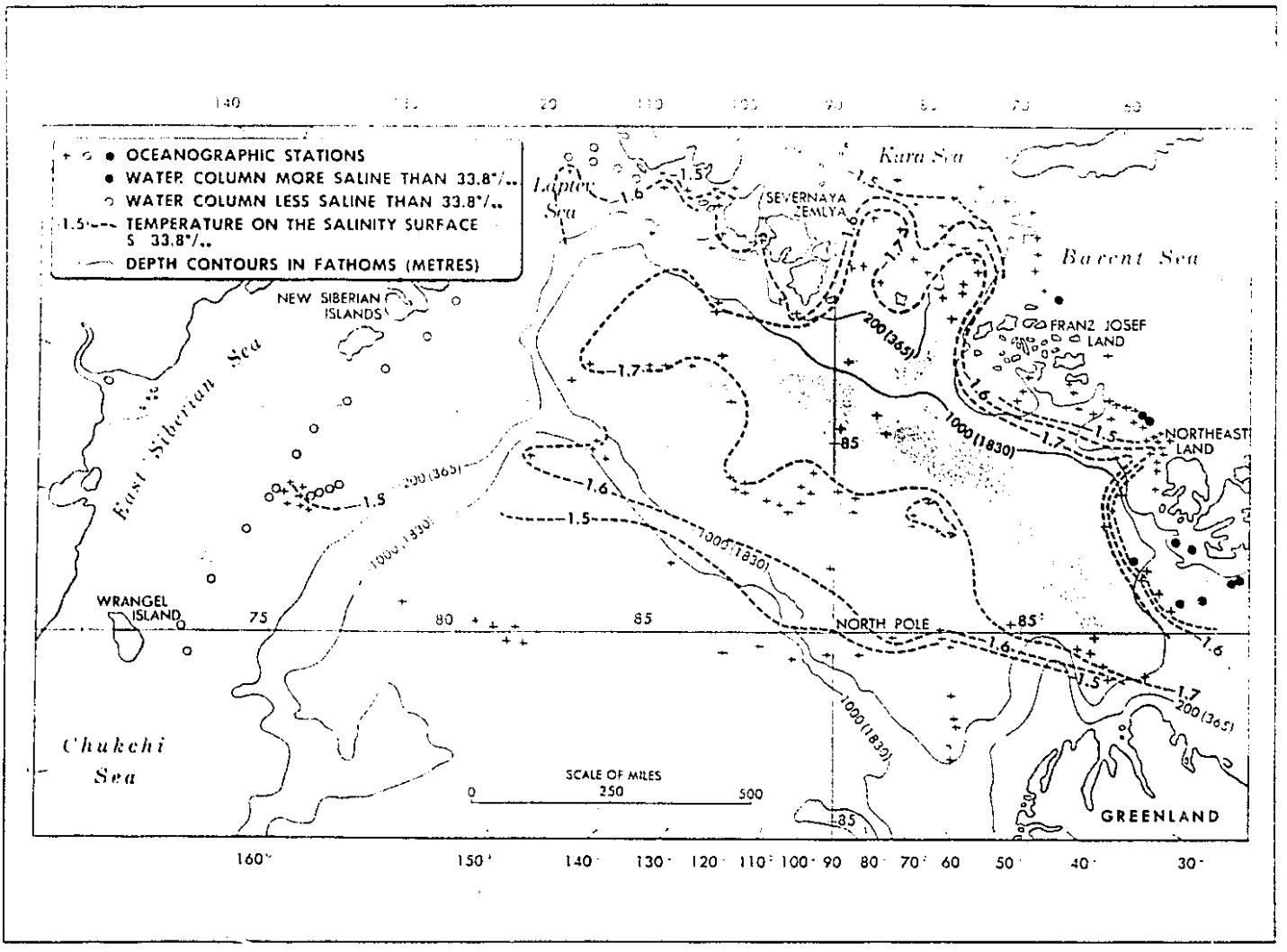

Figure 4.13a Observed temperature on the salinity surface 33.8 *psu*, which is about 100 *m* below the sea surface. Clearly evident is a pool of relatively cold (*i.e.* less than -1.7 degrees) water over the Eurasian Basin (from Coachman & Barnes, 1962).

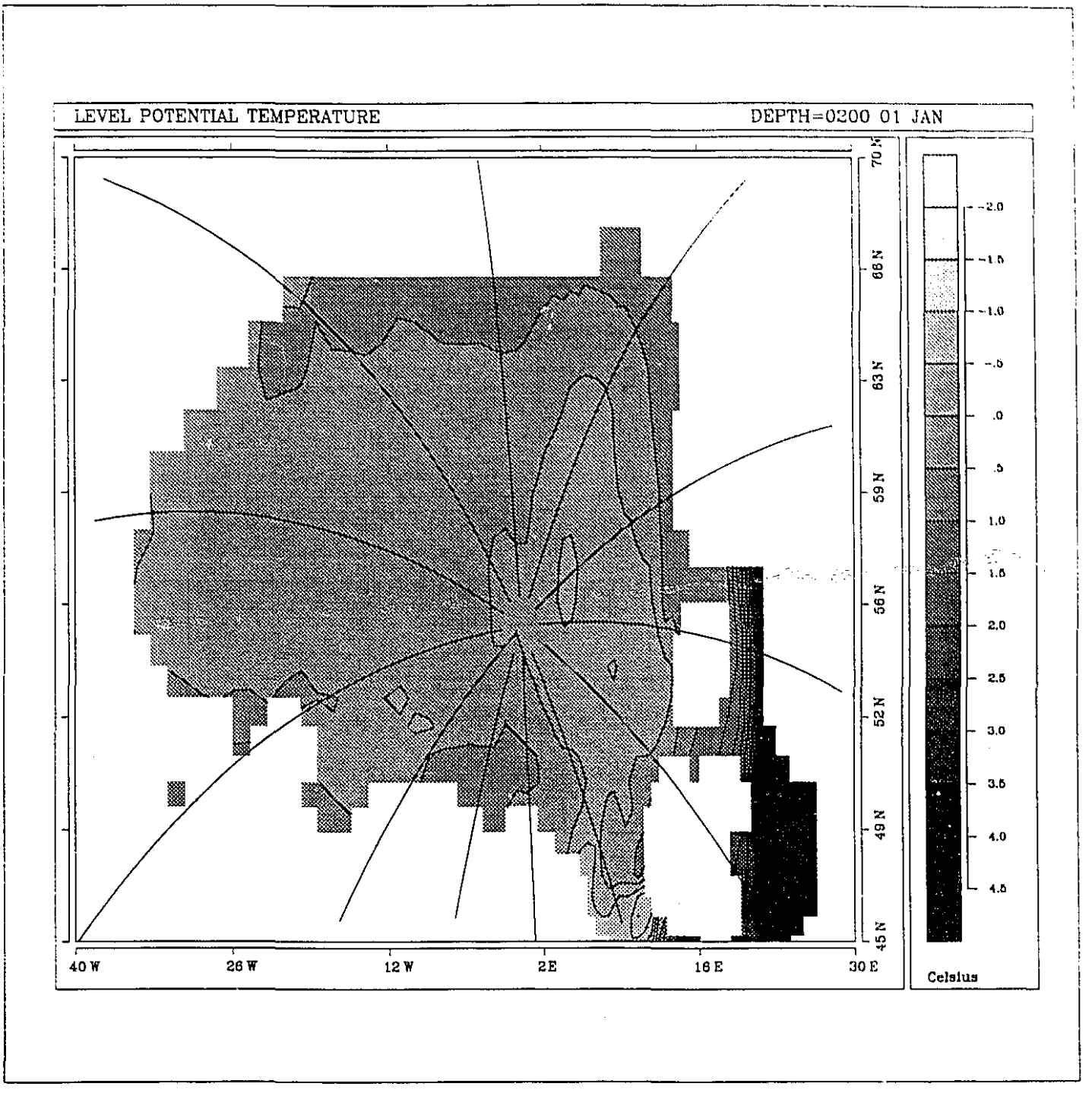

Figure 4.13b Sub-surface potential temperature field for January 1st. The white areas represent land. There is a cold pool at a temperature of -1.5 over the Eurasian Basin.

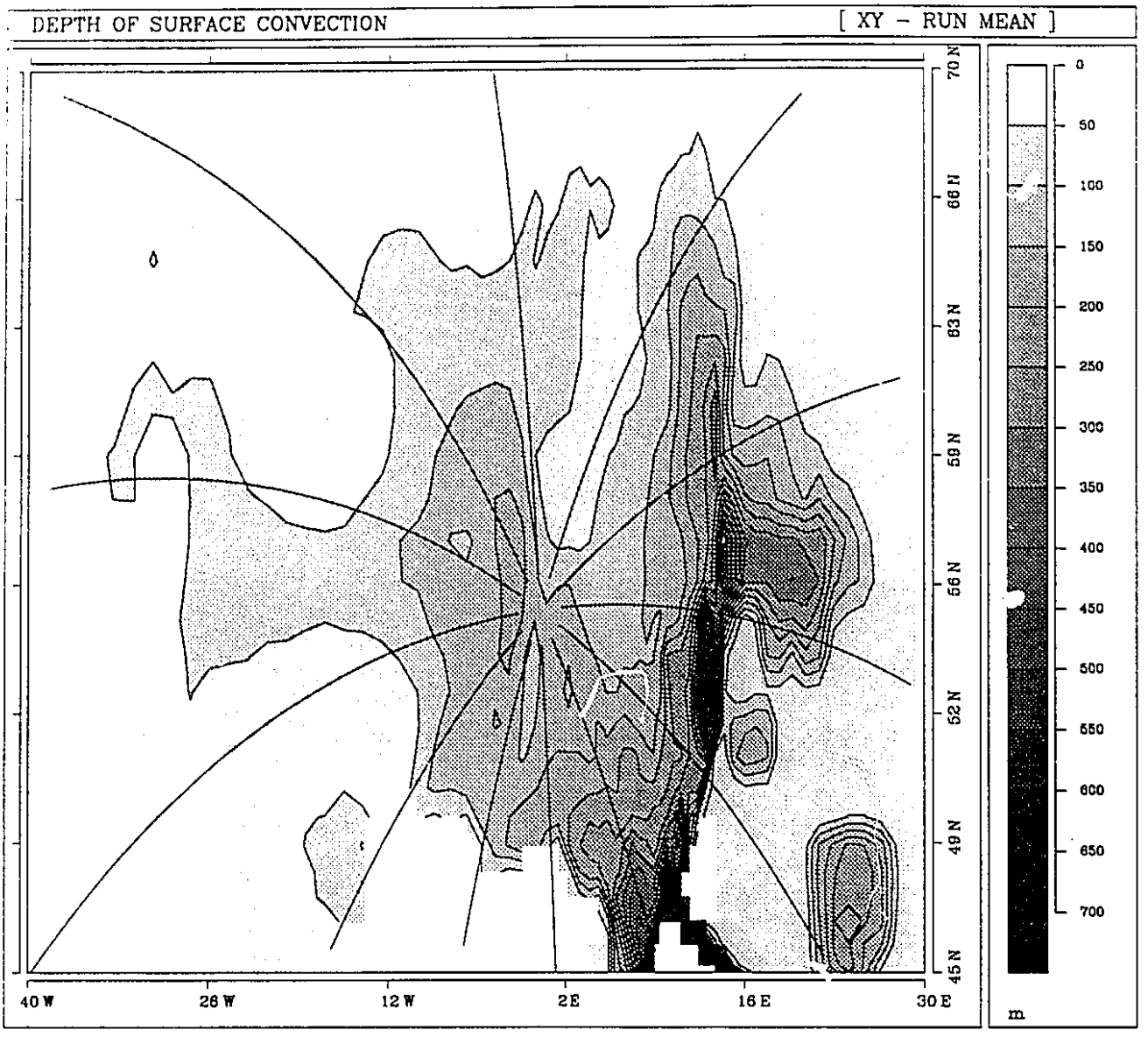

Figure 4.13c Depth of surface convection averaged over a 100 year model run. The white areas represent land. Convection occurs along the continental shelf edge of the Barents Sea.

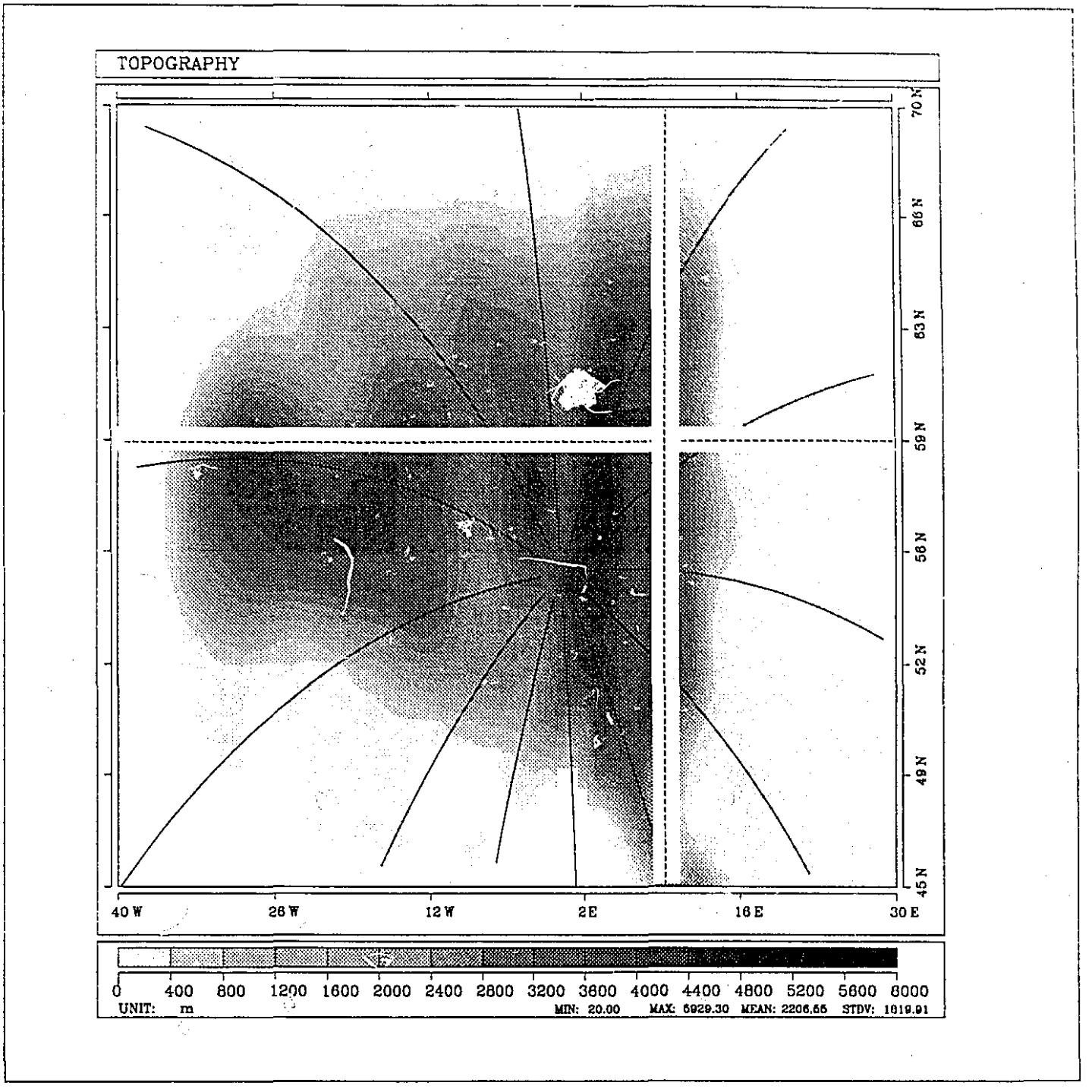

Figure 4.13d Topography of Arctic Ocean only. The thin dashed line running north-south at a longitude of 8 degrees East is the position of a two-dimensional model transect discussed in the text. Similarly, the thin dashed line running in an east-west direction and located at a latitude of 59 degrees North is also the position of a two-dimensional model transect which is discussed in the text.

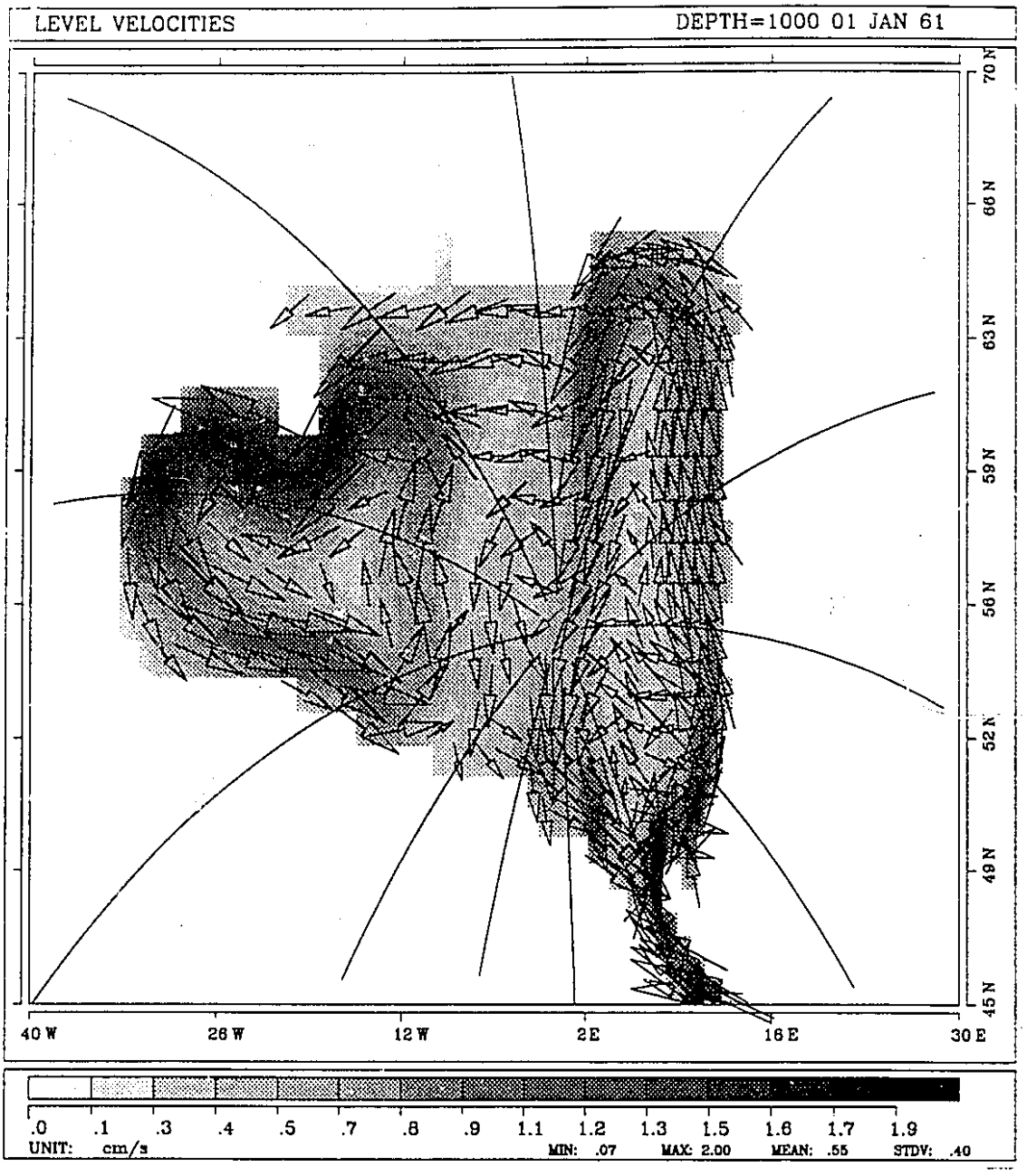

Figure 4.14a Velocity field at 1000 m depth over the Arctic Ocean on January 1st. The white area indicates land.

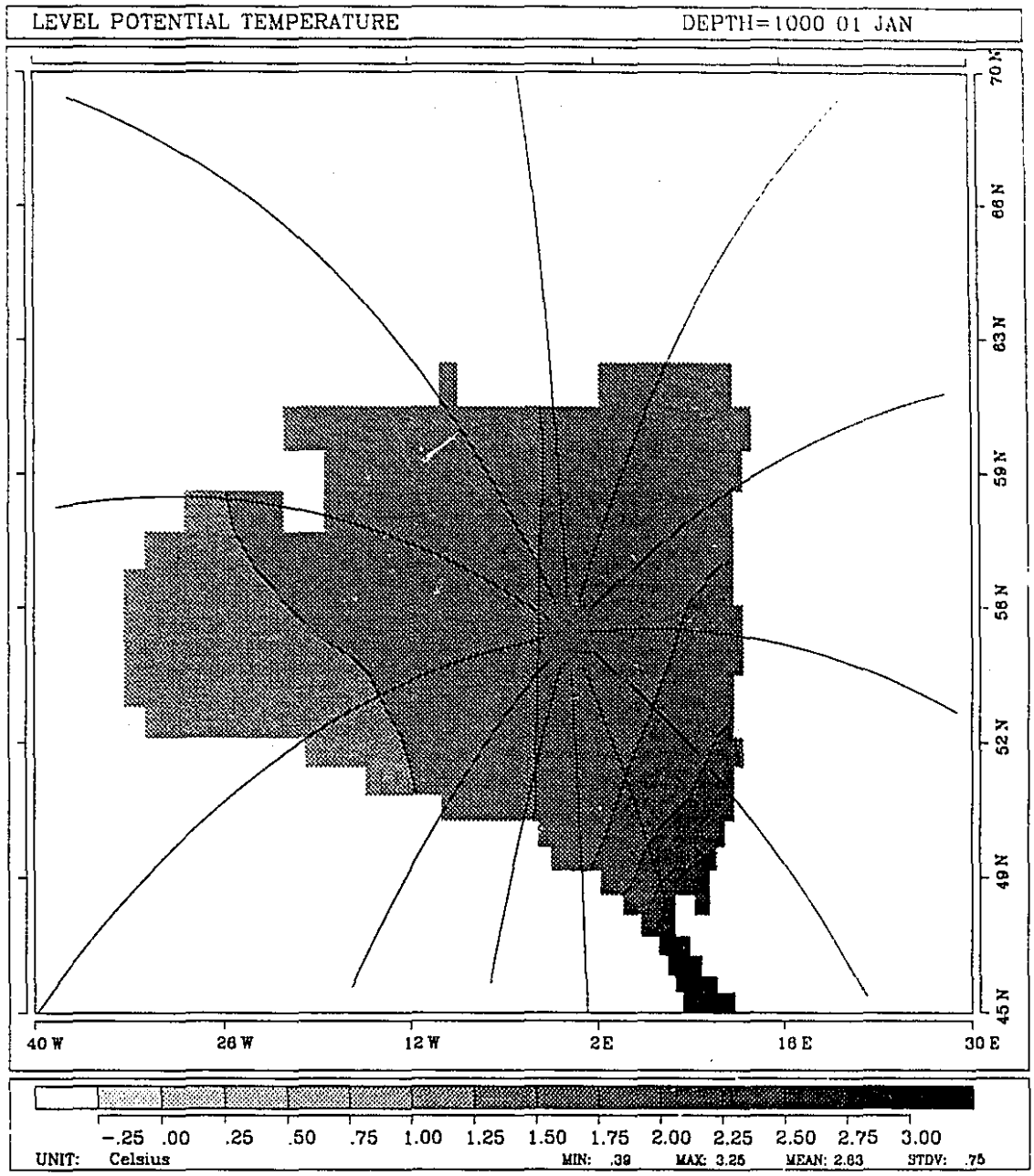

Figure 4.14b Temperature field at 1000 m depth in the Arctic Ocean on January 1st. The white area indicates land.

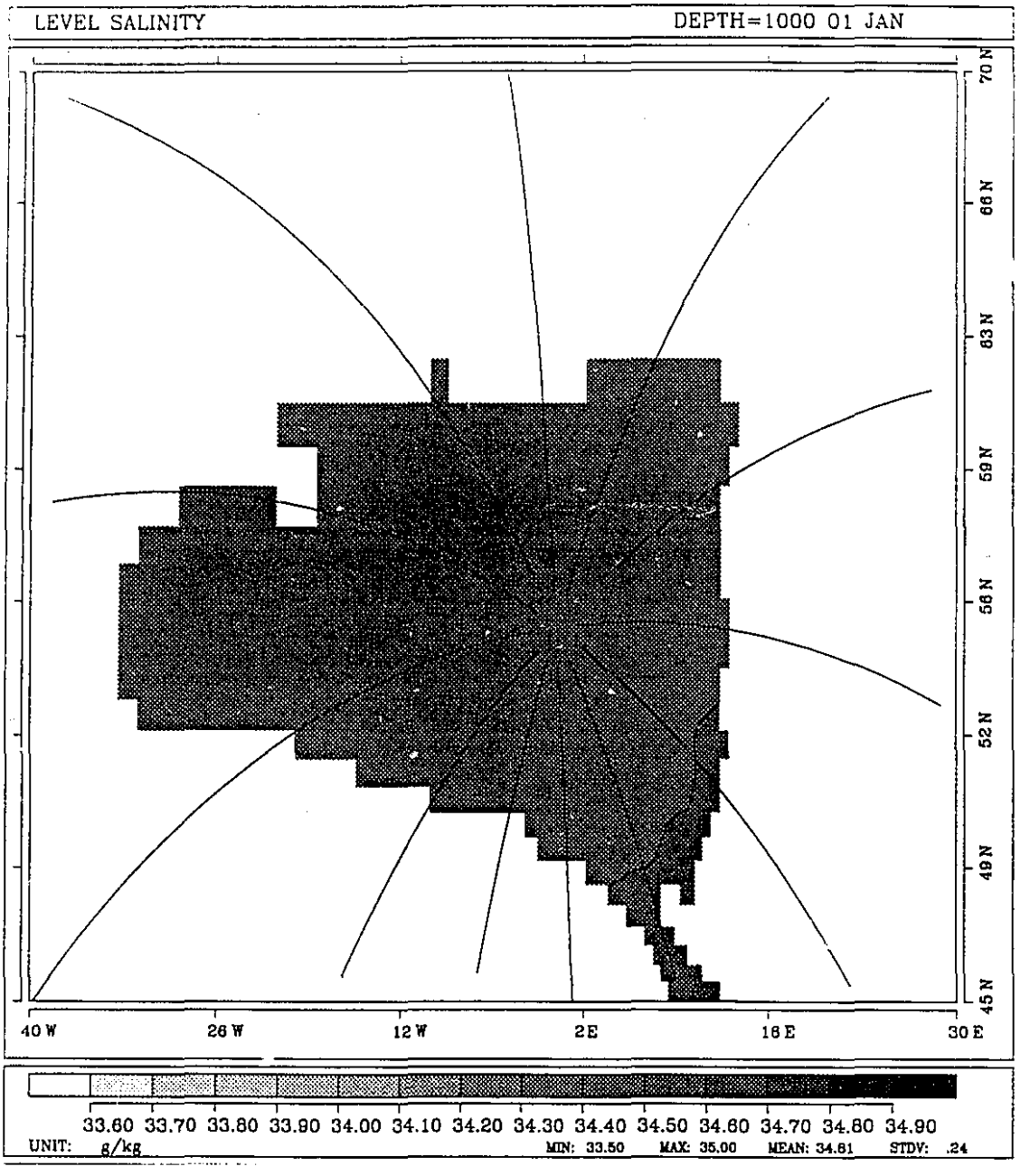

Figure 4.14c Salinity field at 1000 m depth in the Arctic Ocean on January 1st. The white area indicates land.

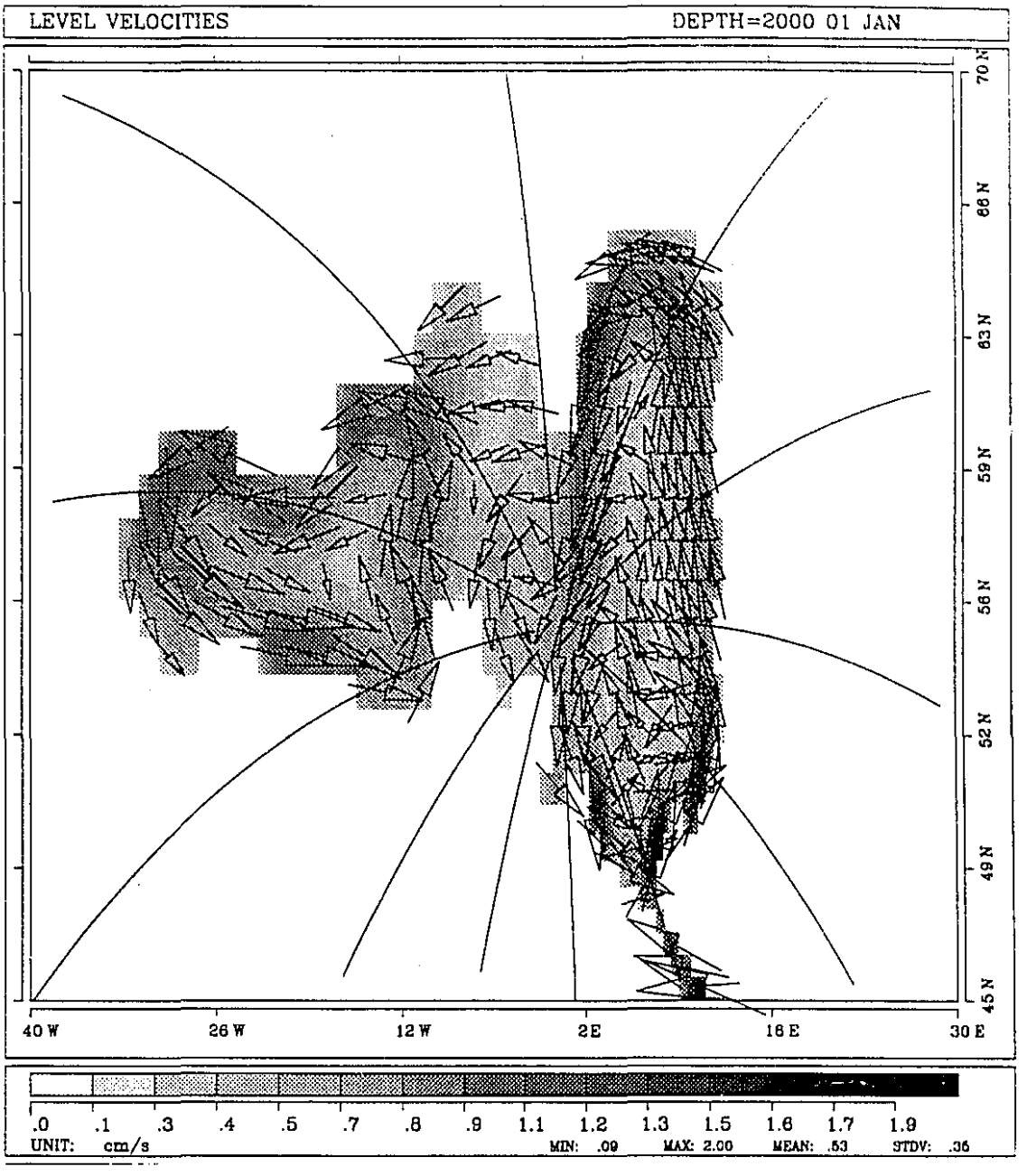

Figure 4.15a Velocity field at 2000 m depth in the Arctic Ocean on January 1st. The white area indicates land.

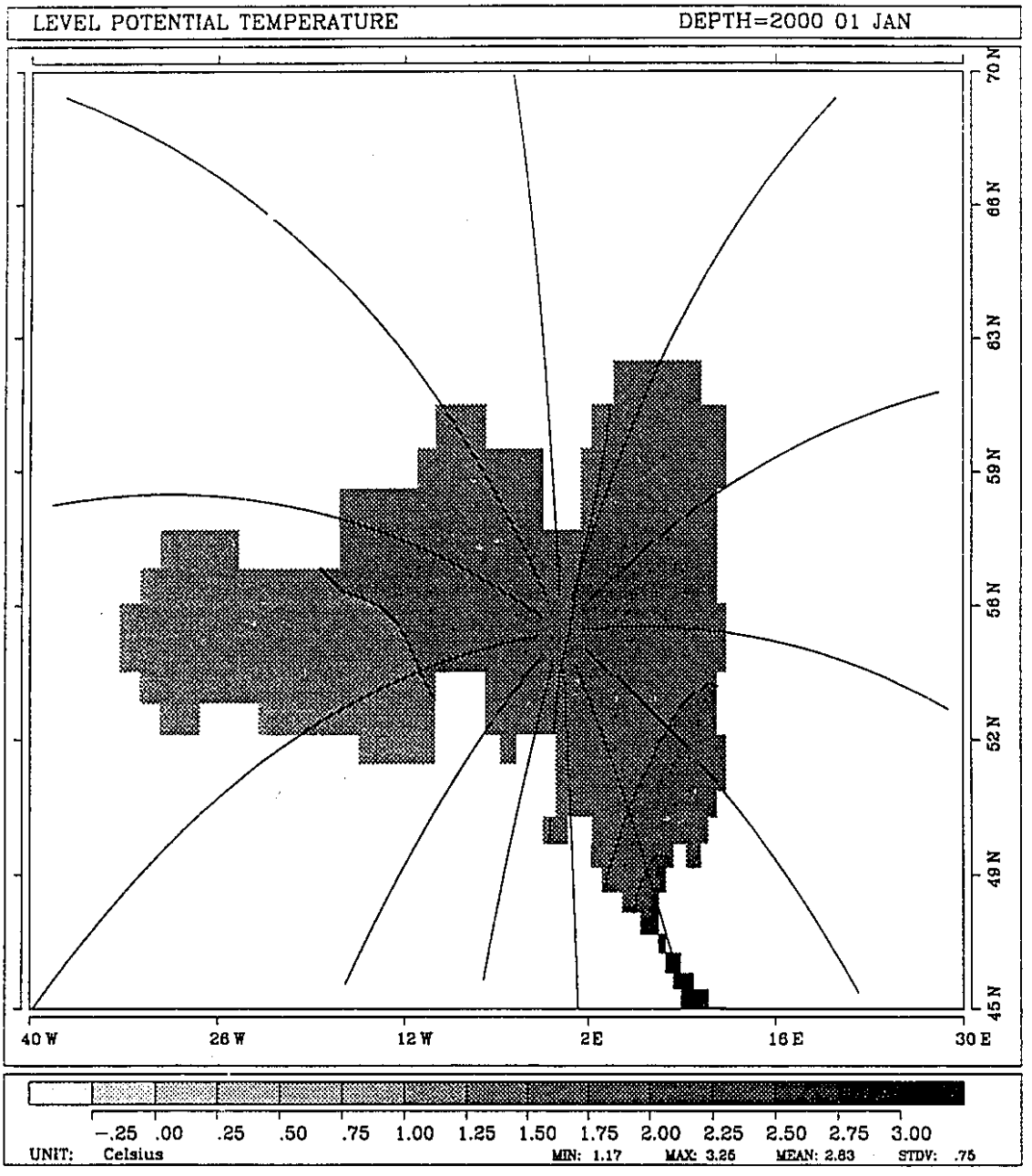

Figure 4.15b Temperature field at 2000 m depth in the Arctic Ocean on January 1st. The white area indicates land.

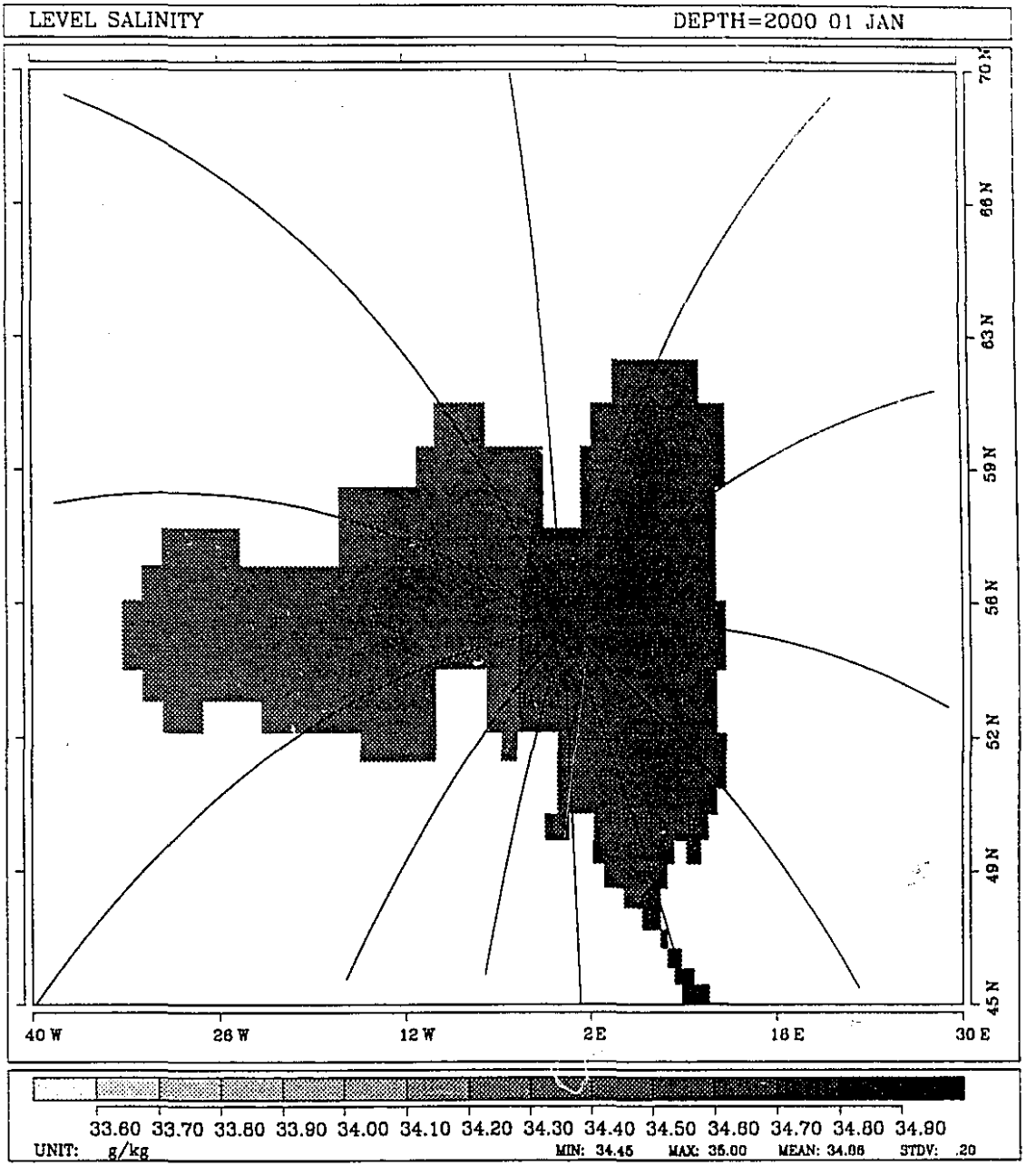

Figure 4.15c Salinity field at 2000 m depth in the Arctic Ocean on January 1st. The white area indicates land.

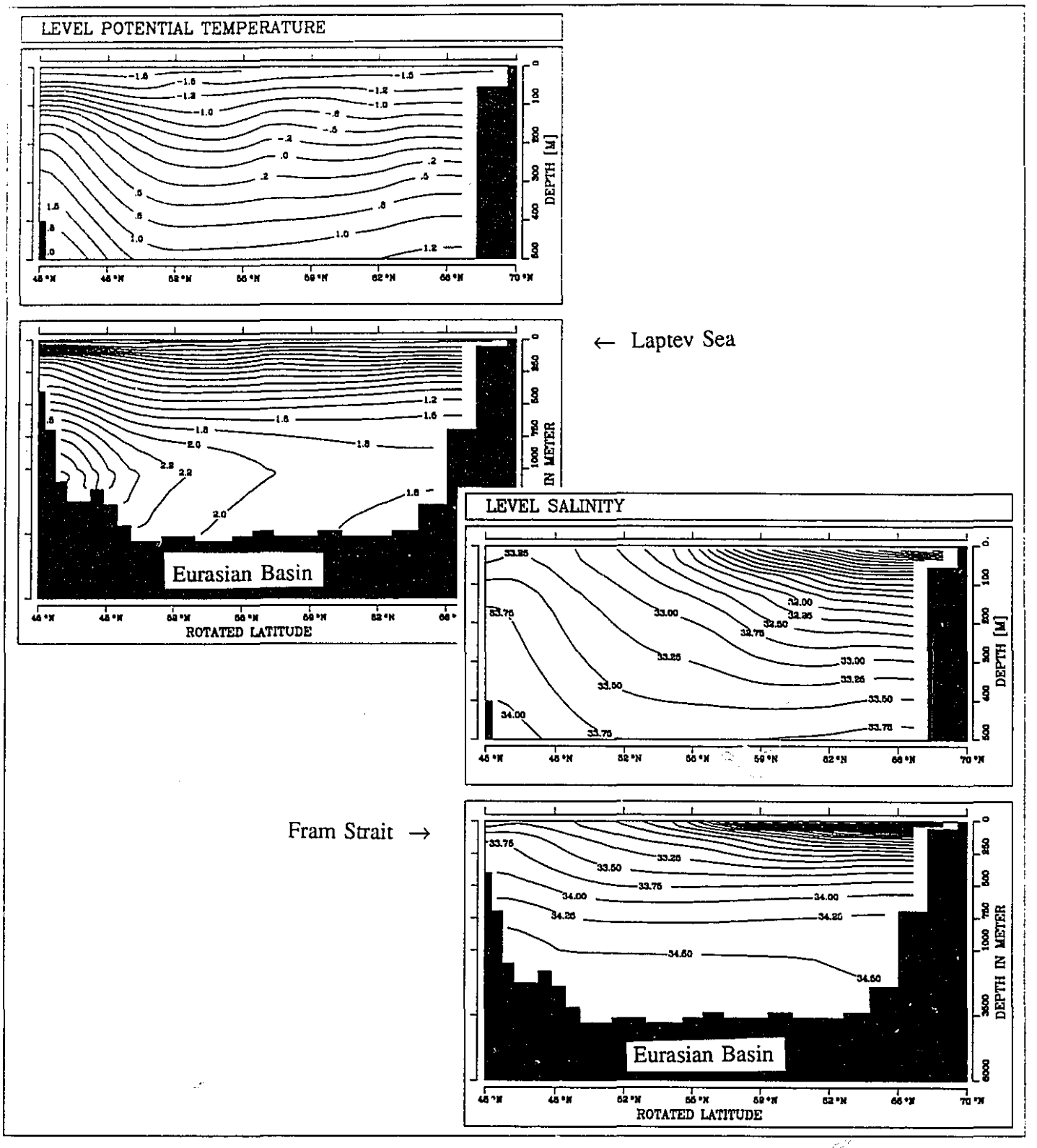

Figure 4.16a North-south transect through the Arctic Ocean showing the distributions of temperature and salinity on January 1st. The black area indicates ocean bottom topography. There are two panels for each of temperature and salinity. The top panel in each case indicates only the top 500 *m* of the ocean in an expanded scale. The transect is taken at 8 longitude degree East (in rotated coordinates) going in a north-south direction. Refer to Fig. 4.13d for orientation.

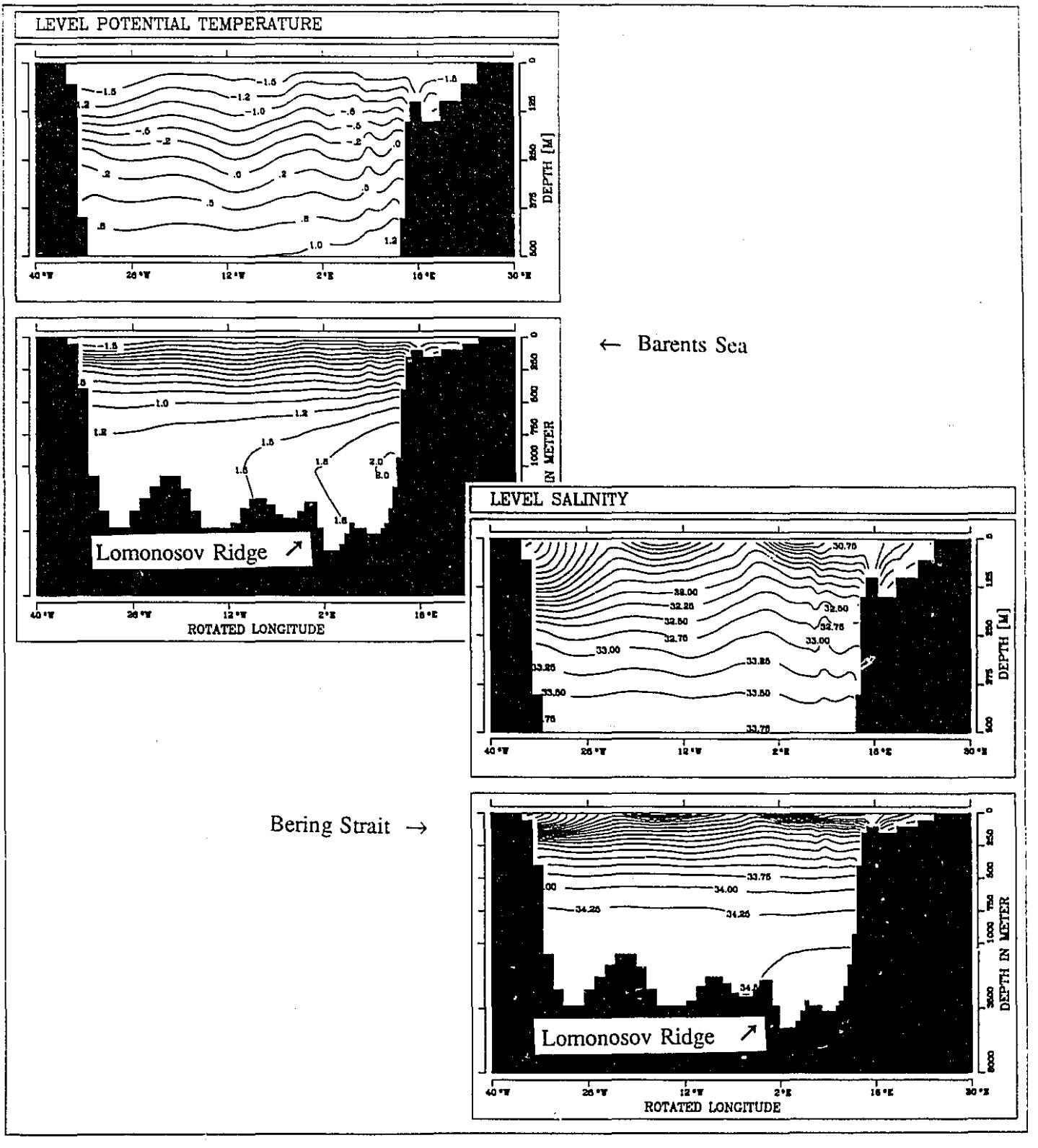

Figure 4.16b East-west transect through the Arctic Ocean showing the distribution of temperature and salinity on January 1st. The black area indicates ocean bottom topography. There are two panels for each of temperature and salinity. The top panel in each case indicates only the top 500 *m* of the ocean in an expanded scale. The transect is taken at 55 degree North (in rotated coordinates) going in an east-west direction. Refer to Fig. 4.13d for orientation.

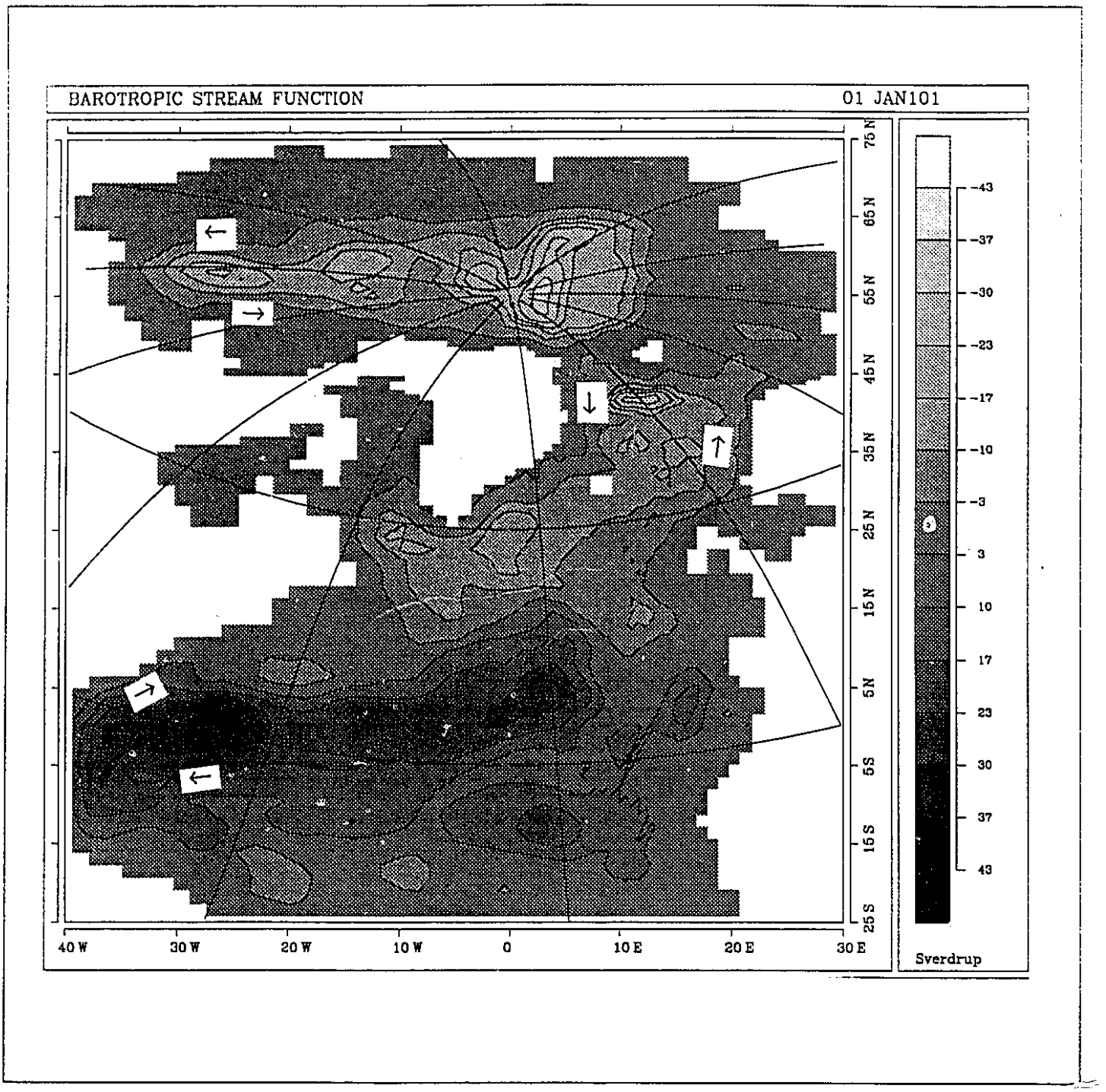

Figure 4.17 Barotropic stream function on January 1*st*. White areas indicate land.

§ 5 Simulation of the Mixed-Layer Circulation in the Arctic

§ 5.1 Introduction

This chapter investigates the mixed-layer circulation of the Arctic Ocean using a coupled sea ice - mixed layer - isopycnal ocean general circulation model (Oberhuber, 1993a). In the Arctic, the interaction of the atmosphere with the mixed layer is different than in other ocean basins because of the presence of sea ice. The sea ice diminishes the wind-driven ocean circulation by absorbing the wind stress that would otherwise directly force motions in the mixed layer. Furthermore, ice melt and growth provides a freshwater flux to the surface above and beyond that of river runoff and that of precipitation minus evaporation. This modifies the buoyancy-driven circulation. Consequently, the Arctic has a mixed-layer circulation in which the relative importance of the wind-driven and buoyancy-driven components is different than in other basins. The purpose of this chapter is to simulate the mixed-layer circulation and to identify the relative importance of each component for the total circulation.

Although this study uses a fully coupled sea ice - mixed layer - isopycnal ocean model, the results presented emphasize only the mixed-layer response. Throughout this chapter the "circulation" refers to that of the mixed layer. The sea-ice model above the mixed layer and the deep-ocean model below are considered as providing forcing for the mixed layer. From the point of view of the mixed layer, the sea ice supplies a drag due to ice motion, a freshwater flux due to ice growth and melt, and a reduced heat exchange due to the insulating effect of sea ice. Also, it is important to note the following feedback: not only does the sea-ice cover affect the mixed layer, but the mixed layer is equally effective in altering the sea-ice cover. Concerning the deep ocean (*i.e.*, that part of the ocean beneath the mixed layer), the mixed layer exchanges momentum, mass, heat, and salt with the deep ocean via interfacial stresses, entrainment, and

diffusion. Again, feedback processes are present as the deep ocean can produce changes in the mixed layer and vice-versa.

A brief review of observational studies of the mixed-layer water-mass properties and circulation is now presented. This is followed by a brief review of previous modelling studies. A complete review of observational and modelling studies can be found in Smith (1990).

§ 5.1.1 Observed Features

The observed features of the mixed layer that are of relevance to this study include the temporal and spatial variations of the temperature and salinity distribution, the mixed-layer depth, and most important of all, the circulation. The long-term means of the above quantities are not well known. The remoteness of the Arctic has thus far prohibited the collecting of sufficient data to determine a satisfactory climatology.

Ice-covered regions have a mixed-layer temperature equal to that of the freezing point of sea water at the ambient salinity. The ocean waters directly beneath the permanent ice cover thus show little variation in temperature. The marginal ice zone does show significant variations in temperature; however, it is the northward transport of warm North Atlantic waters into the Norwegian Sea and on into the Barents Sea that provides the warmest mixed-layer water temperatures and the greatest seasonal variations (see Parkinson *et al.*, 1987, their Fig. 2.5).

Large spatial variations in salinity are caused by river runoff, ice growth/melt, and to a lesser extent, evaporation/precipitation. The spatial pattern shows large-scale freshwater tongues extending from the mouths of the major rivers along both the Siberian and North American coastlines. Conversely, the inflow of saline water from the Greenland, Iceland, and Norwegian (GIN) Sea produces a saline tongue into the Arctic just north of Spitsbergen as well as into the Barents Sea. There is a weaker saline tongue of Pacific water that enters the Arctic via the

Bering Strait. The seasonal variation (see Parkinson *et al.*, 1987, their Fig. 2.4) is the greatest during the summer months when river runoff is at a maximum.

The mixed-layer depth in the Arctic is between 25 and 50 *m* (Björk, 1989). The presence of a strong halocline (pycnocline) prevents the mixing of the mixed-layer waters with the deeper waters. (We recall that near freezing temperatures, the use of the term halocline or pycnocline is interchangeable.) In contrast to the relatively shallow mixed-layer depths in the Arctic, the GIN Sea has large mixed-layer depths, of order 1000 *m*, due to convective overturning in that region during winter. There is no observational evidence for the seasonal variation of the mixed-layer depth in the Arctic on the large scale.

The mixed-layer circulation is generally assumed to consist of the anticyclonic Beaufort Gyre (BG) in the Canadian Basin and the Transpolar Drift Stream (TDS) in the Eurasian Basin extending from Siberia towards Fram Strait (Fig. 5.1). Average speeds in the BG are of the order of 2 - 3 *cm/s*. This view of the mixed-layer circulation is based upon the work of Coachman & Barnes (1961) who deduced the circulation from some 300 oceanographic stations and constructed a dynamic height field. They assumed a level of no motion at a depth of 1200 *m*. It is not evident why there should be a level of no motion at such a depth. Furthermore, in terms of actual current measurements, they mention that in many instances the actual currents were not measured, but rather that they were inferred from the motion of the sea-ice under the assumption that the sea-ice and ocean circulation follow one another. This may not be a good assumption. An apparently stronger argument, in support of the ocean circulation following the sea-ice flow, is that the observed motion of large ice islands with deep drafts (40 *m*) followed an anticyclonic BG trajectory and a TDS. The assumption is that the motion of these ice deep-draft islands is controlled by the ocean circulation. This assumption ignores the important fact that the ice

islands are not floating in isolation but are immersed in a field of sea-ice which is capable of transmitting stresses on the ice islands that may exceed the stress transmitted by the ocean currents. This means that large-scale wind patterns can cause the sea ice to produce an internal stress field that may force the motion of an ice island independent of the ocean currents.

An update to the circulation pattern of Coachman & Barnes was made by Newton (1973). He concluded that the general circulation of the Arctic (surface) water in the Canada Basin to be the same as Coachman & Barnes (1961). He reiterated that the circulation has been confirmed by the drift tracks of both deep (40-50 *m*) ice islands and shallow (2-3 *m*) ice floes. He used data from the Arctic Ice Dynamics Joint Experiment (AIDJEX) from 1970 to 1972 in which current meters were placed down through holes cut in the ice. The current meters were secured to the ice which moves with respect to the water; thus, the recorded currents were relative to the ice and were corrected for ice drift to present a true picture of the currents with respect to the earth. Furthermore, no error bounds were formally established on the AIDJEX current meter data. Newton notes that the current meters were often operating below their accuracy threshold of about 2.5 *cm/s*. In fact many of the currents reported were of this magnitude. Interestingly enough, during the 1972 AIDJEX experiment, the measured surface currents at one of the three camps were opposite to the general circulation picture of Fig 5.1. This anomalous current was located along the Siberian shelf.

An intriguing report of circulation in the southern Beaufort Sea was made by Aagaard (1984) who took current meter measurements and station data over the continental slope in that area. He reported a large-scale circulation (the Beaufort Undercurrent), flowing in the direction of Fram Strait (see Fig. 5.2) and not in the direction of Bering Strait as in Fig 5.1. He suggested that this flow is part of the large-scale general circulation over the basin. As these measurements probably represent the best measurements of flow in that region, it is possible to conclude that

the currents in the southern half of the BG are moving opposite to the ice circulation. Furthermore, since the circulation measured by Aagaard is opposite to that of Fig 5.1, then the question must be raised of the validity of an anticyclonic mixed layer circulation over the entire Canadian Basin as suggested by Fig. 5.1.

A large-scale view near the surface of the Arctic Ocean is to consider it as a system of three overlying geophysical fluids. The top layer of air is the atmospheric planetary boundary layer of thickness of order 1 *km*. The surface winds that are associated with the mean atmospheric pressure field (Fig. 5.3) would show a pattern similar to that of the ocean circulation (Fig. 5.1). The second layer of sea ice is of thickness of order 3 *m*. The mean pattern of ice drift (Fig. 5.4) shows a pattern that is consistent with the atmospheric circulation. The bottom layer is the ocean mixed-layer of thickness of order 40 *m*. Observational evidence collected over the last ten years clearly shows that the mean atmospheric circulation pattern and the mean sea-ice circulation pattern are well known and similar to one another (Colony *et al.*, 1991). The question posed here is whether or not the mixed-layer of the ocean follows the same circulation pattern. The point of view taken is that the winds control the sea-ice circulation but not the mixed-layer circulation. The mixed-layer may not feel the atmospheric wind stress and the stress provided by the slowly rotating pack-ice may be too small to drag the entire mixed layer with it. The mixed layer may then have a significant buoyancy-driven component.

§ 5.1.2 Previous Modelling Results

A concrete hydraulic model of the Arctic Basin was constructed by Gudkovich & Nikiforov (1965); however, their model did not rotate nor did it have a sea-ice cover. The surface circulation was forced by inflow/outflow in both Fram and Bering Straits. In one experiment (their Fig. 3) they obtained a circulation pattern similar to the traditional one (Fig.

5.1). In another experiment (their Fig. 4) they obtained a reversal of the BG (*i.e.* a cyclonic flow) and a TDS that no longer extended all the way from Siberia to Fram Strait. The difference between the two experiments was in the manner in which the inflow/outflow was specified. They disregarded the latter circulation as meaningless because it did not agree with observations.

The first computer simulation of the Arctic Basin circulation was carried out by Campbell (1965) who produced a steady-state circulation of a wind-driven, baroclinic, ice-covered Arctic Ocean. His solution showed an anticyclonic BG (his Fig. 7) over the Canadian Basin in agreement with Fig. 5.1. Galt (1973) carried out a large-scale modelling study of the Arctic which presented a solution of the barotropic vorticity equation forced by the curl of the wind stress. The resulting flow consisted of an anticyclonic BG and a TDS directed toward Fram Strait (his Fig. 14). Both of these studies involved wind-driven flows in which the thermohaline circulation and the exchange of water masses with various straits was ignored. Semtner (1976b) used a baroclinic ocean model which simulated the anticyclonic flow of the BG (his Fig. 7) and the TDS. However, his study did not include an ice cover. The first 3-D coupled sea ice - ocean model was presented by Hibler & Bryan (1987). Although they emphasized the sea-ice simulation, some results were presented for the ocean surface circulation. Their flow showed an anticyclonic BG and a TDS (their Fig. 11). Semtner (1987) presented a coupled sea - ice ocean model similar to that of Hibler & Bryan (with a simplified sea-ice rheology) and obtained the same circulation pattern (Fig 5.5).

Nearly all previous general circulation modelling studies have been based on the Bryan-Cox ocean model (Cox, 1984). Part of the motivation for the present work is the availability of a new type of ocean general circulation model developed by Oberhuber (1993a). This model differs from the Bryan-Cox model in that it uses isopycnal surfaces as the vertical coordinate. The vertical coordinate is thus Lagrangian rather than Eulerian. The flow in the horizontal plane

is then naturally directed along isopycnal surfaces. This new model is applied to the Arctic Basin with the goal of investigating the water-mass properties and circulation of the mixed layer. In Oberhuber (1993b) the model was used to study the circulation in the North Atlantic Ocean.

The remainder of this chapter is organized as follows. Section 5.2 briefly describes the layout of the coupled sea ice - mixed layer - isopycnal ocean model. The simulated mixed-layer water-mass properties and circulation are presented in section 5.3. Section 5.4 presents the water-mass properties and surface circulation for six sensitivity experiments in which (i) the sea-ice model is removed, (ii) the wind-forcing is turned off, (iii) the surface freshwater flux is modified, and (iv) the model is spunup without Levitus initialization data, (v) the exchange with the GIN Sea is eliminated, and (vi) the bottom topography is replaced with a deep basin of uniform depth. Section 5.5 concludes the chapter.

§ 5.2 The Model

The model used for this study is that of Oberhuber (1993a); it consists of three coupled submodels. The sea ice is represented by a dynamic thermodynamic model with viscous-plastic rheology (Hibler, 1979), the mixed layer by a turbulent kinetic energy model, and the deep ocean by an isopycnal-layer model. The models interact via the exchange of momentum, mass, heat, and salt. Forcing occurs via the specification of monthly climatological atmospheric fields and realistic topography is employed. The equations describing each model are fully described by Oberhuber (1993a). They are briefly presented in § 4.2 of the previous chapter. The model layout is now described.

The domain chosen for this study includes the Arctic Ocean and the GIN Sea. The model places a solid wall across the Bering Strait, the Canadian Arctic Archipelago, the Denmark Strait,

and the passage between Iceland and Europe. Consequently, the model does not allow for the inflow of warm-fresh Pacific water via Bering Strait, nor the outflux of cold, fresh Arctic Surface water via the Canadian Arctic Archipelago, nor the interaction with the warm, saline Northern Atlantic.

The model's bathymetry is obtained by interpolating a 1 degree resolution topographic data set onto the model's grid of 2 degree resolution. The main bathymetric features of the Arctic and GIN basins are preserved (Fig. 5.6).

A problem with numerical models written in spherical coordinates for the Arctic Ocean is the convergence of meridians of longitude near the North Pole. The resulting small east-west grid spacing near the Pole leads to unrealistically small time step constraints. This is overcome by rotating the model coordinates by Eulerian angles such that the model coordinates converge to a point in northern Siberia, which is outside the defined model domain. All figures presented in this chapter indicate the rotated latitude and rotated longitude coordinates along their axes. The true geographical coordinates are superimposed on the figures as thin lines (*e.g.* Fig 5.6).

The model resolves the water column using five vertical layers of prescribed potential density. The initial prescribed density and thickness of each layer is obtained via interpolation of the temperature and salinity data of Levitus (1982). As the model integrates in time, these layer thicknesses vary in time and space; however, the densities do not. The first layer, which is the mixed layer, is allowed to develop a temporally and spatially varying potential density because of entrainment and surface buoyancy fluxes.

The model uses spherical coordinates in the horizontal with a resolution of 2 degrees in latitude and longitude. As the model coordinates are rotated by Eulerian angles with respect to geographical coordinates, the result is a spatial resolution of about 100 *km* in the Arctic.

The model spinup is for 100 years with a time step of two days. This is an adequate time for the sea-ice and mixed-layer models to reach an equilibrium; however, the deep-ocean circulation almost certainly is not in equilibrium after such a short period. One simulated year requires two hours of CPU time on an IBM RISC workstation; consequently, integrations for thousands of years are not feasible.

The surface boundary conditions on salinity and temperature are essentially of Newtonian type. The observed salinity field to which the model salinity is relaxed is given in Fig. 5.7. The surface temperature is not directly relaxed to observed values; instead, sea surface temperature is relaxed to an apparent sea surface temperature. The apparent temperature is computed as the result of a complete surface energy balance that includes longwave, shortwave, sensible, and latent heat terms (see Oberhuber (1993a) for details).

The model is forced using monthly climatological fields of wind stress, radiation, air temperature, humidity, rainfall, and cloud cover. These fields are described by Oberhuber (1988) and Wright (1988). The model derives the forcing at a particular time step by interpolating between climatological fields of neighbouring months. The seasonal variation in wind stress is shown in Fig. 5.8, which serves to illustrate the nature of the seasonal cycle in the Arctic.

§ 5.3 Control Run Simulation

As stated in § 5.2, the mixed layer is actually the top layer of the isopycnal ocean model. At each grid point in the model domain, the model solves Eqns. 4.5 - 4.8 to determine the mixed layer velocity, thickness, temperature, and salinity. Thus, over the vertical extent of the mixed layer, the velocity, temperature, or salinity at a particular grid point represents a single depth-averaged value. The vertical variation of properties within the mixed layer, such as the thin

boundary layer between the sea ice and the surface waters, is not simulated. To indicate the seasonal variation in mixed layer properties, the simulation results from the month of April were chosen to represent conditions at the end of winter; on the other hand, the month of October was chosen to represent conditions at the end of summer. For quantities in which little or no seasonal variation was observed to occur, only the simulation results from the end of winter are presented.

The mixed-layer depth over the central Arctic basin has an average value of about 40 *m* (Fig. 5.9), whereas the depth increases drastically in the GIN Sea and in the Barents Sea, which is consistent with the presence of convective overturning in that region. There is little seasonal variation of the mixed layer depth over the central Arctic (*i.e.* over the Canadian and Eurasian Basins); however, the average mixed-layer depth was noted to be slightly greater at the end of winter than at the end of summer. The deeper mixed-layer during winter is consistent with the increased entrainment into the mixed layer during winter. In ice-covered areas this increased entrainment is principally due to salt-injection into the mixed layer during ice formation. In ice-free regions, the increased mixed layer depth in winter is due to vigorous wind stirring and also due to convective overturning caused by the increased heat loss from the ocean surface.

The mixed-layer temperature equals the freezing point of sea water where ice exists in the domain (Fig. 5.10). There is thus little variation in this quantity throughout the year as most of the domain is ice covered, and the waters in that part of the domain corresponding to the marginal ice zone do not significantly increase their temperature much above freezing during the ice free months. The temperature field (Fig. 5.10) does show elevated values in the Arctic where the Siberian rivers flush relatively warm freshwater into the Arctic. This is simply the effect of an elevated freezing point due to a lower salinity.

The mixed-layer salinity is artificially relaxed to remain near the monthly observed value (Fig 5.7) and thus is not shown.

Of particular interest is the simulation of the mixed-layer currents (Fig. 5.11a,b). The pattern for either season is relatively consistent with that of the observations (Fig. 5.1) and other models (*e.g.* Fig. 5.5). Aagaard (1984), however, re-assessed the subsurface circulation in the Arctic to include a strong coastal jet travelling opposite in direction to the overlying ice cover (see Fig. 5.2). This is referred to as the Beaufort Undercurrent. Such a feature does not show up in the simulation here and may be a result of either having the Bering Strait closed or not having high enough grid cell resolution. Also, recent modelling work based on a stochastic model indicates that this current may also be due to a topography-eddy interaction (G. Holloway, *pers. comm.*, 1993). The TDS is evident and extends from the Siberian coast through to Fram Strait. The general circulation in the Eurasian Basin is that of a convergent flow directed towards Fram Strait. In the Barents Sea there is both an inflow of water from the Norwegian Sea and a southward coastal flow of water from the Eurasian Basin. In the GIN Sea the circulation shows the traditional cyclonic gyre. The circulations in Baffin Bay and Hudson Bay are likewise cyclonic. The seasonal variation of currents is minimal except over the Barents Sea (compare Fig 5.11a & 5.11b). This is not surprising as the waters in the Barents Sea are shallow and are directly exposed to the variable wind forcing in that region (compare Figs. 5.8a & 5.8b).

The sea surface elevation (Fig. 5.12) associated with this circulation is similar to the dynamic height field presented by Coachman & Aagaard (Fig. 5.1). The sea surface elevation in this model shows little seasonal variation.

Though not of primary interest in the present study, the fields of sea-ice motion are shown in Fig. 5.13a,b. It is apparent that the winter ice simulation (Fig. 5.13a) is consistent with observations (Fig. 5.3). The pattern consists of a large BG in the western Arctic and a TDS joining with a strong southward flow along the east Greenland coast. This demonstrates the dominance of the winds in driving the sea-ice circulation (Fig. 5.13a) during the strong winter

winds. However, in late summer, when the winds are much lighter, the sea-ice circulation changes significantly (Fig. 5.13b). Observational evidence does exist for the occasional reversal of the sea-ice circulation over the Canadian Basin in late summer (Serreze *et al.*, 1989). They found that the reversals correspond closely to anomalous (interannual) changes in the atmospheric pressure distribution. However, under climatological forcing there is no reversal of the BG.

The driving mechanism of the mixed-layer circulation in the Arctic is not obvious. The presence of an ice-cover reduces the ability of the wind to transmit momentum into the mixed-layer. The extent to which it does this is not known. The cycle of growth and melt of sea ice creates a varying saltflux which drives buoyancy currents, as does the freshwater flux from river runoff. Other possibilities include a large-scale flow driven by the influxes from the various straits connecting the Arctic to other basins. Also, topography-eddy interactions can generate strong boundary flows. In an attempt to elucidate the nature of the driving force behind the mixed-layer currents simulated, a series of sensitivity experiments is carried out to illustrate how the circulation responds to various changes in the forcing.

§ 5.4 Sensitivity Experiments

The mixed-layer circulation pattern is investigated with respect to its sensitivity to (i) ice-cover, (ii) atmospheric winds, (iii) freshwater flux, (iv) initialization without Levitus data, (v) no exchange with the GIN Sea, and (vi) bottom topography. Though each experiment generally presents a physically unrealistic situation, it does allow one to clearly identify the contribution that each of the components (i) through (vi) makes to the maintenance of the mixed-layer circulation. In particular, we wish to determine whether the mixed-layer circulation is mainly wind driven or buoyancy driven. A coupled sea ice - mixed layer - deep ocean general

circulation model as used here contains numerous parameters and parameterizations. It would be an enormous, yet worthwhile task to investigate the sensitivity of the mixed-layer circulation to changes in these parameters and parameterizations. For instance, changes in the drag coefficients between atmosphere and ice, between ice and ocean, the horizontal and vertical diffusion coefficients between layers of the isopycnal model, the parameterization of salt injection into the ocean during the ice growth process are but a few of the items that may significantly alter the model's simulation of the mixed-layer circulation. Nevertheless, these parameters have been tuned by Oberhuber (1993b) to obtain a reasonable simulation of the North Atlantic and consequently the same parameter values were employed here. The goal of this sensitivity study is to identify the dominant mechanism driving the mixed-layer circulation in the Arctic rather than to carry out a thorough sensitivity study of the mixed-layer model. Note that in each experiment, only a single change has been made with respect to the control run setup, and that each experiment was integrated for 100 years.

§ 5.4.1 Removal of Sea-Ice Cover

When the sea-ice model is removed, the mixed layer is directly forced by the atmosphere. As a consequence of the removal of its insulating cover of sea-ice, the mixed-layer loses more heat to the atmosphere and thereby reaches physically impossibly low temperatures of -20°C during winter. Nevertheless, this does allow one to simulate the circulation under direct wind forcing. The resulting circulation (Fig. 5.14a) is similar to the traditional anticyclonic BG and the TDS which flows from Siberia to Fram Strait. The sea-surface elevation is too large, with the dynamic height range between the central Canadian Basin and the GIN Sea of order 150 *cm* (see Fig. 5.14b); in reality, it is only about half this amount. The circulation in the ice-free regions such as the Barents Sea and the GIN Sea have not changed significantly from the control

run (Fig 5.11). This is expected as the shallow water in this region of the domain usually has only a thin ice cover or no ice cover at all. There is little difference in the atmospheric momentum flux or buoyancy flux over the Barents Sea between the control run and this sensitivity run. It cannot immediately be concluded that it is the direct transfer of momentum from the atmosphere to the ocean that is responsible for the dramatic change in circulation pattern. One must keep in mind that an ice cover alters the ocean-atmosphere interaction by not only inhibiting the transfer of momentum but also by modifying the surface freshwater flux. Over the Arctic Basin there is an average of 50 *cm* of ice growth each year (Maykut & Untersteiner, 1971). This freshwater flux is an especially important contributor to the mixed layer density structure in regions of high ice production such as along the Siberian shelves.

§ 5.4.2 Removal of Wind Stress

In this experiment, only the atmospheric wind stress is removed. The goal is to observe the circulation pattern in a situation in which the sea ice does not impart momentum to the mixed layer, but does impart a freshwater flux. The experiment is unrealistic in the sense that the wind is important in producing Ekman divergence and convergence which in turn sets up sloping isopycnals that have associated geostrophic currents. In this experiment we continue to relax to the model salinity to the observed salinity which in reality, however, is partially setup from the wind. Nevertheless, the fact that there is little change in the circulation between this experiment (Fig. 5.15) and that of the control run (Fig. 5.11a) suggests that the drag between ice and water is not of first order importance. This is a surprising result and suggests that the buoyancy forcing is very important.

§ 5.4.3 Modification of Freshwater Flux

To keep the model's cyclo-stationary state near climatology, the surface salinity in the control run, is relaxed to that of climatology (Fig 5.7). The model feels the large freshwater impact of the peripheral rivers of the Arctic Basin. This relaxation is analogous to the model maintaining these low salinities by the addition a surface freshwater flux. In this experiment, the annual climatological surface salinity field is replaced by a constant field of 32 *psu* everywhere. This value was chosen as an intermediate value between the low salinities near river mouths and the high salinities found in the GIN Sea. The result is that the near-surface isopycnal surfaces across the Arctic Basin become much more horizontal (Fig. 5.16b). In the control run, the presence of large surface gradients of surface salinity produces strong slopes in the isopycnic surfaces, even in the mixed layer (Fig. 5.16a). These sloping isopycnals give rise to baroclinic currents which contribute to the total circulation. Note that in this experiment the wind is allowed to exert a drag force on the ice; however, it is not permitted to setup sloping isopycnals via Ekman convergence or divergence.

The impact of uniform surface salinity on the circulation is that it is now basically cyclonic everywhere in the domain (Fig. 5.17). The flow along the Siberian shelf has changed from an eastward flow to a westward flow. A similar reversal is found in the vicinity of the Bering Strait. The general strength of the flow has increased everywhere. A dramatic change in flow is noted over the Eurasian Basin, where the current changes from a flow directed from the Siberian Coast towards the pole (Fig. 5.11) to a cyclonic gyre which essentially follows the pattern of the bottom topography. In fact, the general outline of the flow in this experiment is that of one following the contours of bottom topography (compare to Fig. 5.6). There is basically a cyclonic flow in each of the Eurasian and Canada Basins.

The conclusion is that the observed surface salinity spatial pattern, which is caused by ice growth, river runoff, and Ekman convergence of the mixed layer, has a major impact on the

simulation of the mixed-layer currents. The freshwater fluxes and Ekman convergence introduce sloping isopycnals and stratification that reduces the extent to which the mixed-layer circulation feels the bottom topography.

§ 5.4.4 Initialization without Levitus Data

Ordinarily, the model's isopycnal surfaces are initialized based on the temperature and salinity data set of Levitus (1982). This data set is spotty in the Arctic Ocean where there are an inadequate number of observations to specify the temperature and salinity fields in a satisfactory manner. Thus as an experiment, the model was spunup using level isopycnals. It is important to note that the surface boundary conditions on temperature and salinity both relax back to observed monthly temperatures and salinities even in this experiment. The idea is to test how the deep circulation affects the surface circulation. The deep circulation is of course very much affected by the Levitus data. The surface circulation pattern shown in Fig. 5.18 shows little qualitative difference from that of the control run (Fig. 5.11a). There is in fact little difference (not shown) in the deep circulation in this experiment from that of the control run.

§ 5.4.5 No Exchange with GIN Sea

To determine the importance of the inflow of warm, saline Atlantic water and the outflow of cold, fresh Arctic water, a barrier was placed so at to cutoff all exchange between the Arctic and the GIN Sea. The resulting circulation (Fig. 5.19) does not differ significantly from the control run (Fig. 5.11), except of course in the vicinity of the artificial barrier. The conclusion is that the flow through Fram Strait does not control the large-scale mixed-layer circulation.

§ 5.4.6 Removal of Bottom Topography

The extent to which mixed layer circulation is influenced by the shelves, the various basins, and the ridges in the model domain is investigated by setting the depth to a uniform value

of 5000 m everywhere. The isopycnals are set everywhere to be horizontal at the beginning of the integration to be consistent with the flat-bottom topography. The resulting circulation (Fig. 5.20) is very different than the control case (Fig. 5.11). This new circulation shows a surface circulation flowing in some places perpendicular to the Lomonosov Ridge rather that parallel to the ridge as in the control run. This is assumed to be due to the elimination of the Lomonosov Ridge. Thus, bottom topography plays an important role in the simulation of mixed-layer currents in this model.

§ 5.5 Conclusions

The application of a recently developed coupled sea ice - mixed layer - isopycnal ocean general circulation model (Oberhuber, 1993a) to the Arctic Ocean has produced some new results for the mixed-layer circulation and water-mass properties. In comparing the circulation simulated here with other circulation patterns, either observed or modelled, the depth at which the currents are being referred to must be made clear. All results presented here are vertically averaged over the mixed-layer depth of approximately 40 m. In the one-to-two meters of water below the ice there exits a boundary layer in which the ocean surface may indeed follow the large-scale flow pattern of the sea ice. However, the flux of momentum between the sea-ice and the mixed-layer will be determined not by the currents in this thin boundary layer but rather by somewhat deeper currents. The position taken here is that it is the vertically averaged mixed-layer currents which best indicate the contribution of the ocean to the stress at the bottom of the sea ice.

An important result of this study is that the sea-ice simulation was satisfactory in that it showed a well developed anticyclonic BG and TDS extending from the Siberian coast to Fram Strait. This was achieved despite an ocean circulation which did not mimic the sea-ice flow.

This indicates the dominance of the winds in controlling the ice drift pattern over most of the Arctic.

The six sensitivity experiments proved useful in elucidating the contribution made by various processes or features to the mixed-layer circulation. The removal of the sea-ice cover demonstrated that in the absence of a sea-ice cover the mixed-layer circulation would be wind-driven and would very closely follow the traditional circulation pattern. The removal of wind stress gave a circulation pattern that differed from the control run only in regions of thin ice-cover located over large continental shelves (*i.e.* Siberian Shelf and Barents Sea). This indicates that the circulation over shelves may be wind-driven in the mixed-layer. The modification of the freshwater flux diminished the horizontal density gradients in the mixed layer and accordingly weakened the buoyancy driven component of the circulation. As a result, the Arctic Ocean essentially becomes a barotropic fluid and the surface circulation follows along with that of the deep circulation, *i.e.* is cyclonic. Initializing the model without using Levitus data did not produce a significant change in the surface circulation. Eliminating the exchange with the GIN Sea produced a very different circulation near the Fram Strait and over the Barents shelf; however, it did not cause a significant change in the large-scale circulation. The final sensitivity experiment, in which continental shelves and ridges were removed by making the depth everywhere constant at 5000 *m* showed surface waters that in some places flowed perpendicular to the Lomonosov Ridge rather that parallel to the ridge as in the control run. This is assumed to be due to the elimination of the Lomonosov Ridge.

A limitation of the present study is the discretization of the vertical into only five layers and the use of a horizontal resolution of only 2 degrees. Further studies are in progress involving an increased number of vertical layers and a higher horizontal resolution as well as a larger domain that will include the North Atlantic and North Pacific Oceans.

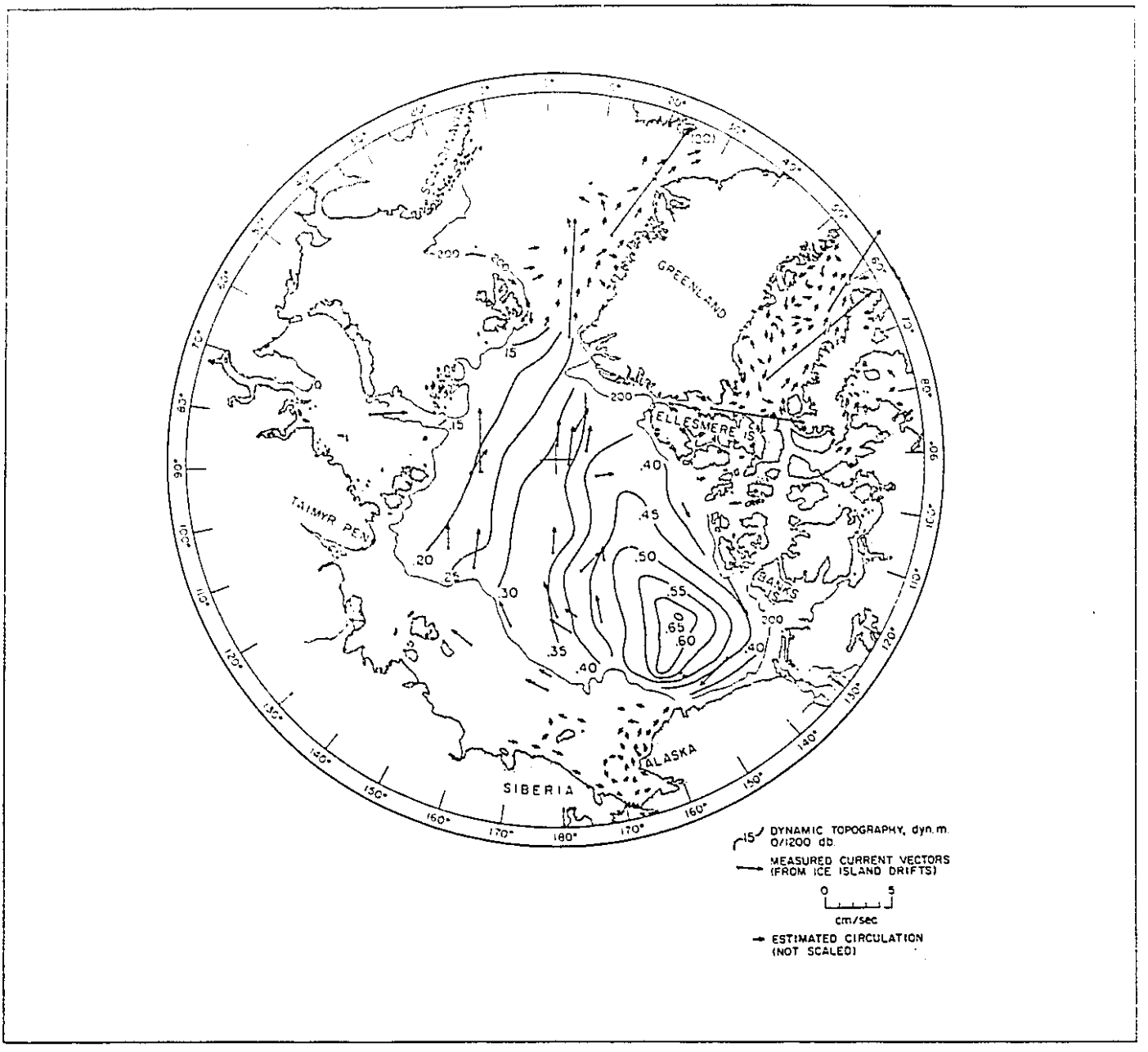

Figure 5.1 Composite surface circulation inferred from dynamic topography, station drifts, and temperature and salinity distributions (after Coachman & Aagaard, 1974). Dynamic topographic is based on a level of no motion at 1200 *db*.

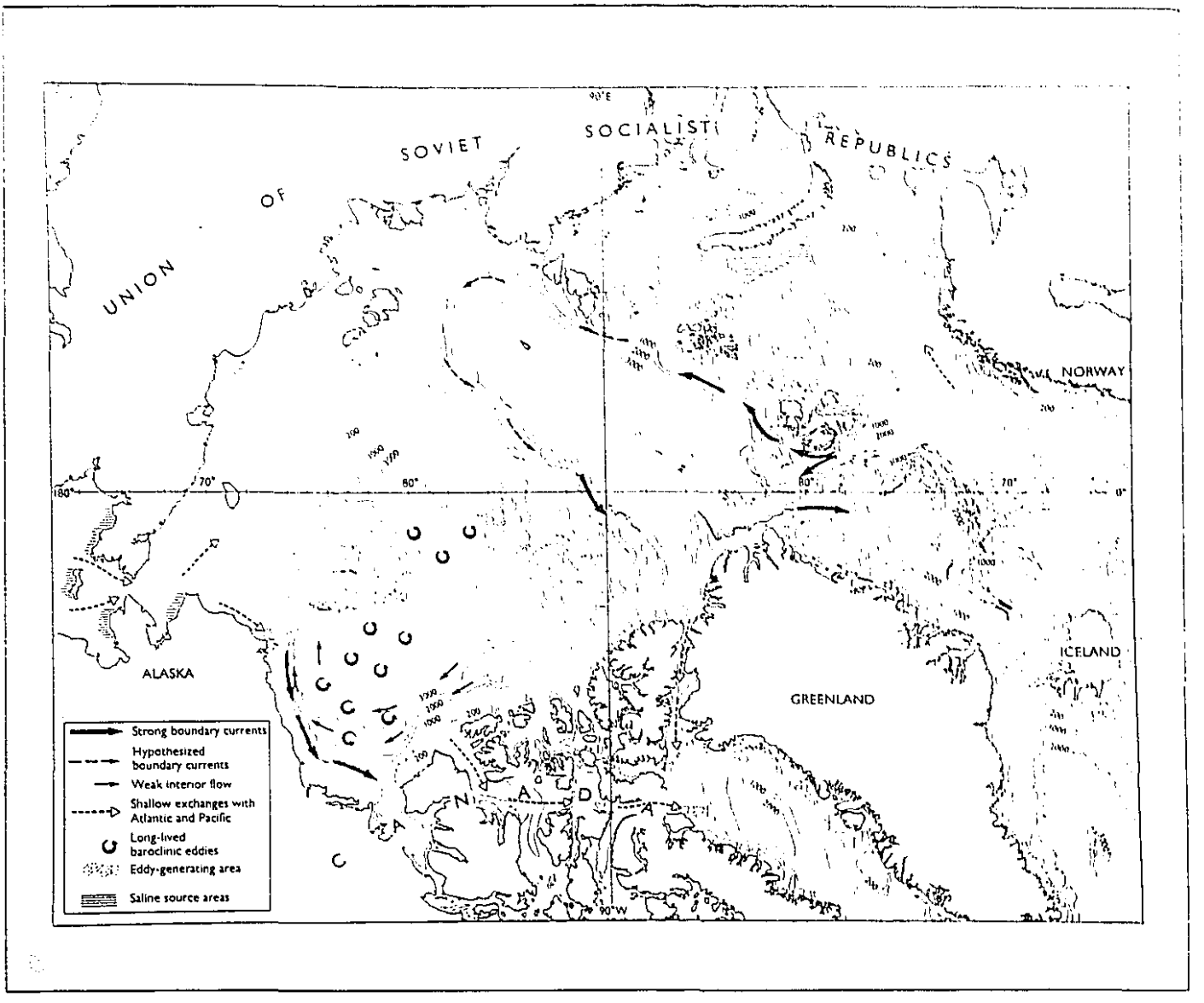

Figure 5.2 Re-assesed subsurface circulation in the Arctic Ocean (from Aagaard, 1988).

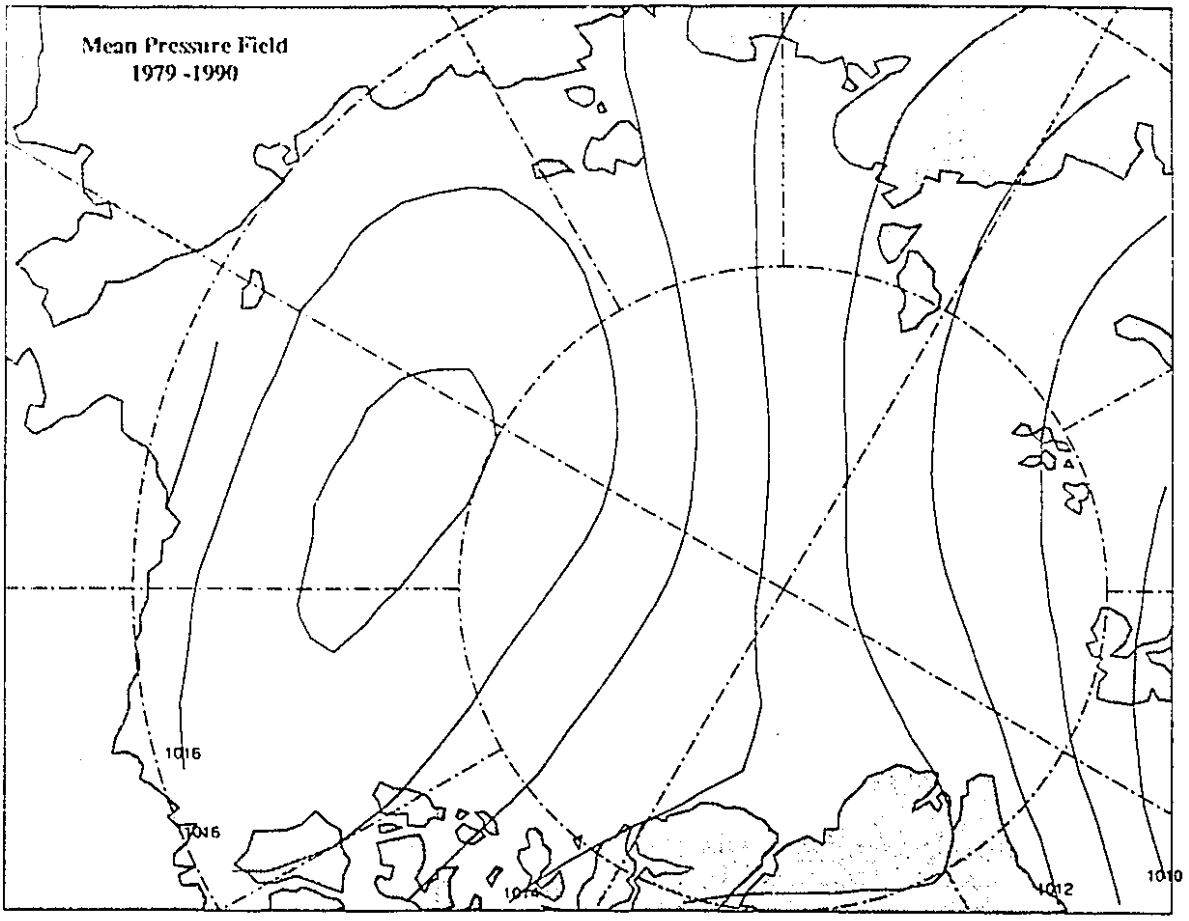

Figure 5.3 Mean atmospheric pressure field (*mb*) over the Arctic during the period 1979-1990. The contour interval is 1 *mb*. A high pressure cell over the Canadian Basin produces an anticyclonic atmospheric surface flow. Also present is a flow pattern over most of the Eurasian Basin directed from the Siberian coast towards Fram Strait (from Colony *et al.*, 1991).

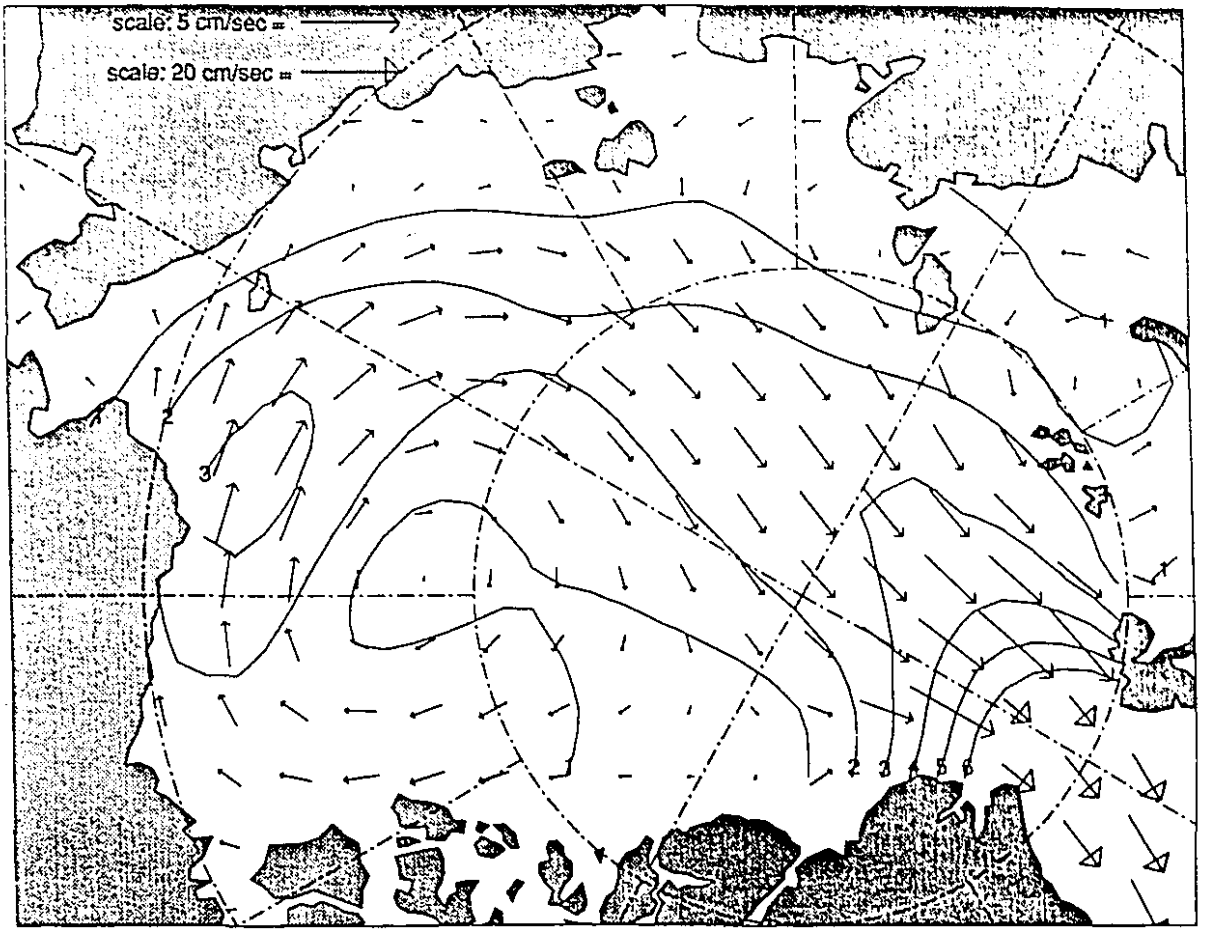

Figure 5.4 Mean field of ice motion interpolated spatially and temporally from manned ice stations and automated data buoys (from Colony *et al.*, 1991).

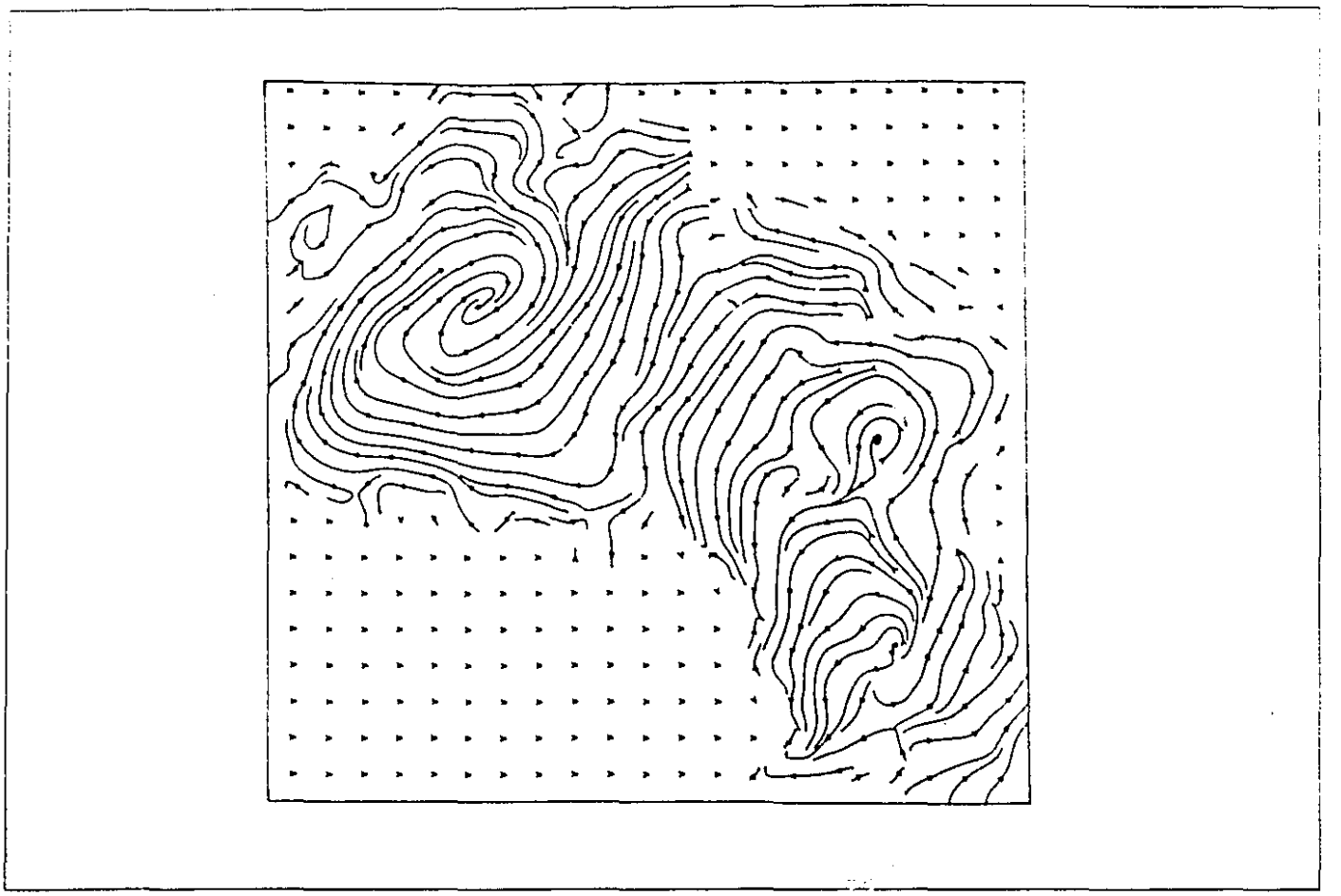

Figure 5.5 Streamlines of January currents at the surface from Semtner's (1987) coupled ice-ocean model. The flow shows an anticyclonic BG and a TDS extending from Siberia to Fram Strait. The pattern at 40 *m* depth is similar.

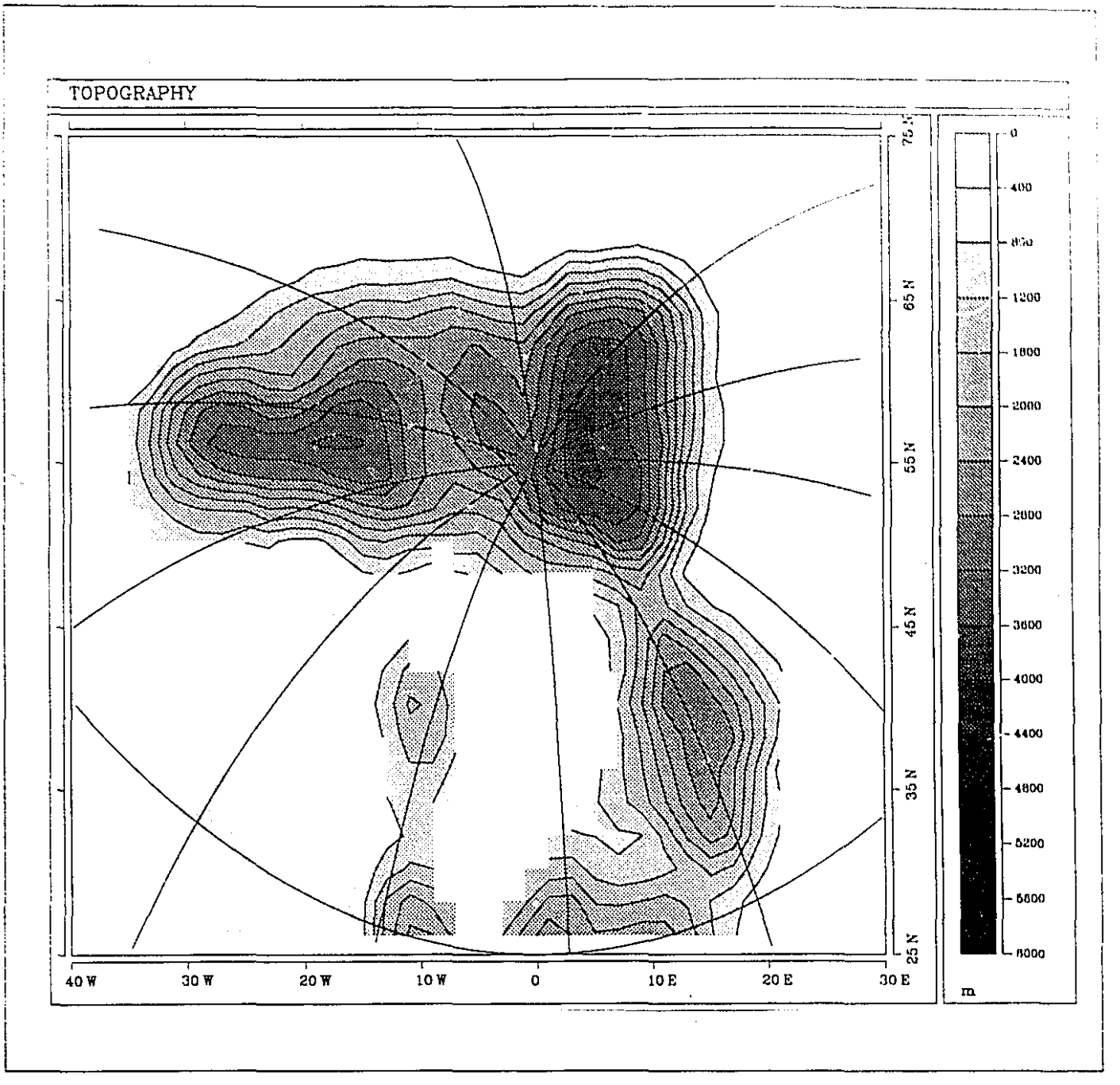

Figure 5.6 Bathymetry and model domain. The domain includes the Arctic Ocean and the GIN Sea. The bathymetry resolves the Canadian Basin and the Eurasian Basin by the Lomonosov Ridge which runs from Siberia to Greenland as it passes beneath the North Pole. The Fram Strait sill has a depth of about 2500 *m*. Baffin Bay and Hudson Bay are also included; however, they have no connection with any other part of the domain.

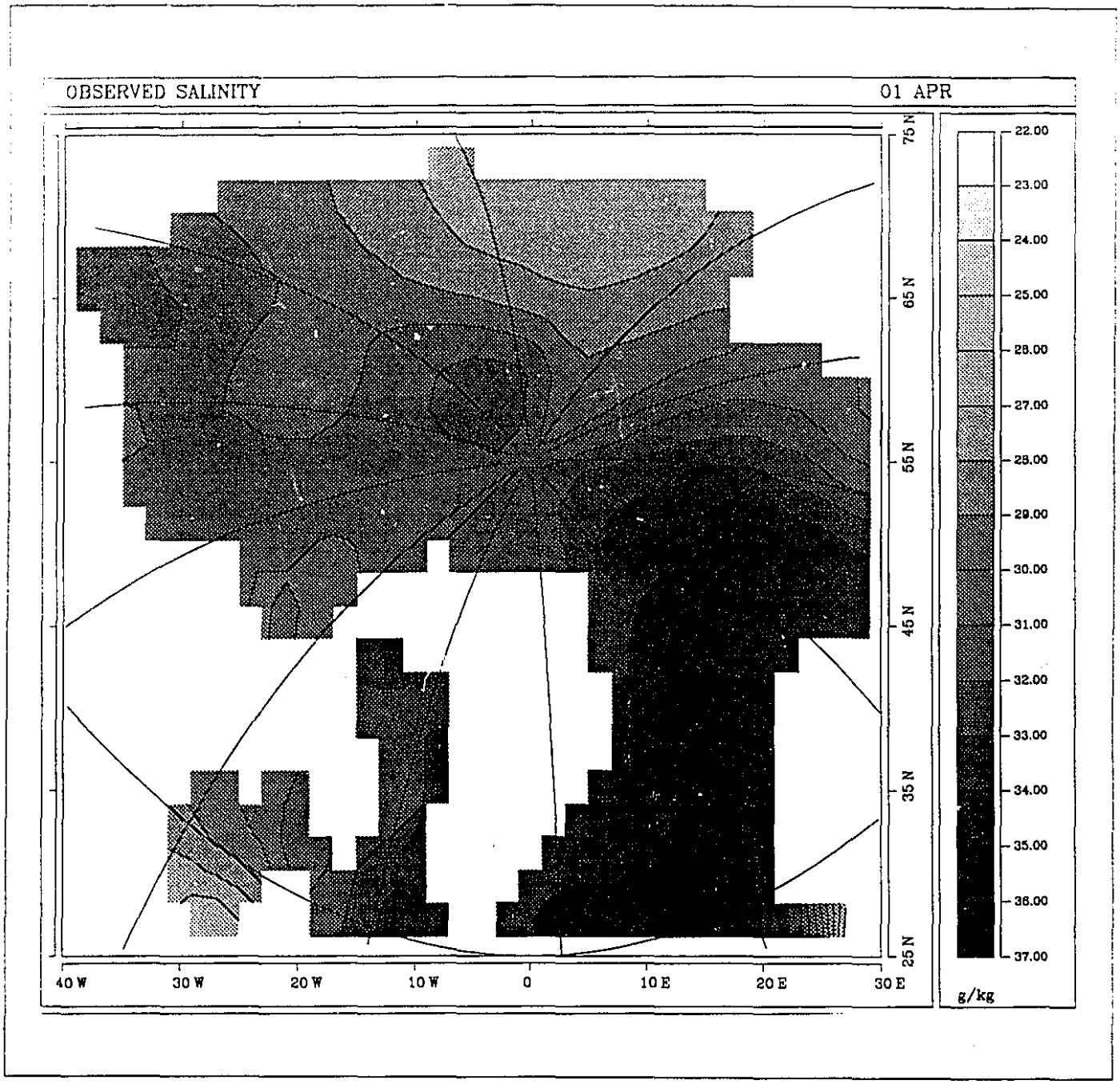

Figure 5.7a The observed April surface salinity distribution based on data from Levitus (1982). The model relaxes its surface salinity to this field at every timestep. Note the low salinity values along the peripheral of the Arctic corresponding to river freshwater input. Also evident is the salinity of the Bering Strait inflow of 31 *psu*. The highest salinity is associated with the inflow to the Arctic of the saline (35 *psu*) water from the GIN Sea.

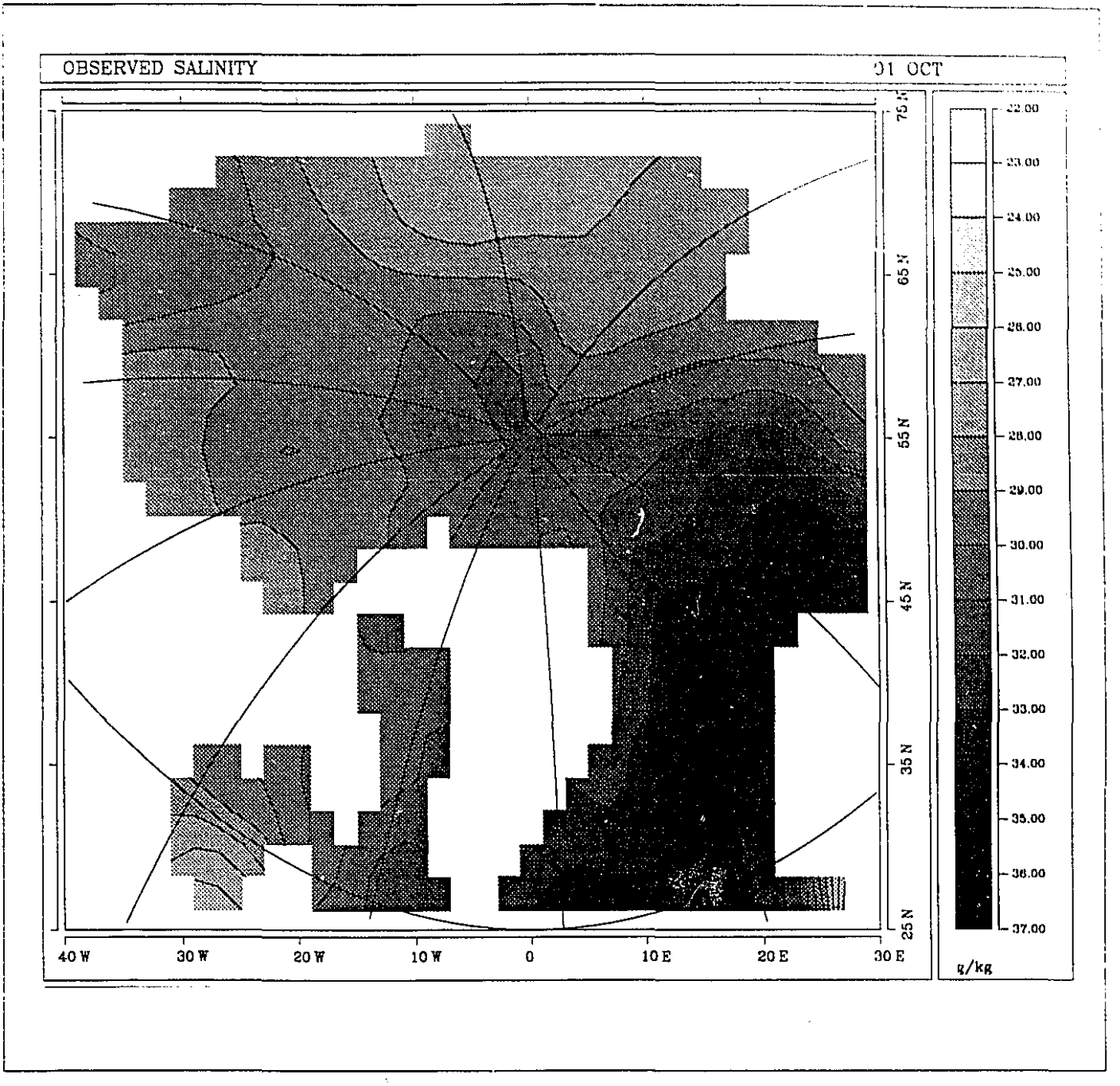

Figure 5.7b The observed October surface salinity distribution based on data from Levitus (1982). The freshwater tongues along the Siberian and Canadian coasts are much more evident than in April.

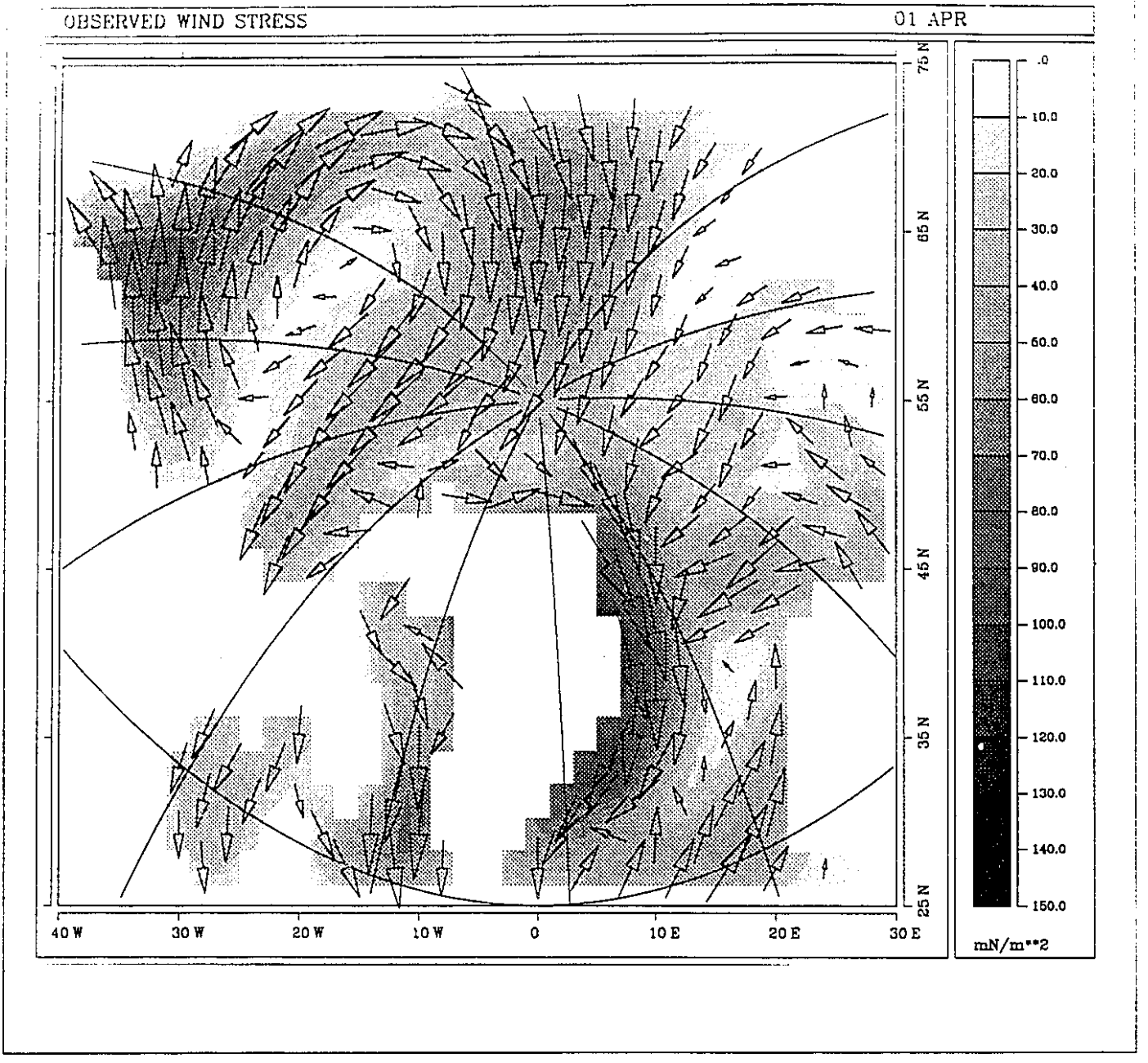

Figure 5.8a The wind stress (N/m^2) for April. A large-scale anticyclonic gyre is evident over the Arctic Basin (the BG). As well, there is a strong flow directed across the Eurasian Basin towards Fram Strait (the TDS). Since each plotted vector corresponds to an actual model grid point, the horizontal resolution used in the model can be inferred from this diagram.

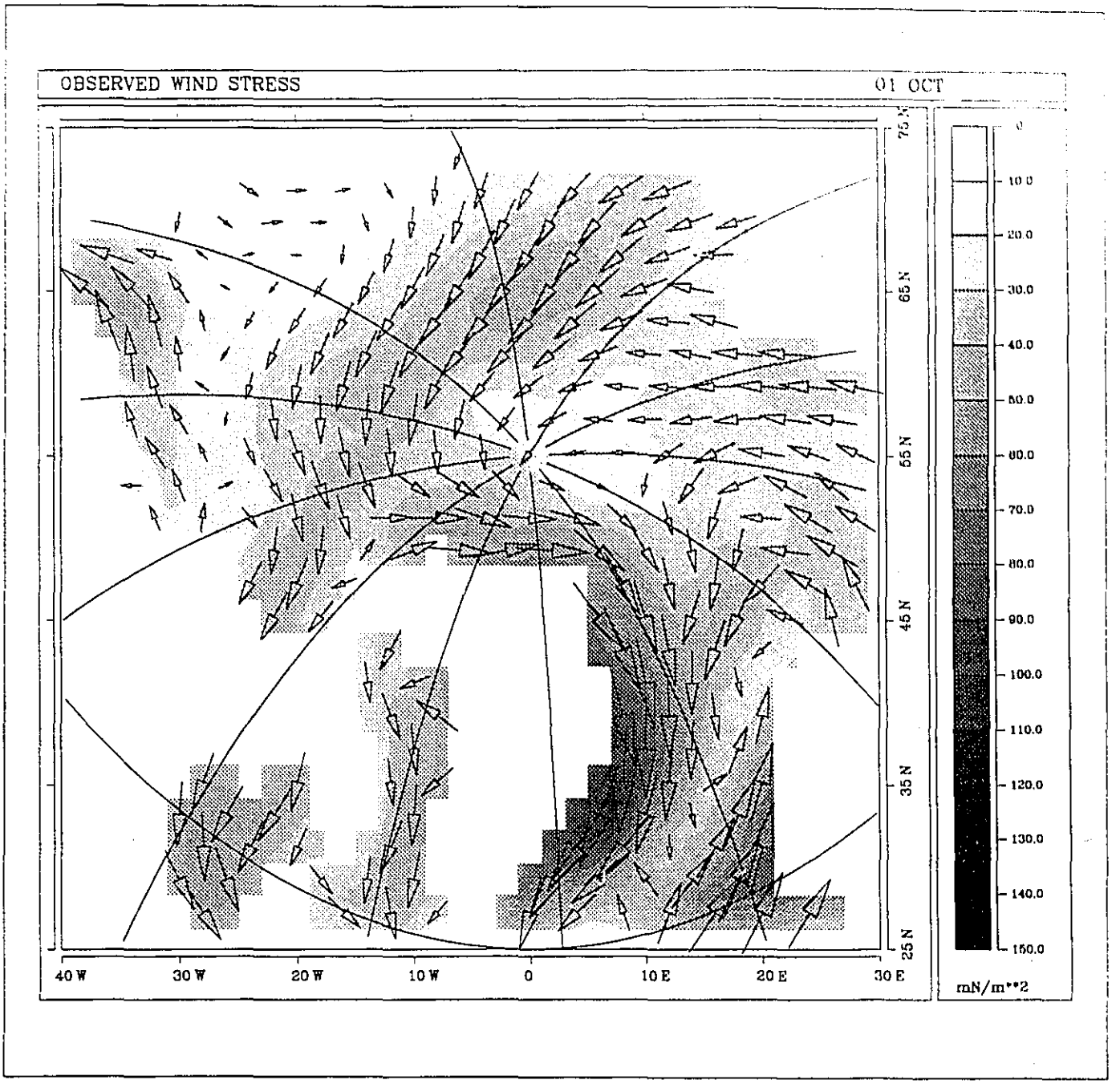

Figure 5.8b The wind stress (N/m^2) for October. There is a change in the wind patterns as compared with April, most notably over the Barents Sea.

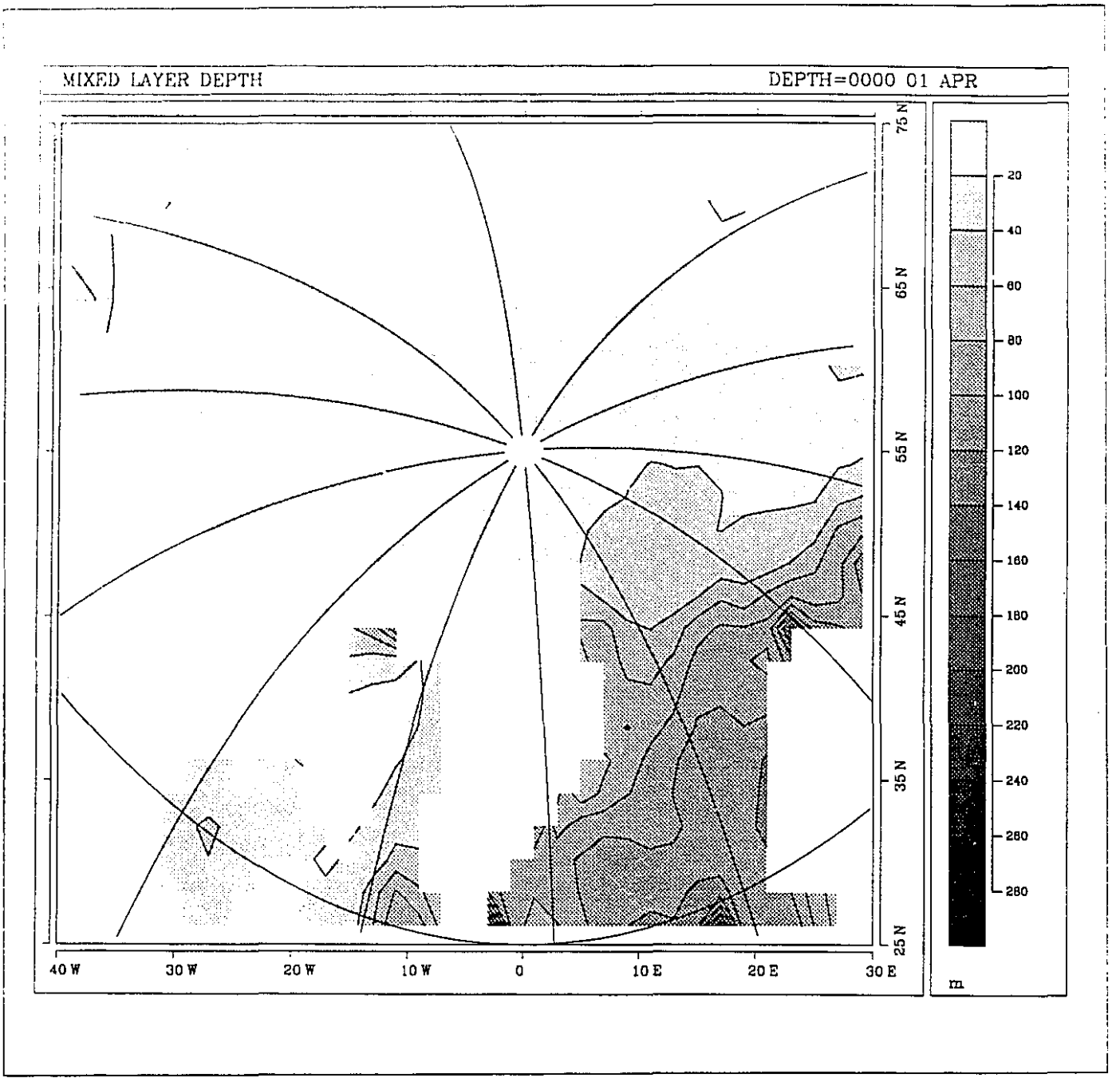

Figure 5.9 Mixed-layer depth (m) for April. The depth is not shown for October.

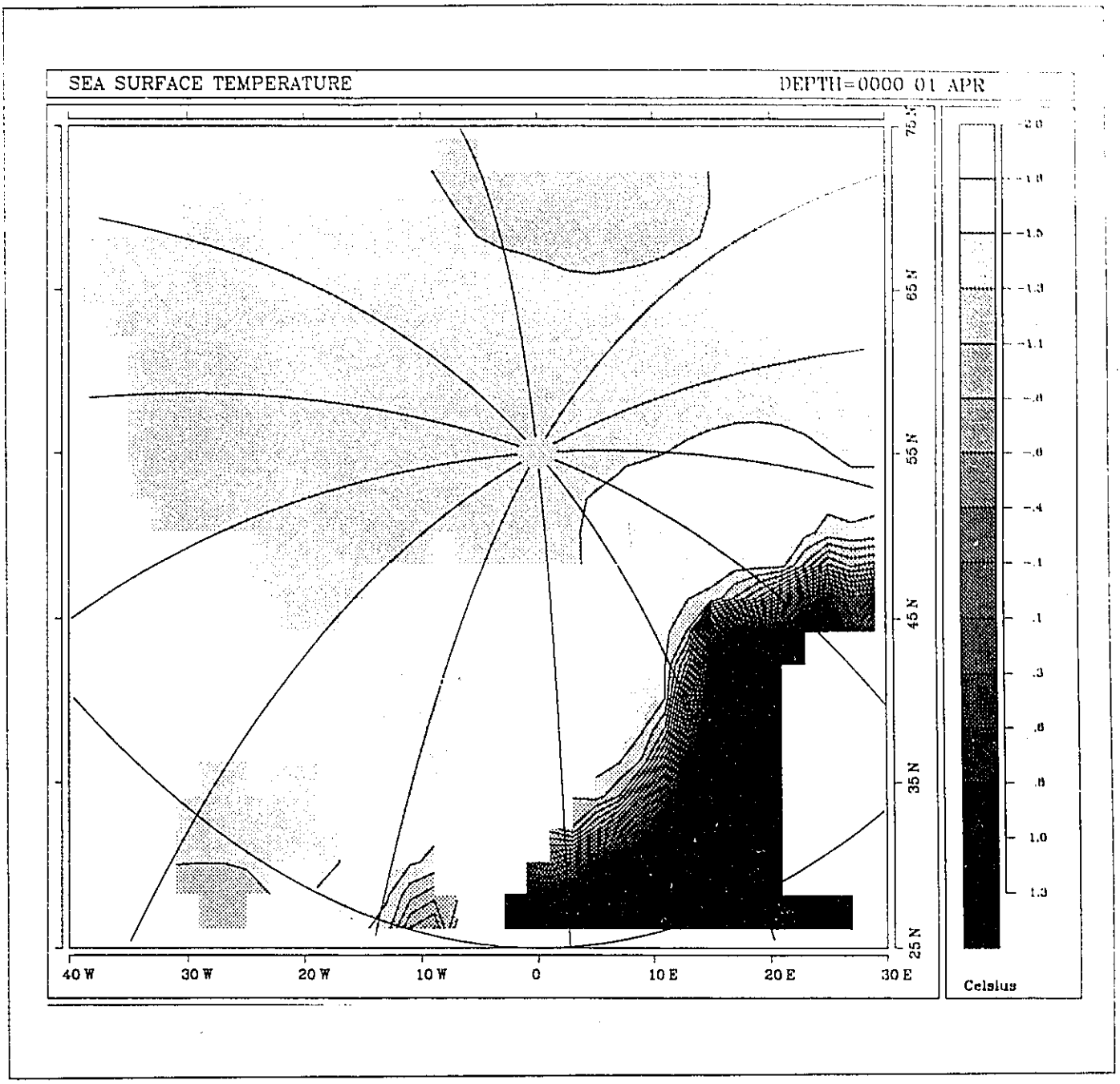

Figure 5.10 Mixed-layer potential temperature (°C) for April. The temperature is not shown for October.

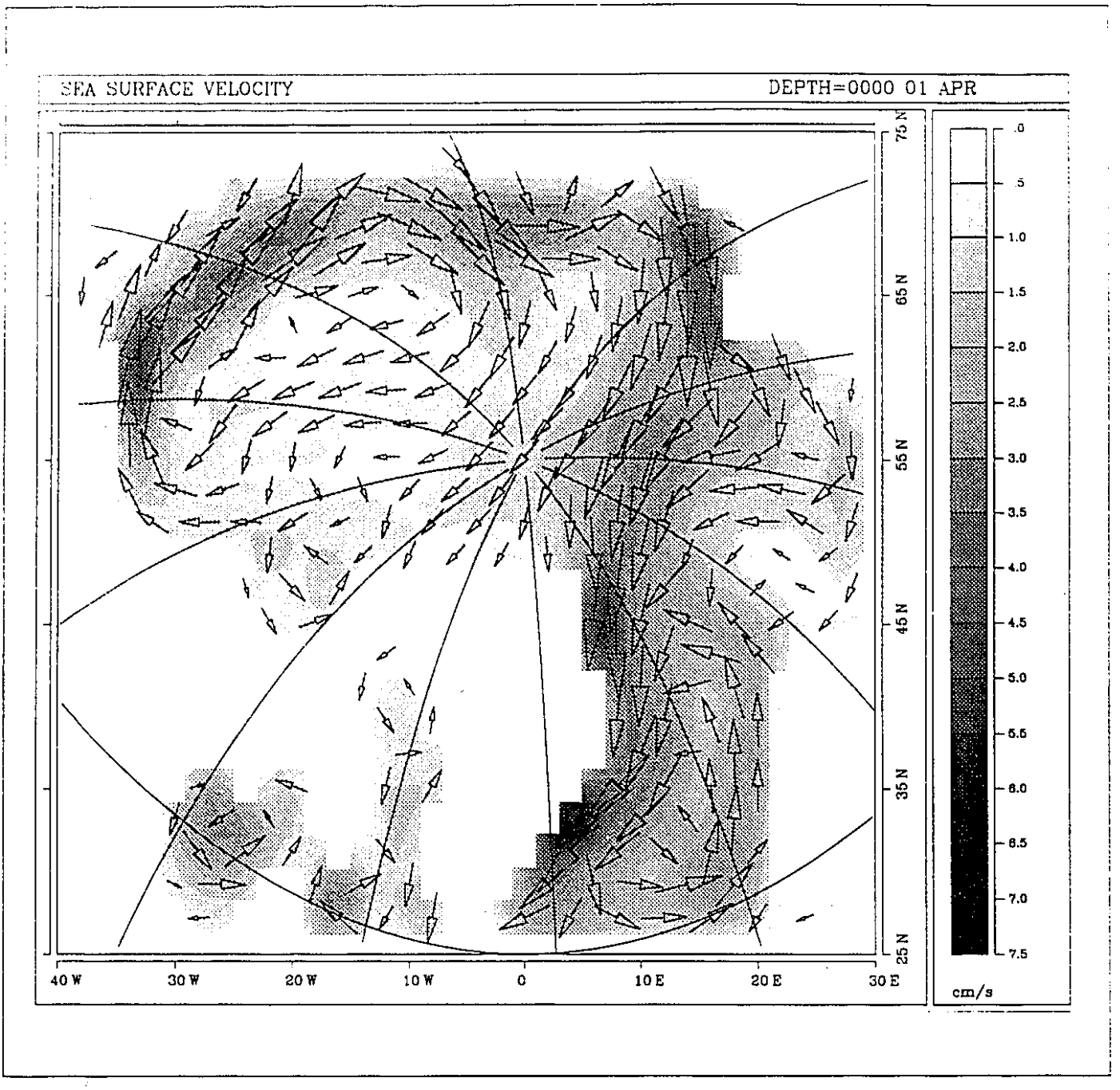

Figure 5.11a Mixed-layer velocities (*cm/s*) for April.

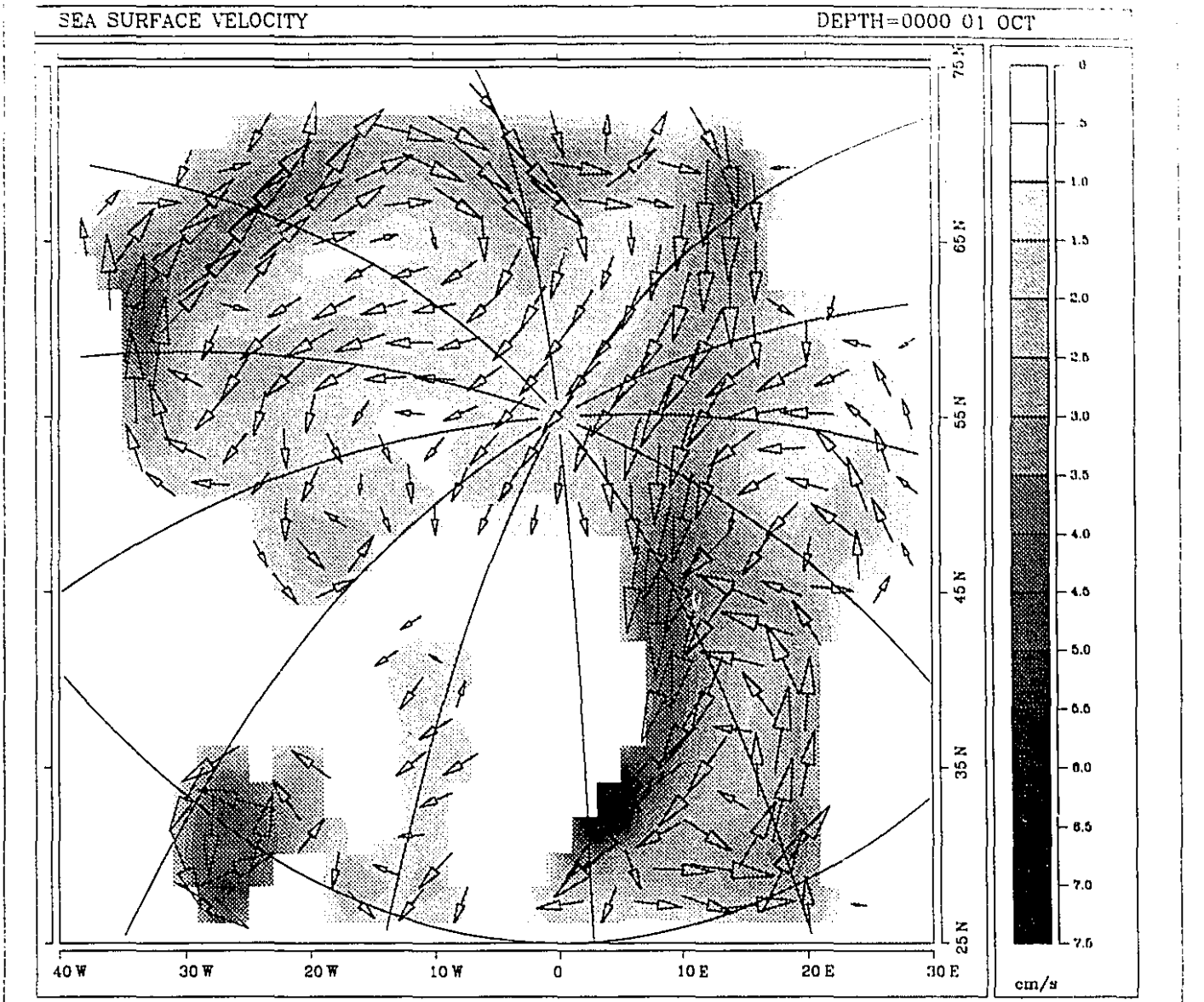

Figure 5.11b Mixed-layer velocities (*cm/s*) for October.

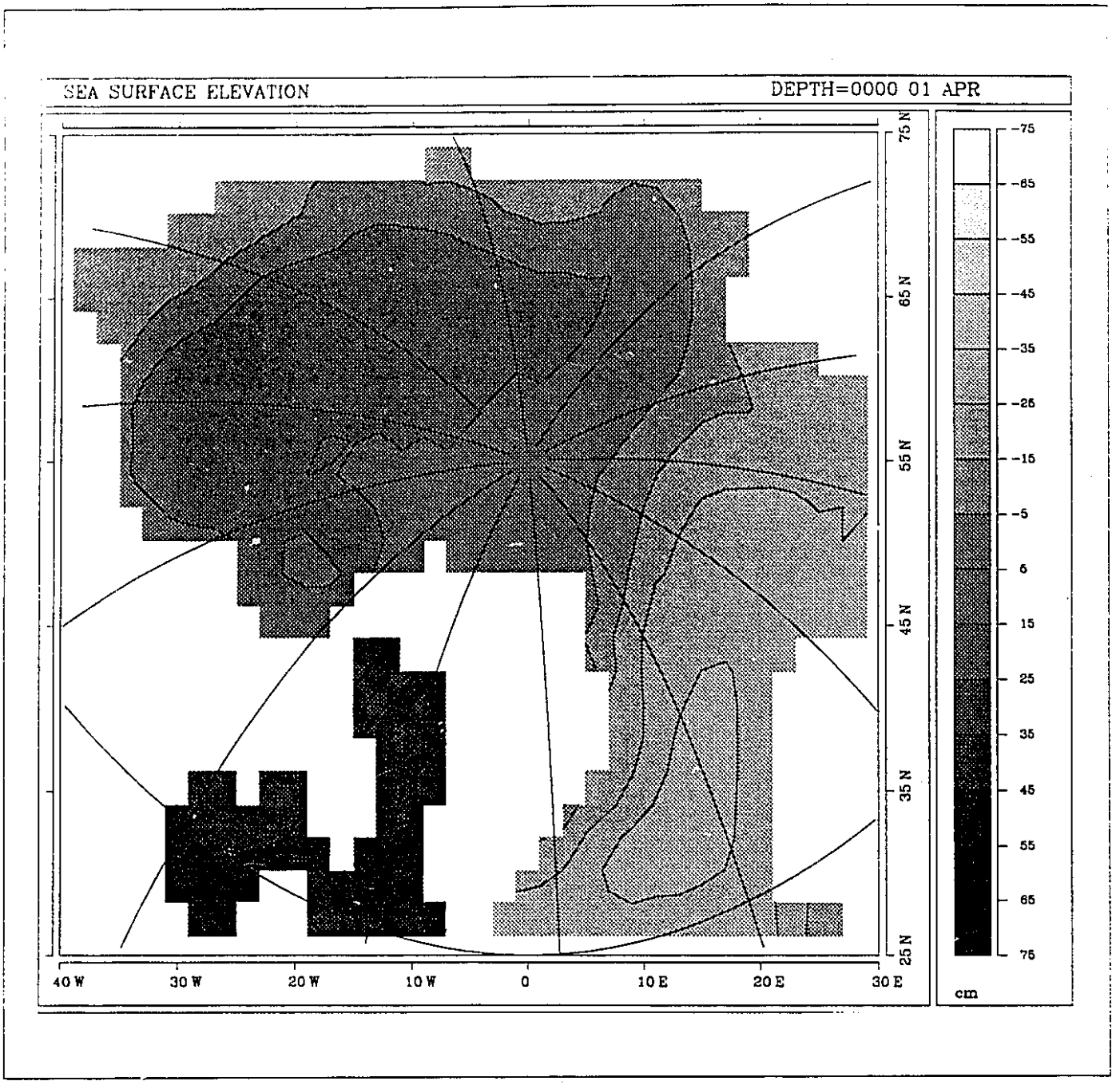

Figure 5.12 Sea-surface elevation (*cm*) for April. The absolute values are not important; rather it is the relative change in sea surface elevation throughout the domain.

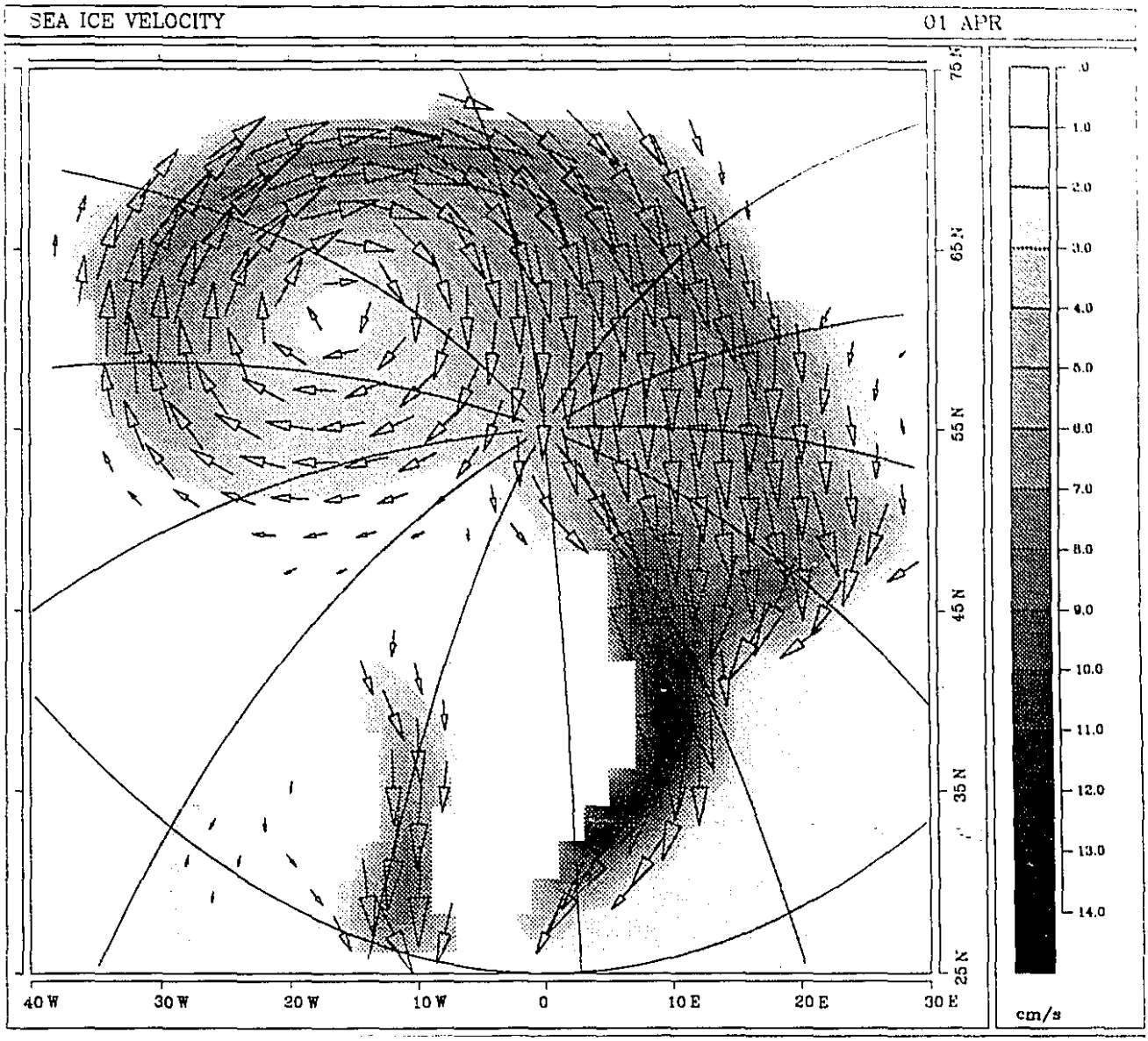

Figure 5.13a Sea-ice velocity (*cm/s*) for April.

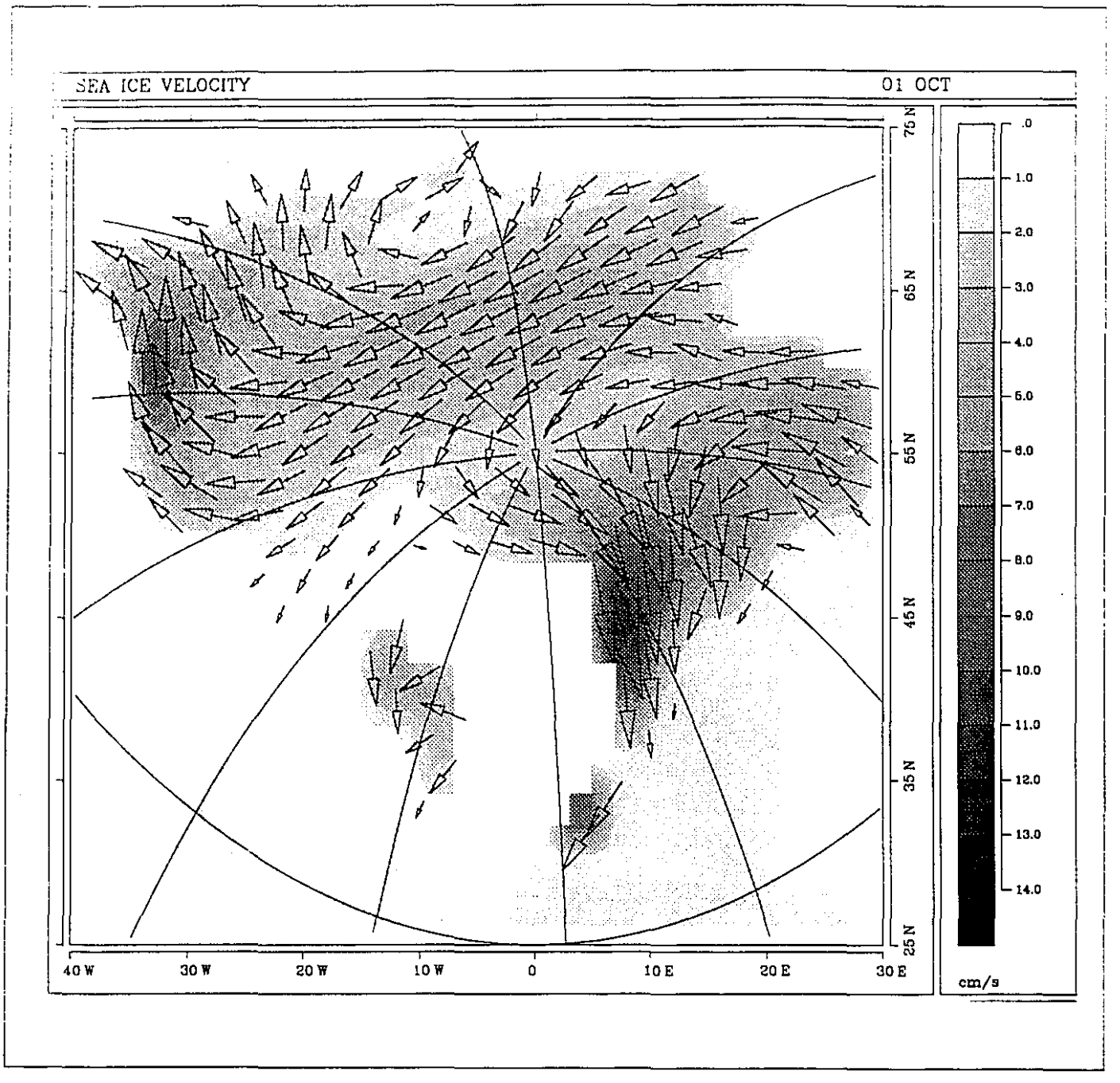

Figure 5.13b Sea-ice velocity (*cm/s*) for October.

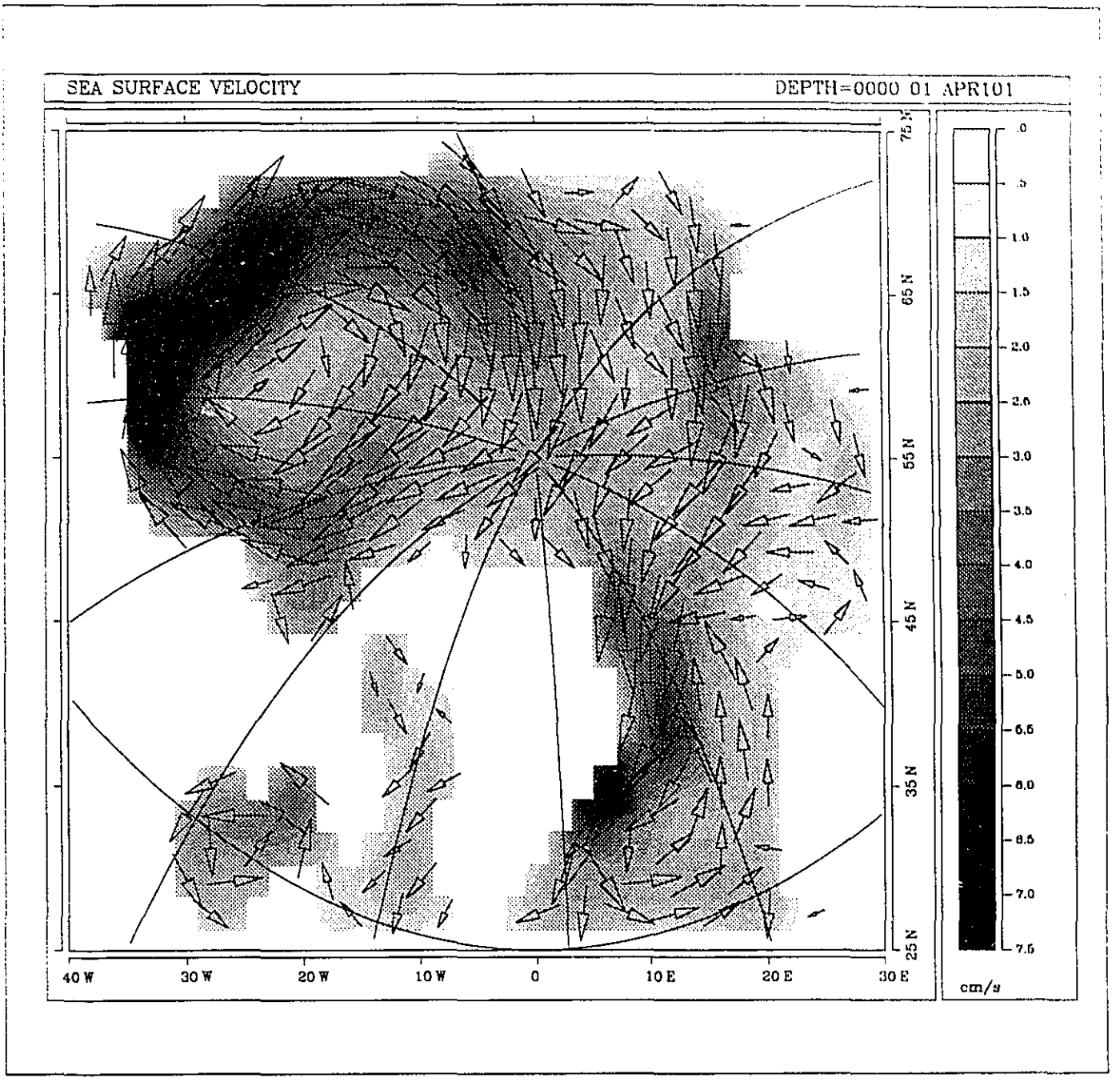

Figure 5.14a Mixed-layer velocities (*cm/s*) for April for the experiment with the sea-ice cover removed.

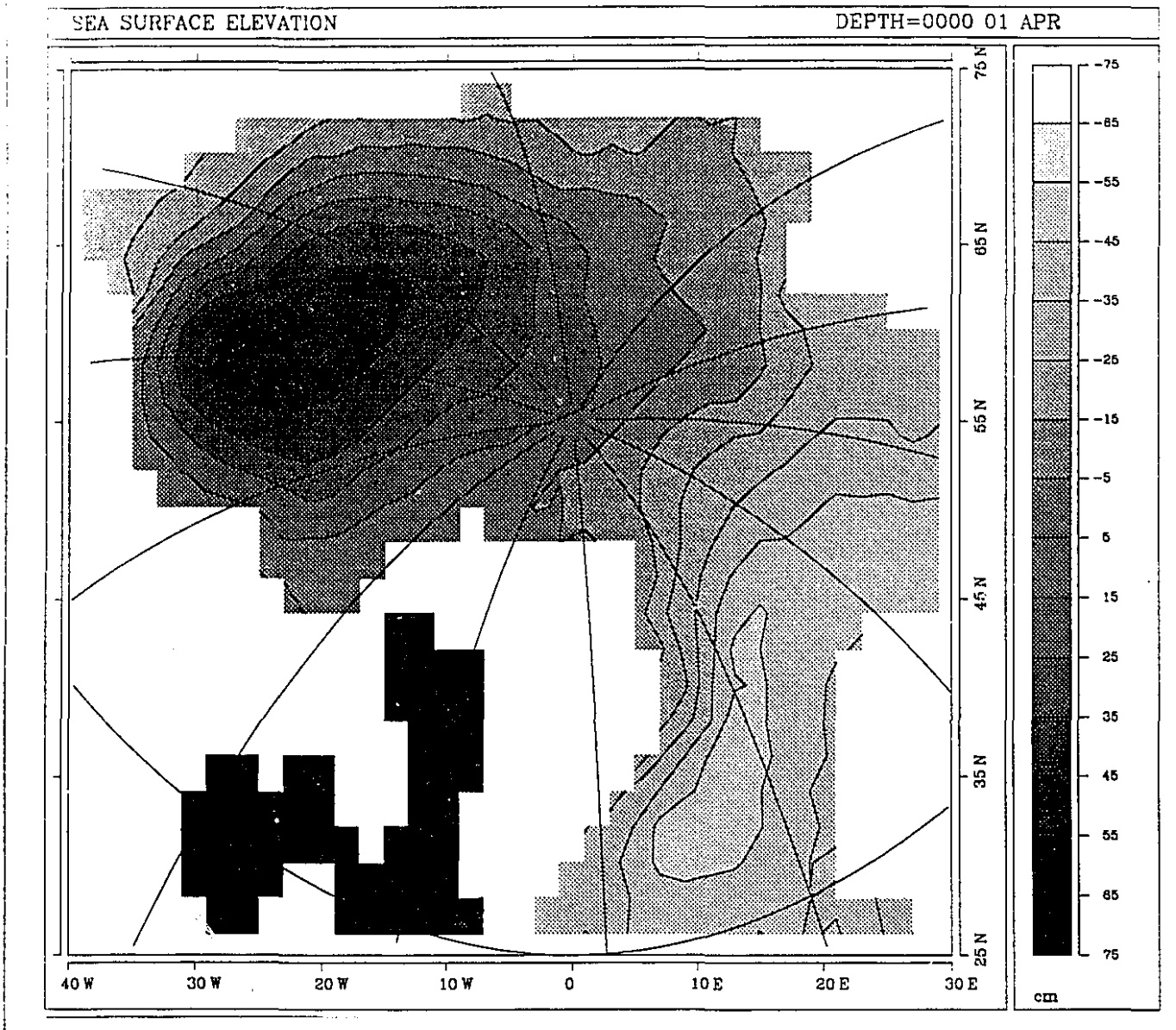

Figure 5.14b Sea-surface elevation (*cm*) for April for the experiment with the sea-ice cover removed. The surface dome over the Canadian Basin is considerably increased in amplitude.

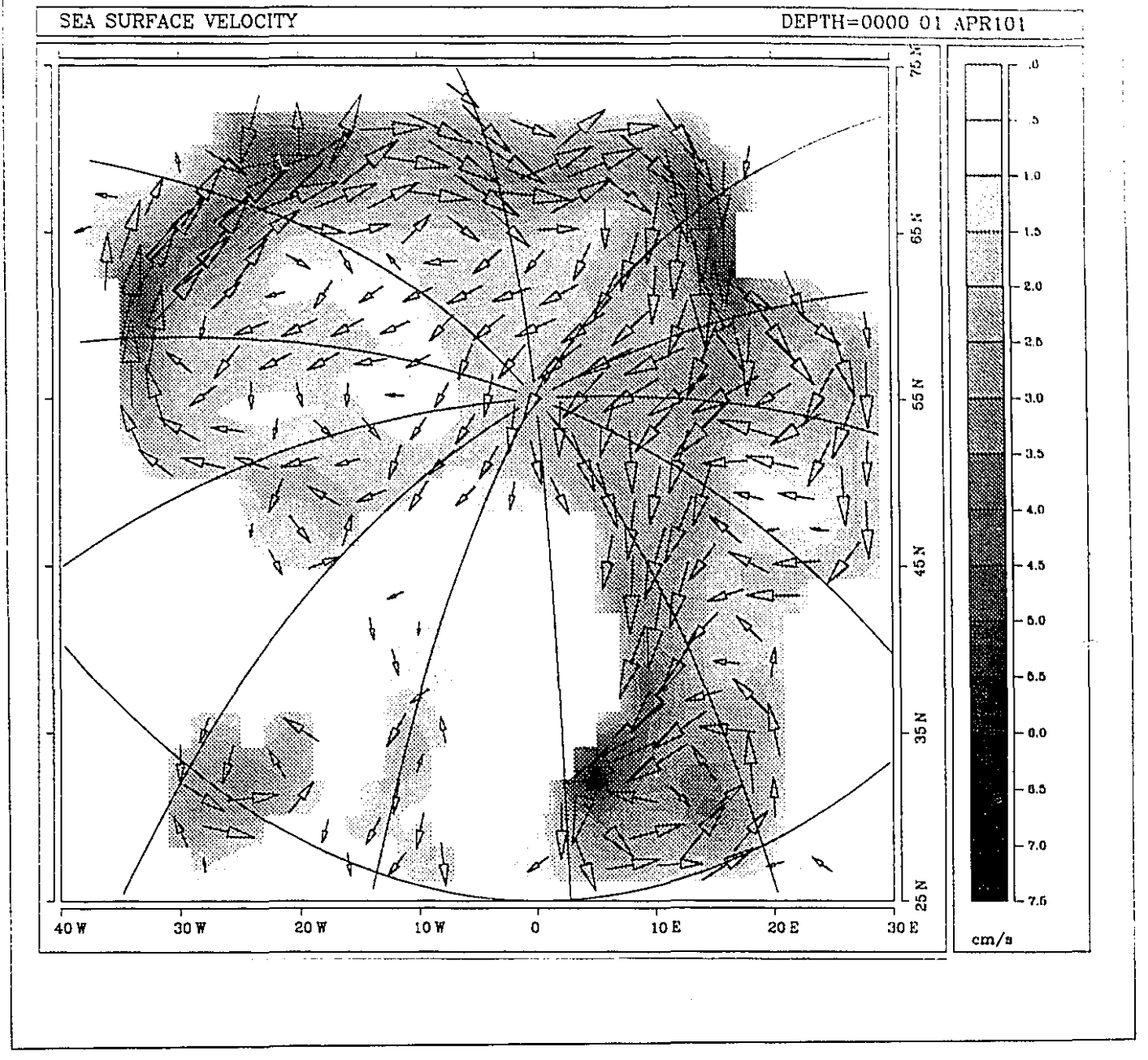

Figure 5.15 Mixed-layer velocities (*cm/s*) for April for the experiment with the wind-stress removed.

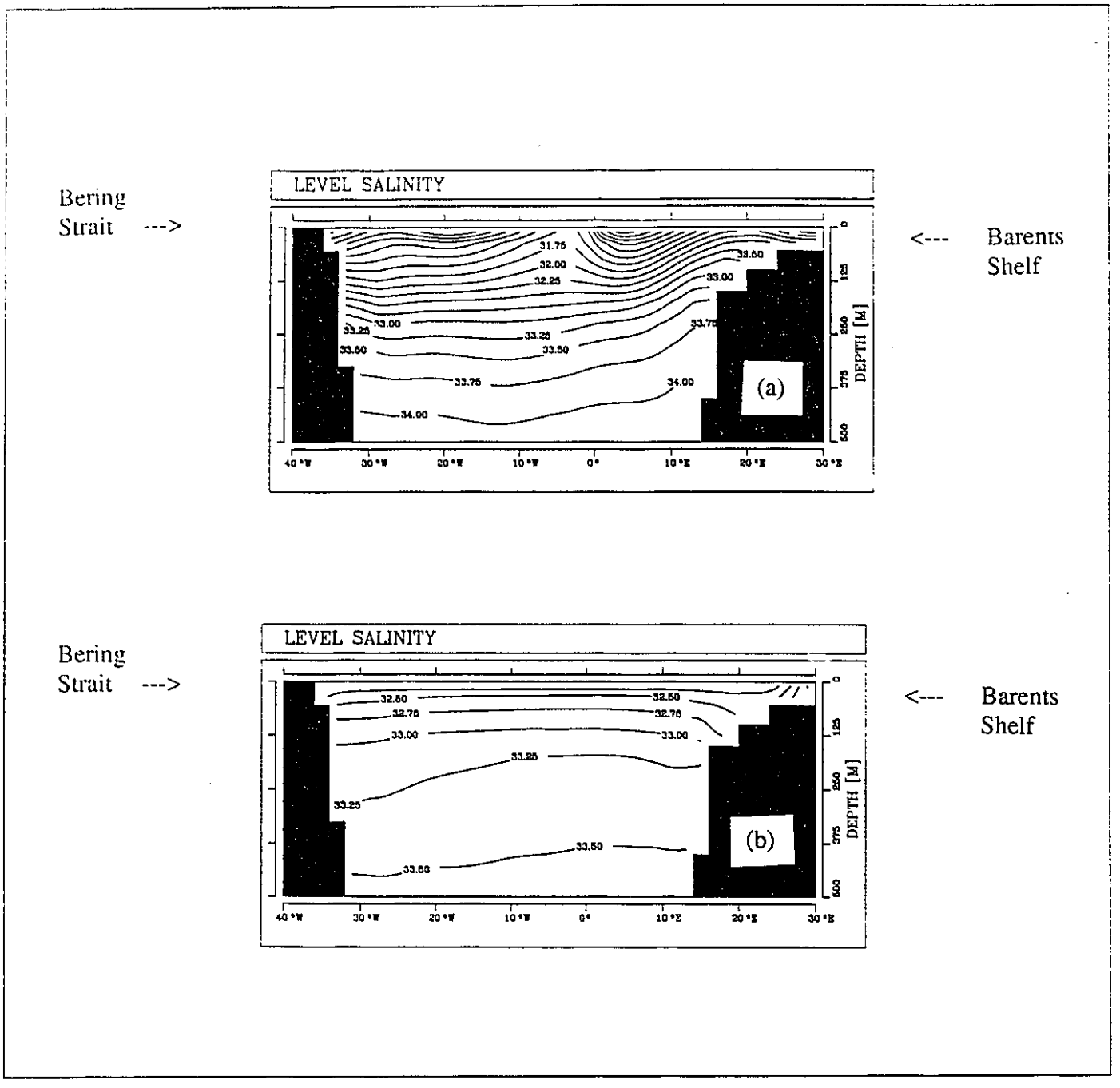

Figure 5.16 Two-dimensional transect across the middle of the Arctic Basin from Bering Strait (*i.e* left side of diagram) to the Barents Sea (*i.e.* right side of diagram). Only the top 500 *m* of the water column is shown. The stratification in the control run (a) has isopycnals with much greater slopes than for the experiment with modified freshwater flux (b). The Lomonosov ridge runs perpendicular to the transect as is located at 0 degrees in the rotated coordinate system. The east-west orientation of the transect is also shown in Fig. 4.13d.

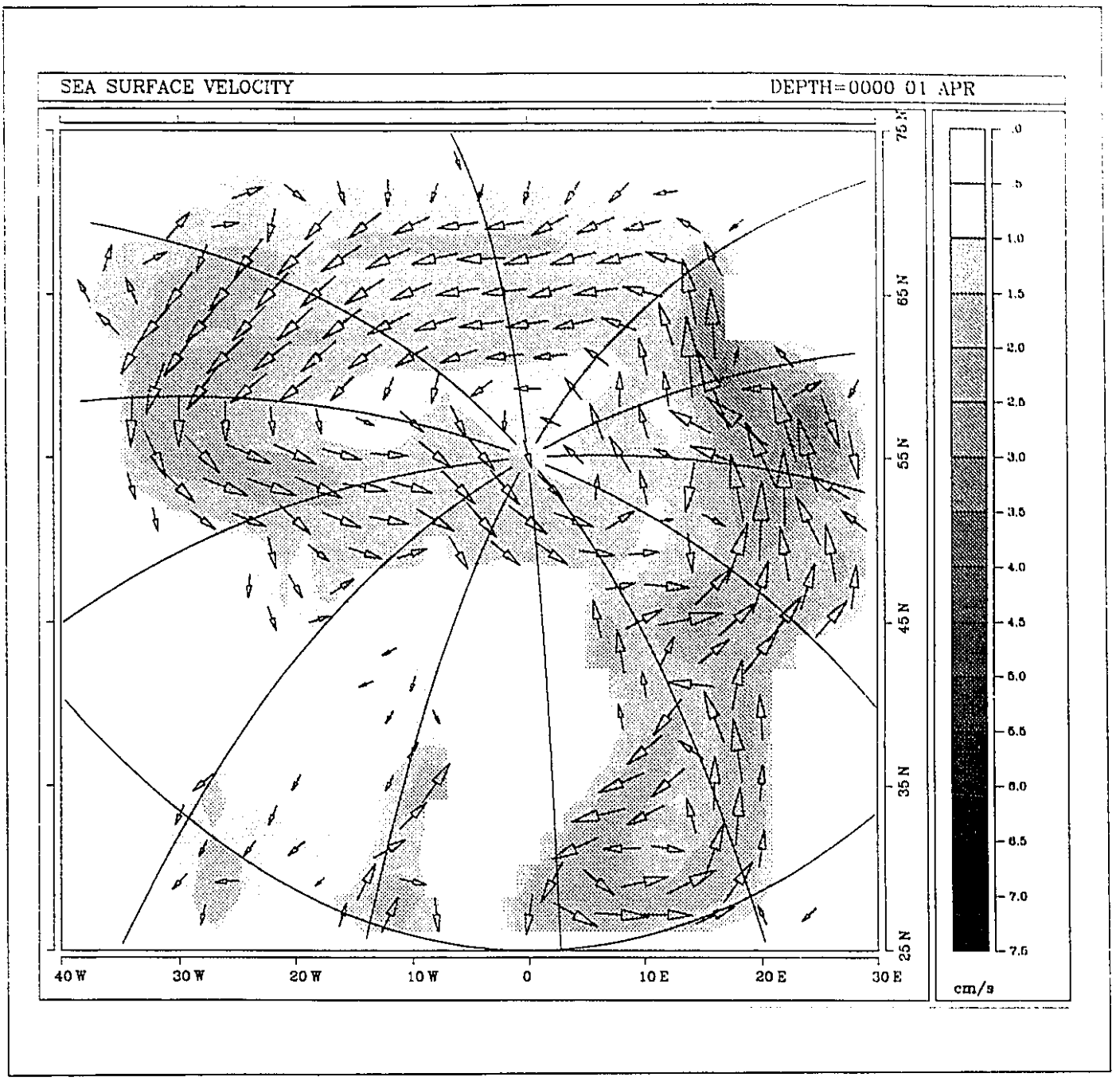

Figure 5.17 Mixed-layer velocities (*cm/s*) for April for the experiment with modified surface freshwater flux. The wind forcing, however, is the same as in the control run.

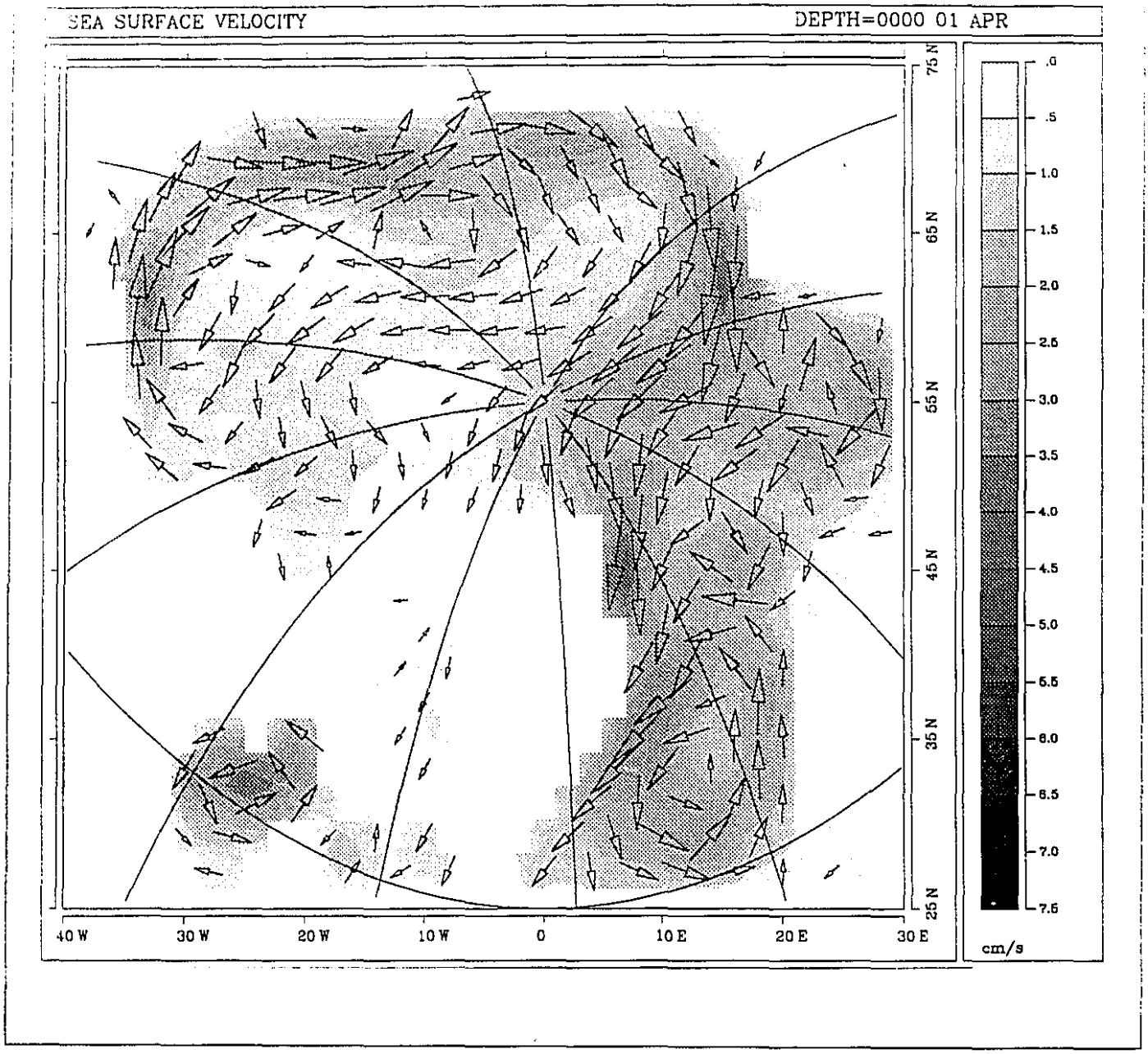

Figure 5.18 Mixed-layer velocities (*cm/s*) for April for the experiment in which the model was not initialized using Levitus data (1982); however, the surface salinity was still relaxed to the observed monthly climatology.

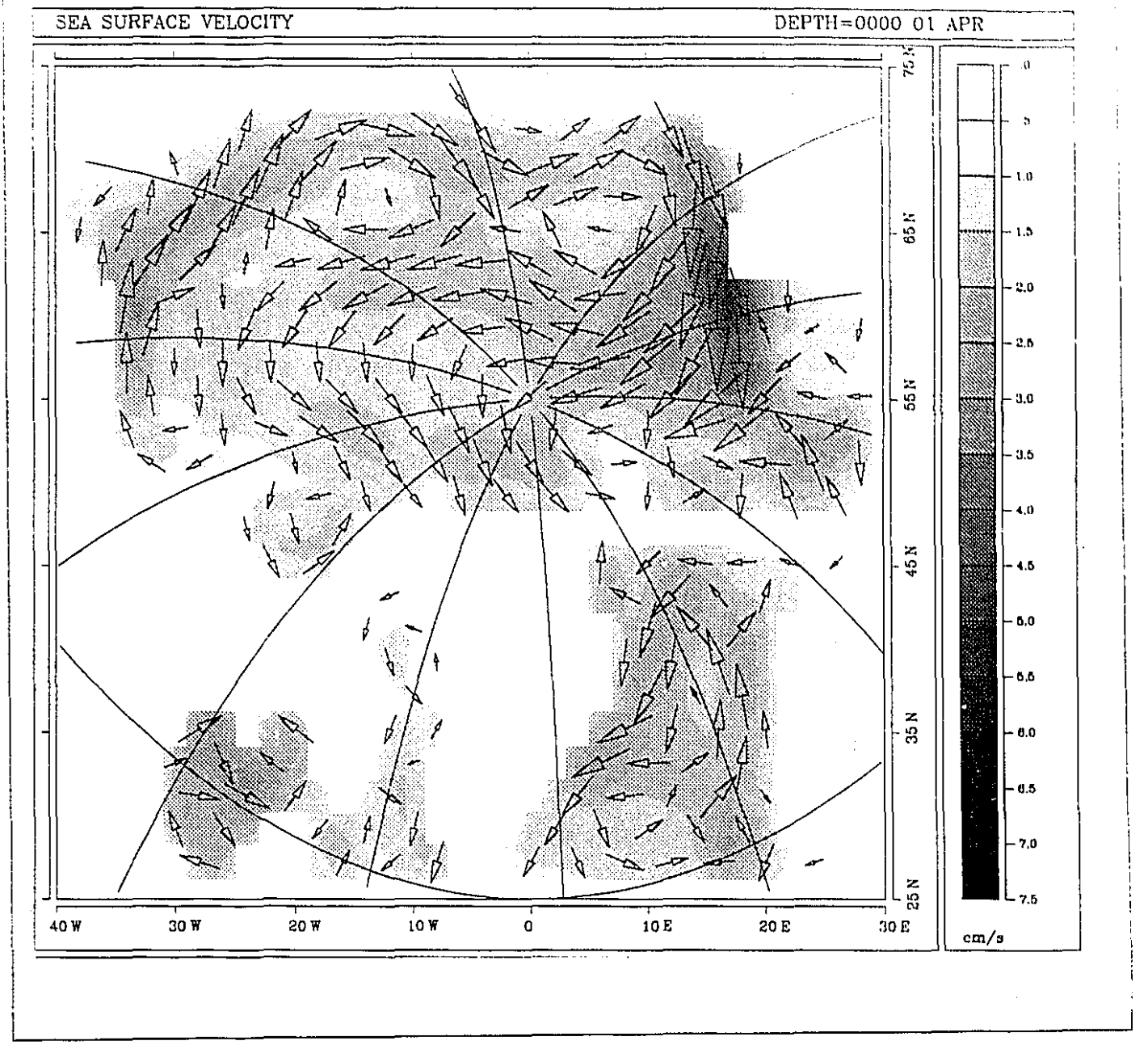

Figure 5.19 Mixed-layer velocities (*cm/s*) for April for the experiment in which the exchange with the GIN Sea has been eliminated.

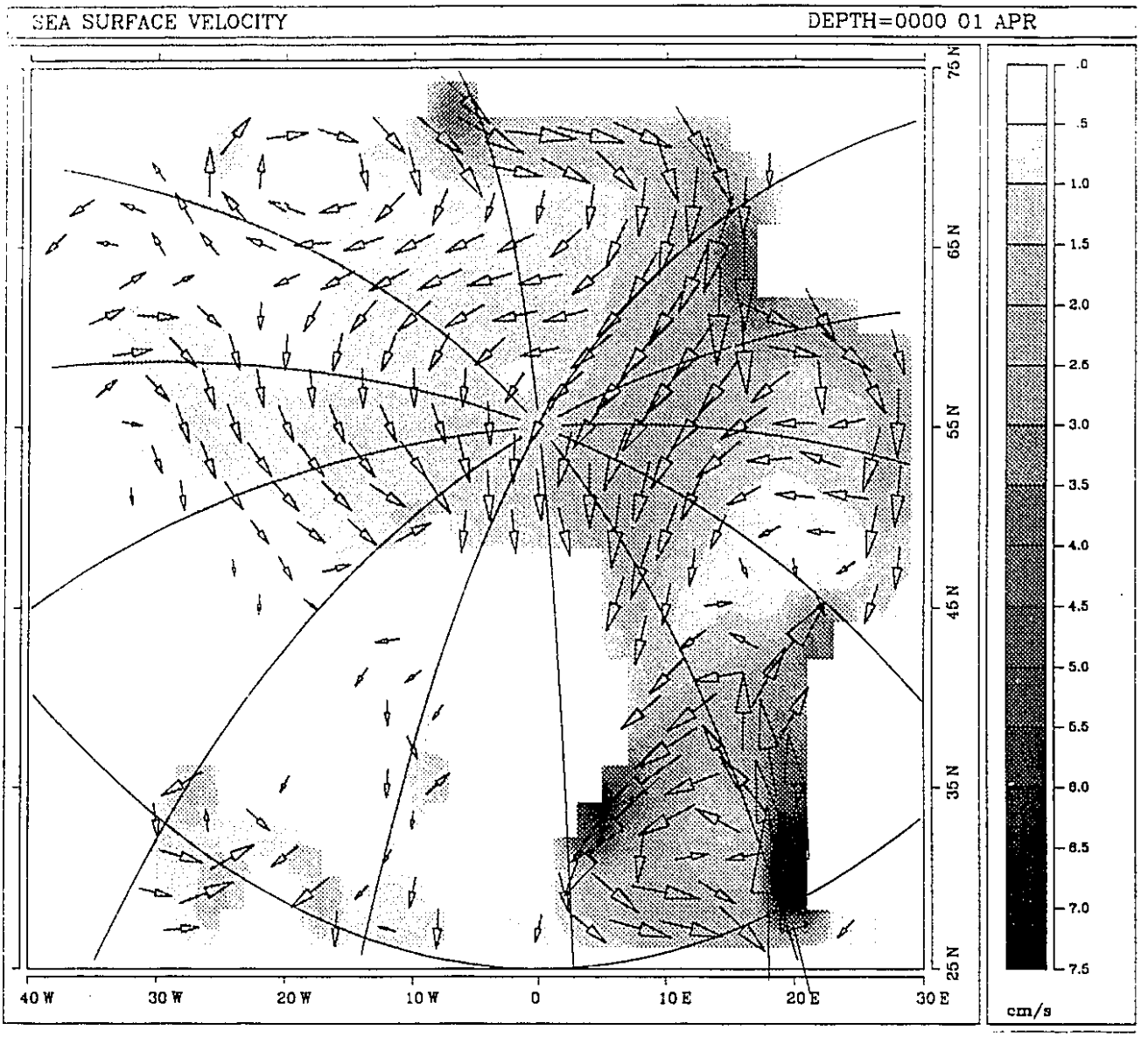

Figure 5.20 Mixed-layer velocities (*cm/s*) for April for the experiment in which the depth is a constant (5000 *m*).

§ 6 Conclusions

This thesis has presented a series of four modelling studies dealing with the Arctic sea ice and ocean circulation. The coupled sea ice - ocean model used in this study is that of Oberhuber (1993a). This is the first application of the Oberhuber model to the Arctic region. Overall, this study has validated the usefulness of the model for simulating the general circulation of the sea ice and ocean in the Arctic.

There are limitations of the model which prevent a direct application of the results presented here to that of the global climate system. First, only in Chapter 3 was a global model domain used, other chapters presented limited domain models, *e.g.* the Arctic Ocean and the North Atlantic Ocean. In reality the Arctic Ocean is intricately connected to the global ocean. Variations in the global thermohaline circulation could have impacts on the Arctic Ocean and vice versa. Such variations are not simulated in this work. Limited computing power is cited as the reason for the limited model domain; future studies will allow for a global ocean model to produce a more realistic simulation of the connection between the Arctic and the other oceans.

Secondly, a major limitation of the model is that it consists only of a coupled ice-ocean model with the atmosphere specified. In reality, the polar climate system includes three freely interacting systems, namely the atmosphere, sea ice, and ocean, with various feedback processes. Only the sea ice and ocean were modeled here while the atmosphere was specified; consequently, there was not a feedback operating between the atmosphere and the sea ice or ocean. Again, this limitation will be overcome with the availability of increased computing power; however, it is important to first carry out studies such as the present one, in which some components of the system are taken as specified, so that we can isolate the sea-ice and ocean components to better understand their behaviour.

Thirdly, the sensitivity experiments that were conducted throughout the thesis have a limited validity because they were carried out by varying one parameter or parameterization at a time, while holding all others in the model fixed. The main difficult with this approach is that in nature, when one thing is altered it almost certainly affects other things; consequently, such "feedbacks" are not addressed in this work.

The main conclusions of each of the four studies is now reviewed. First, the sensitivity study using the uncoupled sea-ice model showed that the Oberhuber formulation in spherical coordinates produced a very robust and reasonable simulation of the sea ice in the Arctic. The numerous sensitivity studies showed that the model can be easily tuned to produce a simulation very close to today's sea-ice climate. Secondly, the incorporation of a snow model into the Oberhuber dynamic-thermodynamic sea-ice model was found to be important, particulary in regions of thin ice-cover that have significant snow cover. This study was performed using the coupled sea ice - ocean model in a global domain. It demonstrated that a reasonable simulation of sea-ice cover could be obtained in both hemisphere using the same set of parameter values for each hemisphere. Thirdly, the simulation of the general circulation of the Arctic Ocean, in a model domain that included the Arctic Ocean and the North Atlantic, produced realistic patterns for the Atlantic layer and the deeper layer. The circulation in the Eurasian Basin was found to be very much controlled by the contours of bottom topography. The vertically integrated flow in the Canadian Basin was found to have a cyclonic sense. Fourthly, the sensitivity study of the mixed-layer circulation in the Arctic showed that both the wind stress and buoyancy forcing are the dominant mechanisms that drive the mixed-layer circulation. Other effects, such as open and closed boundaries, had only second-order effects.

The results of this thesis indicate that further studies of the polar regions can be profitably carried out using the Oberhuber model. Further work will involve simulating the general

circulation of the Arctic Ocean and its connection to the global circulation. The model will likewise be used to investigate the circulation in the Antarctic to make comparisons with observations and other modelling studies. As originally intended, studies of the interannual variability of the sea-ice and ocean circulation in the Arctic will be undertaken using interannually varying atmospheric forcing fields as well as interannually varying river runoff.

References

Aagaard, K., 1989: A synthesis of the Arctic Ocean Circulation. Rapp. P-v Réun. Cons. int. Explor. Mer, **188**, 11-22.

Aagaard, K., 1984: The Beaufort Undercurrent. In The Alaskan Beaufort Sea, Ecosystems and Environments (eds. P.W. Barnes, D.M. Schell, & E. Reimnitz), Academic Press, Florida, pp. 47-71.

Aagaard, K., 1988: Some thoughts on the large-scale circulation of the Arctic Ocean. Preprint Volume Second Conference on Polar Meteorology and Oceanography, march 29-31, 1988, Madison, Wisconsin. Pub. Am. Met. Soc., Boston, Mass., 160 pp.

Aagaard, K., and E.C. Carmack, 1989: The role of sea ice and other fresh water in the Arctic circulation. *J. Geophys. Res.*, **94**, 14,485-14,498.

Anderson, L. G., G. Björk, O.Holby, E.P. Jones, G. Kattner, K.P. Koltermann, B. Liljeblad, R. Lindegren, B. Rudels, and J. Swift, 1993: Water masses and circulation in the Eurasian Basin: Results from the Oden 91 North Pole Expedition. (Article in preparation).

Anderson, R. J., 1987: Wind stress measurements over rough ice during the 1984 Marginal Ice Zone Experiment. *J. Geophys. Res.*, **92**, 6933-6941.

Aukrust, T., and J.M. Oberhuber, 1993: Modelling of the Greenland, Iceland, and Norwegian Seas with a coupled sea ice - mixed layer - isopycnal ocean model. (in preparation).

Björk, G., 1989: A one-dimensional time-dependent model for the vertical stratification of the upper Arctic Ocean. *J. Phys. Oceanogr.*, **19**, 52-67.

Bourke, R.H., and R.P. Garrett, 1987: Sea ice thickness distribution in the Arctic Ocean. *Cold Regions Science and Technology*, 13, 2107-2117.

Budyko M.I., 1966: Polar ice and climate, in *Soviet Data on the Arctic Heat Budget and its Climatic Influence*, edited by J. O. Fletcher, B. Keller, and S. M. Olenicoff, Rand Corporation, RM-5003-PR, Santa Monica, Calif., pp. 9-24.

Campbell, W.J., 1965: The wind-driven circulation of ice and water in a polar ocean. *J. Geophys. Res.*, **70**, 3279-3301.

Carmack, E.C., 1990: Large-scale physical oceanography of polar oceans. In Polar Oceanography, Part A, Physical Science, (ed. Smith), Academic Press, New York, pp. 171-222.

Coachman, L.K., 1963: Water Masses of the Arctic, Proc. Arctic Basin Symp., Arctic Inst. N. America, Washington, DC, pp. 66.

Coachman, L.K., and K. Aagaard, 1974: Physical Oceanography of Arctic and Subarctic Seas. In: Marine Geology and Oceanography of the Arctic Seas (ed. Herman), Springer-Verlag, New York, pp. 1-72.

Coachman, L.K., and C.A. Barnes, 1961: The contribution of Bering Sea water to the Arctic Ocean. *Arctic*, **14**, 147-160.

Coachman, L.K., and C.A. Barnes, 1962: Surface water in the Eurasian Basin of the Arctic Ocean. *Arctic*, **15**, 251-277.

Colony, R., 1991: Seasonal mean fields of ice motion in the Arctic Basin. Polar Science Centre Report, August 1991. University of Washington, Seattle.

Colony, R., and A.S. Thorndike, 1984: An estimate of the mean field of Arctic sea-ice motion. *J. Geophys. Res.*, **89**, 10623-10629.

Colony, R.L., I. Rigor, and K. Runciman-Moore, 1991: A summary of observed ice motion and analyzed atmospheric pressure in the Arctic Basin, 1979-1990. Tech. mem. APL-UW TM13-91, University of Washington, Seattle, Wash., 106 pp.

Cox, M.D., 1984: A primitive equation, three-dimensional model of the ocean. GFDL Ocean Group Tech. Rep. No. 1, GFDL/NOAA, Princeton University, Princeton, 250 pp.

Cubasch, U., K. Hasselmann, H. Höck, E. Maier-Reimer, U. Mikolajewicz, B.D. Santer, R. Sausen, 1992: Time-dependent greenhouse warming computations with a coupled ocean-atmosphere model. *Clim. Dyn.*, (in press).

Flato, G.M., and W.D. Hibler III, 1992: On modelling pack ice as a cavitating fluid. *J. Phys. Oceanogr.*, **22**, 626-651.

Fleming, G. H., 1992: An examination of several ice-control mechanisms in a coupled ice-ocean numerical model of the Arctic. *Atmosphere-Ocean*, **30**, 479-499.

Fletcher, J.O, B. Keller, and S.M. Olenicoff, 1966: Soviet data on the Arctic heat budget and its climatic influence. Rand Corporation, Santa Monica, California, RM-5003-PR, 205 pp.

Galt, J.A., 1973: A numerical investigation of Arctic Ocean dynamics. *J. Phys. Oceanogr.*, **3**, 379-396.

Garwood, R.W., Jr., P.C. Gallacher, and P. Müller, 1985: Wind direction and equilibrium mixed-layer depth: General Theory. J. Phys. Oceanogr., **15**, 1525-1531.

Gudkovich, Z.M., and Y.G. Nikiforov, 1965: A study of the nature of water circulation in the Arctic Basin using a model. *Okeanologiya* (Moscow), **5**, 52-60.

Hibler, W.D. III, 1979: A dynamic thermodynamic sea ice model. *J. Phys. Oceanogr.*, **9**, 815-846.

Hibler, W.D. III, and K. Bryan: 1987. A diagnostic ice-ocean model. *J. Phys. Oceanogr.* **17**, 987-1015.

Holland, D.M., L.A. Mysak, and J.M. Oberhuber, 1991a: Simulation of the seasonal Arctic sea ice cover with a dynamic thermodynamic sea ice model. Centre for Climate and Global Change Research Res. Rep. **91-17**, McGill University, Montréal, Qué. 68 pp.

Holland, D.M., L.A. Mysak, and J.M. Oberhuber, 1991b: Sensitivity Study of a Dynamic Thermodynamic Sea-Ice Model. Centre for Clim. and Global Change Res. Rep. **91-22**, McGill University, Montréal, Qué., 400 pp.

Holland, D.M., L.A. Mysak, D.K. Manak, J.M. Oberhuber, 1993: Sensitivity study of a dynamic - thermodynamic sea-ice model. *J. Geophys. Res.*, **98**, 2561-2586.

Hunkins, K., E.M. Thorndike, and G. Mathieu, 1969: Nepheloid layers and bottom currents in the Arctic Ocean. *J. Geophys. Res.*, **74**, 6995-7008.

Huschke, R.E., 1969: Arctic cloud statistics from air calibrated surface weather observations. Rand Corporation, RM-6147-PR, Santa Monica, Calif.

Idso, S.B., and R.D. Jackson, 1969: Thermal radiation from the atmosphere. *J. Geophys. Res.*, **74**, 5397-5403.

Laevastu, T., 1960: Factors affecting the temperature of the surface layer of the sea. *Comment. Phys. Math.*, **25**, 1.

Large, W.G., and S. Pond, 1982: Sensible and latent heat flux measurements over the sea. *J. Phys. Oceanogr.*, *12*, 464-482.

Legates, D.R., and C.J. Willmott, 1990: Mean seasonal and spatial variability in gauge-corrected, global precipitation. *Inter. J. of. Clim.*, **10**, 111-127.

Levitus, S., 1982: Climatological atlas of the world ocean. NOAA Publ. **13**, U.S. Dept. of Commerce, Washington, D.C., 173 pp.

Lewis, E.L., 1982: The Arctic Oceans: Water masses and energy exchanges. In: The Arctic Ocean (ed. L. Rey), Macmillan Press, London, pp. 43-68.

Manabe, S., R.J. Stouffer, M.J. Spelman, and K. Bryan, 1991: Transient responses of a coupled ocean-atmosphere model to gradual changes of atmospheric CO_2. Part I: annual mean response. *J. Climate*, **4**, 785-818.

Marashunova, M. S., 1966: Principal characteristics of the radiation balance of the underlying surface and of the atmosphere in the Arctic, in *Soviet Data on the Arctic Heat Budget and its Climatic Influence*, edited by J. O. Fletcher, B. Keller, and S. M. Olenicoff, Rand Corporation, Santa Monica, Calif., pp. 51-131.

Maykut, G.A., and N. Untersteiner, 1971: Some results from a time dependent, thermodynamic model of sea ice. *J. Geophys. Res.*, **76**, 1550-1575.

Miller, A.J., J.M. Oberhuber, N.E. Graham, and T.P. Barnett, 1992: Tropical Pacific Ocean response to observed winds in a layered general circulation model. *J. Geophys. Res.*, **97**, 7317-7340.

Mysak, L.A., 1991: Current and future trends in Arctic climate research: Can Changes of the Arctic sea ice be used as an early indicator of global warming? Centre for Climate and Global Change Research Rep. **91-1**, McGill University, Montréal, Canada, 27 pp.

Mysak, L.A., and S.B. Power, 1992: Sea-ice anomalies in the western Arctic and Greenland-Iceland Sea and their relation to an interdecadal climate cycle. *Clim. Bull.* **26**, 147-176.

Mysak, L.A., D.K. Manak, and R.F. Marsden, 1990: Sea-ice anomalies observed in the Greenland and Labrador Seas during 1901-1984 and their relation to an interdecadal Arctic climate cycle. *Clim. Dyn.*, **5**, 111-133.

Oberhuber, J.M., 1988: An atlas based on the COADS data set: The budgets of heat, buoyancy, and turbulent kinetic energy at the surface of the global ocean. Max-Planck-Institute for Meteorology, Hamburg, Report **15**, 199 pp.

Oberhuber, J.M., 1993a: Simulation of the Atlantic circulation with a coupled sea ice - mixed layer - isopycnal general circulation model. Part I: Model Description. *J. Phys. Oceanogr.*, (in press).

Oberhuber, J.M., 1993b: Simulation of the Atlantic circulation with a coupled sea ice - mixed layer - isopycnal general circulation model. Part II: Model Experiment. *J. Phys. Oceanogr.*, (in press).

Oberhuber, J.M, D.M. Holland, and L.A. Mysak, 1993: A thermodynamic-dynamic snow sea-ice model. Ice in the Climate System, NATO ARW Series, Series C: Mathematical and Physical Sciences, W.R. Peltier (ed.), (in press).

Owens, W.B., and P. Lemke, 1990: Sensitivity Studies with a sea ice-mixed layer-pycnocline model in the Weddell Sea. *J. Geophys. Res.*, **95**, 9527-9538.

Parkinson, C.L., and W.M. Kellogg, 1979: Arctic sea ice decay simulated for a $C0_2$-induced temperature rise. *Clim. Change.*, **2**, 149-162.

Parkinson, C.L., and W.M. Washington, 1979: A large scale numerical model of sea-ice. *J. Geophys. Res.*, **84**, 311-337.

Parkinson, C.L., C.J. Josefino, H.J. Zwally, D.J. Cavalieri, P. Gloersen and W.J. Campbell, 1987: Arctic Sea Ice 1973-1976: Satellite Passive Microwave Observations. NASA SP-489, National Aeronautics and Space Administration, Washington, D.C., 296 pp.

Press, W.H., B.P. Flannery, S.A. Teukolsky, and W.T. Vetterling, 1988: Numerical Recipes: The Art of Scientific Computing. Cambridge University Press, 818 pp.

Rey, L., 1982: The Arctic Ocean: The hydrographic environment and the fate of pollutants. Gresham Press, Great Britain, 411 pp.

Ranelli, P.H., and W.D. Hibler III: Seasonal Arctic sea-ice simulations with a prognostic ice-ocean model. *Annals of Glaciology*, **15**, 45-53.

Ries, J.E., and W.D. Hibler III: Interannual characteristics of an 80 *km* resolution diagnostic Arctic ice-ocean model. *Annals of Glaciology*, **15**, 155-162.

Warn-Varnas A., R. Allard, and S. Piacsek, 1991: Synoptic and seasonal variations of the ice-ocean circulation in the Arctic: a numerical study. *Annals of Glaciology*, **15**, 54-62.

Roach, P.J., 1985: Computational Fluid Dynamics. Hermosa Publishers, Albuquerque, New Mexico, 446 pp.

Ross, B., and J.E. Walsh, 1987: A comparison of simulated and observed fluctuations in summertime Arctic surface albedo. *J. Geophys. Res.*, **92**, 13,115-13,125.

Semtner, A.J., Jr., 1976a: A model for the thermodynamic growth of sea ice in numerical investigations of climate. *J. Phys. Oceanogr.*, **6**, 379-389.

Semtner, A.J., Jr., 1976b: Numerical simulation of the Arctic Ocean circulation. *J. Phys. Oceanogr.*, **6**, 409-425.

Semtner, A.J., Jr., 1987: A numerical study of sea ice and ocean circulation in the Arctic. *J. Phys. Oceanogr.*, **17**, 1077-1099.

Serreze, M. C., R.G. Barry, A.S. McLaren, 1989: Seasonal variations in sea-ice motion and effects on sea-ice concentrations in the Canada Basin. *J. Geophys. Res.*, **94**, 10955-10970.

Shine, K.P., and R.G. Crane, 1984: The sensitivity of a one-dimensional thermodynamic sea ice model to changes in cloudiness. *J. Geophys. Res.*, **89**, 10,615-10,622.

Smith, W.O., 1990: Polar Oceanography: Part A Physical Science. Academic Press, San Diego, California, 406 pp.

Stommel, H., A.B. Arons, and A.J. Faller, 1958: Some examples of stationary planetary flow patterns in bounded basins. *Tellus*, **10**, 179-187.

Thorndike, A.S., and R. Colony, 1982: Sea ice motion in response to geostrophic winds. *J. Geophys. Res.*, **87**, 5845-5852.

Trenberth, K.E., J.G. Olson, and W.G. Large, 1989: A Global Ocean Wind Stress Climatology based on ECMWF Analyses. NCAR Tech. Note NCAR/TN-338+STR, Boulder, Colo., 93 pp.

Treshnikov, A.F., 1977: Water masses of the Arctic Basin. In: Polar Oceans (ed. Dunbar), Arctic Institute of N. America, pp. 17-31.

Washington, W.M., and G.A. Meehl, 1989: Climate sensitivity due to increased CO_2: experiments with a coupled atmosphere and ocean general circulation model. *Clim. Dyn.*, **4**, 1-38.

Washington, W.M., A.J. Semtner, C.L. Parkinson, and L. Morrison, 1976: On the development of a seasonal change sea ice model. *J. Phys. Oceanogr.*, **6**, 679-685.

Wright, P., 1988: An atlas based on the COADS data set: Fields of mean wind, cloudiness, and humidity at the surface of the global ocean. Max-Planck-Institute for Meteorology, Hamburg, Report **14**, 70 pp.

Zillman, J.W., 1972: A study of some aspects of the radiation and heat balance of the southern hemisphere oceans. Meteorol. Stud., 26, Bur. of Meteorol., Dep. of the Interior, Canberra, Australia, 562 pp.

Zubov, N.N, 1943: Arctic Ice. Izd. Glavsevmorputi, Moscow.

Zwally, H.J, J. C. Comiso, C.L. Parkinson, W.J. Campbell, F.D. Carsey, P. Gloersen, 1983: Antarctic Sea Ice, 1973-1976 Satellite passive-microwave observations. NASA SP-459, National Aeronautics and Space Administration, Washington, D.C., 206 pp.

Zwally, H.J., A.C. Brenner, J.A. Major, R.A. Bindschadler, J.G. Marsh, 1989: Growth of Greenland ice sheet: Measurement. *Science*, **246**, 1587-1589.